Interaction of water droplets residing on a solid surface with wall-bounded shear flows

by

Xueqing Zhang

A thesis presented to the University of Waterloo
in fulfillment of the thesis requirement for the degree of
Doctor of Philosophy
in
Mechanical and Mechatronics Engineering

Waterloo, Ontario, Canada, 2021

Examining Committee Membership

The following served on the Examining Committee for this thesis. The decision of the Examining Committee is by majority vote.

External Examiner: Alidad Amirfazli
Professor, Dept. of Mechanical Engineering,
York University

Supervisors: Serhiy Yarusevych
Professor, Dept. of Mechanical and Mechatronics Engineering,
University of Waterloo

Sean D. Peterson
Associate Professor, Dept. of Mechanical and Mechatronics Engineering,
University of Waterloo

Internal Members: Cecile Devaud
Professor, Dept. of Mechanical and Mechatronics Engineering,
University of Waterloo

Andrew J. B. Milne
Lecturer, Dept. of Mechanical and Mechatronics Engineering,
University of Waterloo

Internal-External Member: Boxin Zhao
Professor, Dept. of Chemical Engineering,
University of Waterloo

Author's Declaration

I hereby declare that I am the sole author of this thesis. This is a true copy of the thesis, including any required final revisions, as accepted by my examiners.

I understand that my thesis may be made electronically available to the public.

Abstract

Droplet depinning under wind-forcing arises in a wide range of engineering scenarios. Better understanding of this phenomenon not only can optimize the design of relevant engineering systems, but also can help preventing system failures caused by unwanted droplet accumulation. This thesis focuses on physical phenomena associated with the onset of droplet motion in wall-bounded shear flows formed by a flow over a flat plate and impinging jets. Specifically, (i) the critical droplet depinning conditions, and (ii) the influence of droplets on the surrounding flows are considered.

Boundary layer flows and impinging jets were generated by the recirculating wind tunnel and a custom jet facility at the University of Waterloo. The freestream velocity and the jet centreline velocity were programmed to ramp up at three accelerations $\mathrm{d}U/\mathrm{d}t = 1.2$, 2.2, and 4.4 $\mathrm{m/s^2}$. Comprehensive characterization of the background shear flows for droplet depinning tests were carried out using hot-wire anemometry and particle image velocimetry (PIV).

The influence of droplets on ambient shear flows were investigated using scaled-up droplet models representative of the morphological shapes of a sessile droplet (sessile) and a deformed droplet on the verge of depinning (runback). At a Reynolds number representative of critical depinning condition, flow development over droplet models exhibits general similarities to that over other surface-mounted smooth obstacles. In laminar boundary layers, the presence of droplet models significantly modifies the near-wall velocity profiles and promotes laminar-to-turbulent boundary transition in a similar fashion as in bypass transition.

Aerodynamic drag on droplet models submerged in a laminar boundary layer of thickness comparable to the model height was estimated based on flow field measurements using control volume analysis. The drag coefficients of the sessile and runback models are

$C_D \approx 0.36$ and 0.35, respectively, approximately 10% lower than the drag coefficient of the hemisphere. Although the difference in drag coefficients is not significant for the two droplet models, the runback model demonstrated a reduction in drag force as compared to the sessile model, which is proportional to its reduction in the frontal area. For a given solid model, drag decreases significantly with elevated turbulence intensity in the incoming flow.

Real water droplets of 75, 90, 105, and 120 μL were tested in the flat plate boundary layer and impinging jets at orientation angles of 30°, 45°, 60°, and 90° on substrate of anodized aluminium. Droplets in flat plate boundary layer have a constant depinning threshold of $\mathrm{We}_{h,\mathrm{crit}} = 7.5 \pm 0.5$. By contrast, droplets in impinging jets exhibit much lower thresholds in the range $2 \lessapprox \mathrm{We}_{h,\mathrm{crit}} \lessapprox 4$. The effect of droplet volume and flow acceleration on depinning thresholds is small as compared to that of the flow orientation angle. A strong power-law relation is demonstrated between $\mathrm{We}_{h,\mathrm{crit}}$ and volumetric shape factor $\mathcal{K}$, and an empirical relation is established to predict the critical depinning velocity based on droplet volume, length, and height.

Acknowledgements

I would like to sincerely acknowledge my advisors, colleagues, faculty members, technicians, and support staff at University of Waterloo. I would also like to deeply thank the committee members for reviewing this thesis work.

More importantly, I would like to thank all the people who supported me along the way over past five years. Special mentions to my landlords Mr. Fritz and Mrs. Eva Bratan, without whose care, encouragement, and delicious meals, I might have quit in my first year. To my roommates, Yiyue Wang, Xiaoxuan (Cassie) Du, Dr. Pranav Agrawal, Naman Gupta, and Abhinav Dahiya, for all the fun time after work. To my friends, Dr. Xing Meng, Yili (Elain) Tan, Amitvikram Dutta, Prarthana Bhattacharyya, Bo Hu, Shengling Lai, Yifei He, Chunhui Liu, and Zehua (Wedward) Wei, for always being there to back me up despite the distance in space and time. To Auntie Queenie and Uncle Yoho, for providing me a household to fall back on. To Dr. Stefan Pröbsting, without whom I wouldn't have embarked on this journey to Canada. Last but not least, to cats Rice (Whitey) and Milk Tea (Orangy), for curling up beside me and giving me company through most part of the thesis writing.

感谢我的父母，在我十五六岁的时候对我说："当读万卷书，行万里路。如果你愿意，我们支持你游学到三十岁。"仿佛冥冥之中的应誓，自弱冠至而立，十年间辗转客居了四个国度，而今又将开启新的旅程。是你们的智慧、远见、信任、与开明让我有勇气一次又一次背起行囊，踏上征途，虽万千曲折，不畏前行。धन्यवाद यश।

Xueqing Zhang (Caddie)
张 雪晴
February, 2021

Dedication

曒将出兮东方，照吾槛兮扶桑。
抚余马兮安驱，夜皎皎兮既明。
驾龙舟兮乘雷，载云旗兮委蛇。
长太息兮将上，心低徊兮顾怀。

——屈原《九歌·东君》[144]

"It was better to know the worst than to wonder."

——Margaret Mitchell, *Gone with the Wind*[123]

To all the people who inspired me and frustrated me, and made me who I am today.

Table of Contents

List of Tables

List of Figures

List of Symbols, Nomenclature, and Abbreviations

A	Frontal area
AR	Aspect ratio
Au	Streak amplitude
B	Jet nozzle width
B.L.	Boundary layer
BV	Base vortex
c	Droplet (model) width
Ca	Capillary number
CAH	Contact angle hysteresis
C_D	Drag coefficient
$C_{D\mathrm{cl}}$	Centreline drag coefficient
C_f	Skin friction coefficient
CV	Control volume
f	Frequency
$f_\#$	Numerical aperture
F_{adh}	Adhesion

F_D	Aerodynamic drag
F_μ	Viscous force
FOV	Field-of-view
h	Droplet (model) height
H	Nozzle-to-plate spacing
H	Boundary layer shape factor
HSV	Horseshoe vortex
k	Contact angle distribution
$\mathcal{K}$	Volumetric shape factor
K-H	Kelvin-Helmholtz
La	Laplace number
L	Jet nozzle span
La	Laplace number
L_b	Droplet contact length
M	Magnification factor
p	Static pressure
p_γ	Laplace pressure
$\mathcal{P}$	Turbulence production
P_∞	Freestream pressure
PIV	Particle image velocimetry
POD	Proper orthogonal decomposition
Re	Jet Reynolds number
Re_h	Reynolds number based on droplet (model) height
Re_x	Reynolds number based on streamwise distance
Re_Θ	Reynolds number based on momentum thickness

Sk	Stokes number
SP	Stagnation point
St	Strouhal number
t	Time
T-S	Tollmien-Schlichting
u	Streamwise velocity
u_{def}	Streamwise velocity deficit
u_{max}	Local maximum wall jet velocity
u_τ	Frictional velocity
U_{crit}	Critical droplet depinning velocity
U_∞	Freestream velocity
U_j	Jet centreline velocity
v	Wall-normal velocity
v_{drop}	Droplet velocity
V	Droplet volume
w	Spanwise velocity
We	Weber number
x	Streamwise coordinate
x_i	Droplet initial location
x_d	Advancing contact point location
x_r	Length of recirculating region
x_u	Receding contact point location
x_0	Stagnation point
x^*	Streamwise distance from stagnation point
y	Wall-normal coordinate

$y_{1/2,\mathrm{i}}$	Local jet half-width
z	Spanwise coordinate
α	Flow orientation angle
δ	Boundary layer geometric thickness
δ^*	Boundary layer displacement thickness
γ	Surface tension
γ_{lg}	Interfacial tension at liquid-gas interface
γ_{sg}	Interfacial tension at solid-gas interface
γ_{sl}	Interfacial tension at solid-liquid interface
Γ	Circulation
μ	Dynamic viscosity of air
μ_L	Dynamic viscosity of liquid
ν	Kinematic viscosity of air
ω	Vorticity
Π	Dimensionless parameter
Φ	POD mode energy
Ψ	Contact line distribution
ρ	Density of air
ρ_L	Density of liquid
σ	Wall jet growth rate
τ_w	Skin friction
$\overline{\theta_c}$	Mean contact angle
$\theta_{\mathrm{contact}}$	Apparent contact angle
θ_{Cassie}	Apparent contact angle under the Cassie-Baxter state
θ_d	Advancing (downstream) contact angle

θ_u	Receding (upstream) contact angle
θ_{Wenzel}	Apparent contact angle under the Wenzel state
θ_{Young}	Young's contact angle
θ_0	Initial contact angle
Θ	Boundary layer momentum thickness
ζ	Velocity decay rate

Chapter 1

Introduction

This thesis considers the interaction between a droplet resting on a surface and an incoming shear flow. This phenomenon can be so common that one can ignore the small rolling droplets on the windshield when driving in a rainy day. But it can also be so intriguing that it inspires timeless arts, such as a quote by Rabindranath Tagore: *"Let your life lightly dance on the edge of time like dew on the tip of a leaf* [181]*."*

The following sections provide a technical overview of the problem under investigation. Specifically, Sect. 1.1 introduces the conceptual background of the problem and its relevance to engineering applications. Sect. 1.2 identifies the research gaps in existing studies. Sect. 1.3 states the motivations and objectives of this study. Sect. 1.4 presents the thesis outline and highlights the major topics discussed in the remaining chapters.

1.1 Conceptual and engineering background

When a droplet resting on a surface is exposed to an incoming shear flow, the droplet experiences a downstream-directed force exerted by the flow and an upstream-directed force due to the adhesion between the droplet and the surface. Fig. 1.1 shows the typical side and top-view conformations of a droplet in response to increasing flow speed. At low flow speed, the droplet deforms from its initial axisymmetric shape to resist depinning and may oscillate under the flow. The droplet dislodges from its initial location when the critical flow speed is reached and the aerodynamic loading overcomes the adhesion. At still higher flow speeds, the droplet sheds along the surface.

Droplets under the action of shear flow arise in a large number of engineering ap-

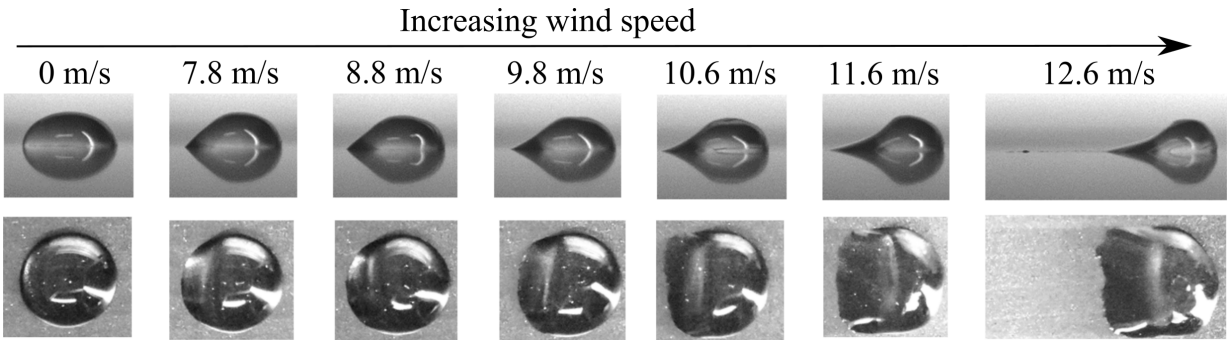

Figure 1.1: Shedding of a 120 μL droplet under accelerating shear flow formed by an oblique impinging slot jet at 45°. The acceleration measured at the jet centreline at the jet exit is $\mathrm{d}U_j/\mathrm{d}t = 1.2\,\mathrm{m/s^2}$. The droplet is initially deposited at around four slot widths downstream of the impingement point.

plications, such as aircraft and wind turbine icing [200, 94, 52, 6, 124, 80], PEM fuel cells [215, 188, 66, 47], heat exchangers [87], oil recovery [165, 111], and numerous surface cleaning and drying processes [190, 6, 57, 104]. The associated phenomena can be broadly divided into two categories, namely, droplet dynamics under wind-forcing and flow development over droplets. For example, ice accretion on wings and wind turbines is closely

related to whether the impinging droplets on the leading edge can shed before freezing [90]. Flow perturbations introduced by the presence of droplets and the subsequent ice formation significantly affect the aerodynamic performance of aircraft [61] and power efficiency of wind turbines under icing conditions [37]. Understanding the associated changes in flow development aids in predicting the changes in service envelope and avoiding the catastrophic consequences caused by premature stall. On the other hand, insights into droplet behaviours under the typical shear flow conditions at an airfoil leading edge enables better modeling of ice accretion rates and designs of anti-icing surface materials.

In PEM fuel cells, electricity is generated by the reaction between hydrogen and oxygen. The byproduct of this process is water, which forms droplets on the membrane interface and impedes the proton exchange. Water exhaust systems use air flow over the membrane to sweep away these droplets. Thus, finding the flow speed to shed the smallest droplets on the membrane is critical for the efficiency of the fuel cells.

A similar concept of water management is required for the condenser surfaces of heat exchangers. Since the efficiency of heat transfer is largely associated with condensation of liquid droplets, removing existing droplets from the condenser surface effectively and allowing the formation of new ones are crucial for heat exchanger performance [87].

In non-touch cleaning/drying procedures of medical devices, food processing, and textile industries [157], impinging jets are usually used to remove non-volatile liquid contaminants from surfaces. Unlike in the previous examples, the incoming flow and the target surface are non-parallel. Hence, apart from jet velocities, jet angle and position relative to the surface may also affect the effectiveness of droplet removal [104]. Identifying optimal jet parameters for the expected range of liquid droplets and surface material is key to optimizing the non-touch cleaning system, in terms of improving effectiveness, reducing energy consumption, and controlling noise emission.

1.2 Research gaps

Driven by the wide-spread engineering applications, droplet depinning under wind-forcing has been investigated with analytical (e.g. [42]), computational (e.g. [40]), and experimental approaches (e.g. [121, 80, 201]). Much attention has been focused on finding the critical flow conditions for depinning of an isolated droplet submerged in a flat plate boundary layer. These studies explored the dependencies of critical depinning velocities as functions of droplet volume [200, 121, 201], surface wettability [121, 153, 124], ambient flow temperature [153], and turbulence intensity [200, 57]. Attempts have also been made to develop a universal model to predict depinning velocities for varying droplet-flow-substrate systems. For instance, Milne and Amirfazli [121] proposed that the exponential relation between the critical depinning velocity and the square root of the ratio of droplet contact length to frontal area at sessile states; using this model, their test results acquired for droplet-substrate systems with varying wetting properties and droplet volumes collapses reasonably well on a self-similar curve. Roisman *et al.* [153], instead, proposed that the critical velocity is proportional to the cubic root of droplet volumes; their test results acquired at room temperature and under icing conditions were used to develop and support this model. However, comparing test results of these two studies for the same combination of droplet-flow-substrate systems and similar droplet volumes reveals discrepancies in both critical velocities and droplet geometries at depinning (see Table 7.3 for detail). The source of these discrepancies may lie in the effects of the near-wall velocity profile and relative submergence of droplet height to boundary layer thickness, which were not taken into consideration by most studies, but can significantly affect the flow momentum experienced by the droplet [200].

Another important input parameter that has not previously been explicitly consid-

ered, to the author's knowledge, is the flow acceleration before critical depinning velocity is reached. Many experimental studies used quasi-steady flow conditions by 'slowly' increasing the velocity [120, 170, 201], while others assumed negligible flow ramp-up time using flow generated by high pressure gradient along a flow duct [124]. By introducing air flow from the high pressure tank and setting the end velocities at 5 m/s and 90 m/s, Moghtadernejad *et al.* [124] investigated the coalescence of two droplets in a tandem configuration on a superhydrophobic surface and observed more significant deformation and lift-off for the coalesced droplet at high end velocity. Although the authors did not explicitly study the effect of flow accelerations, the distinctive droplet response observed at the high end velocity may potentially result from a higher flow acceleration than that at the low end velocity. It is unclear, however, how flow acceleration may quantitative affect droplet depinning conditions, if at all.

Furthermore, unlike the richer literature available for droplet behaviours in flat plate boundary layers, limited attention has been given to droplet removal by impinging jets despite its close relevance to cleaning and drying applications. To the best of the author's knowledge, there is only one study reporting jet exit velocity required for surface droplet removal. Leung *et al.* [104] suggested jet velocity requirements for removing distributed millimeter-sized droplets with an impinging round jet. The critical condition was defined as the jet exit velocity with which around 50% of the scattered droplets were displaced. Although this study might be informative for a specific jet configuration, it is not sufficient to instruct cleaning/drying system designs due to the lack of information of flow fields, surface wetting parameters, and droplet behaviours under varied jet configurations.

In addition, despite the advances made towards understanding droplet dynamics in the depinning processes, flow development over droplets is limitedly considered [40, 110, 45]. Given a significant separation between the time scales associated with relatively slow

droplet deformations [122, 20] and comparatively fast hydrodynamic fluctuations in the surrounding flow [178], this can be approximated by flow development over surface-mounted solid obstacles with the morphological shapes of droplets under wind-forcing. The morphological configurations of wind-forced droplets have similarities with smooth surface-mounted obstacles. Previous studies have considered the flow fields over a variety of smooth obstacles [159, 133, 72, 21]. Typically, the presence of such surface-mounted objects induces multiple interacting vortex systems and modifies the near-wall velocity profile, accelerating the laminar-to-turbulent transition in a similar fashion to bypass transition [210]. The presence of droplets in a laminar boundary layer may play similar roles as surface-mounted obstacles. Several droplet studies have pointed to general similarities between the flows over liquid droplets deposited on surface and those over surface-mounted obstacles, *i.e.* mean flow topologies [40, 110, 45], vortical structures [110], and vortex shedding frequencies [178]. However, being focused primarily on droplet dynamics, Ding and Spelt [40] and Ma *et al.* [110] do not elucidate flow development over representative droplet shapes. A recent study by Emami [45] characterized the flow fields at the symmetry planes of real water droplets and their corresponding solid models. The comparison indicated the influence of morphable liquid-gas interface on flow development within the symmetry plane is negligibly small. However, with flow measurements confined within the symmetry plane, a comprehensive view of the three-dimensional flow development is missing from the picture.

Droplet depinning is governed by the macroscopic balance between aerodynamic loading and adhesion. Quantitative description of the process is often hindered by the lack of reliable measurements of the minuscule forces (commonly below 1 mN). Direct measurement of aerodynamic drag using floating element sensors are restricted by resolution and susceptibility to test facility vibrations [120]. Estimations of adhesion, on the other hand, are challenged by the complexity of measuring the three-dimensional droplet geome-

try with high spatial resolution. Alternative approaches for force measurements in droplet depinning processes are still open to be explored.

1.3 Research objectives

With the identified research gaps, this thesis primarily focuses on the interactions between droplets and wall-bounded shear flows, in particular, (i) droplet dynamics under varied impinging jet configurations and (ii) impacts of droplets on the development of wall-bounded shear flows. The specific research objectives are to:

1. Provide a comprehensive characterization of impinging jet flows, which serves as the background flow fields for droplet depinning. Specifically, characterize the effects of jet Reynolds number (Re) and jet orientation angle (α) on the time-averaged near-wall flow development and uncover the relation between the development of dominant coherent structures and time-averaged flow characteristics.

2. Investigate the impact of an isolated droplet on laminar boundary layer flow development. Specifically, provide a comprehensive view of statistical three-dimensional flow development over representative solid droplet models, gain insight in the salient aspects of vortex dynamics, and explore the effect of droplets on boundary layer transition.

3. Develop a diagnostic method for estimating drag coefficients of representative droplet geometries under wind-forcing. Furthermore, explore the effects of boundary layer profile on drag coefficients of solid droplet models.

4. Understand the dependencies of critical depinning velocities on droplet volumes, incoming flow orientation angles, flow ramp-up rates, and local near-wall velocity profiles. Further, identify the key parameters dominating the dynamics in droplet depinning processes by performing dimensional analysis. Additionally, provide typical shape factor values for estimating adhesion of wind-forced droplets based on side-view geometries.

1.4 Thesis outline

This thesis is organized as follows. Ch. 2 presents a review of relevant literature. First, the state of the art of fluid dynamics in boundary layer and impinging jet flows is discussed, providing information of flow events that can be expected in background flow fields. Then, previous studies of flow developments over surface-mounted three-dimensional smooth obstacles and their aerodynamic performances are inspected, setting baseline for flow field measurements over droplet-shaped obstacles. Lastly, literature pertinent to droplet behaviours under wall-bounded shear flows is reviewed, primarily focusing on the depinning of isolated droplets, and then briefing on the behaviours of droplet arrays.

Ch. 3 describes the research methodologies, which include experimentations in wind tunnel and impinging jet facilities. The experiments can be broadly categorized into background flow characterizations, solid droplet model tests, and water droplet tests. The results of flow characterizations are presented in Ch. 4. Steady and accelerating wall-bounded shear flows formed by flow over a flat plate model and impinging jets are discussed. For impinging jets in particular, effects of Reynolds number and jet angles are analysed quantitatively, with insights provided for the link between transient flow behaviours and mean flow statistics.

Ch. 5 and 6 relate to experimental investigations over solid droplet models. Ch. 5 presents flow developments over droplet-shaped obstacles submerged in a laminar boundary layer flow and the mechanisms through which they contribute to laminar-to-turbulent transition. These flow field measurements are then used in Ch. 6 to estimate drag coefficients of the representative droplet geometries. Furthermore, impacts of relative submergence and boundary layer turbulence intensity on drag coefficients are explored.

Ch. 7 is dedicated to the analysis of the depinning process of real water droplets. The chapter starts with analyzing the dependencies of critical velocities on flow configurations. Thereafter, dimensionless parameters governing droplet dynamics at depinning are identified through parametric study. In addition, links between water droplet behaviours and observations made with solid droplet models are established.

Ch. 8 summarizes the thesis and presents the conclusions. It also suggests the directions for future studies, including experiments that can be performed to further the understanding of the impact of transient flow events on droplet shedding and droplet behaviours in droplet arrays.

Chapter 2

Research Background

This chapter reviews the literature relevant to the present study. Sect. 2.1 inspects the fluid dynamics aspect of flat plate boundary layer (Sect. 2.1.1) and impinging jet flows (Sect. 2.1.2). Sect. 2.2 discusses flow development over various three-dimensional obstacles (Sect. 2.2.1) and the consequent aerodynamic drag exerted on these obstacles (Sect. 2.2.2). Sect. 2.3 first introduces droplet physics in the sessile state (Sect. 2.3.1), then reviews the studies on depinning of an isolated droplet (Sect. 2.3.2) and droplet arrays (Sect. 2.3.3).

2.1 Wall-bounded shear flows

2.1.1 Flat plate boundary layer

When a viscous fluid flows over a flat plate, a region is formed between the flat plate surface and the freestream in which the flow is influenced by viscosity. At sufficiently large Reynolds numbers, the effect of viscosity is confined to a thin layer in the close proximity

of the wall [142]. Consequently, the rate of viscous diffusion in the wall-normal direction is minuscule as compared to the rate of downstream convection. For a flow at freestream velocity of U_∞ (see Fig. 2.1 for schematic), the ratio of the time required for downstream convection over the surface and for viscous diffusion across the near-wall streamlines is on the order of $\sqrt{\mathrm{Re}_x}$, where $\mathrm{Re}_x = U_\infty x/\nu$ is the Reynolds number based on the distance x from flat plate leading edge and ν is the fluid kinematic viscosity. The boundary layer is likely to be laminar close to the flat plate leading edge, and then undergoes laminar-to-turbulent transition with increasing Re_x (see Fig. 2.1(a)).

Boundary layer thickness δ is the wall-normal distance over which the streamwise ve-

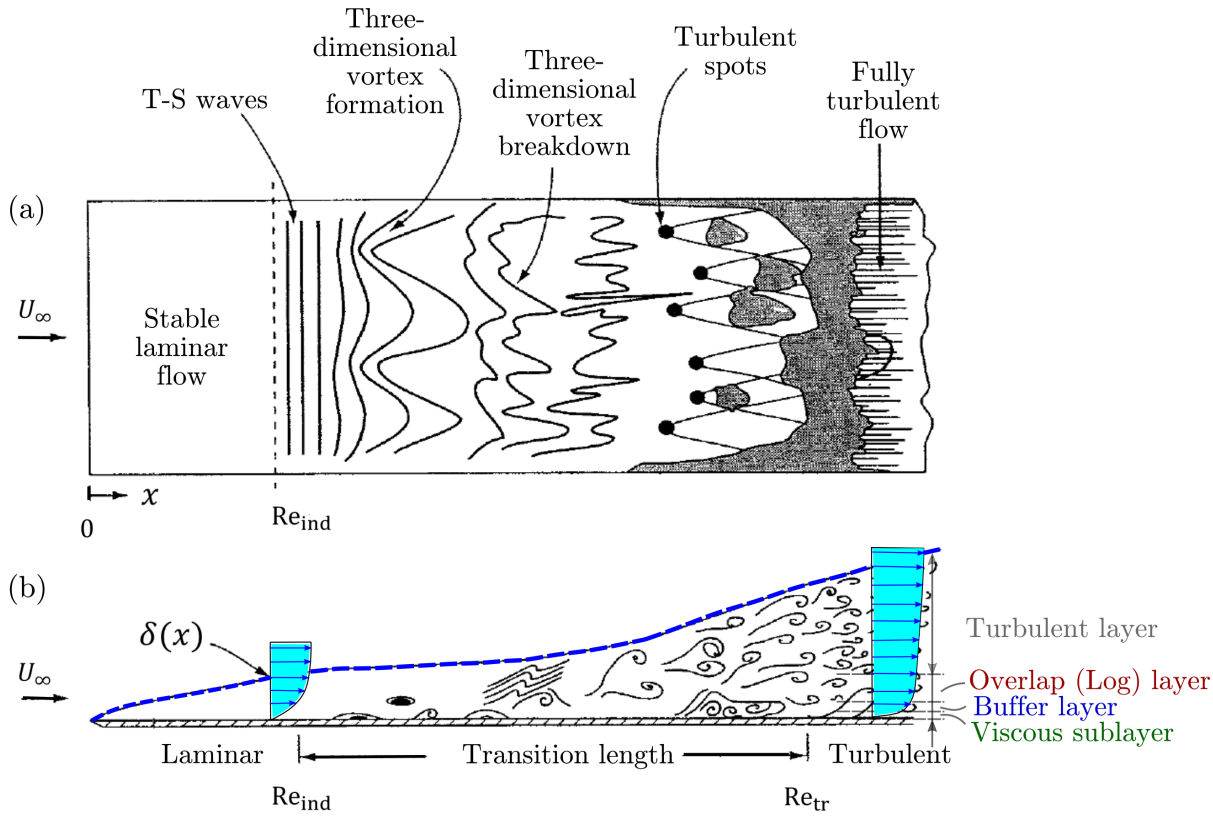

Figure 2.1: Schematics of (a) top- and (b) side-view of boundary layer development over a flat plate. Figure adapted from White [203].

locity u recovers the freestream velocity, as indicated by the blue dashed line in Fig. 2.1(b). In practice, it is difficult to define the exact location at which the freestream velocity is recovered, and thus the location where $u = 99\%U_\infty$ is used to define the boundary layer thickness. Deficits in mass and momentum flux due to the formation of the boundary layer are characterized by displacement thickness δ^* and momentum thickness Θ, respectively, defined as [203],

$$\delta^* = \int_0^\infty \left(1 - \frac{u}{U_\infty}\right) \mathrm{d}y, \tag{2.1}$$

$$\Theta = \int_0^\infty \frac{u}{U_\infty}\left(1 - \frac{u}{U_\infty}\right) \mathrm{d}y. \tag{2.2}$$

For a laminar boundary layer under a constant freestream velocity U_∞, Blasius [17] proposed a similarity solution to the Prandtl boundary layer equations. By introducing a similarity variable $\eta = y\sqrt{U_\infty/2\nu x}$ and a stream function $\psi = \sqrt{2\nu x U_\infty} f(\eta)$, a dimensionless ordinary differential equation $f''' + ff'' = 0$, eponymously the Blasius equation, is obtained with invariant boundary conditions. The solution of the Blasius equation correlates boundary layer thickness and skin friction τ_w with Reynolds number Re_x,

$$\frac{\delta}{x} = \frac{5.0}{\sqrt{\mathrm{Re}_x}}, \quad \frac{\delta^*}{x} = \frac{1.72}{\sqrt{\mathrm{Re}_x}}, \quad \frac{\Theta}{x} = \frac{0.664}{\sqrt{\mathrm{Re}_x}}, \tag{2.3a}$$

$$C_f = \frac{\tau_w}{\rho U_\infty^2/2} = \frac{0.664}{\sqrt{\mathrm{Re}_x}}, \tag{2.3b}$$

where ρ is the fluid density and τ_w is the wall shear stress.

Although turbulent flows exhibit random velocity fluctuations, the time-averaged velocity profile of a turbulent boundary layer remains self-similar to each other, though different from that for laminar flow, and can be characterized by the law of the wall. When scaled

using frictional velocity $u_\tau = \sqrt{\tau_w/\rho}$ and plotted on a semi-logarithmic scale, the dimensionless near-wall velocity profile consists of a viscous sublayer, a buffer layer, and a log layer. These layers can be identified by the relative contributions of viscous and Reynolds shear stresses [34, 106, 203]. Prandtl [143] suggested a one-seventh power-law profile is sufficient to approximate the turbulent boundary layer,

$$\frac{u}{U_\infty} \approx \left(\frac{y}{\delta}\right)^{1/7}, \tag{2.4}$$

except very near the wall. By assuming $\delta = 0$ at $x = 0$, boundary layer properties assuming the power-law profiles are,

$$\frac{\delta}{x} \approx \frac{0.16}{\mathrm{Re}_x^{1/7}}, \quad \frac{\delta^*}{x} \approx \frac{0.02}{\mathrm{Re}_x^{1/7}}, \quad \frac{\Theta}{x} \approx \frac{0.0156}{\mathrm{Re}_x^{1/7}}, \tag{2.5a}$$

$$C_f \approx \frac{0.027}{\mathrm{Re}_x^{1/7}}, \tag{2.5b}$$

Conventionally, a shape factor $\mathcal{H} = \delta^*/\Theta$ is used to differentiate laminar and turbulent boundary layers. A shape factor of $\mathcal{H} = 2.59$ is typical for laminar boundary layers, while $\mathcal{H} \approx 1.3 - 1.4$ corresponds to turbulent boundary layer [166].

For a flow with a low freestream turbulence intensity (*i.e.*, $Tu < 0.1\%$) over a smooth flat plate surface, natural transition from a laminar to a turbulent boundary layer flow takes place, as illustrated by Fig. 2.1. Two-dimensional Tollmien-Schlichting (T-S) waves are superimposed onto the initially stable laminar boundary layer at the indifference Reynolds number $\mathrm{Re}_x = \mathrm{Re}_{\mathrm{ind}} \approx 9.1 \times 10^4$ [203, 166]. Further downstream, three-dimensional instabilities are superimposed and lead to the formation of characteristic Λ-structures. The breakdown of these Λ-structures gives rise to turbulent spots which initiate the transition to turbulent boundary layer. The transition process is complete at $\mathrm{Re}_x = \mathrm{Re}_{\mathrm{tr}}$ and the

flow is fully turbulent further downstream; typically, $\mathrm{Re}_{\mathrm{tr}}$ ranges from 3.5×10^5 to 10^6.

Bypass transition occurs when the boundary layer is subjected to disturbances of large

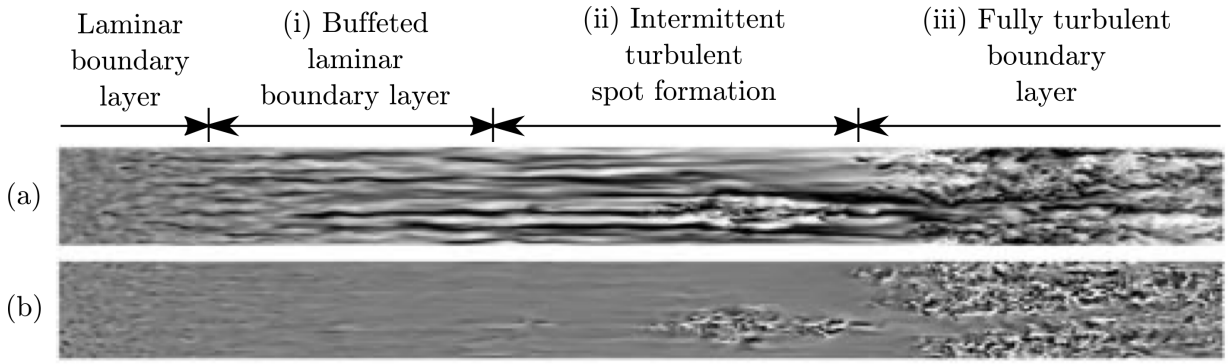

Figure 2.2: Visualization of (a) streamwise and (b) wall-normal velocity contours from DNS solution showing streaks proceeding turbulent breakdown in bypass transition at a freestream turbulence intensity of 3.5%. Figure is adapted from Jacobs and Durbin [82]. Flow is from left to right.

amplitude, such as high freestream turbulence and/or distributed surface obstacles [166]. The presence of these external disturbances triggers instabilities that evolve into patches of irregular motions, providing an alternative mechanism for the formation of turbulent spots and bypassing the route of T-S waves [127, 82]. As visualized in Fig. 2.2, bypass transition consists of three distinctive regions: (i) buffeted laminar boundary layer, (ii) intermittent turbulent spot formation, and (iii) fully turbulent boundary layer [82]. In region (i), external perturbations enter the boundary layer at a low frequency and amplitude. These perturbations are amplified by shear and form streaks of negative streamwise velocity [151, 82]. The boundary layer, however, remains stable in region (i) and preserves most of the characteristics of a normal laminar boundary layer with only a slight increase in skin friction. In region (ii), the elongated velocity streaks lead to the formation of turbulent spots. Initially minuscule in size, they quickly spread laterally and grow longitudinally, eventually becoming fully turbulent [46]. Region (ii) is thus characterized by juxtaposed

zones of laminar and fully turbulent motions. Eventually in region (iii), the boundary layer is turbulent across the entire span. The presence of a droplet in a laminar boundary layer may potentially trigger the bypass transition, which is discussed in detail in Sect. 2.2.

2.1.2 Impinging jets

Impinging jets are found in many engineering fields requiring high levels of surface heat and mass transfer, including cooling systems of turbine blades [73] and electronic chips [97], textile drying [157], food processing [157], and ground vehicle deicing [88]. As a result, investigations of impinging jets have been focused on enhancing the relevant transfer properties [22]. Flow and geometric parameters that influence heat and mass transfer include the jet Reynolds number [141, 36, 139], nozzle-to-plate spacing [141, 5, 130, 191], jet obliqueness [12, 29, 132], acoustic excitation [56, 154], jet swirling [2, 81], target wall temperature [86], target wall motion [7], nozzle exit geometry [100, 59, 114, 196, 93, 180], and curvature [141, 36] and roughness [146] of the target surface.

As the impinging jet approaches the target surface, its axial velocity decreases, forming a time-averaged 'stagnation zone' of low velocity and high pressure [171]. The flow then reorients to become aligned with the surface, after which a wall jet develops. The mean flow field formed by an impinging jet hence consists of the following three regions with distinctively different flow features [22]: (i) the free jet region, characterized by a potential-core surrounded by mixing layers formed between the jet and ambient air; (ii) the reorientation region, in which flow decelerates and deflects towards the wall-tangential direction; and (iii) the wall jet region, where the reoriented flow gradually develops into a turbulent wall jet (see Fig. 2.3 for schematic).

Previous studies have largely focused on normal jet impingement and the associated

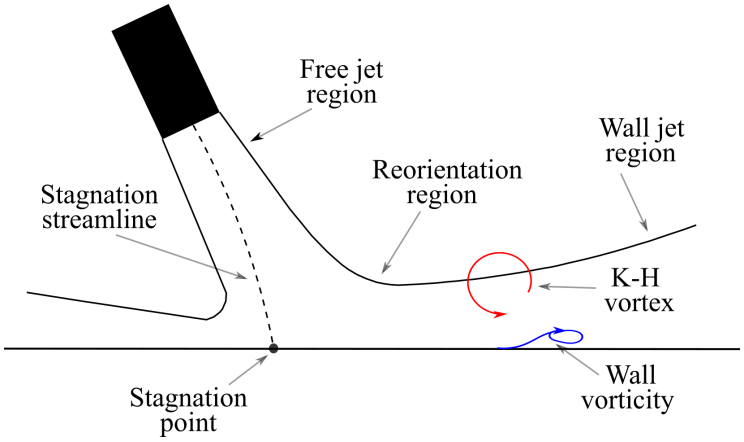

Figure 2.3: Schematic of an impinging jet flow.

heat transfer properties. A free jet without confinement typically features a potential-core that extends $4.7 - 7.7$ slot widths downstream of the nozzle exit [107]. For impinging jets with a nozzle-to-plate spacing larger than the potential-core length of an unconfined jet (transitional impingement), Gardon and Akfirat [60] and Yokobori *et al.* [213] found the maximum surface heat transfer rate in the stagnation zone. For impinging jets with a nozzle-to-plate spacing smaller than the potential-core length (potential-core impingement), in contrast, Hoogendoorn [76] and Lytle and Webb [109] found a non-monotonic trend in heat transfer rate, exhibiting two peaks downstream of the stagnation region. Yokobori *et al.* [212] and Goldstein *et al.* [65] emphasized large-scale, coherent structures in the flow play a predominant role in surface heat transfer for transitional and potential-core impingement. Kataoka *et al.* [89] confirmed the influence of Kelvin-Helmholtz (K-H) vortices forming in the free jet region at moderate Reynolds number on the surface heat transfer enhancement. A surface-renewal parameter was found to be proportional to the Strouhal number and magnitude of the impinging K-H vortices in the range of nozzle-to-plate spacing ratios from 2 to 10.

The interaction of K-H vortices with the target surface also plays a role in the laminar-

to-turbulent transition in the wall jet region. In transitional impingement, high velocity and pressure fluctuations are observed in the direct vicinity of the stagnation point. Narayanan *et al.* [130] showed that these fluctuations result in strong turbulent transport from the mixing layer in the free jet region to the jet centreline, and trigger turbulent transition in the wall jet region. Potential-core impingement, in contrast, is not associated with strong flow fluctuations along the stagnation streamline. Instead, the impinging K-H vortices enhance the entrainment in the reorientation region [89]. Flow visualization by Popiel and Trass [141] suggested that the deformation and breakdown of K-H vortices as they are convected downstream promotes transition to a turbulent wall jet. In addition, Didden and Ho [39] showed that the passage of K-H vortices along the wall causes the roll-up of vorticity in the near-wall region, and leads to the shedding of boundary layer vorticity into the flow, forming wall vortices. Hadžiabdić and Hanjalić [71] showed that the instantaneous flow reversals that occur in the thin region near the wall just ahead of the roll-up of wall vortices contribute to the enhancement of the local heat and mass transfer rate. In spite of the profound impact of vortex-wall interactions on the near-wall flow development and heat transfer, quantitative analysis of vortex dynamics over an extensive wall jet region is lacking.

Most of the impinging jet studies are focused on heat transfer and/or fluid mechanics of axisymmetric normal impingement. In contrast, much less attention has been given to fluid mechanics of slot jet impingement or oblique jet impingement. To the best knowledge of the author, very few have reported on both aspects despite their relevance to cleaning and drying applications. Beltaos [12] established models for oblique impinging jets, however, the derivations were based on measurements of transitional impingement of axisymmetric jets. Experiments on potential-core impingement of slot jets carried out by Chin and Agarwal [29] were focused on surface heat and mass transfer, where velocity field infor-

mation was lacking. O'Donovan and Tadhg [132] extensively characterized the flow fields of oblique jet impingement using particle image velocimetry, but the investigations were limited to axisymmetric jets. Although Pieris *et al.* [139] detailed the spatial-temporal behaviour of impinging slot jets, their characterization was restricted to normal impingement. Thus, characterization of flow development in impinging slot jets of systematically varied jet parameters, such as jet Reynolds number and orientation angles, is essential for understanding the background flow conditions of droplet depinning process, which is discussed in Ch. 4.

2.2 Flow over surface-mounted obstacles

2.2.1 Flow development over surface-mounted three-dimensional obstacles

The morphological configurations of wind-forced droplets have similarities with smooth surface-mounted obstacles. Previous studies have considered a variety of such objects, including hemispheres [1, 158, 159, 160, 33, 53, 23, 207, 210], hemisphere-capped cylinders [134, 159], spheres [133], ellipsoids [72], and hill-shaped bumps [179, 21, 197]. In general, the presence of these protuberances in the boundary layer induces multiple interacting vortex systems [158, 197, 207], which modify the near-wall velocity profiles and enhance the energy transfer between scales of motion [160, 207, 26]. This highly unsteady, three-dimensional flow phenomenon is influenced by a number of parameters, such as Reynolds number, obstacle geometry, boundary layer profile, relative submergence, and incoming flow turbulence intensity levels [8, 72]. Specifically for obstacles submerged in a laminar boundary layer, the low- and high-streaks of streamwise and wall-normal velocities induced

by these vortex interactions may alter the laminar-to-turbulent transition mechanism and accelerate the transition process in a similar fashion to bypass transition [210].

A surface-mounted hemisphere is a prototypical smooth obstacle geometry that has

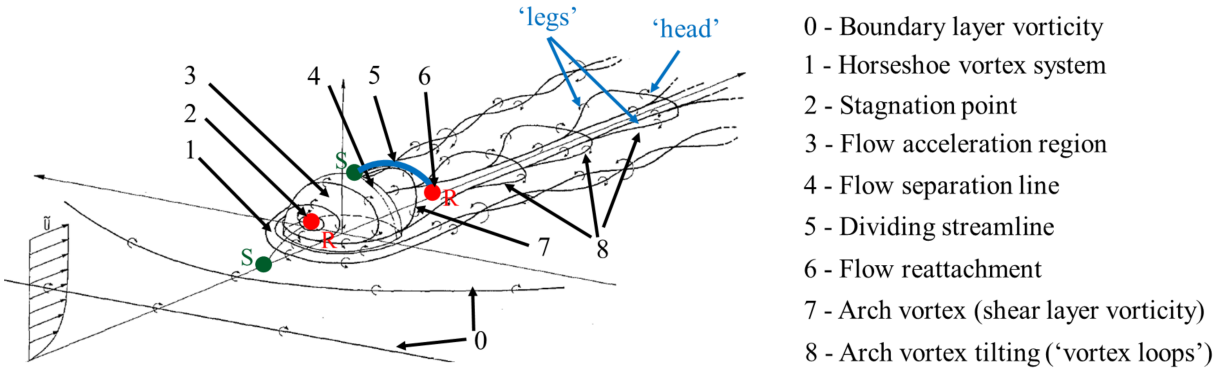

Figure 2.4: A schematic of flow development over a surface-mounted hemisphere. S: separation; R: Reattachment. Figure adapted from Savory and Toy [158].

been considered in a number of previous studies, *e.g.* [158, 159, 23, 207, 210]. The mean flow topology can be roughly divided into: i) a horseshoe vortex system that forms upstream and necklaces around the obstacle, ii) a recirculating region immediately downstream of the obstacle, and iii) a trailing vortex system formed due to the shedding of shear layer vortices. A canonical topological sketch for the flow over a surface-mounted hemisphere was illustrated by Savory and Toy [158] (see Fig. 2.4). As the flow approaches the hemisphere, a stagnation region is formed on the upstream surface. The adverse pressure gradient induced by the presence of the obstacle causes the boundary layer to roll up and form horseshoe vortices. The flow reorients and eventually separates, forming a separated shear layer. A dividing stream surface directly downstream of the obstacle serves to outline the region of reverse flow immediately downstream of the obstacle up to mean reattachment [207]. The vortex lines of the horseshoe vortex system wrap around the hemisphere and orient predominantly in the streamwise direction downstream. These vortex lines

curve in towards the centreline as the separated flow reattaches to the substrate, resulting in the characteristic 'necklacing' vortex topology in the wake. Beyond flow reattachment, the horseshoe vortices move outwards due to the image vortex system in ground effect. The formation and necklacing of the horseshoe vortex system has been observed for both laminar [158] and turbulent [158, 207] incoming boundary layers, and for different smooth obstacle geometries [159, 21, 72].

For similar incoming boundary layer characteristics, the time-averaged length of the recirculating region downstream of a smooth obstacle has been shown to shorten with decreasing obstacle aspect ratio, commonly defined as the ratio of obstacle height to its width, h/c [159, 72]. Previous studies also indicate the significance of the free-end geometry of the obstacle. Qualitative observation by Park and Lee [138] of flow over cylinders with flat, chamfered, beveled, and hemispherical tops also showed elongation of the recirculating regions with rounded free-ends. Simpson *et al.* [179] and Byun and Simpson [21] compared the recirculating regions formed downstream of a hemisphere and a hill-shaped bump of the same aspect ratio submerged in the same boundary layer. The tapered geometry of the latter featured delayed separation and promoted reattachment, resulting in a shorter recirculating region.

At low to moderate Reynolds numbers, the amplification of disturbances in the separated shear layer due to the Kelvin-Helmholtz instability leads to periodic shedding of arch-shaped vortices [1], which are also referred to as 'vortex loops' [158, 159]. These vortices strongly influence the turbulence statistics in the near wake, including Reynolds stresses, turbulent kinetic energy, and triple correlations [14]. The dynamics of arch vortices is influenced by two competing effects, namely, the mean shear flow that advects the vortices and Biot-Savart self-induction [72]. When the former dominates, arch vortices tilt downstream and induce upwash at the obstacle symmetry plane, forming base

vortices [159, 72]. When the latter dominates, arch vortices tilt upstream and induce downwash, forming tip vortices [72, 23]. For smooth obstacles, the strength of the induced base vortices is closely related to the obstacle aspect ratio. Hajimirzaie *et al.* [72] investigated the influence of obstacle aspect ratio by comparing the flow fields formed by a surface-mounted ellipsoid with different orientations with respect to the incoming flow. The two aspect ratios, 0.67 (transverse) and 0.89 (streamwise), were achieved by aligning the minor and major axes with the streamwise direction, respectively. Base vortices were shown to be more pronounced for the ellipsoid with smaller aspect ratio (streamwise). The influence of obstacle aspect ratio on base vortices is also found to couple with the relative submergence of the obstacle in the boundary layer. For aspect ratios around 0.25, the strength of the central upwash induced by base vortices increases significantly with decreasing boundary layer thickness, while for aspect ratios greater than unity, the strength of the induced central upwash decreases with decreasing boundary layer thickness [116, 159, 72].

An appropriately sized surface obstacle subjected to a laminar boundary layer can induce laminar-to-turbulent transition. The critical Reynolds number based on obstacle height ($\mathrm{Re}_h = U_\infty h/\nu$) has been shown to correlate with the aspect ratio of the obstacle (h/c), with $\mathrm{Re}_h \propto (h/c)^{2/5}$ [198]. For an obstacle with $h/c \approx 1$, this critical value lies in the range of $600 < \mathrm{Re}_h < 900$. The underlying transition process can involve a combination of instability modes [38, 209]. Both the varicose mode induced by the Kelvin-Helmholtz instability and the sinuous mode induced by the streamwise velocity streaks may coexist in the obstacle wake [31]. For instance, De Tuillo *et al.* [38] attributes the transition process to the fast growth of varicose instabilities. In contrast, Ye *et al.* [209] argued that the large-scale hairpin structures formed at lateral locations of the wake due to the strong interaction of secondary and tertiary streamwise vortex pairs initiates the transition. Nonetheless, both studies ascribe the mode of transition to streamwise vortex interactions.

The flow topology of the last stages of laminar-to-turbulent transition exhibits a wedge shape, known as the turbulent wedge, with a fully turbulent core bounded by transitional regions [172].

Several similarities in flow development over liquid droplets and surface-mounted smooth obstacles have been observed by previous studies. Using numerical simulation of a droplet in an accelerating laminar boundary layer, Ding and Spelt [40] briefly considered the three-dimensional flow development within approximately one droplet length around the droplet. The velocity field features the roll-up of horseshoe vortices upstream of the water droplet, formation of a recirculating region directly downstream, and induction of central upwash at the droplet symmetry plane. The authors compared the flow topology to that in the proximity of a surface-mounted cube. With similar Reynolds numbers and incoming boundary layer profiles, mean velocity and vorticity topologies of the two scenarios bear high resemblance. More recently, hot-wire measurements were performed by Simon and White [178] to characterize the velocity fluctuations in the flow downstream of a water droplet submerged in a laminar boundary layer prior to depinning. The characteristic frequencies were found to be comparable to those in the flow downstream of a surface-mounted hemisphere submerged in similar incoming flows [158]. Ma *et al.* [110] used planar, two-component particle image velocimetry (PIV) to capture uncorrelated velocity field snapshots over a droplet going through runback under the influence of an accelerating laminar boundary layer at the droplet symmetry plane. A recirculating region downstream of the droplet was clearly visualized from the velocity field and vortex shedding was observed in the separated shear layer. Emami [45] compared the flow development within the symmetry planes of real water droplets and their corresponding solid models using PIV. For water droplets of volumes ranging from 10 μL to 30 μL tested on PMMA, PEMA, PS, and Teflon surfaces, ordered in decreasing wettabilities, no significant difference in flow fields within the sym-

metry planes was observed.

Regardless of the similar flow features observed in the proximity of a liquid droplet as compared to those of solid obstacles, the streamwise and spanwise extent of the ambient flow influenced by the flow perturbations introduced by a liquid droplet before depinning is yet to be assesed. For instance, whether laminar-to-turbulent transition will be promoted depends on the Reynolds number Re_h and droplet aspect ratio at depinning, which is explored in Ch. 5.

2.2.2 Aerodynamic drag measurements on three-dimensional obstacles

Unlike the substantial amount of literature characterizing flow development over surface-mounted 3D obstacles, far fewer studies considered the aerodynamic loadings. Among the available studies, most investigations focus on aerodynamic drag exerted by the flow on surface-mounted hemispheres [185, 131, 147] and spheres [35, 96]. In general, as the incoming flow approaches the obstacle, pressure increases in the near-wall region directly upstream of the obstacle surface and reaches the maximum at the stagnation point. Further, surface pressure decreases until flow separates from the surface, forming a recirculating region of low pressure downstream of the obstacle, leading to an downstream-directed drag and a wall-normal lift. Previous studies suggest that for a given obstacle geometry, surface pressure distribution and the resultant aerodynamic drag are influenced mainly by Reynolds number, relative submergence, and incoming flow turbulence intensity levels. Maher [112] investigated the mean pressure distribution over hemispheres within $0.92 \times 10^6 \leq \mathrm{Re}_h \leq 1.84 \times 10^6$ with surface pressure taps; for $\mathrm{Re}_h \geq 1.4 \times 10^6$, pressure distribution was found to be invariant with Reynolds number. Savory and Toy [158]

observed that, by increasing the turbulence intensity in the incoming flow, surface pressure distribution represents that of higher Reynolds number flows with lower turbulence intensity and leads to lower aerodynamic drag. A similar effect has been observed for spheres in freestream where an increase in freestream turbulence leads to a decrease in drag coefficient [126]. Pressure measurements by Taniguchi *et al.* [185] showed the reduction in pressure extrema over hemispheres with increasing submergence in water flows; as a result, drag coefficients decrease from 0.35 to 0.2 as the ratio between incoming flow depth to hemisphere height increases from 1 to 5. Similar values and trends were reported for water flow over spheres by Nardone and Koll [131]. Drag coefficients reported by other studies investigating water flow over surface-mounted spheres, however, fall around 0.7 [168, 99, 96]. The scattering in values suggested high sensitivity of drag coefficients to flow configurations and measurement techniques. Furthermore, the studies discussed above and summarized in Fig. 2.5 are either civil engineering studies with high Reynolds numbers ($\mathrm{Re}_h > 10^5$) [112, 185] or hydraulic studies where the effect of shallow water waves is significant [131, 168, 99, 96]. As a result, drag coefficients reported in these studies may not be directly applicable to the aerodynamic drag experienced by droplets at depinning.

Under sufficiently large Reynolds number (*e.g.*, $\mathrm{Re}_h \sim \mathcal{O}(10^3)$), while the drag largely results from the pressure difference between the upstream and downstream regions, the generation of the pressure difference between the top and bottom regions of the obstacle which leads to lift is not as clear. Wiberg and Smith [204] proposed that the lift should be scaled with the difference in streamwise velocity measured at the top and bottom of the obstacle following Bernoulli's principal. Schmeeckle *et al.* [168], however, showed that any horizontal asymmetry in the wake may contribute to the lift. In addition, direct lift measurements using a force balance demonstrated high variability in lift and insofar found no systematic trends with submergence and obstacle geometry [167, 168]. Nevertheless,

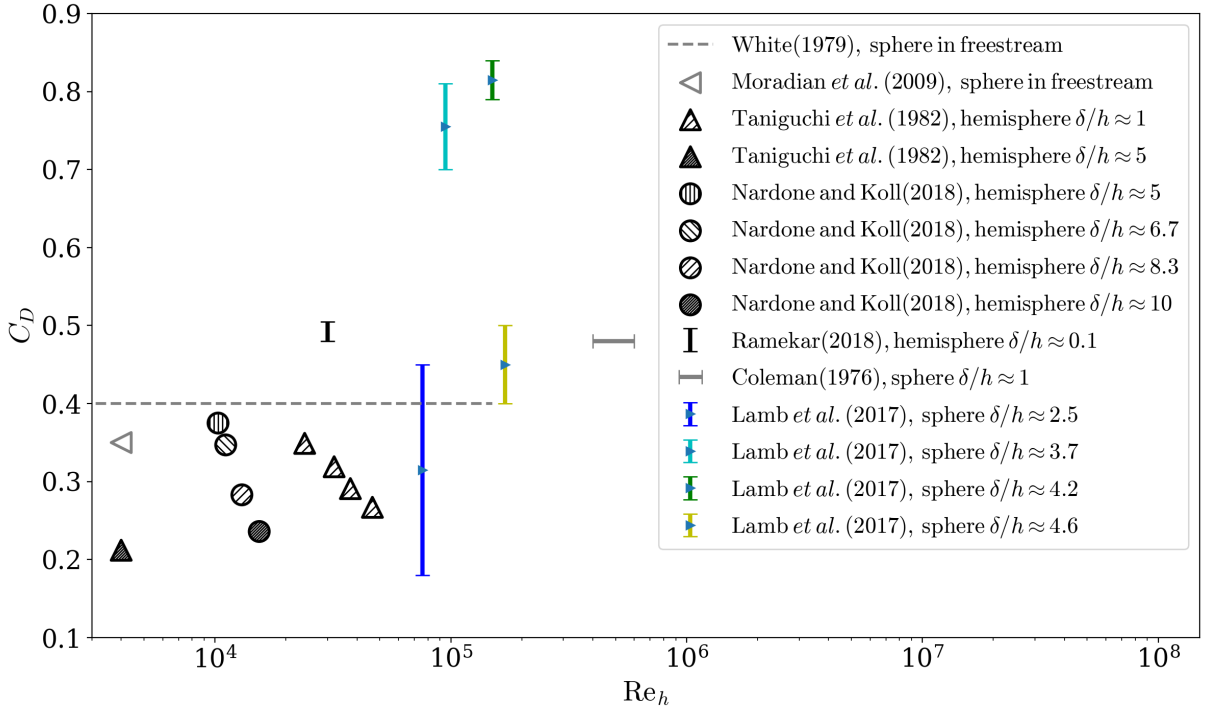

Figure 2.5: Summary of drag coefficients of hemispheres and spheres in existing literature. For conciseness of the legend, obstacles are surface-mounted unless otherwise specified with 'in freestream'.

force measurements (*e.g.*, [83, 167]) showed that the time-averaged lift of surface-mounted obstacles is either much smaller than drag or negative. In other cases, lift is negligible as compared to the obstacle weight or countered by the mounting structure [96], and thus its effect is not discussed extensively. Specifically for the consideration of droplet depinning, lift-off of droplets usually occurs for droplet removal from superhydrophobic surfaces [124]. This is beyond the scope of discussion of the present study and hence the effects of lift will not be considered.

Given the small model size, miniscule drag magnitude, and complex fluid motions associated with droplets, drag estimation based on analysis of flow field measurements is ad-

vantageous for minimizing intrusiveness, eliminating disturbances from test facilities, *e.g.*, ambient vibrations, and providing insights into components of drag [115, 69, 70, 3]. The analysis invokes conservation of momentum across a control volume (CV) containing the model [16, 85, 64]. Early applications used pressure-based wake rakes to measure the wake patterns and diagnose drag generation on wings [115] and ground vehicles [69, 70]. With the development [68] and optimization [193, 136, 117] of PIV-based pressure field reconstruction, aerodynamic load estimation with PIV (or 'PIV wake rake') has become a viable substitute for traditional pressure-wake rakes. The whole-field measurement capacity and non-intrusive nature of PIV broadened the application of CV-based drag estimation. Van Oudheusden *et al.* [194] proved the high fidelity of the method with uncertainty within 1 drag count (*i.e.*, $\varepsilon_{C_D} = 10^{-3}$) for time-averaged drag coefficient by comparing to the results given by traditional pressure-based wake rake. With these advancements, PIV-based force diagnosis is applied in other challenging scenarios, such as unsteady loading on cylinders [95] and propeller blades[145], animal biomechanics [103], and sport aerodynamics [186, 187]. In particular, the approach taken by Terra *et al.* [187] for estimating the drag of a cyclist mannequin is instructive for the present study. Three-dimensional velocity measurements using 3D particle tracking velocimetry (PTV) were conducted on a transverse slice in the wake of the mannequin with the edges of the field-of-view representing the undisturbed flow. These measurements allowed the computation of drag as integrals of momentum and pressure deficits within the measured wake plane.

Although the CV-based drag estimation has been well-established and widely applied, previous studies benefit from the absence or insignificance of a substrate. In the present study, however, droplets are fully submerged in the wall-bounded shear flow and the contribution of substrate drag cannot be neglected from the momentum balance. The additional term introduced by the influence of the substrate is treated and drag coefficients of surface-

mounted droplet-shaped geometries are suggested in Ch. 6.

2.3 Droplet research

2.3.1 Droplet physics at sessile state

A liquid droplet resting on a solid surface forms three interfaces. The solid-liquid, liquid-gas, and solid-gas interfaces each possess a surface energy with corresponding interfacial tensions γ_{sl}, γ_{lg}, and γ_{sg}, respectively (see Fig. 2.6 for illustration). Connecting the points where all three phases intersect forms the contact line. The interfacial tensions are balanced by pressure jumps across the interfaces. The Young-Laplace equation relates interface curvature to internal pressure, where the coefficient, γ [55], is surface tension,

$$\begin{aligned} \nabla^2 p_\gamma &= -\gamma \nabla \cdot \hat{n} \\ &= -\gamma(\frac{1}{R_1} + \frac{1}{R_2}), \end{aligned} \tag{2.6}$$

where $p_\gamma = p_{\text{drop}} - p_{\text{ext}}$ is the Laplace pressure (*i.e.*, the pressure difference across the interface), $\hat{n}$ is the surface normal, and R_1 and R_2 are the principal radii of curvature of the fluid interface (see the inset of Fig. 2.6). In the absence of external loading (*e.g.*, gravity, electromagnetic force, aerodynamic force, etc.), the droplet forms a spherical cap with a circular contact line. For a droplet resting on a smooth and level surface, gravity flattens the spherical-capped shape while maintaining a circular contact line.

The angle between the solid surface and the tangent of the liquid-gas interface at the contact line is the contact angle θ_{Young}. The contact angle along the circular contact line

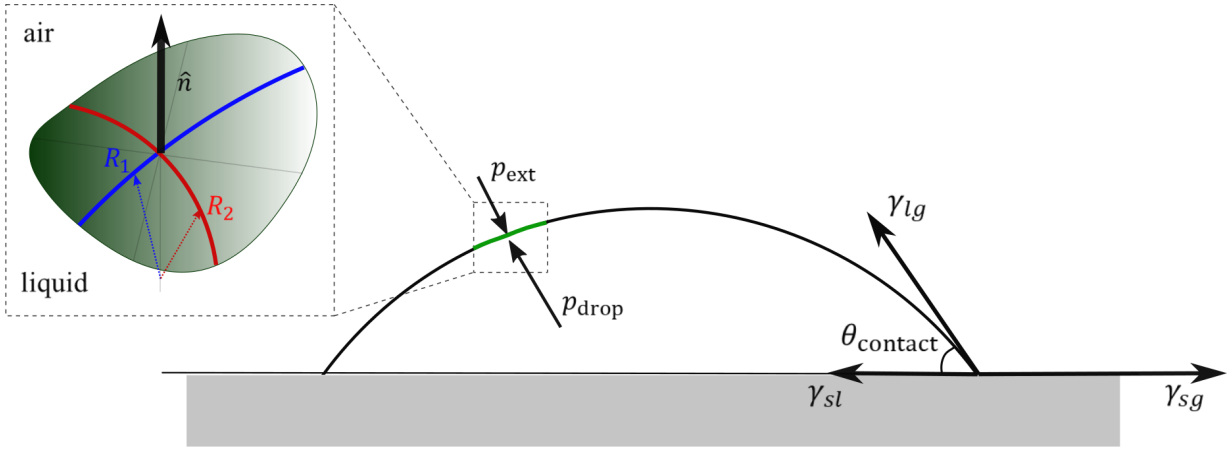

Figure 2.6: Schematic of interfacial tensions γ_{sl}, γ_{lg}, and γ_{sg}. The inset shows a cartoon of a section of air-liquid interface with illustrations of surface normal $\hat{n}$, and principal radii of curvature R_1 and R_2.

formed on an ideal level surface is predicted by Young's relation [214, 32],

$$\gamma_{lg}\cos\theta_{\text{Young}} = \gamma_{sg} - \gamma_{sl}. \tag{2.7}$$

This indicates that for a given surrounding gas, a solid-liquid system of high wettability (low interfacial tension γ_{sl}) results in small contact angle θ_{Young}.

In real applications, solid surfaces are heterogeneous due to surface roughness and chemical inhomogeneity. As a result, droplet contact angles take varied values along the contact line. The apparent contact angle reflects the overall effects of surface inhomogeneity and intrinsic contact angle from Young's relation for a given combination of solid, liquid, and gas. The Wenzel model [199] accounts for rough surface of homogeneous chemical property. The Wenzel state considers the rough surface as an absorptive material, which is defined by a parameter r as the ratio of actual wetting area to the apparent. Consequently, the apparent contact angle is computed by the Wenzel equation (eq. 2.8).

$$\cos\theta_{\text{Wenzel}} = r\cos\theta_{\text{Young}} \tag{2.8}$$

On non-super-hydrophobic smooth surfaces with slight heterogeneity (as the one used in the present study, see Ch. 3.3), droplets are under the Wenzel state with θ_{Wenzel} varying slightly along the perimeter of the contact line due to the local surface imperfections. Although Wenzel equation accounts for the difference between apparent and intrinsic contact angles, free energy is minimized only when droplet has a circular contact line with θ_{Wenzel} distributed along the perimeter [206]. As a result, it does not fully account for the variation of contact angle values observed along the contact line on surface of various materials and/or with many different fractions of surface roughness. The extension is made in the Cassie-Baxter model [25]. Under the Cassie-Baxter state, liquid may not fully penetrate the air pockets trapped in the grooves of surface roughness. The fraction of solid surface area wet by the liquid is characterized by a parameter f and the apparent contact angle is computed by the Cassie-Baxter equation (eq. 2.9 [113]).

$$\cos\theta_{\text{Cassie}} = rf\cos\theta_{\text{Young}} + f - 1 \tag{2.9}$$

Specifically for rough surfaces with microscopic surface patterns, transition from the metastable Cassie-Baxter state to the stable Wenzel state [49] takes place when the energy barrier is overcome. The increase in total surface energy before attaining the Wenzel state is due to the replacement of the low-energy solid-gas interface with high-energy solid-liquid phase [128]. Spontaneous wetting transition is determined by the competing energy barrier and the Laplace pressure [161]. Papadopoulos *et al.* [137] observed two distinctive wetting transition mechanisms on pillar-patterned surface, namely, sagging and unpinning. Sagging takes place for pillars of low height-to-width ratios, in which the three-phase contact line

remains pinned at the top of the pillar and the liquid surface subsides to touch the bottom substrate between the pillars; for pillars of height-to-width ratios, the contact line unpins from the top surface and the liquid column slides down with increasing Laplace pressure inside the droplet. Murakami *et al.* [128] characterized the wetting transition processes of water and several ionic liquids on microscale pillared lattices. Through contact angle measurements and optical microscopy, they found the energy barrier is proportional to the height-to-width ratios of the pillars (h_p/w_p) and the interfacial energy difference between solid-liquid and solid-gas interfaces ($\gamma_{sl} - \gamma_{sg}$). Steady Wenzel and Cassie-Baxter states appear at low and high h_p/w_p values, respectively; in between the two thresholds, wetting transition is observed. Specifically for water droplets, droplets only show stable Wenzel state on surfaces with $h_p/w_p \lessapprox 0.25$, while Cassie-Baxter state is maintained for $h_p/w_p \gtrapprox 1$. Coexisting Wenzel and Cassie-Baxter states were observed on test surfaces of $h_p/w_p \approx 0.5$ and 0.87. However, increase in h_p/w_p significantly reduces the speed and range of wetting transition, *i.e.*, while it took around 5 s for complete wetting transition on $h_p/w_p \approx 0.5$ surface, only 10 % of the initial contact area underwent transition on $h_p/w_p \approx 0.87$ surface before the droplet fully evaporated. Droplets of ionic liquids showed similar trends with surface asperity as water droplets. However, the reduced surface tension of ionic liquids shifts the thresholds of steady Wenzel and Cassie-Baxter states to higher h_p/w_p values. It also accelerates the transition process in the h_p/w_p range in which wetting transition occurs.

2.3.2 Depinning of an isolated droplet

When a sessile droplet resting on a surface is exposed to an external loading, such as gravity or aerodynamic forces, the droplet deforms. Its receding contact angle θ_u (*i.e.* uphill

for gravity and upstream for aerodynamic forcing) decreases, its advancing contact angle θ_d (*i.e.* downhill for gravity and downstream for aerodynamic forcing) increases, and the droplet may also elongate in the direction of the external force [43, 51, 121, 6, 80, 201] (see Fig. 2.7 for illustration). Contact angle hysteresis increases the droplet's ability to adhere to the surface and maintain the static equilibrium until the adhesion limit is reached [43]. Further increase in the applied force leads to the onset of droplet motion and eventually its shedding from the surface.

Adhesive force between the droplet and the substrate can be computed based on

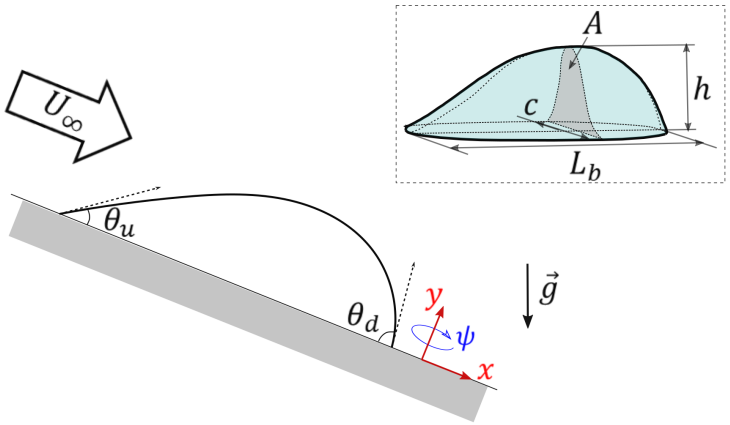

Figure 2.7: Schematic of a droplet under combined gravity- and wind-forcing. The inset shows geometric parameters of droplet under external forcing.

droplet geometry (Eq. [6]), *i.e.*, contact angle distribution (θ_{contact}) along the contact line (l) and contact line shape ($\psi(l)$) described by the angle between the normal vector of the local contact line and the direction of the applied force.

$$F_{adh} = -\gamma \int_0^l \cos(\theta_{\text{contact}}(l)) \cos(\psi(l)) dl \tag{2.10}$$

While the general expression in Eq. 2.10 applies to all liquid-substrate systems, it requires full 3D information of droplet contact line geometry. A few techniques have been

developed to experimentally characterize 3D droplet geometries in the depinning process. A speckle technique was implemented by Schmucker *et al.* [170] to reconstruct dynamic 3D droplet profiles from speckle shift vectors using Snell's law. These speckle shift vectors are acquired by comparing specklegrams of the surface with and without droplets. The applications of the speckle technique [170] shed light on the different contact line evolutions and surface curvatures exhibited by droplets under wind- and gravity-forcing [169]. For droplets under wind-forcing, the entire downstream portion of the contact line experiences motion while the upstream portion remains pinned prior to depinning. Due to the pressure exerted by the incoming flow, negative curvature is observed in the upstream side of wind-forced droplets. For droplets under gravity-forcing, in contrast, a smaller portion of the contact line experiences motion prior to depinning and droplet surface maintains a positive curvature throughout similar to the sessile state. One drawback of the speckle technique, however, lies in the requirement of sufficient surface roughness to form specklegram and thus precludes its applications for droplets on smooth surfaces.

The limitation of speckle method was circumvented by digital fringe projection (DFP) utilized by Hu *et al.* [80], which creates a reference pattern by projecting fringes of sinusoidally-modulated light intensity onto the substrate and reconstructs 3D droplet geometry using the spatial phase shift in reference pattern induced by the presence of the droplets. Measurements of transient behaviours of wind-forced droplet using DFP showed that surface waves can form at the liquid-gas interface in the downstream portion of the droplet and propagate towards the upstream portion. It is suggested that these surface waves contribute to the droplet 'skip' motions (otherwise known as incipient motion [169], lurching [80], stick-slip motion [176], or shuffling gait motion [155]) observed in earlier studies [169]. A major challenge for DFP, however, is posed by the phase error of digital projectors. Methods for correcting this error, such as gamma correction [102] and binary

defocusing [101], often require elaborate calibration procedures and thus make implementation of DFP technique demanding.

For the diagnosis of droplet depinning, quantitative data collected from droplet side-view imaging, *i.e.* droplet contact length (L_b) and contact angles at the upstream and downstream-most contact points (θ_u and θ_d, respectively), can be sufficient to characterize droplet dynamics at depinning with the introduction of an empirical factor k (e.g. [50, 51, 121, 124]). The shape factor k describes the contact line geometry and distribution of contact angles. Adhesion between droplet and surface can be estimated using the simplified equation (Eq. 2.11) with side-view geometries.

$$F_{adh} = k\gamma L_b(\cos(\theta_u) - \cos(\theta_d)) \tag{2.11}$$

Extrand and Gent [50] have shown that surface roughness and chemical properties of the liquid-solid system significantly influence the contact line geometry at depinning, and the numerical constant k needs to be determined experimentally for a given system. Various efforts have been made in previous studies to evaluate the values of k for gravity-forced droplets on inclined plates. For droplets with circular contact lines at depinning, Brown *et al.* [19] suggested $k = \pi/2$ by solving Young-Laplace equation using the finite element method. Extrand and Gent [50], however, showed $k = 4/\pi$ for droplet with circular contact lines in their analytical solution. They further suggested that the cosine of contact angles, *i.e.*, $\cos(\theta_{\text{contact}})$ should vary linearly from the receding contact point to the advancing contact point. For elongated droplets at depinning, Dussan and Chow [43] suggested that, if receding and advancing contact angles (θ_u and θ_d) are constant, then $k = 2$ regardless of the exact contact line shape or length. More generally, Extrand and Kumagai [51] proposed the dependency on length-to-width ratio (L_b/c) following $k = 0.23 + 1.04L_b/c$. Given the difference in geometric configurations observed for gravity- and wind-force droplets at

depinning [169], whether wind-forced droplets exhibit similar trends for k values remains an open question.

Prior to the onset of droplet motion, adhesion is balanced by the sum of all external forces. Specifically, for droplets under wind-forcing, the time-averaged aerodynamic drag acting on the droplet can be expressed by the product of the dynamic pressure of incoming flow at droplet depinning ($\rho U_{\text{crit}}^2/2$), the impact area (A), and the mean drag coefficient of droplet geometry(C_D), as in Eq. 2.12.

$$F_D = \frac{1}{2}\rho U_{\text{crit}}^2 A C_D \tag{2.12}$$

Following Eqs. 2.11 and 2.12, critical depinning velocity can be predicted from the force balance between adhesion and aerodynamic drag, as in Eq. 2.13[121], which indicates that the critical velocity for droplet depinning depends on droplet geometric parameters (*i.e.*, contact length, frontal area, and contact angle hysteresis), aerodynamic properties (*i.e.*, drag coefficient), and fluids physical properties (*i.e.*, density and surface tension).

$$U_{\text{crit}} = \sqrt{\frac{2k\gamma L_b(\cos(\theta_u) - \cos(\theta_d))}{\rho A C_D}}, \tag{2.13}$$

The critical droplet geometry at depinning can be influenced by droplet volume [121, 201], surface wettability [121, 124, 153] and roughness [50]. Physical properties of the working fluids are affected by ambient temperature and humidity, which are of particular interest for droplets under icing conditions [153]. Apart from the critical depinning geometry, drag coefficient is also influenced by the incoming flow conditions, such as turbulence [200, 57], Reynolds number [185, 96, 131], and relative submergence of the droplet in the wall-bounded flows [200].

Extrand and Gent [50] studied the effect of surface roughness on critical depinning

geometry of droplets on a spinning platter, which exerted centrifugal force on droplets when spun at a prescribed angular velocity. Droplet elongation on roughened acrylic glass (PMMA) surface with a surface roughness of $s = 0.38$ almost doubled that on smooth PMMA surface.

Moghtadernejad *et al.* [124] characterized the distinctive droplet behaviours under the impact of laminar boundary layer formed by fixed airspeed on surfaces of low (aluminium) and high (superhydrophobic surface (SHS)) wettabilities. At low airspeed (7 m/s and 5 m/s for aluminium and SHS surfaces, respectively), droplets on aluminium surface remain pinned, oscillate with a slow movement, and elongate moderately with time; droplets on SHS surfaces, however, deform into an oblong shapes and roll along the surface. At high airspeed (90 m/s for both surfaces), droplets on aluminium surfaces elongate significantly and eventually form rivulets; while on hydrophobic surface, contact lengths decrease with time as droplets roll along the surface.

Milne and Amirfazli [121] investigated the fundamental parameters governing the onset of droplet motion under laminar boundary layer flows. Water and hexadecane droplets with heights in the range of 0.9 to 2.5 times the boundary layer thickness on PMMA, Teflon, and SHS were tested. The test results suggested that the wettability of the liquid-solid system are the most influential for the critical conditions required for droplet depinning. From a scaling analysis, the authors proposed an exponential relation between the critical air velocity required for droplet motion and the square root of the ratio of droplet contact length to the side-view area at the sessile state, *i.e.*, $U_{\text{crit}} = ae^{b(L_{b_0}/A_0)^{1/2}}$. With this model, the results for tests using water droplets collapsed to a self-similar curve by normalization. Reasonable agreements were also found for other droplet-substrate systems.

Roisman *et al.* [153] studied the critical depinning velocities for droplets submerged in a laminar boundary layer on substrates at room temperature (24.5°C) and subfreezing tem-

peratures (-5°C and -1°C). Water droplets of volumes ranging from 5 μL to 100 μL were tested on PMMA, PDMS, Teflon, and SHS surfaces ordered in decreasing wettabilities, resulting in droplet heights in the range of 0.35 to 1.4 times the boundary layer thickness. A slight increase in critical velocity was found for droplets on all substrates investigated under subfreezing conditions, which is attributed to the dependence of substrate wettability on temperature by the authors. The critical velocity was shown to be proportional to the cubic root of droplet volume, *i.e.*, $U_{\text{crit}} \propto V^{1/3}$. This cubic-root law is followed by test results acquired from all the substrates and temperatures investigated by [153], as well as by data reported in other studies such as [121, 79]. The trend lines fitted for each given combination of temperature and substrate are staggered by the change in wettability. With the observation that surface wettability mostly affects the relative submergence of droplets with respect to boundary layer thickness, the authors introduced the characteristic velocity at the droplet half-height estimated from the Blasius solution as a correcting factor of aerodynamic loading in their force balance model. The critical velocities predicted by this semi-analytical model matched well with their experimental measurements. However, discrepancies were observed when comparing the values of depinning velocities with those found by Milne and Amirfazli [121] for droplets under the impact of laminar boundary layer of similar submergence and on substrates of comparable wettability.

Recent work by White and Schmucker [201] investigated droplets under combined gravity- and high-Reynolds-number wind-forcing. Water droplets of volumes ranging from 15 to 450 μL on a roughened aluminium surface inclined at 0°, 10°, 20°, and 30° were tested. Droplets under pure wind-forcing were found to depin at a constant critical Weber number of 7.9, defined based on critical velocity and droplet height, *i.e.*, $\text{We}_{\text{crit}} = \rho U_{\text{crit}}^2 h/\gamma$. The critical Weber number decreases with increasing surface inclination angle. Typical contact line shapes at droplet depinning appear as two semicircular arcs joined by straight-line

segments. However, for droplets dominated by gravity-forcing, their contact lines show smaller radius of curvature on the advancing edge as compared to those under pure wind-forcing. This indicate the shape factor k characterizing the contact angle distributions along the contact line may take different values for wind- and gravity-forced droplets.

While many existing studies investigated droplet behaviours under the laminar flow conditions as described above, to the best of the author's knowledge, droplet behaviours in accelerating turbulent boundary layer formed over a flat plate has only been investigated in detail by White and Schmucker [200]. Water droplets of volumes ranging from 5 to 150 μL on aluminium surface were tested under the impact of an accelerating turbulent boundary layer. A relatively constant critical Weber number of 3.45 ± 0.09 was found, which is notably lower than that found in laminar boundary layers [201]. Significant unsteadiness observed at the droplet surface prior to depinning was attributed to the flow separation in the droplet wake [200]. However, a later study by Milne *et al.* [122] suggests that frequency of droplet oscillations associate more with the resonance frequency of the droplet-substrate system which depends on droplet volume, surface tension, and wetting properties, rather than the frequency of external forcing.

A few recent studies investigated droplet motion on a solid surface under the impact of fully developed turbulent channel flows. Barwari *et al.* [11] investigated the depinning criteria for droplets of pure water and solutions of glycerine and ethanol with varied mass fractions on substrates of PMMA and coated silicon wafer (cSW). Critical depinning velocities measured at the droplet height were normalized by droplet density, viscosity, and initial height as droplet Reynolds number $\mathrm{Re}_{\mathrm{droplet}} = \rho_L h_0 U_{\mathrm{crit}}/\mu_L$. When plotted against a modified Laplace number defined based on droplet properties and wetting parameters, $\mathrm{La} = \rho_L \gamma_{sl} L_{b_0}/\mu_L^2$, test results from all liquid-substrate systems investigated collapse along the same power-law curve. By approximating droplet geometries as spherical caps, this

power-law function yields an empirical model predicting critical depinning velocity based on droplet volume and contact angle at the sessile state. However, when normalizing the reported critical velocities for pure water droplets as Weber numbers as proposed in [200], droplets of volumes ranging from 7.8 μL to 39.9 μL exhibit Weber number ranges of $8.2 \lessapprox \mathrm{We}_{\mathrm{crit}} \lessapprox 11.8$ and $8.5 \lessapprox \mathrm{We}_{\mathrm{crit}} \lessapprox 9.1$ on PMMA and cSW surfaces, respectively. Both ranges are significantly higher than $\mathrm{We}_{\mathrm{crit}} \approx 3.45$ for droplets on aluminium surface under turbulent boundary layer formed over flat plate. Unfortunately, detailed flow characterization was not presented in [11]. Whether and how factors such as wetting properties, near-wall flow organizations, and turbulence intensity contribute to the discrepancies in Weber number remain an open question.

Seiler *et al.* [176] experimentally investigated droplet motion on a solid surface after depinning under a fully developed turbulent channel flow. Scaling analysis showed prior to droplet depinning, the viscous force is three to four order of magnitude smaller than the aerodynamic loading and adhesion due to contact angle hysteresis. However, as the droplet propagates along the surface, a thin tail is formed at the receding part of the droplet which changes the characteristic length scale of wall-normal velocity gradient from droplet height to a much smaller tail thickness. Consequently, the viscous force from the droplet tail becomes significant in the force balance and is proposed to follow the scaling $F_{\mu,\mathrm{tail}} \propto \mathrm{Ca}^{2/3}$, with Capillary number $\mathrm{Ca} = v_{\mathrm{drop}}\mu_L/\gamma$ characterizing the propagating velocity of the droplet. As a complementary study, Saal *et al.* [155] considered the same flow-droplet-substrate system and measured adhesion directly using drop adhesion force instrument (DAFI). Aerodynamic loading was estimated from numerical simulation on representative droplet models under the critical velocities measured in [176]. Good agreement with $F_{\mu,\mathrm{tail}} \propto \mathrm{Ca}^{2/3}$ was found for $\mathrm{Ca} > 10^{-4}$; below $\mathrm{Ca} \approx 10^{-4}$, deviation increases with decreasing Capillary number. The authors attributed this discrepancy to the 'skip' motion

of droplets, in which the aerodynamic loading is not sufficient to move the entire contact line. As a result, droplet oscillations are excited by the repeated pinning and depinning of different parts of the contact line.

In summary, depinning process of droplets submerged in flat plate boundary layers has been extensively investigated by existing studies. The effects of surface roughness, wettability, ambient temperature, and incoming flow turbulence has been considered. However, most depinning criteria were reported in dimensional form, making the comparison of test results across the studies difficult. Furthermore, the lack of detailed information of the incoming flow profile leaves discrepancies in depinning criteria reported by different studies for the same liquid-substrate system unexplained. In addition, droplet behaviour in other types of wall-bounded shear flows apart from flat plate boundary layers remains largely unconsidered. As such, droplet depinning under the impact of impinging jets is considered in Ch. 7. The results are compared with those acquired in the flat plate boundary layer with careful inspections of incoming flow velocity profiles and through a systematic dimensional analysis.

2.3.3 Droplet arrays under wind-forcing

Behaviour of multiple droplets in close proximity under wall-bounded shear flows received attention and was investigated experimentally and numerically by a limited number of recent studies. Moghtadernejad *et al.* [124] numerically investigated the depinning and agglomeration of droplets placed in tandem on a superhydrophobic surface with the volume of fluid (VOF) method. Combined with large eddy simulation (LES), they show the variation of ambient flow field and aerodynamic loading on droplets with time. Two droplets move towards each other with motion opposite to the air flow was observed for the

downstream droplet, leading to agglomeration. Hooshanginejad and Lee [77] classified the regimes of droplet upstream motion using a simplified setup with a hemispherical obstacle as the leader to simulate the change in pressure field induced by the uptream droplet. With decreasing initial spacing between the droplet and the leader hemisphere, three distinctive droplet behaviours were observed (i) depinning as an isolated droplet, (ii) drafting, which leads to increase in depinning velocity, and (iii-a) upstream motion, which is observed for small droplet volumes as reported earlier [124] or (iii-b) splitting, which is observed for large droplets volumes ($V \gtrapprox 150\mu$L). Razzaghi *et al.* [148] characterized the depinning velocities for droplet pairs in tandem and side-by-side configurations. Depinning velocity notably increases for the upstream droplets in closely spaced tandem configuration up to around 40% higher as compared to an isolated droplet, which decreases monotonically with increasing spacing. By contrast, droplets in a side-by-side configuration exhibit similar depinning conditions and there exists a critical spacing where the depinning velocity maximizes up to 30% higher than in the isolated droplet case. For both configurations, droplets on hydrophilic surfaces interact within a larger range of spacing than those on hydrophobic surfaces. A complementary study from the same group [149] numerically investigated the flow development around solid sessile droplet arrays of tandem, side-by-side, triangular, square and diamond configurations submerged in laminar flat plate boundary layer with thickness comparable to droplet height. The observations made in the steady-state velocity field simulation indicate extensions of the depinning velocities measured for two-droplet configurations in [148] to multiple-droplet arrangements. While these studies revealed the trends of depinning conditions followed by droplet arrays, they opened up more questions regarding the underlying physical mechanism and the consecutive agglomeration process.

Chapter 3

Experimental Setup and Procedures

This chapter presents the experimental methodologies employed to achieve the research objectives outlined in Sect. 1.3 and is divided into three sections. Sect. 3.1 introduces the jet facility which generates the background flow fields for droplet depinning, and presents the procedures for characterizing the flow development under varied impinging jet configurations. Sect. 3.2 first introduces the recirculating wind tunnel, flat plate, and droplet models used to simulate the critical flow condition at droplet depinning, and then presents the experimental setup for flow measurements and drag diagnostics. Sect. 3.3 identifies the key variables and test matrix for investigating the droplet dynamics in shear flows, and describes the experimental setup for controlling the identified parameters.

3.1 Flow measurements of impinging jets

3.1.1 Impinging jet facility

Impinging jet flows were generated using a custom jet facility at the University of Waterloo. The facility and apparatus employed in the impinging jet experiments are shown schematically in Figure 3.1(a). The flow from a blower was first conditioned by passing it through honeycomb (nominal cell diameter of 5 mm), one coarse screen (porosity of 82.3%), and three fine screens (porosities of 64.7%). The conditioned flow was then accelerated through a 9 : 1 two-dimensional contraction. The flow exited from a rectangular nozzle of span $L = 200$ mm and width $B = 10$ mm. An anodized aluminium plate with dimensions of $60B \times 80B$ served as the impingement target.

3.1.2 Impinging jet characterization

Visual observations suggested most droplets depin at a jet exit velocity between 5 and 10 m/s. Slot jets with nominal centreline velocity $U_j = 5$ and 10 m/s, equivalent to jet Reynolds numbers of Re = 3000 and 6000, were investigated to analyse the bounding scenarios. At the nozzle exit, the velocity profile was uniform, with maximum deviation of less than $\pm 1\%$ across 95% of the span. Mean flow properties were measured for the two jet Reynolds numbers at four jet orientation angles $\alpha = 30°$, 45°, 60°, and 90°. Reynolds number effects on the vortex dynamics were investigated for both Reynolds numbers at $\alpha = 90°$. In all cases, the nozzle-to-plate spacing ratio was fixed at $H/B = 4$. The experimental conditions are summarized in Table 3.1.

Statistical flow field characterization was performed using a non-time-resolved, two-dimensional, two-component (2D-2C) particle image velocimetry (PIV) system. A single

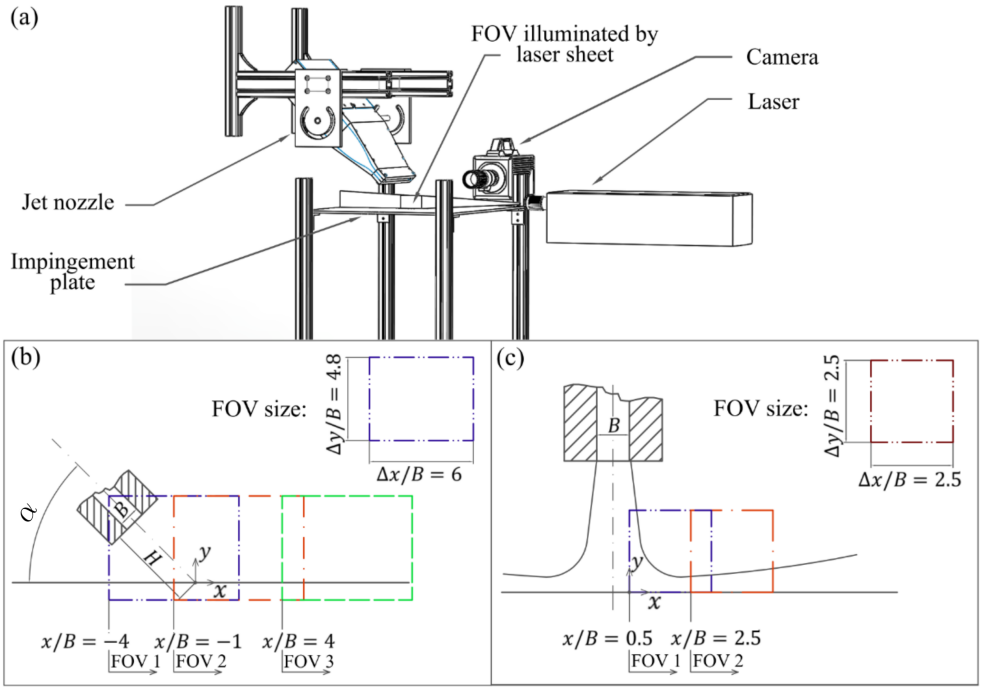

Figure 3.1: (a) Experimental setup of PIV measurements of oblique impinging jet flows. Schematics of field of view (FOV) for (b) mean flow measurement and (c) vortex dynamic investigation.

Imager ProX camera was equipped with a 105 mm Nikon lens to capture a field of view (FOV) of 60×48 mm^2 with a cropped sensor size of 1200×960 px. Light provided by an Evergreen 70 Nd-YAG laser was conditioned into a light sheet of approximately 1 mm thickness to illuminate the flow at the mid-span location of the jet to guarantee the two-dimensionality of the measurements. The flow within the jet and in the ambient air was seeded uniformly with water-glycol based fog particles with a mean diameter of around 1 μm, corresponding to a Stokes number of Sk $= 0.003$ for jet flow at Re $= 6000$. While the particle size distribution was not assessed, larger seed particles potentially generated by the fog machine were naturally filtered out by the flow conditioning (honeycomb and screens) upstream of the nozzle exit. This was confirmed by visual inspection of the impingement

Table 3.1: Jet configurations for PIV measurements.

Parameter	Value	Unit
Nominal centreline velocity, U_j	5, 10	m/s
Nominal Reynolds number, Re	3000, 6000	–
Nozzle-to-plate spacing ratio, H/B	4	–
Jet orientation angle, α	$90°, 60°, 45°, 30°$ (Flow statistics)	–
	$90°$ (Vortex dynamics)	–

plate, which showed virtually no fog fluid residue in the stagnation region after multiple runs. The numerical aperture and magnification factor were $f_{\#} = 2.8$ and $M = 0.148$, respectively. The illumination and imaging systems were synchronized by a LaVision High-Speed controller and DaVis 8 program, with the latter also used for image processing. Three FOVs, as shown in Fig. 3.1 (b), ranging from $-4 \leqslant x/B \leqslant 2$ (FOV 1), $-1 \leqslant x/B \leqslant 5$ (FOV 2), and $4 \leqslant x/B \leqslant 10$ (FOV 3), were investigated consecutively. A total of 1200 particle image pairs were acquired in double-frame mode at 15 Hz for each FOV. A sequential cross-correlation algorithm with multi-pass iterations of decreasing window sizes was used to process the images. The final interrogation window size was 48×48 px, with an overlap of 75%, resulting in a vector pitch of 0.6 mm. An elliptical Gaussian weighting with an aspect ratio of $2 : 1$ was used for the final interrogation. Flow statistics retrieved from the three FOVs were stitched by blending the measurements in the overlapping regions of different cameras with a cosine weighting function. The combined FOV spans $-4 \leqslant x/B \leqslant 10$. The estimated calibration error of $x - y$ coordinate was half of the pixel size. The uncertainty of instantaneous velocity due to random errors was estimated to be less than 1% of the jet exit velocity with 95% confidence. The quantification of uncertainties associated with mean flow and turbulence statistics is detailed in Appendix A.

A high-speed, two-component PIV system was used to obtain time-resolved (TR)

Table 3.2: Recording parameters for PIV measurements of impinging slot jets.

Parameter	Value (non-TR-PIV)	Value (TR-PIV)	Unit
FOV, single camera	60×48		mm^2
FOV, combined	–	45×25	mm^2
Sensor size	1200×960	1024×1024	px
Magnification factor, M	0.148	0.819	–
Focal length, f	105	200	mm
Numerical aperture, $f_\#$	2.8	4	–
Particle image diameter, $d\tau$	0.564	0.47	px
PIV acquisition frequency, f_{acq}	0.015	0.5(Re = 3000) 1.95(Re = 6000)	kHz
Pulse separation, dt	80 (Re = 3000) 40 (Re = 6000)	50 (Re = 3000) 25 (Re = 3000)	μs
Number of images, N	1200	2778	–
Vector pitch	0.6	0.15	mm

velocity measurements. Two Photron SA4 high-speed cameras were used simultaneously. The cameras were equipped with 200 mm Nikon lenses to capture a combined FOV of 25×45 mm^2 (25×25 mm^2; 1024×1024 px for each camera), as shown in Fig. 3.1 (c). Light provided by a Photonics DM20-527 Nd-YLF laser was conditioned and synchronized with the cameras in the same manner as for non-time-resolved PIV measurements described earlier. The numerical aperture and magnification factor were $f_\# = 4$ and $M = 0.819$, respectively. A total of 2728 particle image pairs were acquired in double-frame mode at 500 Hz and 1950 Hz for Re = 3000 and 6000, respectively. A sequential cross-correlation algorithm with multi-pass iterations of decreasing window sizes was used to process the images. The final interrogation window size was 24×24 px, with an overlap of 75%, resulting in a vector pitch of 0.15 mm. An elliptical Gaussian weighting with an aspect ratio of 2 : 1 was used for the final interrogation window. The essential PIV parameters for both non-time-resolved and time-resolved measurements are summarized in Table 3.2.

3.2 Flow measurements over flat plate

3.2.1 Wind tunnel facility and flat plate setup

Flat plate experiments were conducted in the closed-loop wind tunnel at the University of Waterloo with a $0.6 \times 0.6\ \mathrm{m}^2$ test section and free-stream turbulence intensity of less than 0.06%. A 1.5 m-long black anodized aluminium plate spanning the test section was employed as the test surface, see Fig. 3.2. The leading edge had a super-elliptic profile [105] to minimize flow disturbances due to curvature discontinuities and a trailing edge flap controlled the stagnation point location at the leading edge. Thin rubber inserts were used to seal the gaps between the plate and the wind tunnel side walls. The freestream velocity above the plate was set by means of a Pitot-static tube, with an associated uncertainty of less than 2%. Both laminar and turbulent boundary layers were considered. Laminar boundary layers developed naturally over the flat plat model. To obtain turbulent boundary layers of desired thickness over a short distance, zig-zag tape was installed at 200 mm downstream of the flat plate leading edge to trip the boundary layer.

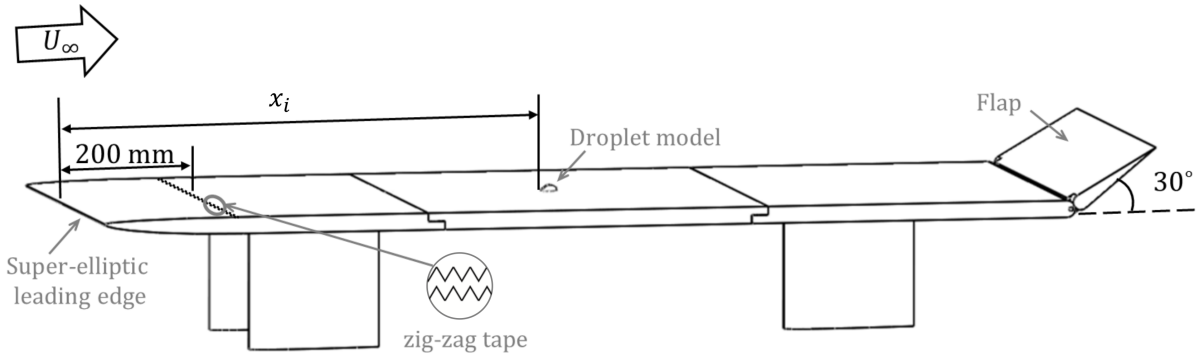

Figure 3.2: Schematic of flat plate arrangement.

3.2.2 Flow over surface-mounted droplet-inspired geometries

Given a significant separation between the time scales associated with relatively slow droplet deformations [122, 20] and comparatively fast hydrodynamic fluctuations in the surrounding flow [178], the flow development over representative solid droplet models was considered as a lower-order approximation of that over water droplets.

3D-printed solid models representative of a sessile (undisturbed) droplet (referred to as 'sessile') and a deformed droplet under wind-forcing immediately prior to depinning (referred to as 'runback') were considered. These two geometries were generated based on simultaneous side and top view images of 120 μL water droplets in quiescent and wall-bounded flows, respectively (see Fig. 1.1). The droplet models were scaled up by a factor of 2.5 for better spatial resolution of the flow measurements. The 3D model volumes, shown in Table 3.3, are within 6% of the nominal scaled water droplet volume of 1875 mm^3. A spherical cap geometry with height approximately equal to that of the sessile model (referred to as 'chopped') was generated to evaluate the validity of using a spherical cap as a simplified sessile droplet model. The chopped model volume is roughly 10% less than that of the sessile model. A hemispherical geometry (referred to as 'hemisphere') was used as a baseline model to validate the drag estimation based on PIV measurements. The height of the hemisphere model is comparable to those of the other models to guarantee the similarity in relative submergence, *i.e.*, the ratio between the boundary layer thickness in the absence of the model versus the model height (δ/h). Following 3D printing with a resolution of 0.13 mm, each model was contour sanded to achieve a smooth surface finish, ending with 800-grit sandpaper. The smoothed models were then spray-painted with black matte finish to mitigate reflections and further smooth the surface. All four models are shown schematically in Fig. 3.3(a). The geometric parameters of the models, including model height (h), width (c), length (l), frontal area (A), volume (V), aspect ratio (h/c),

and upstream and downstream contact angles (θ_u and θ_d, respectively), are summarized in Table 3.3. The downstream-most point of the model on the flat plate serves as the origin of the coordinate system, with the x, y, and z axes corresponding to the streamwise, wall-normal, and spanwise directions, respectively, as shown in Fig. 3.3(b).

The models were installed along the flat plate centreline. The flap of the flat plate

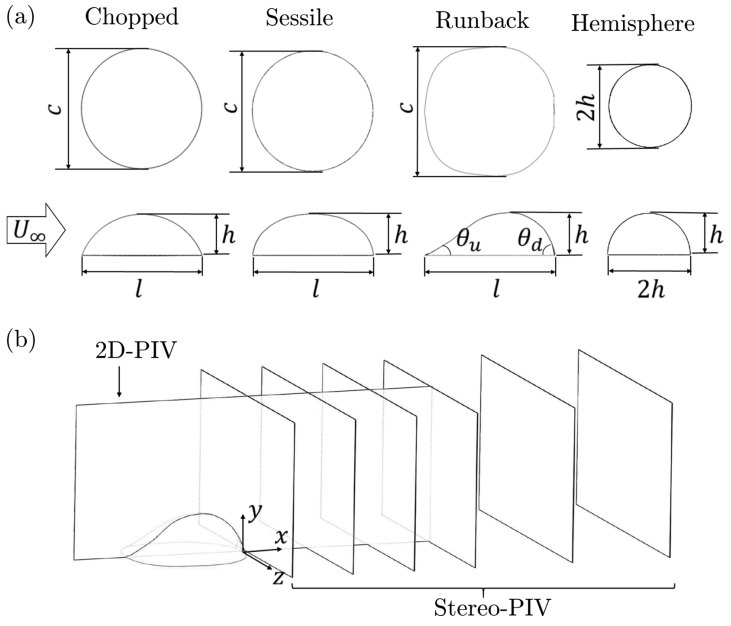

Figure 3.3: (a) Geometry of droplet-inspired and reference models. (b) Fields of view for PIV measurements of flow development over surface-mounted 3D obstacles.

Table 3.3: Geometric parameters of droplet-inspired and reference models.

Model	h [mm]	c [mm]	l [mm]	A [mm^2]	V [mm^3]	h/c	θ_u	θ_d
Chopped	7.64	22.39	22.39	124.0	1781	0.341	67°	67°
Sessile	7.69	22.41	22.41	136.1	1984	0.343	82°	82°
Runback	7.94	23.99	24.08	123.9	1922	0.331	23°	84°
Hemisphere	7.73	15.45	15.45	93.7	965.5	0.500	90°	90°

model was positioned at an angle of 30° (see Fig. 3.2). To guarantee the dynamic similarity, the Reynolds number based on the height ($\mathrm{Re}_h = U_\infty h/\nu$) of the solid models should match that of the water droplets at depinning. Since the droplet models were scaled up by a factor of 2.5 in linear dimensions, the freestream velocity was scaled down by the same factor and was set to $U_\infty = 4$ m/s, corresponding to a Reynolds number based on model height of approximately $\mathrm{Re}_h \approx 2070$. This Reynolds number simulates the critical depinning condition for water droplets of volumes $75\ \mu\mathrm{L} \leq V \leq 120\ \mu\mathrm{L}$ from an anodized aluminium surface under forcing from a laminar boundary layer based on droplet tests (see Sect. 3.3). The models were placed at varied distance x_i from the flat plate leading edge to investigate the effect of relative submergence. Both laminar and turbulent boundary layers were considered to investigate the effect of incoming flow turbulence on flow development over droplet models. The baseline laminar boundary layer profiles were verified to match the Blasius solution, as evidenced from the shape factor of around 2.60, which deviates by less than 1% from that expected for the laminar flat-plate boundary layer. Around the model half-height, the turbulence intensities in the laminar and turbulent boundary layers were $TI \approx 0.5\%$ and 13%, respectively. The integral parameters of the boundary layers in the absence of the model are summarized in Table 3.4.

Time-resolved 2D-2C PIV was used to capture instantaneous velocity fields in the xy plane. Illumination was provided by a Photonics DM20-527 Nd-YLF pulsed laser, with a laser sheet thickness of approximately 1 mm. The flow was seeded with water-glycol-based fog particles with mean diameter of approximately 1 μm. Two 1024×1024 px Photron SA4 high-speed cameras, each equipped with a Nikon 200 mm lens, were used to capture a combined field of view (FOV) of $85 \times 45\ \mathrm{mm}^2$ ($45 \times 45\ \mathrm{mm}^2$ for each camera), covering a streamwise range of $-4.2 \lesssim x/h \lesssim 6.3$, see Fig. 3.3(b). The numerical aperture and magnification factor were $f_\# = 4$ and $M = 0.455$, respectively. The illumination

Table 3.4: Incoming flow conditions and boundary layer parameters for flow development over surface-mounted 3D obstacles. For turbulent cases marked with ✠, the flow was tripped by zig-zag tape installed 200 mm downstream of the flat plate leading edge (see Fig. 3.2).

U_∞ [m/s]	x_i [mm]	B.L. regime	δ [mm]	δ^* [mm]	Θ [mm]	δ/h	$\mathcal{H}$	Re_{x_i}	Re_h	Re_Θ
4	735	laminar	7.95	2.59	0.99	1.0	2.61	1.96×10^5	2070	265
4	1256	laminar	10.54	3.72	1.43	1.4	2.60	3.35×10^5	2070	381
4	428	turbulent✠	11.51	1.90	1.41	1.5	1.35	1.14×10^5	2070	377
4	608	turbulent✠	16.12	2.55	1.92	2.0	1.33	1.62×10^5	2070	511
4	1114	turbulent✠	27.69	3.94	2.87	3.5	1.37	2.97×10^5	2070	765

Table 3.5: Recording parameters for PIV measurements of flow development over surface-mounted droplet-inspired obstacles.

Parameter	2D-2C PIV	Stereo-PIV	Units
Single camera FOV	45×45	–	mm^2
Combined FOV	85×45	45×45	mm^2
Streamwise range	$-4.2 \leq x/h \leq 6.3$	$0.3 \leq x/h \leq 14.6$	
Sensor size	1024×1024	1024×1024	px
Magnification factor, M	0.455	0.455	–
Focal length, f	200	200	mm
Numerical aperture, $f_\#$	4	11	–
PIV acquisition frequency, f_{acq}	1000	15 1000 (at $x/h = 4.0$)	Hz
Pulse separation, dt	155	30	μs
Number of images, N	2560	1500 2560 (at $x/h = 4.0$)	–
Vector pitch	0.25	0.25	mm

and image acquisition were controlled by a LaVision High-Speed controller using DaVis 8 software; the latter was also used for image processing. The particle images were ac-

quired in double-frame mode at 1 kHz, with a total of 2560 image pairs collected for each set of experimental conditions. A sequential cross-correlation algorithm with multi-pass iterations of decreasing interrogation window sizes was used to process the images. The final interrogation window was 24×24 px with 75% overlap, resulting in a vector pitch of 0.25 mm.

Stereoscopic PIV (stereo-PIV) was used to capture the three-dimensional attributes of the flow development downstream of the droplet models in a series of 31 yz planes (see Fig. 3.3(b)) located within $0.3 \lesssim x/h \lesssim 14.6$. The first 15 planes ($x/h \lesssim 4$) were spaced 2 mm apart starting at $x = 2$ mm for the sessile and chopped models and $x = 3$ mm for the runback model; the next 12 planes were spaced 4 mm apart; and the final 4 planes were 8 mm apart. Light provided by an Evergreen 70 Nd-YAG laser was formed into a sheet of approximately 1 mm thickness at its waist. The two Photron SA4 cameras, equipped with Nikon 200 mm lenses and Scheimpflug adapters, captured a FOV of 45×45 mm^2. The numerical aperture and magnification factor were $f_{\#} = 11$ and $M = 0.455$, respectively. The images were acquired in double-frame mode at 15 Hz. A total of 1500 image pairs were collected for each set of experimental conditions. The laser and the cameras were positioned on synchronized, high-precision traverses that allowed consistent laser sheet alignment relative to the imaging planes. In addition to target calibration, particle-based self-calibration was also employed [205]. Cross-correlation with multi-pass iterations of decreasing interrogation window sizes was used to process the images. The final interrogation window was 24×24 px with 75% overlap, resulting in a vector pitch of 0.25 mm.

For spectral analysis, time-resolved stereo-PIV measurements were performed in the yz plane at $x/h \approx 4.0$. The same hardware was employed as those used for the time-resolved 2D-2C PIV measurements. The light sheet and cameras were set up in the same manner as in the non-time-resolved stereo PIV measurements. Images were acquired in double-frame

mode at 1 kHz, with a total of 2560 image pairs collected for each set of experimental conditions.

Table 3.5 summarizes the recording parameters of the 2D-2C PIV and stereo-PIV measurements. With self-calibration, the uncertainty of the stereo-PIV measurements is dominated by the planar uncertainty [205]. For both PIV setups, the uncertainty in the instantaneous velocity fields was estimated to be less than 1% of the freestream velocity in the freestream with 95% confidence level. The quantification of uncertainties associated with mean flow and turbulence statistics is detailed in Appendix A).

3.3 Droplet tests under accelerating shear flows

Droplet behaviour under the impact of wall-bounded shear flows was investigated under two background flow configurations: a laminar boundary layer formed by flow over a flat plate (Fig. 3.4(a)) and wall jets formed by slot jet impingements. 3.4(b)).

Experiments of droplet depinning in the laminar boundary layer were performed in the closed-loop wind tunnel described in Sect. 3.2.1. A 0.9 m-long flat plate model with similar super-elliptic leading edge geometry and trailing edge flap as described in Sect. 3.2.1 was used to generate the laminar boundary layer, with the flap positioned at an angle of 15° to create a boundary layer thickness comparable to the water droplet height investigated (Fig. 3.4(a)). Experiments of droplet depinning in impinging jets were performed using the jet facility as described in Sect. 3.1.1. Droplets of distilled water were tested on anodized aluminium substrates. The substrates installed on the flat plate model and the jet facility were both polished to 1000-grit and black-anodized to guarantee comparable wettabilities.

Water droplets of four volumes of 75, 90, 105, and 120 μL were investigated. The sessile droplets were generated using a micro-pipette, with the uncertainty in droplet volume

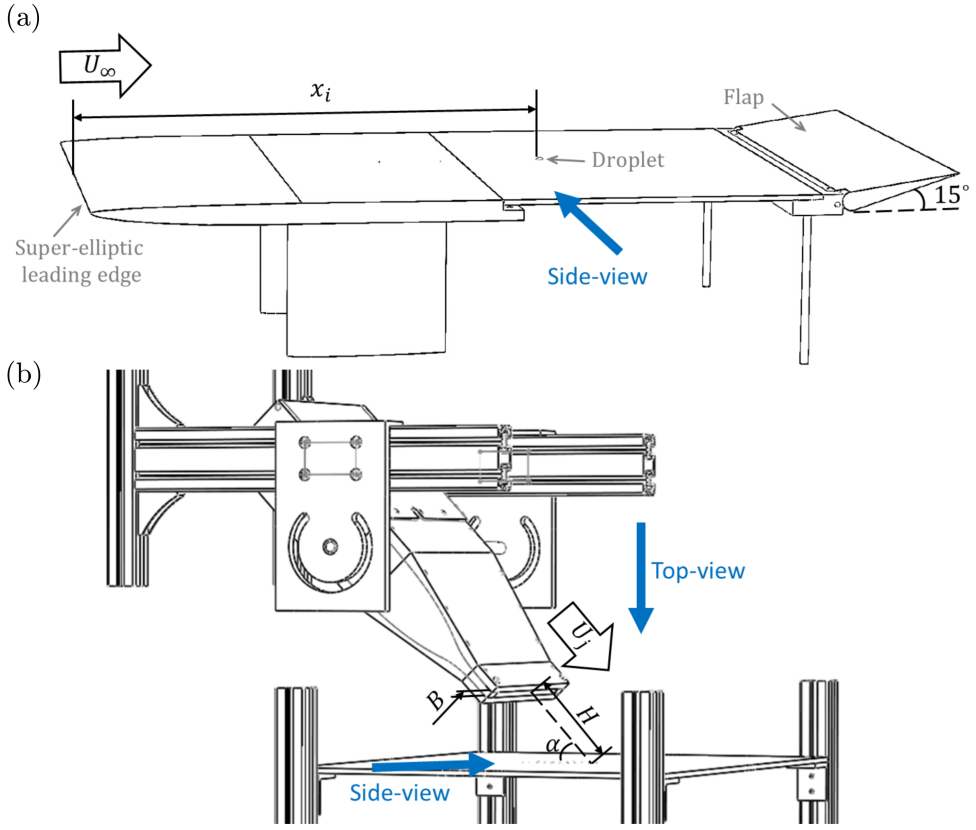

Figure 3.4: Experimental setup for droplet depinning under the impact of wall-bounded shear flows formed by (a) flat plate boundary layer and (b) impinging jet.

estimated to be within 3% of the smallest droplet volume investigated, quantified based on weight measurement using an analytical balance. In both facilities, the freestream (or jet centreline) velocity was varied from 0 to 20 m/s via accelerations of $\mathrm{d}U_\infty/\mathrm{d}t$ (or $\mathrm{d}U_j/\mathrm{d}t$) = 1.2, 2.2, and 4.4 m/s^2. The ramp-up end velocity (U_∞ or U_j = 20 m/s) was selected to produce a nearly-constant acceleration around the velocity of interest (U_∞ or $U_j \approx 10$ m/s, see Figs. 4.2 and 4.16 for detailed characterization). The ramp-up velocity profiles of the wind tunnel and the jet facilities were characterized using a Dantec Streamline Pro constant-temperature anemometer, with the overheat ratio of the P-11 hot-wire set to 0.5

Table 3.6: Test matrix for droplet depinning under the impact of wall-bounded shear flows.

α [°]	x_i [mm]	x^* [mm]	Re_{x^*} ($U = 10$ m/s)	δ [mm] ($U = 10$ m/s)	V [μL]	$\mathrm{d}U/\mathrm{d}t$ [m/s^2]
0	550	650	4.33×10^5	4.7	75, 90, 105, 120	1.2, 2.2, 4.4
45	10	20	1.33×10^4	2.6		
45	30	40	2.67×10^4	2.2		
45	40	50	3.33×10^4	3.1		
45	60	70	4.67×10^4	4.2		
90	70	70	4.67×10^4	3.2		
30	39	60	4.00×10^4	3.4	75, 120	1.2, 2.2, 4.4
60	45.5	50	3.33×10^4	3.5		

and acquisition frequency of 10 kHz. The hot-wire measurements were performed within the freestream of the wind tunnel, along the centreline at the exit of the jet facility, and at the wall locations where droplets were deposited. The hot-wire position was measured via calibrated side-view camera images, with the hardware and settings being the same as those used for imaging droplets as described later in this section. The uncertainty of the hot-wire position was estimated to be approximately 88 μm, or 5 px, which is associated with identifying the hot-wire tip from the image. Detailed results of the flow fields formed over flat plate and by jet impingements are presented in Ch. 4. Table 3.6 summarizes the testing parameters for droplet depinning experiments. The flow orientation angle (α) follows the same definition as jet orientation angle (see Fig. 3.1(b)) for impinging jets, and $\alpha = 0°$ represents the flat plate boundary layer. Droplet initial location (x_i) is defined as the streamwise distance from the flat plate leading edge for the laminar boundary layer (see Fig. 3.4(a)), and as the distance from the intersection point of the jet centreline and the target surface for impinging jets (see Fig. 3.4(b)). An additional parameter (x^*) is defined to characterize the streamwise distance from the virtual origin of the flat plate model or the stagnation point of the impinging jet at a given jet configuration (x_0), which

is discussed in detail in Ch. 4. Visual observations suggested most droplet depinning occurs at a freestream (or jet exit) velocity of around 10 m/s, and thus the boundary layer thickness of the near-wall shear flows formed at this velocity was used to indicate the relative submergence of boundary layer thickness versus droplet height (δ/h). Fourteen runs were performed for each combination of parameters listed in Table 3.6.

A pco.edge 5.5 CMOS camera operating at 40 Hz was used to capture the side-view profile of the droplets. The camera was equipped with a 200 mm Nikon lens to capture a FOV of $45 \times 20\,\text{mm}^2$ with a cropped sensor size of 2560×1162 px. This resulted in a magnification factor of $M = 0.199$ and a spatial resolution of 17.6 μm/px. A cold diffused light provided by an LED light array was used as backlight to improve the image contrast. A Nikon D7200 camera equipped with a 50 mm Nikon lens and operating at 1 Hz was used to provide additional top-view perspective (see Fig. 3.4 (b)). Triggering signals for the freestream velocity control, the side-view, and top-view cameras were synchronized as illustrated by the timing diagram in Fig. 3.5.

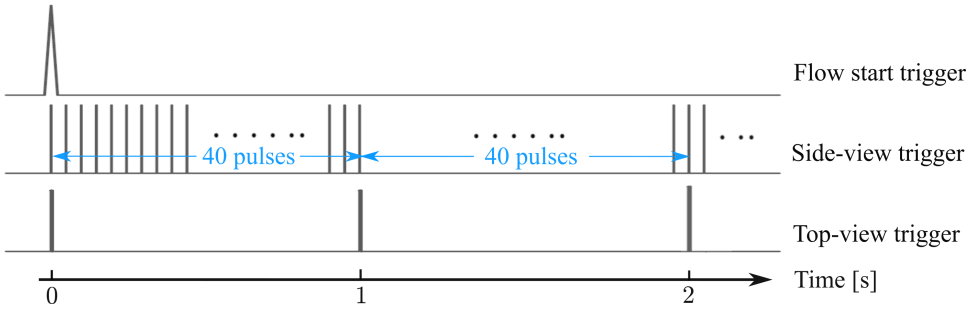

Figure 3.5: Trigger signals for blower, side-view and top-view cameras.

Chapter 4

Background Flow Characterization for Droplet Dynamics Experiments

This chapter presents the characterization of wall-bounded shear flows which serves as the background flow fields for depinning water droplets from a substrate. This chapter is divided into three sections. Sect. 4.1 presents the hot-wire measurements of steady and accelerating boundary layer flow development over the flat plate model used in water droplet tests (see Fig. 3.4(a)). Sect. 4.2 presents the flow fields formed by steady and accelerating slot jet impingements at several jet configurations (see Table 3.1). Sect. 4.3 summarizes the main findings of this chapter.

Parts of this chapter have been published in Experiments in Fluids 60(1) (2019) [217]. The final authenticated version is available online at: https://doi.org/10.1007/s00348-018-2653-6.

4.1 Flat plate boundary layer flow development

4.1.1 Steady boundary layer

The steady flow development over the flat plate model used for droplet tests (see Fig. 3.4(a)) is characterized at a freestream velocity of 10 m/s. The boundary layer thickness measured at this freestream velocity is used to indicate the relative submergence of boundary layer versus droplet height (δ/h). The time-averaged velocity profiles were acquired at $x = 245$, 305, 365, 450, and 550 mm downstream of the flat plate leading edge using a hot-wire and following the procedures as described in Sect. 3.3. For each streamwise location, the measurement covered a wall-normal range of $0.5\,\text{mm} \lessapprox y \lessapprox 6.5\,\text{mm}$, with an increment of $\Delta y \approx 0.5$ mm for the first five measurement locations, and $\Delta y \approx 1$ mm from $y \approx 2.5$ mm and above.

The streamwise velocity profiles are normalized with freestream velocity and are illus-

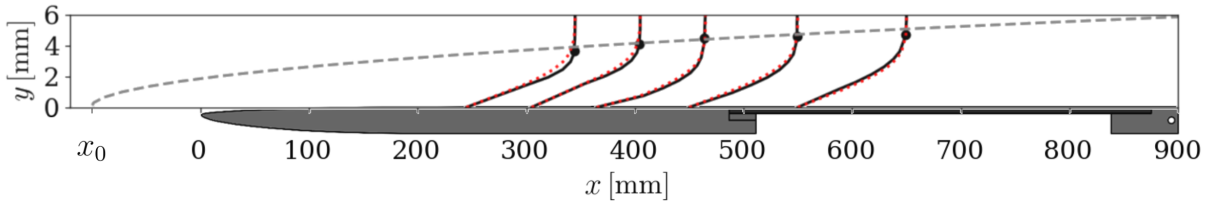

Figure 4.1: Boundary layer development over flat plate model shown in Fig. 3.4(a). Solid black lines show the mean boundary layer profiles at a freestream velocity of $U_\infty = 10$ m/s and black markers indicate the geometric boundary layer thickness where local streamwise velocity reaches $u = 99\%U_\infty$; Dotted red lines show the boundary layer profile predicted by Blasius solution [202]; Dashed gray line shows the fitted Blasius boundary layer development.

trated by solid black lines in Fig. 4.1. Boundary layer thickness, defined as the locations where local streamwise velocity reaches $u = 99\%U_\infty$, was determined through interpola-

tion. The virtual origin of the flat plate (x_0) was found at $x = -100.6$ mm by fitting a power-law relation of $\delta \propto x^{1/2}$ between the measured boundary layer thickness and streamwise locations as prescribed by the Blasius solution (see Eq. 2.3), with the fitted curve illustrated by the dashed gray line. The measured boundary layer profiles (solid black lines) show good agreement with the profiles predicted by Blasius solutions (dotted red lines) using the streamwise distance x^* measure from the virtual origin, indicating the naturally developed boundary layer within the streamwise range of $245 \leq x \leq 550$ mm is laminar.

4.1.2 Accelerating boundary layer

To validate the consistency of velocity ramp-up performance of the recirculating wind-tunnel, the velocity time histories were characterized using hot-wire following the procedures as described in Sect. 3.3. The instantaneous velocities were sampled within the freestream along the centreline of the recirculating wind tunnel (at around $y \approx 150$ mm), and at three near-wall locations close to the mean droplet height (around $y \approx 2.6$) at the streamwise location of $x_i \approx 550$mm for droplet depinning tests (also reported in Table 3.6). Fig. 4.2(d) shows the three wall-normal locations with respect to the local streamwise velocity profile of the steady boundary layer formed at $U_\infty = 10$ m/s (see Sect. 4.1.1).

The ramp-up time histories corresponding to the three investigated accelerations $\mathrm{d}U_\infty/\mathrm{d}t = 1.2$, 2.2, and 4.4 m/s are shown in Fig. 4.2(a), (b), and (c), respectively. Measurements were repeated for five trials at each wall-normal location for each acceleration. The instantaneous velocities measured by hot-wire are indicated by the gray lines. Moving average of the velocity measurements of each trial was calculated using a second-order Savitzky-Golay filter [162] with a window width of five seconds. For all three accelerations,

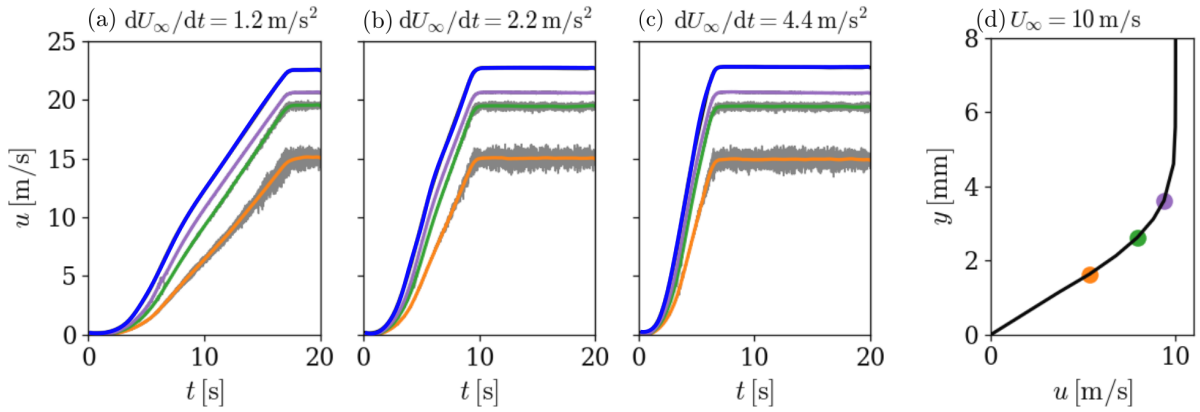

Figure 4.2: Sliding average of velocity sampled in the freestream (blue lines) and three near-wall locations as the wind tunnel freestream velocity ramps up at around (a) $1.2\,m/s^2$, (b) $2.2m/s^2$, and (c) $4.4m/s^2$, overlaid with the instantaneous velocities measured over five runs (gray lines). (d) Steady near-wall velocity profile measured at $x_i = 550\,mm$ downstream of the flat plate leading edge at a freestream velocity of $U_\infty = 10\,m/s$, with dots showing the wall-normal locations where the near-wall velocity ramp-up time histories are sampled.

at the sampling location closest to the wall (orange lines), the ramp-up slope (*i.e.*, the local flow acceleration) and the end velocity (*i.e.*, the velocity attained at the end of flow acceleration), are notably smaller than those in the freestream (blue lines). This is expected given the velocity gradient in the steady velocity profile in the near-wall region (see Fig. 4.2(d)). Velocity fluctuations around the moving-averaged ramp-up curve are the strongest among the three near-wall sampling locations. At distances off the surface of around the droplet height (green lines), the ramp-up slope is similar to that of the freestream, and velocity fluctuations diminish with increasing distance from the wall. Further away from the flat plate surface (purple lines), both ramp-up slope and end velocity approaches those in the freestream. Velocity fluctuations at this location is negligibly small, similar to the amplitude of those in the freestream.

The instantaneous and moving-averaged ramp-up time histories of the five trials of

each combination of acceleration and wall-normal location show high repeatability. Given the consistency in the ramp-up performance of the recirculating wind tunnel, velocity measurements can be decoupled from the measurements of droplet geometry in response to accelerating boundary layer flows. This facilitates the experimental setup for droplet imaging by avoiding the optical obstructions introduced by the hot-wire and its supporting structures.

4.2 Impinging jet flow development

For the slot jet system, the flow fields formed by impinging jets were characterized at jet exit velocities of $U_j = 5$ and 10 m/s, corresponding to jet Reynolds number of $\mathrm{Re} = 3000$ and 6000. The thickness of the wall layer at $U_j = 10$ m/s is used to indicate the relative submergence of boundary layer versus droplet height (δ/h). Unlike for laminar boundary layers in which flow development demonstrates self-similarity, near-wall flow development in impinging jets are sensitive to change in Reynolds number [140]. Flow development at $U_j = 5$ m/s, which is midway from zero to the ballpark estimate of droplet depinning velocity (see Sect. 3.3), is investigated to provide additional insights of impinging jet flows.

4.2.1 Definition of pertinent variables and coordinate system

Figure 4.3 shows a schematic of an oblique impinging slot jet considered in this study, along with pertinent variable and coordinate system definitions. The intersection of the jet geometric centreline and the target surface is defined as the geometric centre, which serves as the origin of a Cartesian coordinate system, with the x-axis oriented along the target surface, and the y-axis normal to the target plate pointing towards the nozzle.

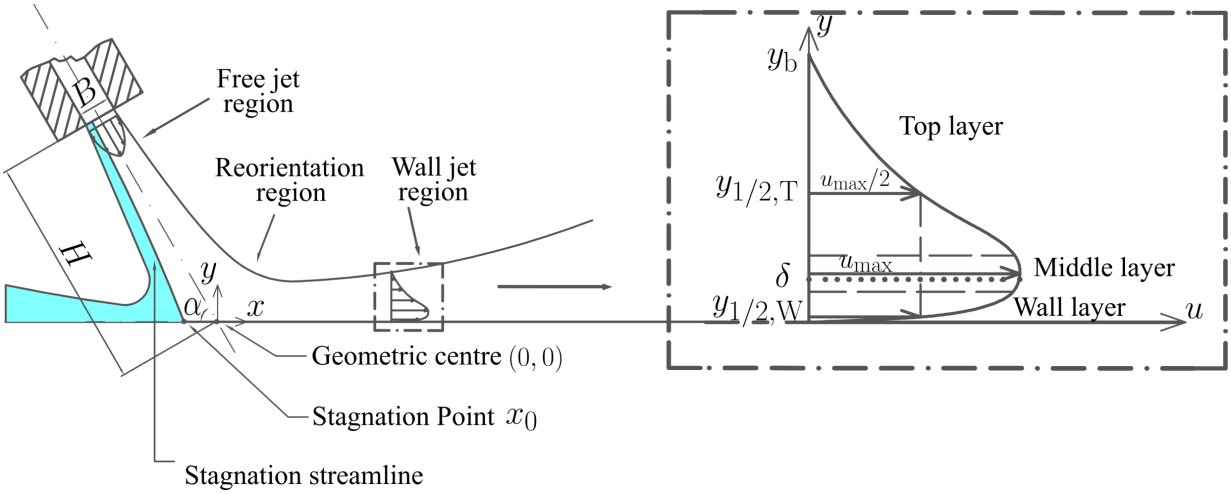

Figure 4.3: Schematic of oblique impinging jet flows. The inset shows a cartoon of the wall jet velocity profile with the three layers demarcated by long dashed lines.

Due to stagnation point eccentricity with jet angle, the actual stagnation point is defined at x_0. The velocity components in the x, y, and z directions are denoted as u, v, and w, respectively. The jet orientation angle α is the angle formed by the jet geometric centreline and the target surface (negative x-axis). An air jet of kinematic viscosity ν exits from a slot of width B at a centreline velocity U_j. The nozzle-to-plate spacing H is the distance between the slot exit plane and the origin $(0, 0)$. As such, the flow physics are governed by the following dimensionless parameters: Reynolds number $\mathrm{Re} = U_j B/\nu$, the nozzle-to-plate spacing ratio H/B, and the jet orientation angle α.

The velocity profile in the wall jet region consists of two self-similar layers, namely, the top layer and the wall layer, which are bridged by a middle layer, thus forming a triple-layered structure [10], see Fig. 4.3. Following [10], the middle layer, which bridges the top and wall layers, is loosely defined as the region in the vicinity of $u_{\max}$. To facilitate discussion, the y location where u reaches a maximum is defined as the geometric boundary layer thickness δ; the y locations where $u = u_{\max}/2$ are defined as the local jet half-

widths, $y_{1/2,\mathrm{i}}$ ($\mathrm{i} = \mathrm{T}, \mathrm{W}$ for top and wall layer, respectively); the y location where $u = 0.01u_{\max}$ with $y > y_{\max}$ is defined as the wall jet thickness y_{b}. Due to the measurement uncertainty limitations, the wall layer half-width $y_{1/2,\mathrm{W}}$ is estimated as half the thickness of the geometric boundary layer thickness, *i.e.* $y_{1/2,\mathrm{W}} = \delta/2$.

4.2.2 Time-averaged steady impinging jet flow development

The mean velocity fields for varying α at both Reynolds numbers investigated are presented in Fig. 4.4. Locations of δ and $y_{1/2,\mathrm{i}}$, defined in Fig. 4.3, are shown by solid and dash-dotted lines, respectively. In all cases considered, the nozzle-to-plate spacing H is smaller than the potential core length of a free jet, resulting in potential-core impingement. The jet exiting the nozzle experiences a sudden deceleration at approximately $0.5B$ above the target surface, as a stagnation zone forms for all cases. Oblique impingement cases exhibit bias of the stagnation point towards the nozzle due to the Coandă effect [150]. That is, the jet centreline in the free jet region skews from the nozzle centreline and the stagnation point shifts towards the nozzle. With decreasing α, the stagnation point eccentricity increases, agreeing with previous results [29]. Stagnation point eccentricity can be affected by aspect ratio of slot jet exit for values under 4 [54]; the results of the current study are expected to hold well for larger aspect ratios. In the stagnation zone, the flow bifurcates into two fractions, one reoriented towards the positive x direction and the other towards the negative x direction. At smaller jet orientation angles, a higher percentage of the incoming flow is reoriented towards the positive x direction. Downstream of the stagnation region, the reoriented flow first accelerates, and then decelerates as the jet spreads in the wall-normal direction, eventually forming a wall jet. Noticeably, for $\mathrm{Re} = 3000$ at orientation angles of $\alpha = 90°$ and $60°$, the wall jets are deflected away from

the wall at around $x/B = 3$. This deflection diminishes at lower α and is not observed at all at the higher Reynolds number.

The stagnation point locations for the cases presented in Fig. 4.4 are at $x_0/B = 0$,

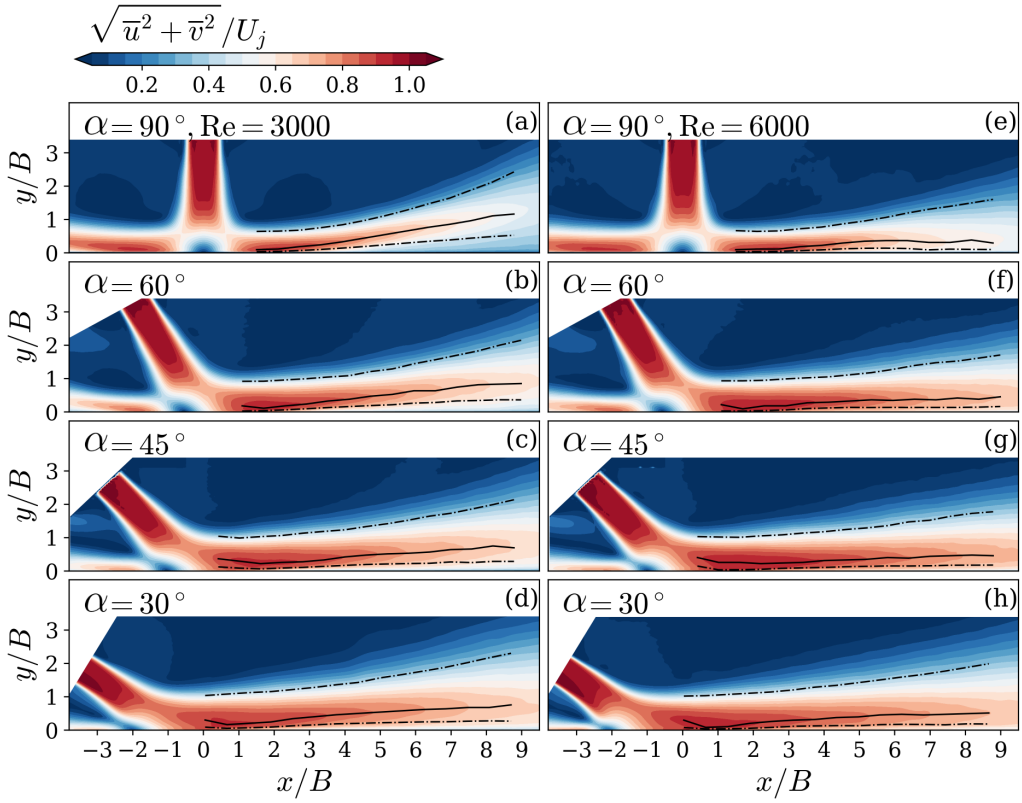

Figure 4.4: Contours of mean velocity magnitude at four oblique angles for Re = 3000 (left column) and Re = 6000 (right column) for $\alpha = 90°$, 60°, 45° and 30°. Locations of δ and $y_{1/2,\mathrm{i}}$ are marked by solid and dash-dotted lines, respectively.

-0.54, -1.01 and -2.12 for $\alpha = 90°$, 60°, 45°, and 30°, respectively, for both Reynolds numbers. Based on potential flow theory, Schauer and Eustis [164] proposed Eq. 4.1 for predicting the eccetricity of transitional oblique jet impingement for $\alpha \geq 30°$,

$$x_0/H = -0.154\cot\alpha. \tag{4.1}$$

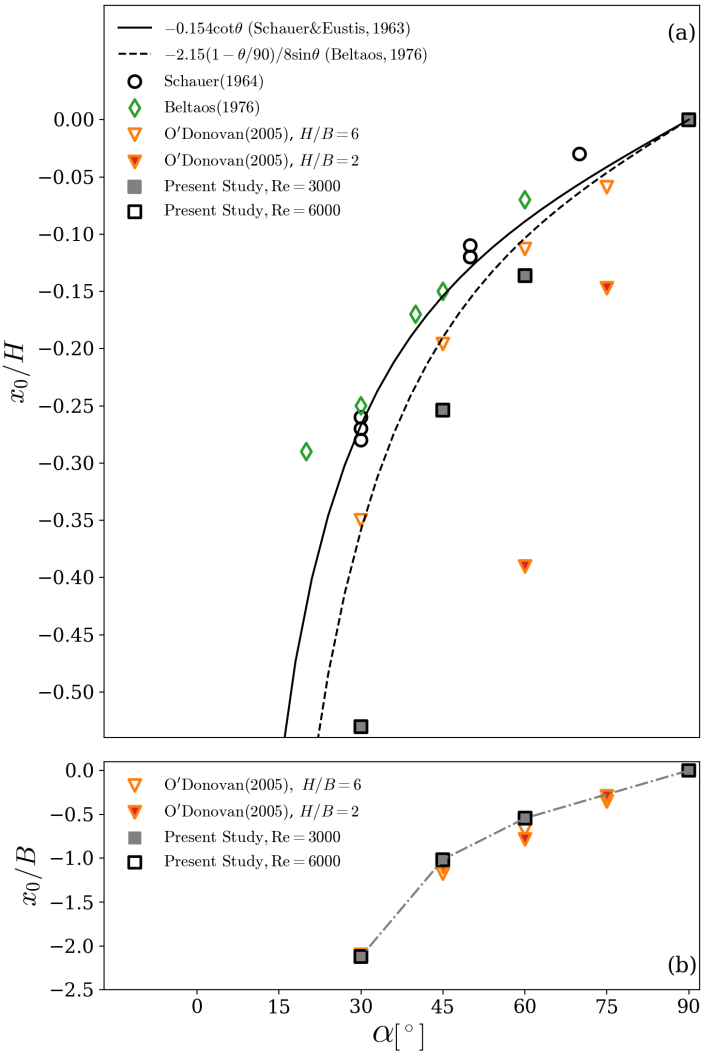

Figure 4.5: Eccentricity of stagnation point from geometric center versus α normalized by (a) nozzle-to-plate spacing ratio H, and (b) nozzle width B. The uncertainty of the measurement is smaller than the size of the symbols.

Beltaos [12] generalized the model by taking into account the skewness of velocity profile in the free jet region due to the presence of the target wall, predicting

$$\frac{x_0}{H} = \frac{1 - \alpha/90}{8\sin\alpha}. \tag{4.2}$$

Fig 4.5(a) shows x_0 measured in the present study compared with Eqs. 4.1 and 4.2, as well as the data from other studies summarized in Table 4.1. The figure shows that x_0/H deviates from the proposed models as H/B decreases. This discrepancy is due to the change from the transitional impingement regime to the potential-core impingement regime, since both models were derived based on the assumption of a self-similar velocity profile in a fully-developed jet prior to impingement. The strength of entrainment in the reorientation region of potential-core impingement is higher than transitional impingement, and consequently, the pressure difference impressed on both sides of the stagnation point in the near-wall region is more significant, leading to larger stagnation point eccentricity. Fig 4.5(b) shows the eccentricity normalized by nozzle width B, which exhibits better collapse of the present data and that of O'Donovan [132]. This indicates that within the regime of potential-core impingement, when normalized by nozzle exit width (diameter), a universal scaling can be attained for the x_0/B with α despite of the differences in H/B and jet nozzle geometry.

The flow development of the wall jet that reorients towards the positive x direction is quantified in terms of the decay of the maximum wall-tangential velocity $u_{\max}$ and the growth of jet half-width $y_{1/2,\mathrm{i}}$, with respect to the actual stagnation point x_0. Barenblatt *et al.* [10] proposed incomplete self-similarity for $u_{\max}$ and $y_{1/2,\mathrm{i}}$ in the following form

$$\frac{u_{\max}}{U_j} \propto \left(\frac{x - x_0}{B}\right)^{\zeta} \tag{4.3}$$

and

$$\frac{y_{1/2,\mathrm{i}}}{B} \propto \left(\frac{x - x_0}{B}\right)^{\sigma}_{\mathrm{i}}, \text{ where } \mathrm{i} = \mathrm{T}, \mathrm{W} \tag{4.4}$$

For traditional 2D turbulent wall jets, van der Hegge Zijnen [192] suggested a decay rate of $\zeta = -0.5$, which was validated by experimental measurements in the far-field of

Table 4.1: Eccentricity of stagnation point from geometric center: x_0 values reported in literature.

	α [°]	H/B	Re	x_0/H	x_0/B
Schauer (1964) [163]	90	10 - 40	30 800 - 53 000	0	
	70	30	40 500 - 52 500	0.03	
	50	40	40 500 - 52 500	0.12	
	50	20	20 300	0.12	
	50	20	41 300	0.11	
	30	30	52 300	0.26	
	30	30	40 500	0.27	
	30	30	20 300	0.28	
Beltaos (1976) [12]	60	45.5, 68.2	8 550, 12 060	0.07	
	45	45.5, 68.2	8 550, 12 060	0.15	
	40	45.5, 68.2	8 550, 12 060	0.17	
	30	45.5, 68.2	8 550, 12 060	0.25	
	20	45.5, 68.2	8 550, 12 060	0.29	
O'Donovan (2005) [132]	75	6	10 000	0.059	0.354
	60	6	10 000	0.113	0.678
	45	6	10 000	0.196	1.176
	30	6	10 000	0.35	2.1
	75	2	10 000	0.147	0.294
	60	2	10 000	0.39	0.78
	45	2	10 000	0.549	1.098

Table 4.2: Decay rate of u_{max} for wall jets: ζ values reported in literature.

	ζ	General comments
Glauert (1956)[63]	-0.583	Plane, Wall jet
Sigalla (1958)[177]	-0.5	Plane, Wall jet
Seban and Back (1961)[175]	-0.435	Plane, Wall jet
Schwarz and Cosart (1961)[173]	-0.555	Plane, Wall jet
Bradshaw and Gee(1962)[18]	-0.53	Plane, Wall jet
Myers *et al.* (1963)[129]	-0.49	Plane, Wall jet
Cartwright and Russell (1967)[24]	-0.39	Plane, Normal impingement

Table 4.3: Growth rate of $y_{1/2}$ for wall jets: σ_{T} values reported in literature.

	σ_{T}	H/B	Re	x/B range	General comments
Bakke (1957) [9]	0.94	0.5	3 500	5 - 10	Axisymm., Normal
Tanaka & Tanaka (1977) [183]	0.97	NA	7 500 - 55 000	2 - 100	Axisymm., Wall
Knowles & Myszko (1998) [92]	1	2, 4, 8, 10	90 000	1 - 10	Axisymm., Normal
Barenblatt *et al.* (2005) [10]	0.93	NA	9 600	40 - 150	Axisymm., Wall
Tang *et al.* (2015) [184]	0.78	NA	7 500	30 - 80	Plane, Smooth wall
Tang *et al.* (2015) [184]	0.82	NA	7 500	30 - 80	Plane, Rough wall
Guo *et al.* (2017) [67]	1.28	2	1 000	2 - 4	Confined, Normal
Guo *et al.* (2017) [67]	1.34	4	1 000	3 - 5.5	Confined, Normal
Guo *et al.* (2017) [67]	0.89	8	1 000	4.1 - 6.7	Confined, Normal

wall jets [63, 177, 175, 173, 18, 129]. Launder and Rodi [98] suggested a linear wall-normal growth rate $\sigma_{\mathrm{T}} = 1$, with $\mathrm{d}y_{1/2,\mathrm{T}}/\mathrm{d}x = 0.073$. These values are also applicable in the far-field ($x/B \geqslant 20$) of impinging jets of high Reynolds number, where the flow fully develops into turbulent wall jet. In the near-field ($(x - x_0)/B < 20$), where flow goes through laminar-to-turbulent transition, however, Cartwright and Russell [24] found a much lower decay rate of -0.39 in the near-field wall jet formed by a 2D normal impinging jet (see Table 4.2). Furthermore, the near-field wall jet growth rate follows the power law $y \propto x^{\gamma}$, with γ values scattering over a range of $0.78 - 1.34$ [9, 183, 92, 10, 184, 59] (see Table 4.3), indicating that the value of σ_{T} is not a single valued function of Re, H/B, and jet nozzle geometry.

In the present study, the decay rate ζ and the growth rate σ_{i} are calculated from power-law regressions of Eqs. 4.3 and 4.4, respectively, as shown in Figs. 4.6 and 4.7. Specifically, as mentioned in Sect. 3.1, the geometric boundary layer thickness δ is in effect the maximum wall-tangential velocity location, and the wall layer jet half-width $y_{1/2,\mathrm{W}}$ is approximated by $\delta/2$. The top layer jet half-width $y_{1/2,\mathrm{T}}$ is calculated from the PIV measurements by linear interpolation between $u \geq u_{\max}/2$ location and the neighboring

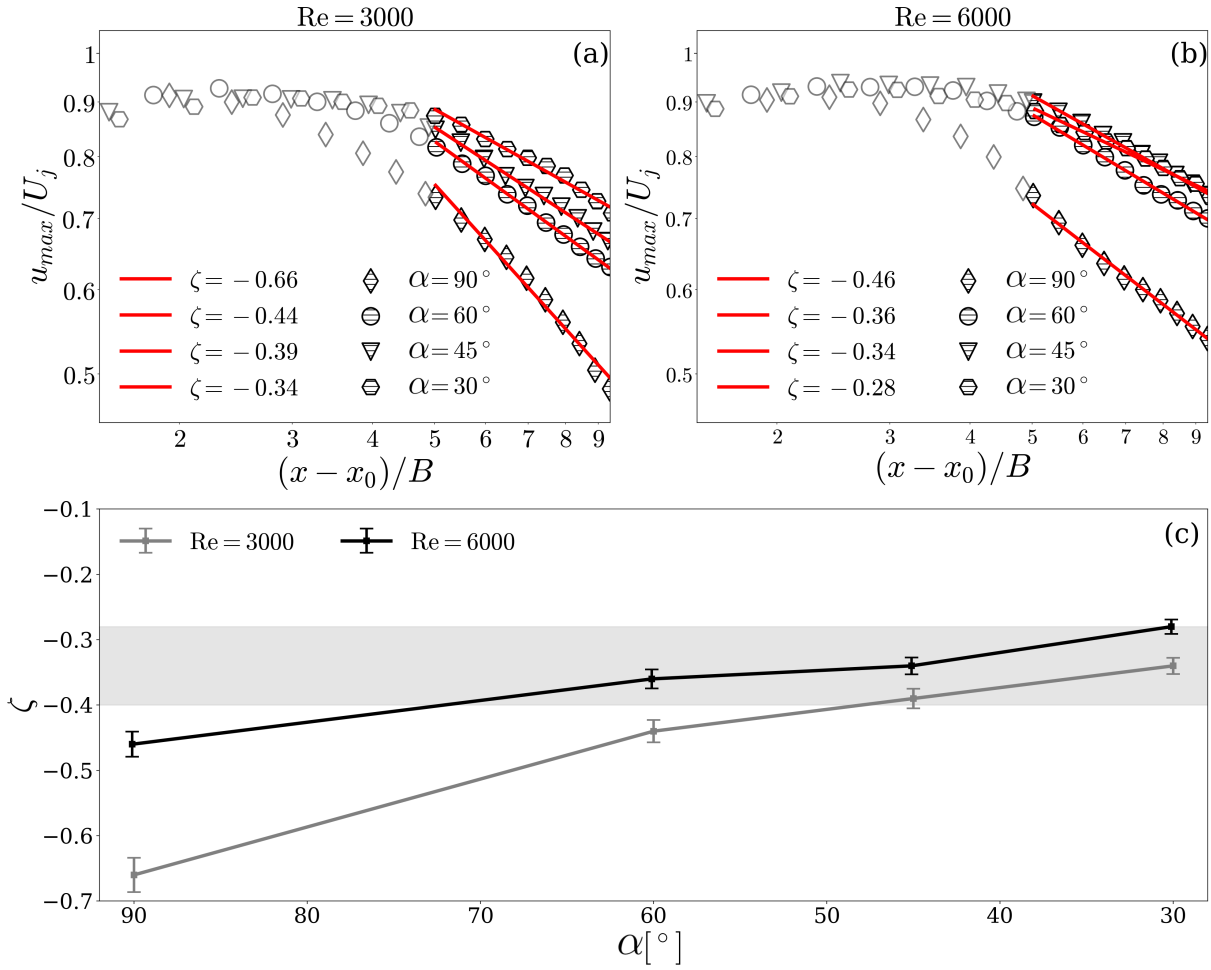

Figure 4.6: Decay of $u_{\max}$ in wall jet middle layer and its power-law regression for (a) $\mathrm{Re} = 3000$ and (b) $\mathrm{Re} = 6000$. (c) The trend of decay rate ζ with jet orientation angles for $\mathrm{Re} = 3000$ and 6000. The gray bar indicates the range of $\zeta = -0.34 \pm 0.04$.

y location where $u \leq u_{\max}/2$. Figs 4.6 (a) and (b) show the curve fit for ζ values on a logarithmic scale for $\mathrm{Re} = 3000$ and 6000, respectively, with hatch-filled markers indicating data used in the curve fit, and red lines indicating the fitted curves. In a similar fashion, curve fits for σ_{T} and σ_{W} at $\mathrm{Re} = 3000$ are shown in Figs. 4.7 (a) and (b), respectively. The choice of data used for the estimation of these parameters is based on the onset of

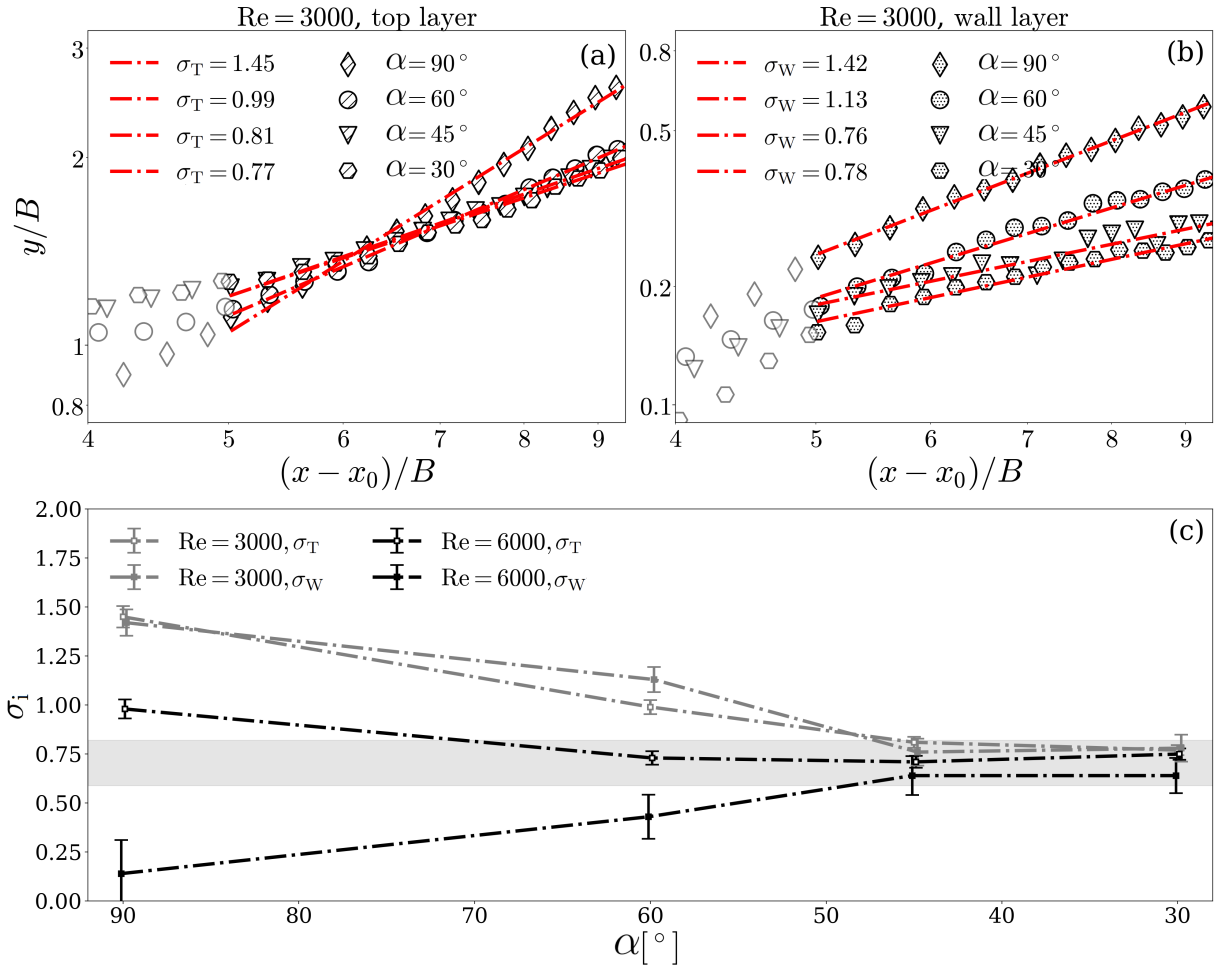

Figure 4.7: Growth of $y_{1/2}$ top layer and wall layer and its power-law regression for (a) Re = 3000 and (b) Re = 6000. (c) The trends of growth rate σ_W and σ_T with jet orientation angles for Re = 3000 and 6000. The gray bar indicates the range of $\sigma_i = 0.70 \pm 0.11$.

self-similarity in the wall jet velocity profiles shown in Figs. 4.8 (a) and (c), for Re = 3000 and 6000, respectively. For Re = 3000 (Fig. 4.8 (a)), at a given α, the velocity profiles collapse onto each other starting from $(x - x_0)/B = 5$, while for Re = 6000 (Fig. 4.8 (c)), the middle and wall layer profiles collapse from $(x - x_0)/B = 5$, and the top layer profiles collapse from $(x - x_0)/B = 7$.

The effects of Re and α on ζ and σ_{i} are summarized by Fig. 4.6 (c) and Fig. 4.7

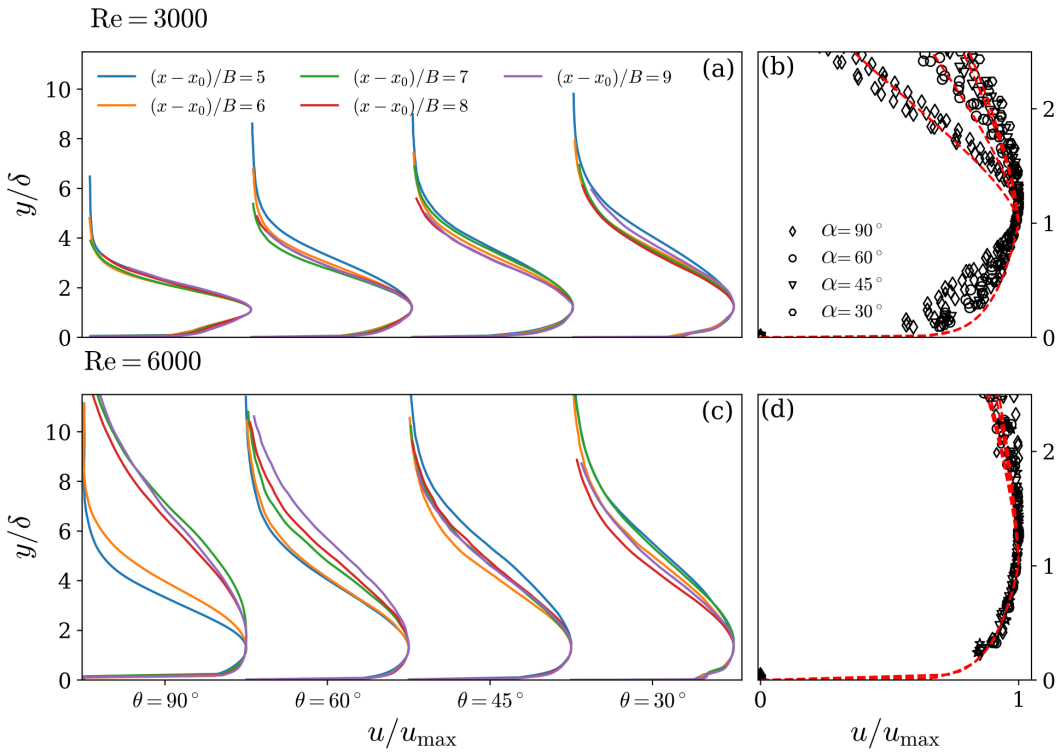

Figure 4.8: Measured velocity profiles in range of $(x-x_0)/B = 5-9$ for (a) Re = 3000 and (c) Re = 6000; Collapsing of velocity profiles across four oblique angles and five sampling locations in the near wall region for (b) Re = 3000 and (d) Re = 6000.

(c), respectively. In general, for $\alpha \leq 45°$, there is minimal effect of Reynolds number and α on both ζ and σ_{i}, with the values falling in the range of $\zeta = -0.34 \pm 0.04$ and $\sigma_{\mathrm{i}} = 0.70 \pm 0.11$ (i = T, W). At larger jet orientation angles ($\alpha \geq 60°$), however, both ζ and σ_{i} are influenced significantly by jet Reynolds number. Specifically, as shown in Fig. 4.6(c), $u_{\max}$ decays faster when Re decreases, or when α increases. Different trends are followed by σ_{T} and σ_{W} with Re as shown Fig. 4.7(c). For Re = 3000 at $\alpha = 30°$,

with $\sigma_T = 1.45$ and $\sigma_W = 1.42$, both values are much higher than 0.70. These faster growth rates in both top and wall layers are attributed to lifting of the wall jet observed in Fig. 4.4(a), (b). For Re = 6000, while the top layer features a high growth rate of $\sigma_T = 0.98$, $\sigma_W = 0.14$ is much lower than 0.70, indicating rapid spreading of the top layer while the wall layer remains attached to the wall, as also observed the in the mean velocity fields (see Figs. 4.4(e), (f)).

Self-similarity in the wall jet velocity profile is eventually expected as the flow develops along the surface. Selected non-dimensional profiles of the u-component of velocity at $(x - x_0)/B = 5,\ 6,\ 7,\ 8$, and 9 for Re = 3000 and 6000 at the four orientation angles are presented in Fig. 4.8. The velocity profiles defined by Schlichting's formula for self-similar, semi-bounded turbulent jets [208], given by Eq. 4.5, are plotted with dashed lines for each α (Figs. 4.8 (b), (d)).

$$\begin{aligned} \frac{u}{u_{max}} &= (1 - \varepsilon^{3/2})^2 \quad \text{for} \quad y \geqslant \delta, \\ \frac{u}{u_{max}} &= (y/\delta)^{1/n} \quad \text{for} \quad y \leqslant \delta. \end{aligned} \tag{4.5}$$

In Eq. 4.5, $\varepsilon = (y - \delta)/(y_b - \delta)$, and $n \approx 10$ are based on experimental data of Sakipov [156]. For Re = 3000, the near-wall velocity profiles for $\alpha = 90°$ differ significantly from the profiles at smaller α. For $\alpha < 90°$, the velocity profiles tend to collapse and show better agreement with Schlichting's formula. For Re = 6000, all near-wall velocity profiles collapse onto one curve and agree well with Eq. 4.5. These results suggest that, for Re = 3000, the wall jet region undergoes laminar-to-turbulent transition in the range $5 < (x - x_0)/B < 9$, while for Re = 6000, transition to turbulence occurs upstream of $(x - x_0)/B = 5$. Similarities in droplet response under the forcing of impinging jets at orientation angles of $\alpha \leq 60°$ may also be expected given the similarities in the mean flow development in the wall jet regions formed at the two bounding jet Reynolds numbers (see Fig. 4.8) for droplet depinning.

To gain further insight into the flow characteristics, turbulent kinetic energy (TKE)

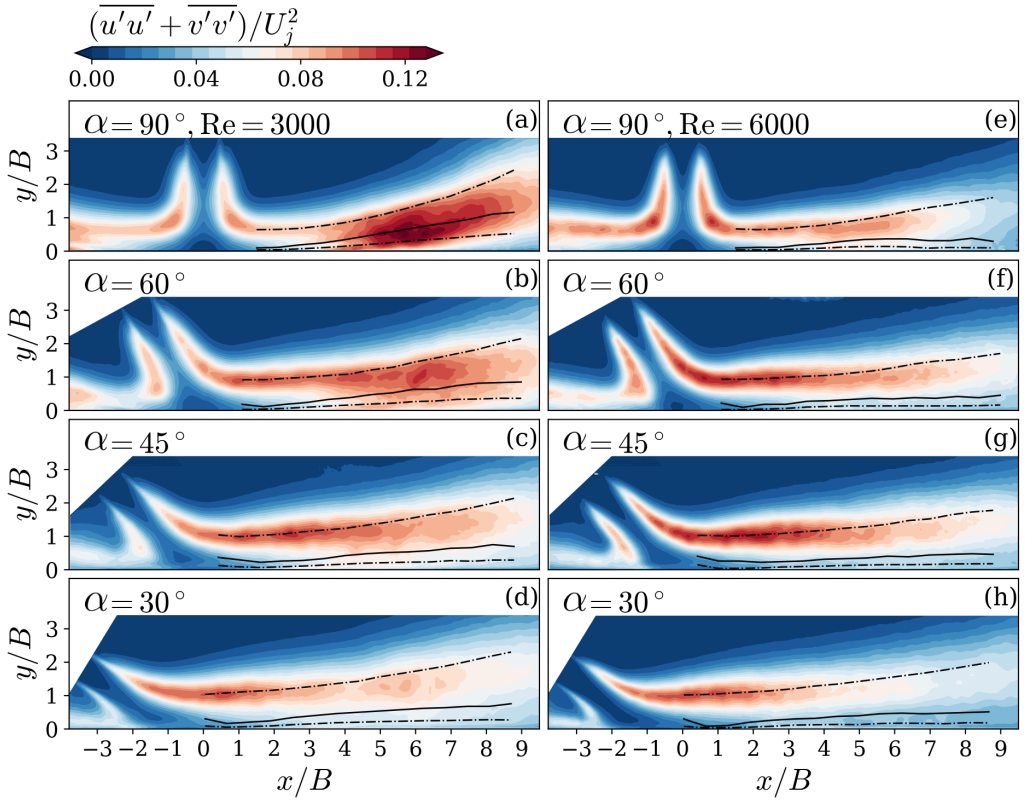

Figure 4.9: Contours of turbulent kinetic energy at four oblique angles for Re = 3000 (left column) and Re = 6000 (right column). Locations of δ and $y_{1/2,\mathrm{i}}$ are marked by solid and dash-dotted lines, respectively.

and turbulence production $\mathcal{P}$ are presented in Figs. 4.9 and 4.10, respectively. These parameters are defined by Eqs. 4.6 and. 4.7 based on two-component velocity measurements.

$$\mathrm{TKE} = \overline{u'u'} + \overline{v'v'}, \tag{4.6}$$

$$\mathcal{P} = \overline{u'u'}\frac{\partial \overline{u}}{\partial x} + \overline{u'v'}\left(\frac{\partial \overline{u}}{\partial y} + \frac{\partial \overline{v}}{\partial x}\right) + \overline{v'v'}\frac{\partial \overline{v}}{\partial y}, \tag{4.7}$$

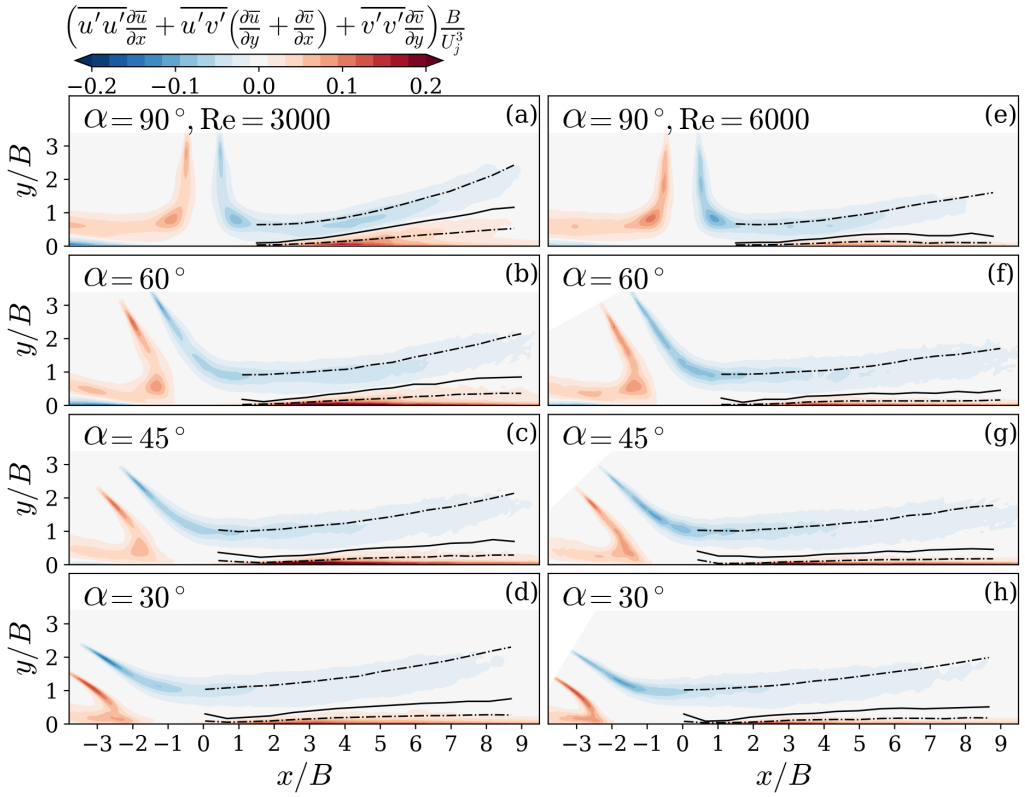

Figure 4.10: Contours of turbulence production at four oblique angles for Re = 3000 (left column) and Re = 6000 (right column). Locations of δ and $y_{1/2,\mathrm{i}}$ are marked by solid and dash-dotted lines, respectively.

where the prime symbol indicates a fluctuating velocity component, and the overbar indicates a time-averaged quantity. For reference, locations of δ and $y_{1/2,\mathrm{i}}$ are marked by solid and dash-dotted lines in both field plots. In general, high TKE is observed in the wall jet top layer, where strong turbulence production takes place in the top layer around $y_{1/2,\mathrm{T}}$, due to the K-H vortices. The primary region of turbulence destruction is confined to the wall layer, around $y_{1/2,\mathrm{W}}$, where the presence of the wall limits the length scale of vortical structures. In the middle layer, turbulence production is nearly zero as expected since

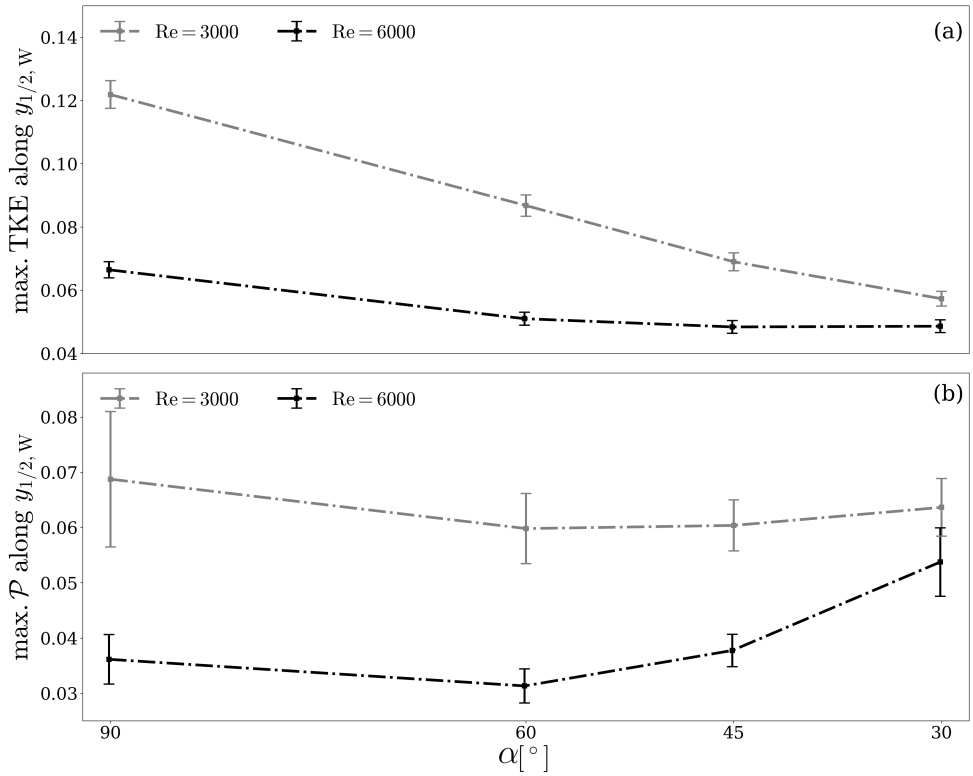

Figure 4.11: Trend of maximum (a) turbulent kinetic energy and (b) turbulence production magnitude of the wall layer as jet orientation angle decreases from $\alpha = 90°$ to 30°.

the flow in the reoriented potential-core is laminar for potential-core impingement. For all cases except Re = 3000, $\alpha = 90°$ and 60° (Fig. 4.9 (c)-(h)), maximum TKE occurs along $y_{1/2,\mathrm{T}}$. TKE values quickly drop close to the middle layer. For the two exceptional cases (Fig. 4.9 (a), (b)), maximum TKE occurs in the middle layer around δ, where significant levels of TKE are also observed in the wall layer. These differences in the distribution of planar TKE for Re = 3000, $\alpha = 90°$ and 60° will later be shown to stem from differences in vortex dynamics observed for these flow conditions (Sect. 4.2.3).

Figs 4.11 (a), (b) show respectively the maximum TKE and turbulence production values sampled along $y_{1/2,\mathrm{W}}$ for $(x - x_0)/B > 5$ at each jet orientation angle. In gen-

eral, the wall layers for the Re = 3000 cases feature higher maximum TKE than those of Re = 6000. At the same time, turbulence destruction in the wall layers is also stronger for the Re = 3000 cases. For a fixed Reynolds number, the maximum TKE in the wall layer decreases with decreasing α. Quantitatively, for Re = 3000, as α decreases from 90° to 30°, the maximum value of TKE in the wall layer decreases from 0.122 to 0.057, while the maximum turbulence production remains constant around $\mathcal{P} = 0.063$ within the range of α investigated. For Re = 6000, as α decreases from 90° to 30°, the maximum values of TKE in the wall layer decreases from 0.073 to 0.049. At the same time, maximum turbulence production remains constant around $\mathcal{P} = 0.034$ within $60° \leq \alpha \leq 90°$, and increases from 0.034 to 0.054 when α decreases from 60° to 30°. Considering the TKE budget, this indicates that around the wall normal location of $y_{1/2,\mathrm{W}}$, at larger α, turbulence destruction and viscous dissipation play equal roles in balancing the TKE influx due to advection and turbulent transport, while at smaller α, turbulence destruction dominates.

4.2.3 Vortex dynamics in steady impinging jet flow

As observed in the mean flow fields for Re = 3000, deflection of the wall jet from the wall is observed around $(x - x_0)/B = 3$ (Fig. 4.4 (a)-(d)), especially at large orientation angles; for Re = 6000, $\alpha = 90°$, the wall jet spreads faster in the y-direction than all the other cases investigated (Fig. 4.4 (e)). Anomalous behaviour in in-plane TKE is also observed for Re = 3000 at $\alpha = 90°$, where significant TKE is present not only in the top layer where turbulence is produced, but also in the middle layer, and the upper part of the wall layer. To shed light on the observed variations in the time-averaged flow characteristics, the development of dominant coherent structures is considered in this section.

As a precursor of quantitative measurements, flow visualization was performed by

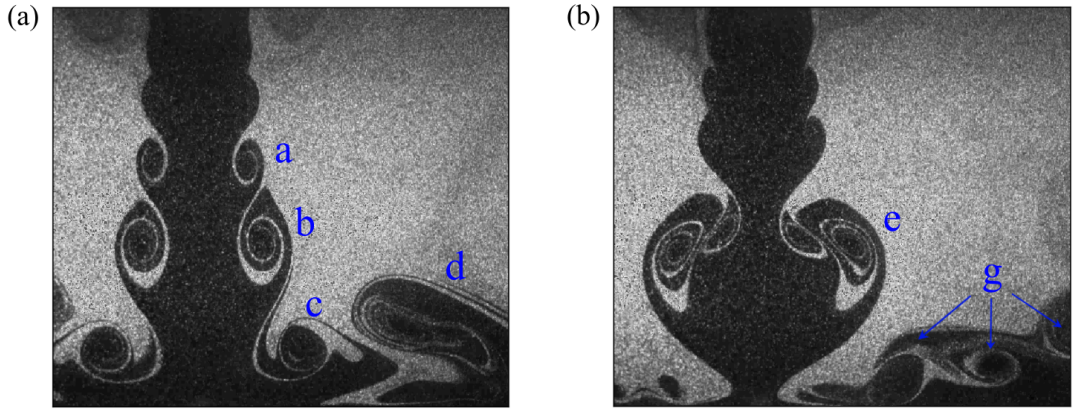

Figure 4.12: Two non-sequential instances of flow visualization for Re = 3000 and $\alpha = 90°$ showing (a) intact K-H vortex impingement and (b) vortex merging events prior to flow reorientation.

overseeding the quiescent fluid. Fig 4.12 shows two non-sequential snapshots of the normal impinging jet at Re = 3000. Fig 4.12 (a) shows the formation of a primary vortex ('a') at around $1.5B$ downstream of the nozzle exit due to the K-H instability [141, 36]. Further shear layer roll-up is observed downstream as an increase in vortex diameter ('b'). Upon impact ('c') and passage along the wall these vortices can induce the roll-up of wall vorticity that can act to entrain the quiescent flow [39, 71], as observed between ('c') and ('d'). Merging of primary vortices when they advect along the wall is also observed 'd'. Fig 4.12 (b) shows another scenario when merging events take place prior to flow reorientation ('e'). The spatial extent of merging events is due to the small variability in shedding frequency as reported in [139]. This cycle-to-cycle variability leads to difference in intra-vortex spacing. As a result, merging of primary K-H vortices sometimes occurs in the free jet region of the flow, leading to the advection of a merged pair through the reorientation and wall jet regions, while at other times primary vortices persist unmerged throughout the observed domain. Triple merging was also observed on occasion for Re = 3000. In Fig. 4.12 (b), 'g'

shows the precursor of such an event.

The development of dominant coherent structures is illustrated in Fig. 4.13 using a series of instantaneous vorticity contours of spanwise vorticity (ω) at five consecutive time instants $t^* = tu_j/B$ for both Reynolds numbers at $\alpha = 90°$. Vortical structures were identified using the λ_2 criterion [84]. In order to reduce the effects of the PIV measurement noise, thresholds for λ_2 and connectivity of identified structures were set to $\lambda_2 \leq -0.5$ and $conn > 50$, respectively. The vortex core locations were defined as the centroid of the identified structures, which are marked by the gray contour lines of $\lambda_2 = -0.5$ in Fig. 4.13. The circulation of each vortex is calculated by integrating the vorticity over the area of the identified structure, which is delineated by the contour of $\lambda_2 = -0.5$, as shown in Fig. 4.13. Sliding windows of $\Delta x/B = 0.3$ were used to reconstruct the principal trajectories of K-H vortices and to compute the mean circulation of vortices convecting along the principal trajectory. As examples, Fig. 4.14 shows histograms of vortex core wall-normal coordinates at three streamwise locations. Two principal trajectories were identified from the dual-peak distributions observed in the histograms. For the trajectory at the top, vortices with core locations falling in the bin of primary peak and four bins to the right were used for the calculation of statistics. Similarly, for the trajectory at the bottom, vortices with core locations falling in the secondary peak and four bins to the left were used. In this way, wall-normal statistics are calculated with windows of $\Delta y/B = 0.3$, the same width as the horizontal sliding windows. The range of bins used for statistics and the averaged vortex core location are marked by gray dashed lines and red dash-dot lines, respectively. The presence of two distinct trajectories, one for merged vortices and one for individual vortices, arises due to spatial extent over which K-H merging events occur in the flow configuration as shown by Fig. 4.12. The two trajectories correspond to the mean path of individual K-H vortices, and that of merged pairs. These are marked by dashed and

dotted lines in Fig. 4.13.

As can be observed from Fig. 4.13 (a)-(e), the merged vortices follow the upper trajectory, while the intact K-H vortices tend to penetrate deeper towards the wall, following the lower trajectory (Fig. 4.15 (a)-(b),P_1). This is corroborated by the mean circulation estimates along the two trajectories shown in Fig. 4.15 (c), wherein the upper trajectory associates with a higher mean circulation, as expected for merged vortices. Merging events of K-H vortices at Re = 3000 occur in both the reorientation region and the wall jet region. When a merging event occurs, the two merging vortices migrate their centre of rotation from the lower trajectory to the upper (Fig. 4.15 (a)-(b),$P_2 + P_3$). The vortex merging and migration result in the significant increase in mean circulation sampled along the lower trajectory (Fig. 4.15 (a)) for Re = 3000. Fig 4.15 (a) and (b) show the locations of the principal K-H vortex trajectories with respect to the locations of $y_{1/2,\mathrm{T}}$ and δ. The principal trajectories for both Reynolds numbers are located in the top layer as expected for shear layer vortices.

For Re = 3000, when a K-H vortex formed in the free jet region convects towards the target surface, its induced velocity at the wall increases local vorticity production. As a result, the vorticity in the boundary layer rolls up into a wall vortex of opposite rotation to the K-H vortex at its direct downstream location (Fig. 4.13 (b)-(c), S_2). The K-H vortex and its induced wall vortex pair up, and as they move downstream together, the wall vortex sources vorticity from the local boundary layer until it eventually sheds from the wall (Fig. 4.13 (d)-(e)). After ejection, the paired vortices mutually advect, with the higher circulation K-H vortex causing the pair to move away from the wall. An inflexion in the mean K-H trajectory occurs at around $(x - x_0)/B = 3$, marking the mean shedding location of wall vortices. At the same location, wall jet deflection is observed in the time-averaged velocity field of Re = 3000, $\alpha = 90°$ (Fig. 4.4 (a)), indicating that the shedding of wall

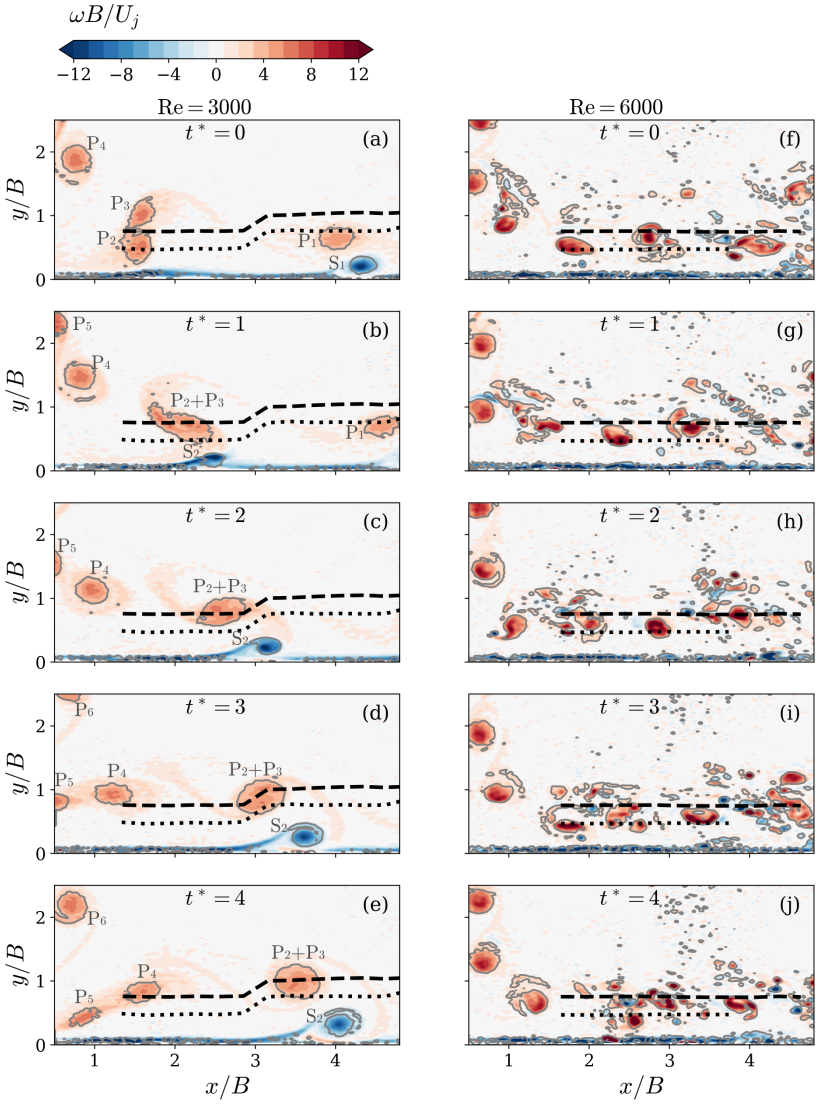

Figure 4.13: Instantaneous vorticity contours overlayed with contour lines of $\lambda_2 = -0.5$ and the two principal trajectories, at five consecutive snapshots at time instant $t^* = tu_j/B = 0,\ 1,\ 2,\ 3$ and 4 for Re = 3000 (left column), and Re = 6000 (right column) at $\alpha = 90°$.

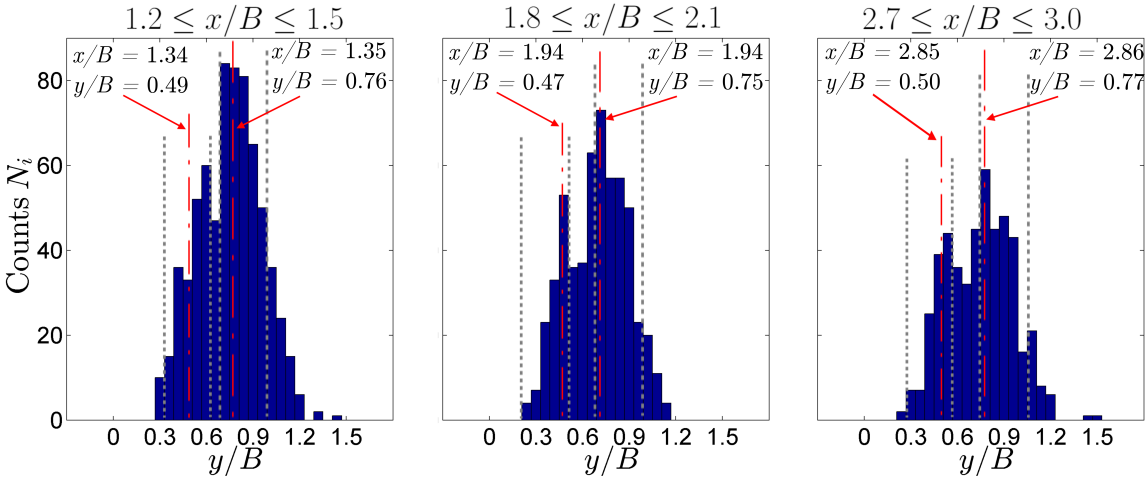

Figure 4.14: Histograms of vortex core locations within different x/B regions for Re = 3000, $\alpha = 90°$. Gray dashed lines mark the bins used to calculate the vortex statistics along the trajectories. Red dash-dot lines mark the averaged y/B of vortex cores falling in the range of calculation.

vortices leads to a higher growth rate in both $y_{1/2,\mathrm{T}}$ and $y_{1/2,\mathrm{W}}$ (Fig. 4.7 (c)). Both single and merged K-H vortices remain coherent until around $(x-x_0)/B = 4.5$. These persistent large eddies drain kinetic energy from the mean flow into their circulating motion, leading to a higher decay rate of $u_{\max}$ for Re = 3000 than Re = 6000 (Fig. 4.6 (c)). The intermittent shedding of large-scale wall vortices leads to strong wall-normal velocity fluctuations, which contribute to the high TKE values in the middle and wall layers (Fig. 4.9 (a)). Starting at around $(x-x_0)/B = 4.5$, interactions with the shed wall vortices become significant (Fig. 4.13 (a)-(b), P_1 and S_1), leading to annihilation of circulation. Also around this location, sudden breakdown events of merged vortices are observed. Vortex breakdown and cross-diffusion of vorticity both contribute to the decrease in mean circulation (Fig. 4.15 (c)). In addition, the cross-diffusion in the near wall region accounts for the wall layer turbulence destruction. At the same time, the breakdown of merged vortices cascades the kinetic energy to smaller eddies, contributing to the viscous diffusion. Both mechanisms

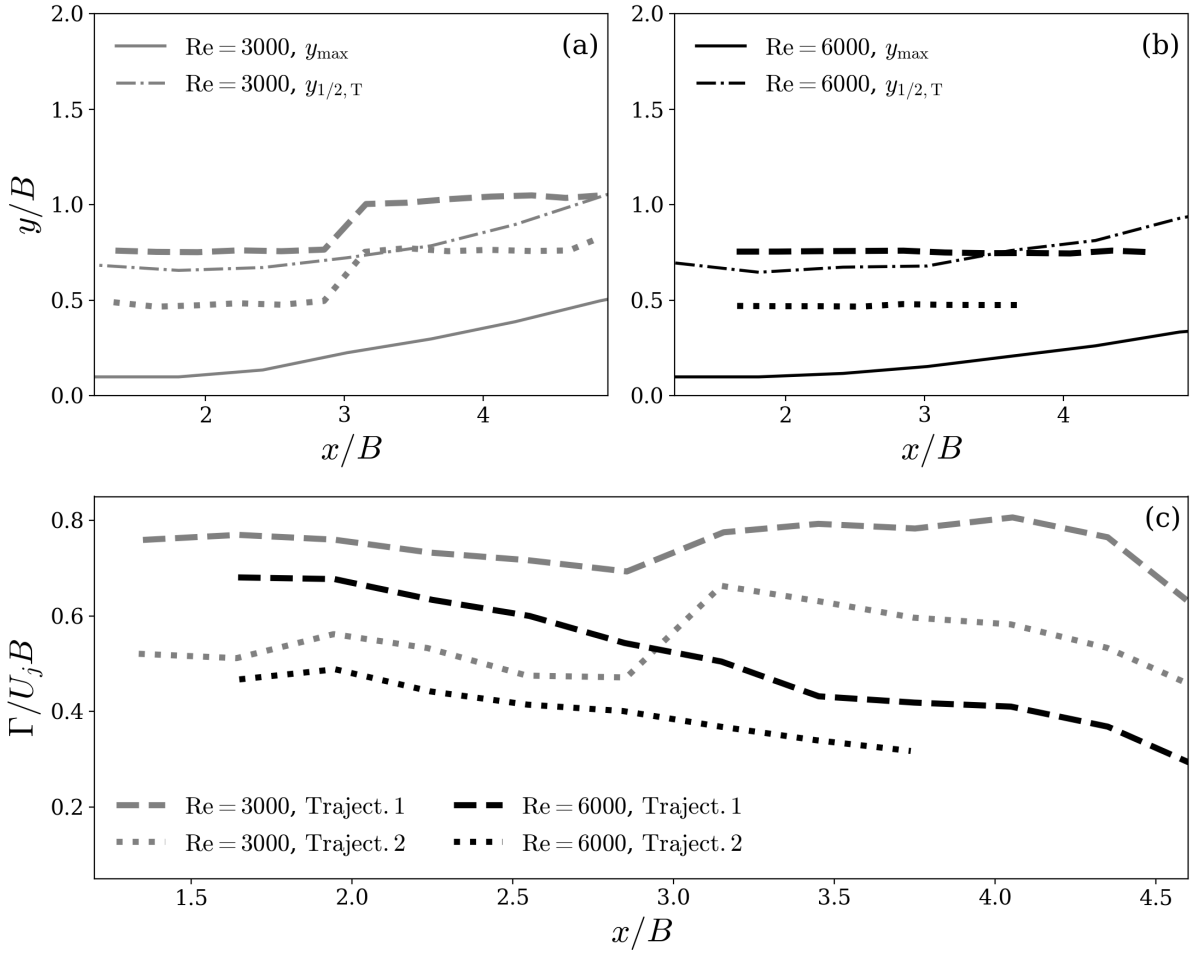

Figure 4.15: Location of the two principal trajectories with respect to jet half-width for (a) Re = 3000, and (b) 6000. (c) Evolution of vortex circulation along the principal trajectories of the K-H vortices. The uncertainty of the principal trajectory is bounded by $\Delta y/B = \pm 0.03$. The maximum uncertainty of mean circulation is 30%.

attribute to the low TKE values in the near-wall region of $(x - x_0)/B > 7$ (Fig. 4.9 (a)).

For Re = 6000, the breakdown of the K-H vortices starts in the flow reorientation region (Fig. 4.13(g), (h)). The earlier breakdown inhibits the penetration of primary K-H vortices towards the wall and reduces the induced wall-normal velocity in the wall layer.

As a result, strong shedding events of wall vortices are not detected and the wall layer remains attached to the surface within the FOV. This leads to the moderate growth rate in $y_{1/2,\mathrm{W}}$ (Fig. 4.7 (c)), and the steep near-wall velocity gradient (Fig. 4.8 (d)). Breakdown events occur along the entire vortex trajectory in the range $(x - x_0)/B \geq 1.5$, resulting in the gradual decrease in mean vortex circulation (Fig. 4.15 (c)). At the same time, vortex breakdown leads to earlier transition into turbulence, resulting in the quick growth in $y_{1/2,\mathrm{T}}$. The steep near-wall velocity gradient (Fig. 4.8 (d)) limits the length scale of eddies and thus suppresses the energy cascade, resulting in turbulence destruction and viscous dissipation in the near-wall region.

For oblique jet impingements at lower Reynolds number of Re = 3000, the absence of strong wall-normal velocity in the wall jet region can be attributed to the shallow penetration of primary K-H vortices towards the wall as a result of reduced wall-normal momentum in the free jet region due to the oblique jet angle. For a droplet residing in the near-wall region, the impact of a penetrating large-scale vortical structure may potentially alter the time history of events that occur on the droplet contact line. The change in the time history of the external loading may potentially alter the pathways by which the droplets achieve the depinning geometry [58] and subsequently lead to changes in droplet depinning criteria.

4.2.4 Accelerating impinging jet flow

To validate the consistency of ramp-up performance of the jet facility, the velocity time histories were characterized using hot-wire following the procedures as described in Sect. 3.3. The instantaneous velocities were sampled along the jet centreline at the jet exit, and at the streamwise locations as listed in Table 3.6 for the investigated jet configurations.

Given the fuller near-wall velocity profiles formed by impinging jets at $U_j = 10\,\mathrm{m/s}$ (see Fig. 4.16, column 4) as compared to those of a laminar boundary layer (see Fig. 4.2), time history does not show significant variation along the wall-normal direction above $y/h \gtrapprox 0.5$. Thus, only the velocity time histories sampled at the wall-normal location at around the mean droplet height (around $y \approx 2.6\,\mathrm{mm}$ (green lines) is presented here and compared against those at the jet exit (blue lines) for brevity.

The ramp-up time histories corresponding to the three investigated accelerations $\mathrm{d}U_j/\mathrm{d}t = 1.2$, 2.2, and $4.4\,\mathrm{m/s}$ are shown in Fig. 4.16 column 1, 2, and 3, respectively. Measurements were repeated for five trials at each streamwise location for each acceleration. The instantaneous velocities measured by hot-wire are indicated by the gray lines. Moving average of the velocity measurements of each trial was calculated using a second-order Savitzky-Golay filter [162] with a window width of five seconds. While velocity fluctuations at jet exit is negligibly small, at all the streamwise locations investigated, the amplitude of velocity fluctuations around the moving-averaged ramp-up curve are significantly higher than that in the laminar boudary layer. This is mainly attributed to the impingement of large-scale vortical structures formed in the free jet region (see Sect. 4.2.3). Similar ramp-up slopes are observed at jet exit and at wall locations, apart from those sampled at $x^*/h = 7$ under the jet orientation angle of $\alpha = 90°$ (Fig. 4.16(G)). The discrepancy in ramp-up slopes lies in the difference between the end velocity at jet exit and that at the streamwise location. The higher discrepancies observed for $\alpha = 90°$ jets are likely attributed to their higher decay rate of streamwise velocity after flow reorientation, as observed in the normally impinging jets with steady jet exit velocity (see Fig. 4.6).

The instantaneous and moving-averaged ramp-up time histories of the five trials of each combination of acceleration and streamwise location show high repeatability. Similar to droplet tests in laminar boundary layer, velocity measurements can be decoupled from the

measurements of droplet geometry in response to accelerating jet impingements.

4.3 Summary

This chapter presents the flow fields formed by flow over a flat plate and impinging jets. Steady flow over a flat plate was characterized using hot-wire. The steady boundary layer formed within $245 \leq x_i \leq 550$ mm agree well with the velocity profiles predicted by Blasius solution, indicating the boundary layer in this range is laminar.

Mean flow fields formed by impinging jets of steady jet exit velocity were characterized using non-time-resolved PIV at four jet orientation angles $\alpha = 90°$, $60°$, $45°$, and $30°$. In all cases, stagnation point eccentricity increases with decreasing α, and is insensitive to Re within the range investigated. The reoriented flow develops along the wall, and eventually forms a self-similar wall jet. The velocity profiles in the wall jet region formed by the impinging jets are fuller than those over the flat plat, indicating higher momentum in the near-wall region. At larger jet orientation angles, the wall jet development is influenced significantly by the jet Reynolds number. Specifically, for Re = 3000, $\alpha \geq 60°$, significant deflection of wall jet from the surface is observed. The wall jet deflection results in higher growth rates of the wall jet top and wall layers, as well as faster decay in the maximum wall-tangential velocity. For Re = 6000, on the other hand, within the range of orientation angles investigated, the wall jet remains attached to the wall. In contrast, at smaller angles, there is minimal Reynolds number effect on both wall jet growth and velocity decay.

As a complement to the time-averaged near-wall velocity profiles formed by impinging jets, 2D-2C time-resolved PIV measurements of high spatial resolution reveals the causal relation between vortex-wall interaction and time-averaged statistics for impinging jets at $\alpha = 90°$. At lower Reynolds number, the observed wall jet deflection is attributed to

the interactions between the K-H vortices formed in the jet shear layer and the target surface. The impinging K-H vortices remain coherent along the wall and induce strong shedding of wall-bounded vorticity. The shed vorticity pairs with the K-H vortices and ejects from the wall, resulting in the deflection of the wall jet from the surface and large wall-normal velocity component. The sudden breakdown of these vortical structures further downstream cascades turbulent kinetic energy to smaller scales, marking the last stages of the laminar-to-turbulent flow transition. At higher Reynolds number, on the other hand, K-H vortices experience breakdown further upstream in the reorientation region, resulting in earlier flow transition. The roll up of wall bounded vorticity is less significant, and consequentially, the wall layer remains attached to the surface. The energy cascade in the near-wall region is suppressed by the steep velocity gradient at the wall, resulting in turbulence destruction and thus reduced turbulence intensity in this region.

In wall-bounded shear flows formed under accelerating freestream or jet exit velocites, hot-wire measurements of time history of velocity ramp-up in the near-wall region show high repeatability at each wall location for each acceleration investigated. With both facilities employed in droplet tests demonstrating high consistency in velocity ramp-up time history, velocity measurements can be decoupled from droplet imaging in droplet depinning tests (as described in Sect. 3.3). By virtue of the decoupling, optical obstruction and light scattering introduced by the presence of hot-wire probe and its supporting structures can be avoided in droplet imaging.

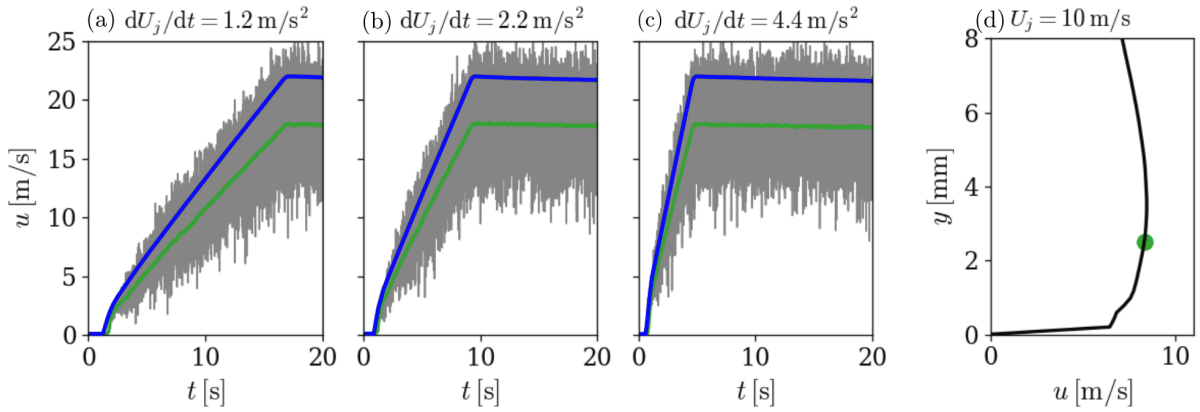

(A) Velocity sampled at $x^*/h = 6$ with jet orientation angle of $\alpha = 30°$.

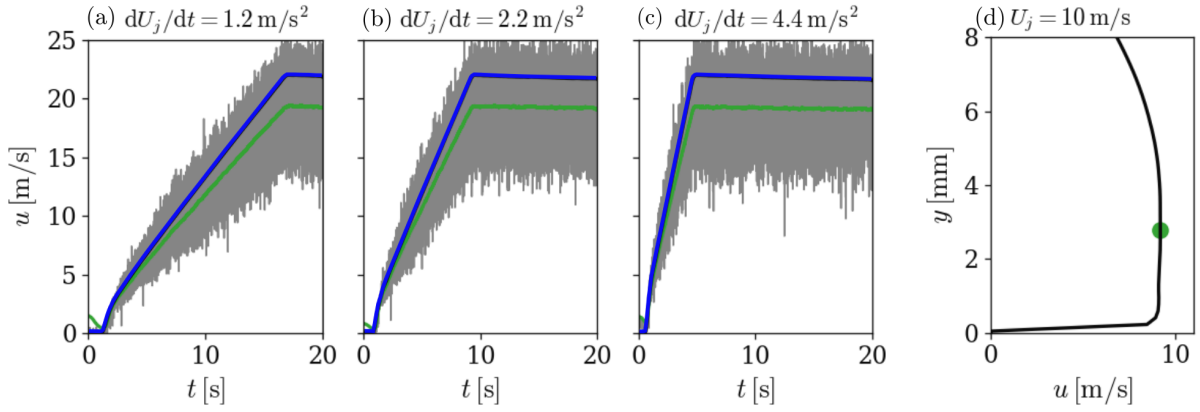

(B) Velocity sampled at $x^*/h = 2$ with jet orientation angle of $\alpha = 45°$.

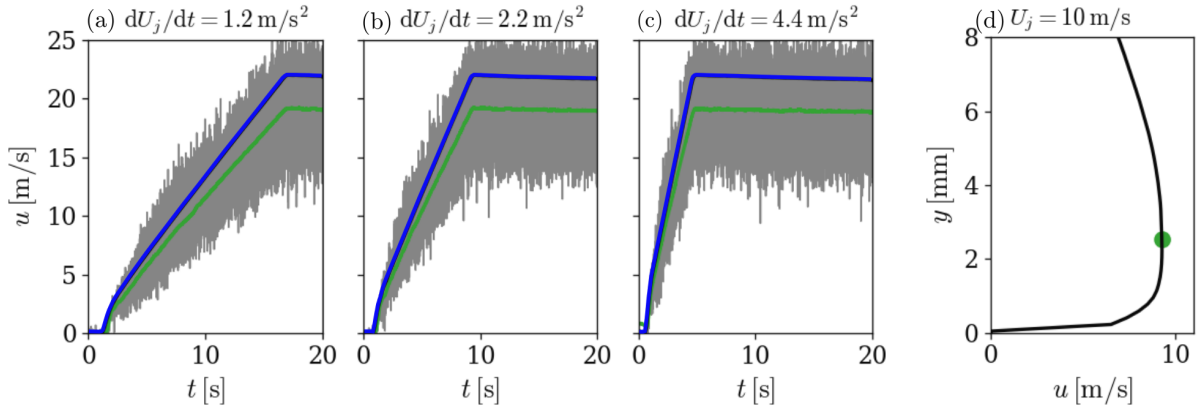

(C) Velocity sampled at $x^*/h = 4$ with jet orientation angle of $\alpha = 45°$.

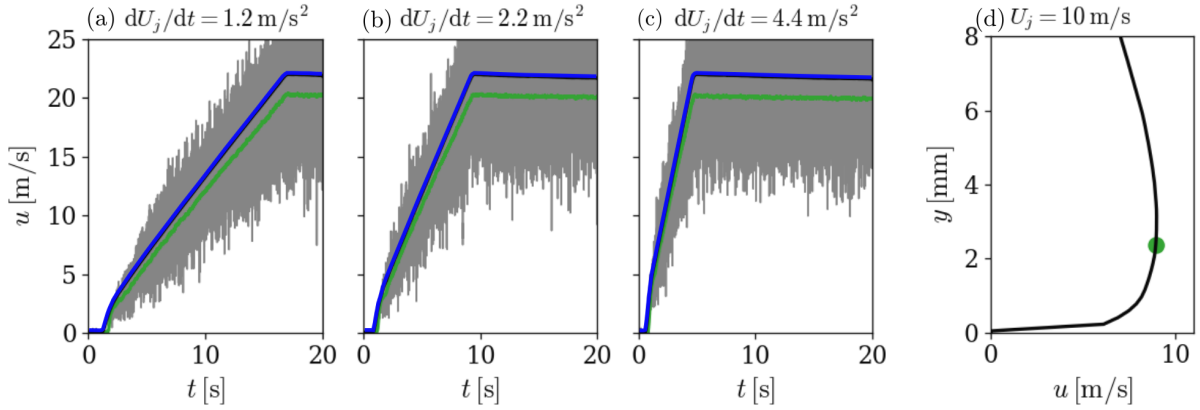

(D) Velocity sampled at $x^*/h = 5$ with jet orientation angle of $\alpha = 45°$.

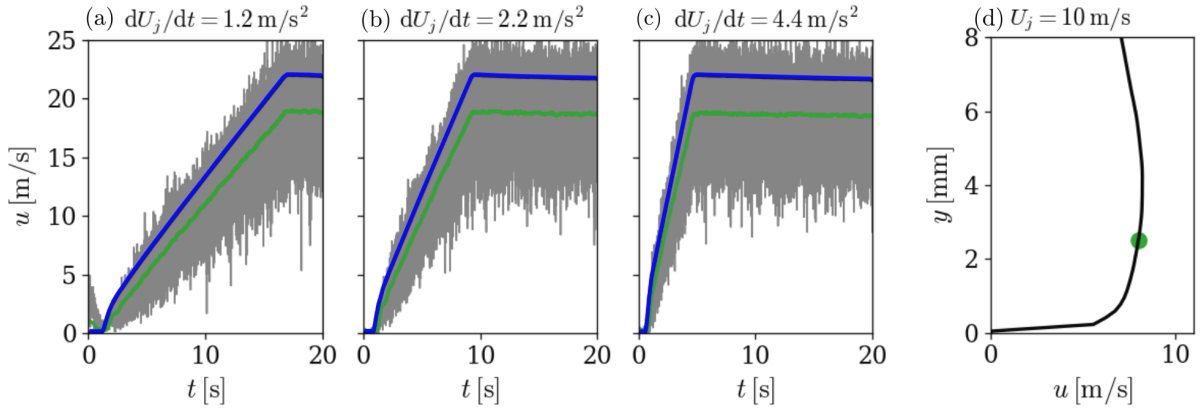

(E) Velocity sampled at $x^*/h = 7$ with jet orientation angle of $\alpha = 45°$.

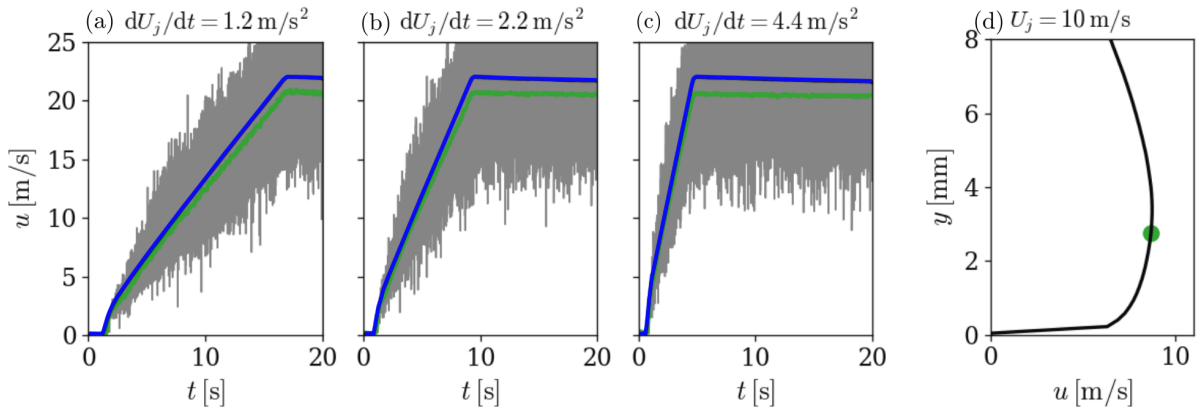

(F) Velocity sampled at $x^*/h = 5$ with jet orientation angle of $\alpha = 60°$.

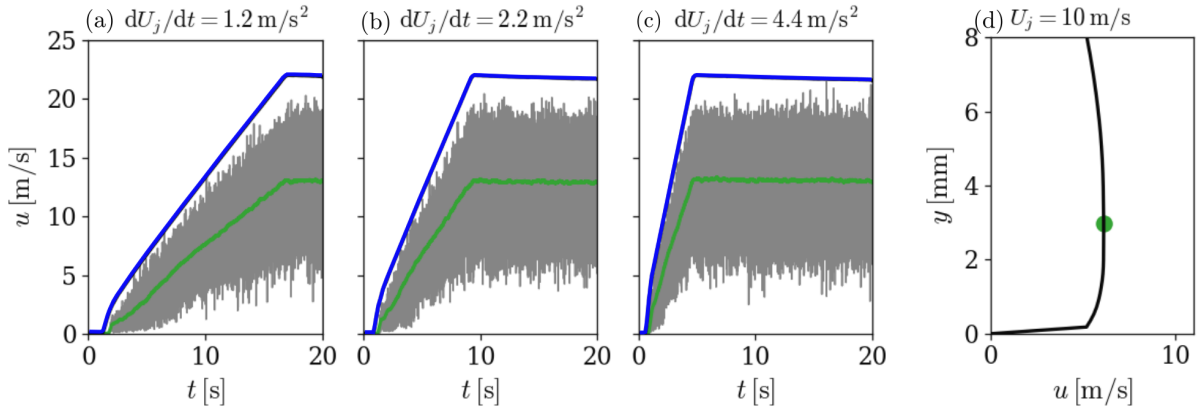

(G) Velocity sampled at $x^*/h = 7$ with jet orientation angle of $\alpha = 90°$.

Figure 4.16: Sliding average of velocity sampled at the jet exit (blue lines) and the near-wall location (green lines) around droplet height as the jet exit velocity ramps up at around 1.2 m/s^2 (column 1), 2.2 m/s^2 (column 2), and 4.4 m/s^2 (column 3), overlaid with the instantaneous velocities measured over five runs (gray lines). Steady velocity profiles measured at streamwise locations as listed in Table 3.6 at a jet exit velocity of $U_j = 10$ m/s, with green dots showing the wall-normal locations where the near-wall velocity ramp-up time histories are sampled (column 4).

Chapter 5

Impact of Droplet-Inspired Geometries on Laminar Wall-Bounded Shear Flows

This chapter discusses the impact of isolated, surface-mounted, droplet-inspired three-dimensional obstacles on laminar boundary layer. The three geometries considered here are those representative of a sessile droplet (sessile), a droplet on the verge of depinning (runback), and a spherical cap (chopped) which serves as a first order approximation of a sessile droplet (see Table 3.3). This chapter is divided into three sections. Sect. 5.1 overviews the flow development over the three investigated geometries. Sect. 5.2 analyses the dominant coherent structures quantitatively, and sheds light on the link between these structures and the mechanism of laminar-to-turbulent flow transition promoted by the

Parts of this chapter have been accepted for publication in International Journal of Heat and Fluid Flow [216].

presence of the droplet geometries. Sect. 5.3 summarizes the main findings of this chapter. Since aerodynamic loading is directly related to the flow development over the models, this chapter also serves as a precursor to the quantification of drag coefficients of typical droplet geometries discussed in Ch. 6.

5.1 Mean flow description

As an overview of the flow development over the chopped, sessile, and runback models, three-dimensional flow fields are reconstructed from the stereo-PIV velocity measurements and presented as contours in Fig. 5.1 for the mean streamwise (first column) and wall-normal (second column) velocity components. For all cases, the flow obstruction caused by the obstacle elicits a streamwise velocity deficit directly downstream of the models, which begins to recover further downstream; there remains, however, evidence of the obstruction at the end of the measurement domain for all models. The furthest downstream measurement plane shows a wider streamwise deficit in the wake for the sessile model than the other two, which is consistent with the greater model width near its apex.

The mean wall-normal velocity component (second column of Fig. 5.1) shows strong central upwash around the symmetry plane ($z = 0$) and lateral downwash further outbound ($z/h \approx \pm 1$) immediately downstream of all three models, indicative of streamwise base vortex formation as the flow wraps around the object. The central upwash in the immediate wake is strongest for the runback model, with the sessile and chopped models exhibiting similar and more modest central upwash, suggesting locally stronger streamwise vortices for the runback case. Up to around $x/h \approx 6$, the central upwash pushes the low momentum wake fluid away from the wall while the lateral downwash brings high momentum fluid towards the wall and thins the local boundary layer (see the first column

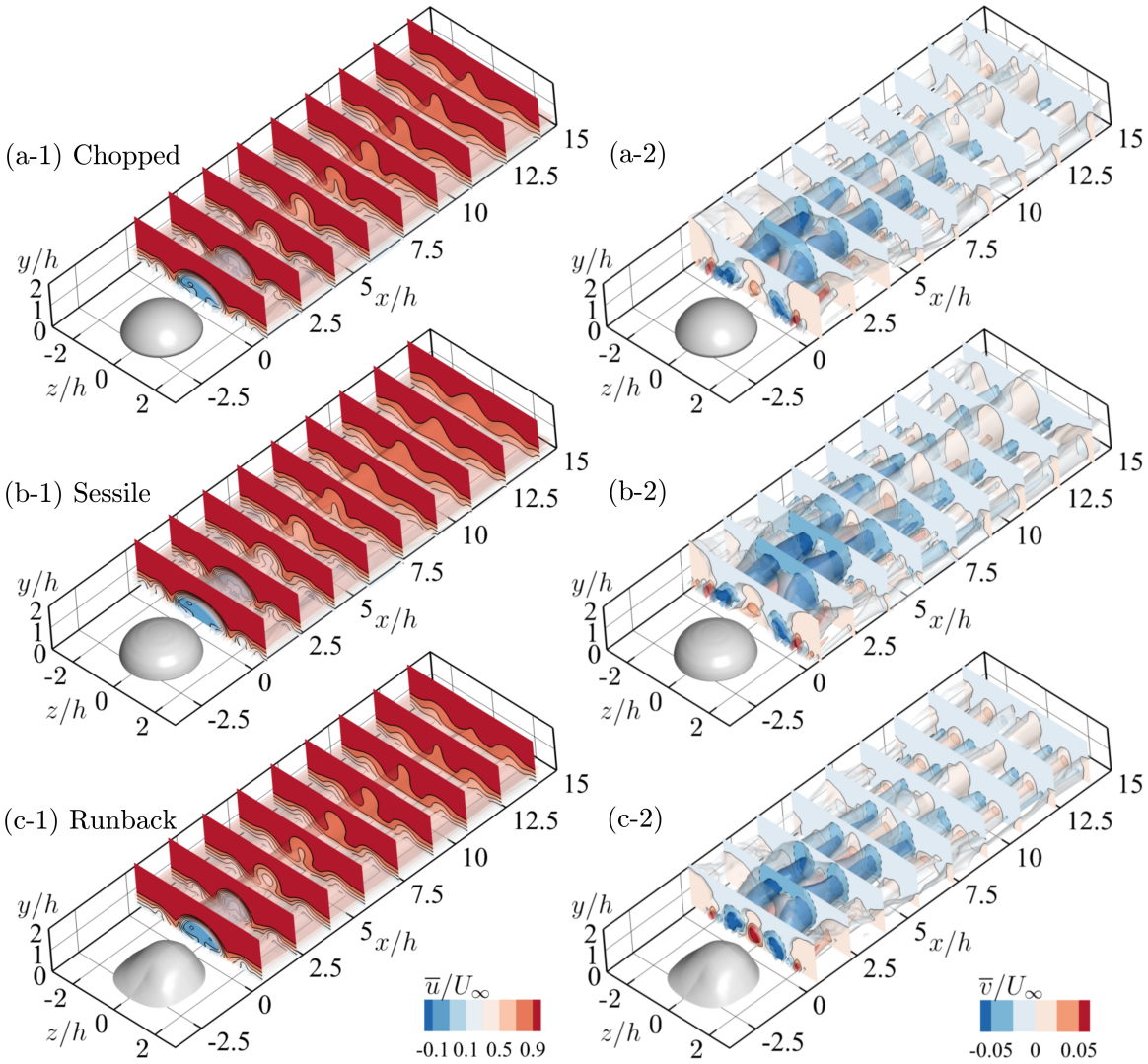

Figure 5.1: Time-averaged streamwise ($\overline{u}$, left column) and wall-normal ($\overline{v}$, right column) velocity in the wake of the chopped (row 1), sessile (row 2), and runback (row 3) models. Solid lines: positive velocity contours. Dashed lines: negative velocity contours.

of Fig. 5.1). Further outboard ($z/h \approx \pm 2$) are imprints of additional streamwise vortices consistent with a horseshoe vortex system that has been documented for wall-mounted obstacles [158, 159].

The near wake and horseshoe vortex system are further elucidated by the time-averaged velocity fields at the symmetry planes of the three models shown in Fig. 5.2. The horseshoe vortex system is evident upstream of each model due to roll-up of the incoming laminar boundary layer. Stagnation streamlines attach to the fore-body regions at heights of $y/h = 0.53$, 0.56, and 0.45 for the chopped, sessile, and runback models, respectively. The height of these stagnation points correlate with the bluntness of the body, which is captured in the upstream contact angle θ_u, see Table 3.3. Past the stagnation point the flow accelerates over the model then separates near the model maximum height. A recirculating region then forms and extends a distance of $x/h = 2.6$, 3.2, and 2.7 for the chopped, sessile, and runback models, respectively. Mean reattachment is identified as the streamwise location of the last reversed flow vector nearest to the wall. The length of the recirculating region measured from the model maximum height is $x_r/h = 4.1$, 4.7, and 3.9 for the chopped, sessile, and runback models, respectively (also reported in Table 5.1). The recirculating region length of the runback model is similar to that found downstream of a depinning water droplet submerged in a laminar boundary layer ($x_r/h \approx 4$) [40]. The sessile model of higher contact angle exhibits a longer recirculating region than the chopped model of lower contact angle, pointing to a potential correlation between the recirculating region length and model contact angle for axisymmetric geometries. A recirculation region then forms and extends a distance of $x/h = 2.6$, 3.2, and 2.7 for the chopped, sessile, and runback models, respectively (also reported in Table 5.1). Mean reattachment is identified as the streamwise location of last reversed flow vector nearest the wall.

As seen in snapshots of instantaneous spanwise vorticity ($\omega_z h/U_\infty$) in the $z = 0$ plane of the runback model in Fig. 5.3, the upstream horseshoe vortex system is relatively stationary in position and strength. These snapshots also highlight the amplification of perturbations in the separated shear layer that results in the roll-up of Kelvin-Helmholz

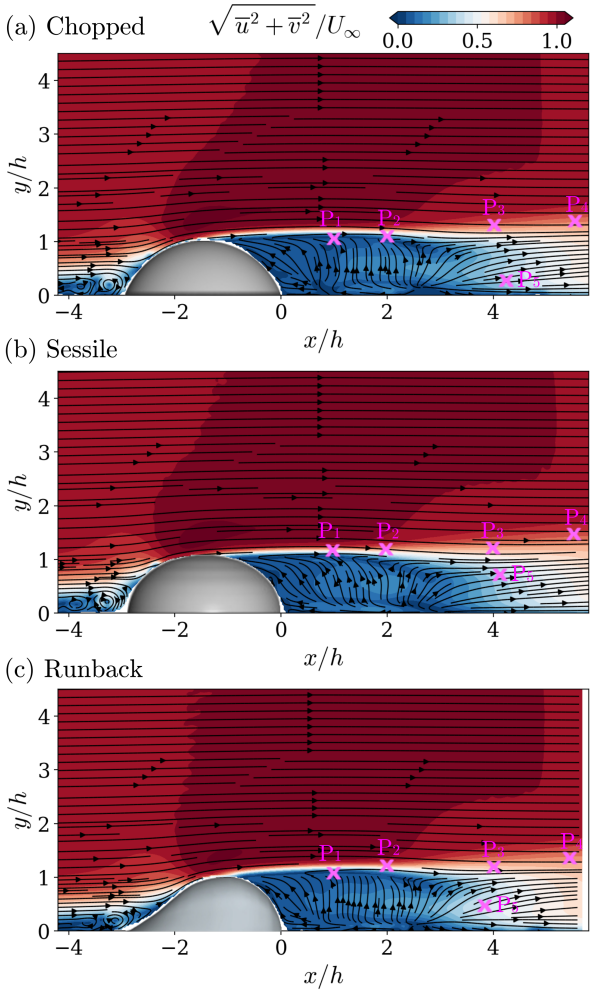

Figure 5.2: Time-averaged velocity magnitude overlaid with streamlines in the model symmetry planes for the (a) chopped, (b) sessile, and (c) runback models. Magenta crosses: sampling locations for power spectra in Fig. 5.8.

vortices around $x/h \approx 2$. For all three models, these shear layer vortices pinch off around the mean reattachment locations. These vortices have generally broken down by $x/h \approx 4$ for all models.

Time-averaged vortex structures identified using $\lambda_2 = -0.005$ contours [84] colored by

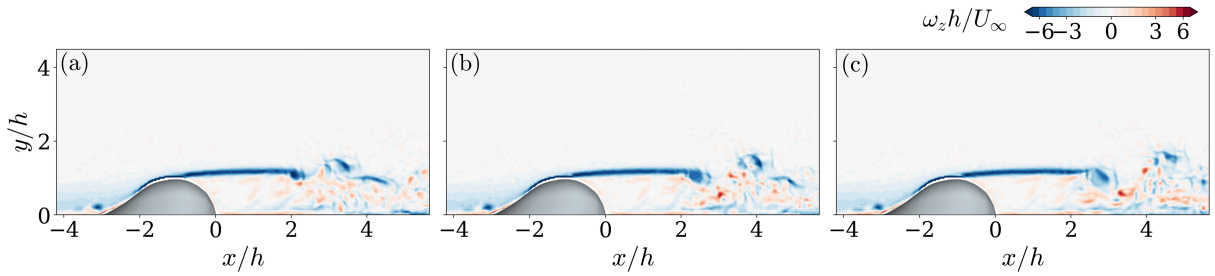

Figure 5.3: Sequential snapshots of instantaneous spanwise vorticity in the $z = 0$ plane of the runback model.

Table 5.1: Flow statistics

	Chopped	Sessile	Runback
Recirculating region length, x/h	2.6	3.2	2.7
Base vortex circulation, $\Gamma/(U_\infty h)$	0.29 ± 0.01	0.30 ± 0.01	0.33 ± 0.01
Velocity deficit recovery rate, ζ	-1.03 ± 0.02	-1.06 ± 0.06	-1.01 ± 0.06
Characteristic frequency, St_1	0.36	0.34	0.42

time-averaged streamwise vorticity ($\overline{\omega_x}$) are presented in the first column of Fig. 5.4 for all three geometries. Streamwise vorticity contours superimposed with wall-normal velocity contour lines are also included in selected yz planes. For all three geometries, there exists a pair of counter-rotating mean streamwise vortices in the immediate wake of the body ($-1 \leq z/h \leq 1$) that persist beyond the mean wake reattachment point. These vortex footprints in the mean vorticity fields are commonly referred to as base vortices and have been attributed to the tilting of arch-shaped vortical structures formed and shed in the separated shear layer downstream of the model [158, 159, 72]. They are further visualized by three-dimensional streamlines colored by local streamwise vorticity in the second column of Fig. 5.4. The non-dimensional circulation of the base vortices computed at $x/h = 2$

is $\Gamma/(U_\infty h) = 0.29 \pm 0.01$, 0.30 ± 0.01, and 0.33 ± 0.01 for chopped, sessile, and runback, respectively. The stronger base vortices for the runback geometry is consistent with the higher upwash velocity in the near wake evident in Fig. 5.1(c), which is also shown in the solid line contours in the yz planes of Fig. 5.4. The non-dimensional circulation of the base vortices computed at $x/h = 2$ is $\Gamma/(U_\infty h) = 0.29 \pm 0.01$, 0.30 ± 0.01, and 0.33 ± 0.01 for chopped, sessile, and runback, respectively. The stronger base vortices for the runback geometry are consistent with the higher upwash velocity in the near wake evident in Fig. 5.1(c), which is also shown in the solid line contours in the yz planes of Fig. 5.4. The base vortices weaken rapidly after $x/h = 2$, decreasing by approximately 50% by $x/h \approx 5$ and becoming difficult to identify by $x/h \approx 10$.

The horseshoe vortex systems suggested by the wall-normal velocity presented in Fig. 5.1 are evident outboard of the base vortices in Fig. 5.4. They are further visualized by in-plane vorticity contours and streamlines at the model symmetry plane in the second column of Fig. 5.4. All three models exhibit a six-vortex horseshoe system as categorized by Baker [8], as evidenced by the two stagnation points (SP_1 and SP_2). The three clockwise-rotating horseshoe vortices are labeled as HSV_1, HSV_2, and HSV_3, respectively, with increasing distance from the model surface. There are significant qualitative differences between the geometries, with the sessile model exhibiting the most pronounced horseshoe vortex system in terms of circulation, followed by the chopped and runback models. The reduction in circulation for the chopped model as compared to the sessile model is likely due to its lower upstream contact angle, as discussed in relation to Fig. 5.1. The runback model exhibits the weakest horseshoe vortex system, correlated with the shallowest upstream contact angle of the model.

Fig. 5.5 presents contour plots of the velocity deficit, defined as the velocity difference relative to the local baseline laminar boundary layer profile in the absence of droplet mod-

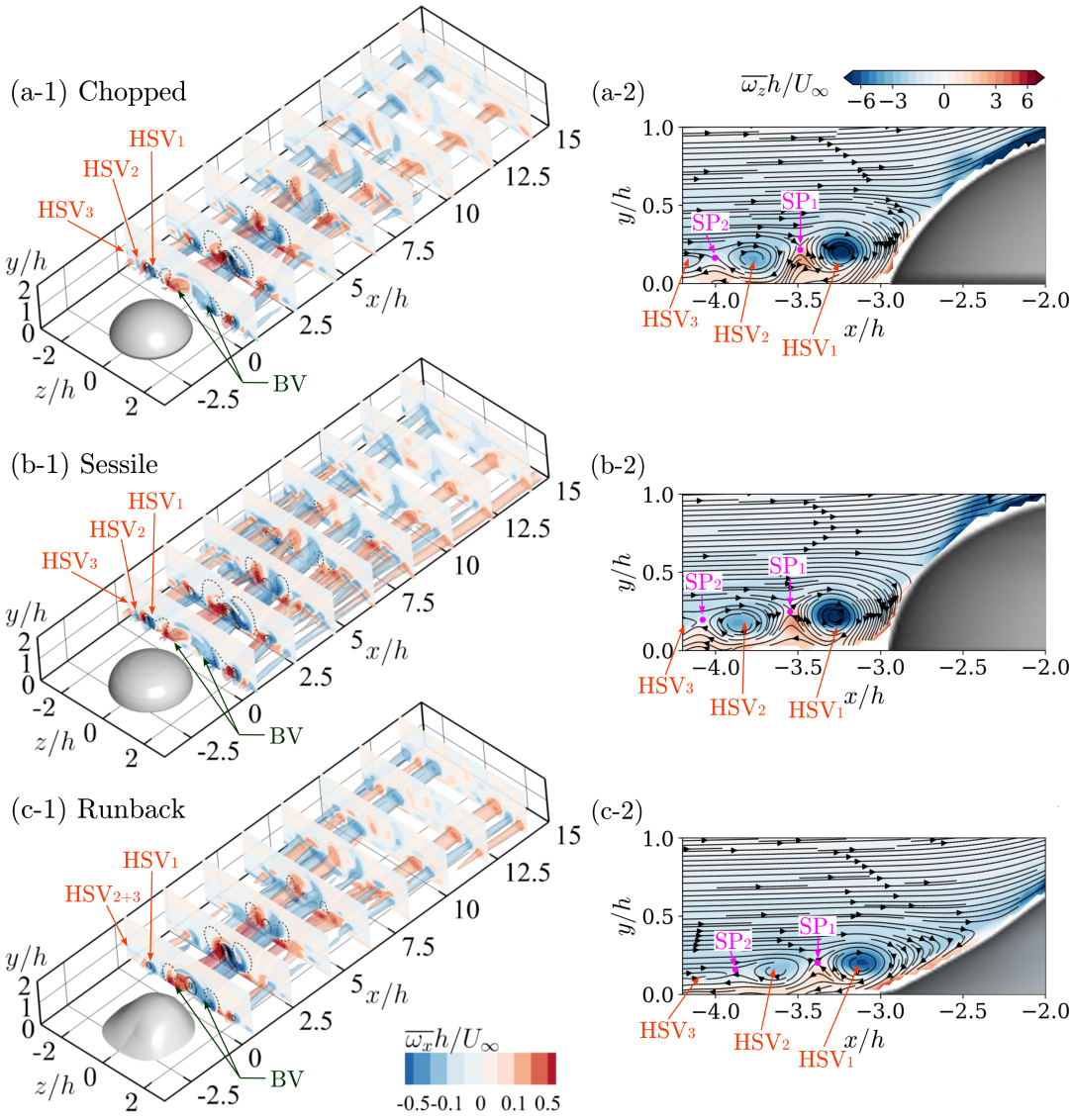

Figure 5.4: Contours of $\lambda_2 = -0.005$ colored by time-averaged streamwise vorticity ($\overline{\omega_x}$ for the (a-1) chopped, (b-1) sessile, and (c-1) runback geometries (left column). Solid and dashed lines in the cross-flow planes indicate positive and negative wall-normal velocity contours, respectively. Flow patterns of horseshoe vortex system upstream of the obstacles at the model symmetry planes (right column) are shown for the three geometries.

els, $u_{\text{def}} = (u_{\text{BL}}(y) - u(y))/U_\infty$ [209], in selected yz planes in the wake of each model. In the immediate wake of the obstacle ($|z|/h \lessapprox 1$) a large velocity deficit is present ($u_{\text{def}} > 0$), with the highest magnitude in the vicinity of the shear layer initiating at the top of the obstacle ($y/h \approx 1$). This deficit decays with streamwise distance, as shown in Fig. 5.6, which presents the streamwise decay of the maximum velocity deficit in the $z/h = 0$ plane. For all three models there is virtually no velocity deficit decay within the recirculating region ($\log_{10}(x/h) \lessapprox 0.4$), after which the velocity deficit begins to decrease rapidly. The slope of a linear fit to all data points for $\log_{10}(x/h) \geq 0.4$ yields the velocity deficit recovery rates $\zeta = -1.03 \pm 0.02$, -1.06 ± 0.06, and -1.01 ± 0.06 for the chopped, sessile, and runback models, respectively, where the error bounds are estimated as twice the standard error of the regression. These values are comparable to that found for micro-ramps of $\zeta = -1.06$ [209], suggesting similar velocity deficit recovery rate over a range of model geometries. The velocity has not yet fully recovered by the end of the measurement domain, as observed in the last row of Fig. 5.5.

Also evident in Fig. 5.5 is advection of free stream fluid towards the wall by the base vorticies, inidicated by $u_{\text{def}} < 0$ contours (local velocity greater than that of an undisturbed laminar boundary layer) in the vicinity of $z/h \approx \pm 1$ for planes near the obstacle (row 1). These regions of higher near wall velocity merge and spread in the spanwise direction with downstream distance. The higher near-wall momentum in the wakes results in more blunt, turbulent-looking, velocity profiles, while the spanwise growth of the higher near wall momentum is reminiscent of turbulent wedges that mark the final stage of roughness-induced boundary layer transition [172]. Comparing models, the spanwise extent of the $u_{\text{def}} > 0$ region appears larger for the sessile model at $x/h \gtrapprox 6$ in comparison with chopped and runback at similar streamwise locations.

The impact of the horseshoe vorticies visualized in Fig. 5.4 appear in Fig. 5.5 as re-

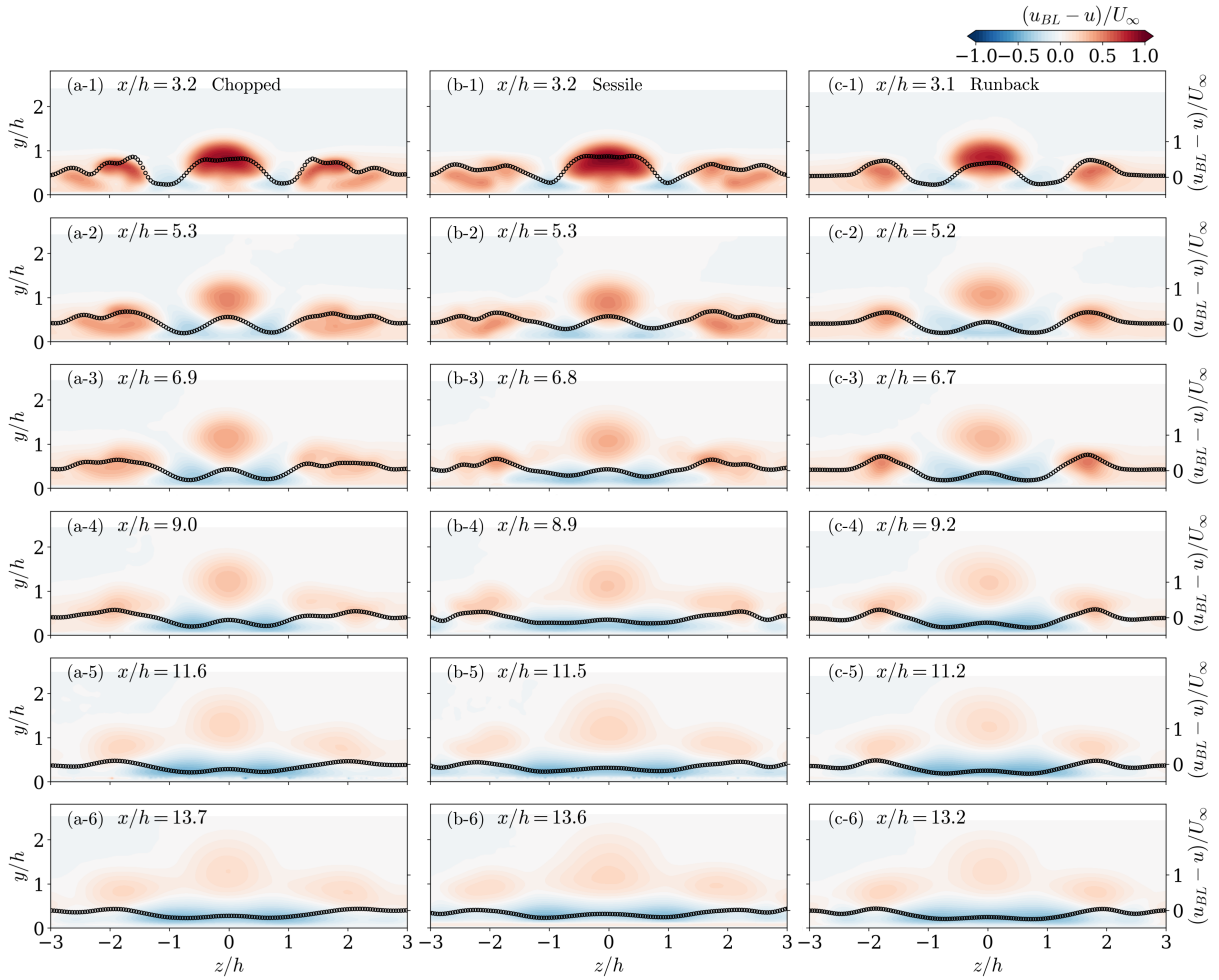

Figure 5.5: Streamwise velocity deficit evolution for the chopped (first column), sessile (second column), and runback (third column) models with downstream distance (rows). The black circles are velocity deficit profiles extracted at $y/h = 0.5$, with the magnitude of velocity deficit indicated by the second vertical axis on the right-hand-side of the figure.

gions of $u_{\text{def}} > 0$ near $z/h \approx \pm 2$, which decays with streamwise distance. Profiles of u_{def} extracted at $y/h = 0.5$ are presented in each frame of Fig. 5.5, which show both the streamwise decay of the velocity deficit, as well as the slight spanwise drift of the horseshoe vortex system.

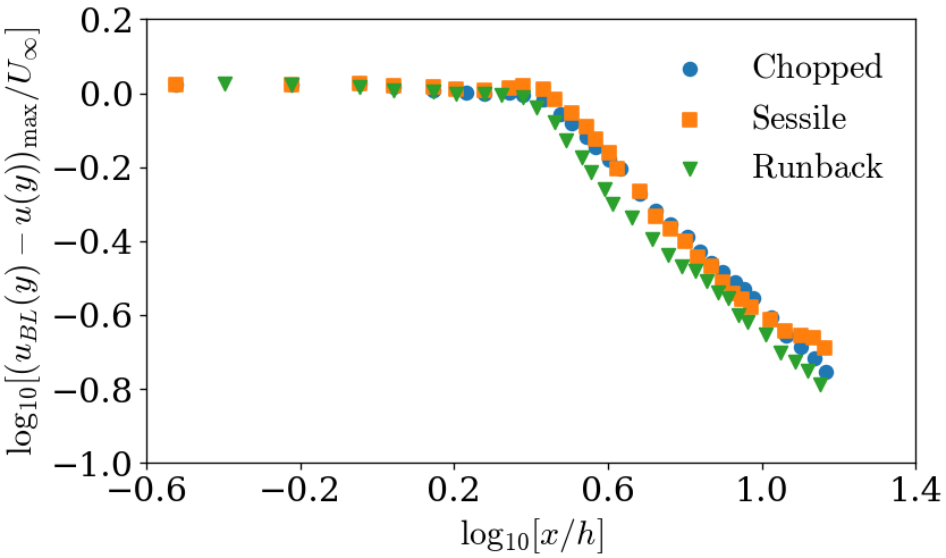

Figure 5.6: Streamwise evolution of maximum velocity deficit in the model symmetry planes.

Streamwise and wall-normal Reynolds normal stresses ($\overline{u'u'}$ and $\overline{v'v'}$, respectively) induced by the three models are presented in Fig. 5.7. For all three cases, strong velocity fluctuations are evident in the separated shear layer downstream of the model, and maximize around the mean reattachment locations, corresponding to the location of vortex pinch-off observed qualitatively in Fig. 5.3. Downstream of the recirculating regions, the wake flows are turbulent, as evidenced by turbulence intensities exceeding 10% for all three models. This is aligned with the prediction based on the von Doenhoff and Braslow diagram [198], which indicates the critical Reynolds number of the droplet-inspired obstacles (that is, the Reynolds number above which the wake is fully turbulent) is roughly in the range of $385 \leq \mathrm{Re}_h \leq 585$; thus the present study with $\mathrm{Re}_h \approx 2070$, corresponds to supercritical conditions. Up to $x/h \approx 6$, the high $\overline{u'u'}$ and $\overline{v'v'}$ values are localized primarily around the model symmetry plane ($z = 0$), associated with separated shear layer develop-

ment. Further downstream, velocity fluctuations around the symmetry plane decay, while those close to the lateral periphery of the wake increase and spread forming a wedge shape, as observed in the relatively high near wall velocity (negative velocity deficit) in Fig. 5.5.

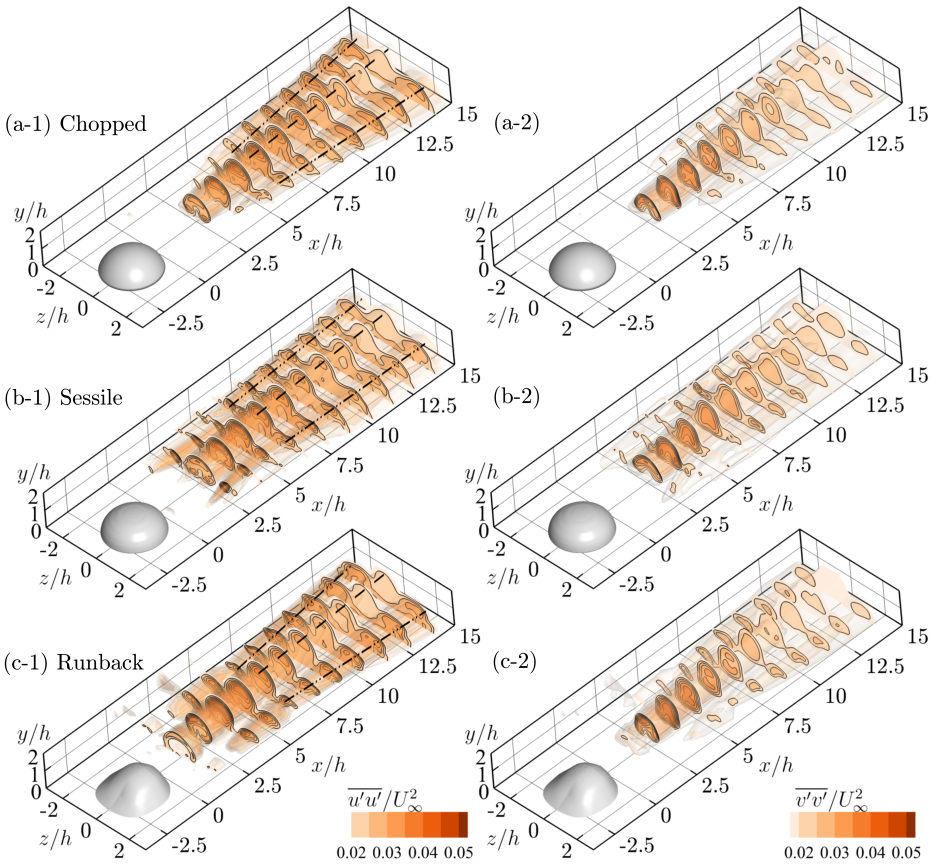

Figure 5.7: Mean square of streamwise ($\overline{u'u'}$, left column) and wall-normal ($\overline{v'v'}$, right column) velocity fluctuations in the wake of the chopped (row 1), sessile (row 2), and runback (row 3) models. Dashed and dash-dotted lines: linear fits of $\overline{u'u'}$ maxima at the symmetry plane and lateral periphery of the wake, respectively.

5.2 Coherent structures and transition mechanisms

This section aims to provide insight into the link between coherent structure formation and shedding, and the mechanism of laminar-to-turbulent flow transition suggested by the characteristic topological wake features in Figs. 5.1, 5.4, 5.5, and 5.7.

5.2.1 Spectra and Proper Orthogonal Decomposition

The spectral content of the wall-normal velocity fluctuations is presented in Fig. 5.8, where normalized frequency is expressed in terms of the Strouhal number $\mathrm{St} = fh/U_\infty$. The results are presented for several locations, P_1 - P_5, with the corresponding locations marked by magenta crosses in Fig. 5.2. Points P_1 through P_4 are located along the shear layer in the xy plane at $x/h = 1$, 2, 4, and 5.8, respectively, whereas P_5 is offset from the model symmetry plane, corresponding to the $\overline{u'u'}$ peak in the yz plane at $x/h \approx 4$.

Close to the model trailing edge (P_1), where the Kelvin-Helmholtz instability just starts to amplify, primary peaks centered around $\mathrm{St}_1 = 0.36$, 0.34, and 0.42 are observed for the chopped, sessile, and runback models, respectively. These values fall in the range of Strouhal numbers of $0.23 - 0.44$ reported by previous studies for surface-mounted hemispheres submerged in laminar boundary layers at Reynolds numbers ranging between 225 and 800 [158]. While the chopped and runback models exhibit a single dominant peak at this streamwise location, a weaker secondary peak is observed for the sessile model at the subharmonic frequency $\mathrm{St}_{1/2}$ (Fig. 5.8(b-1)). The occurrence of a similar subharmonic peak becomes evident further downstream for all three models, and is attributed to vortex merging in the separated shear layer, suggesting that vortex merging occurs further upstream for the sessile model. By P_2, the subharmonic and primary peaks have comparable magnitudes for all models.

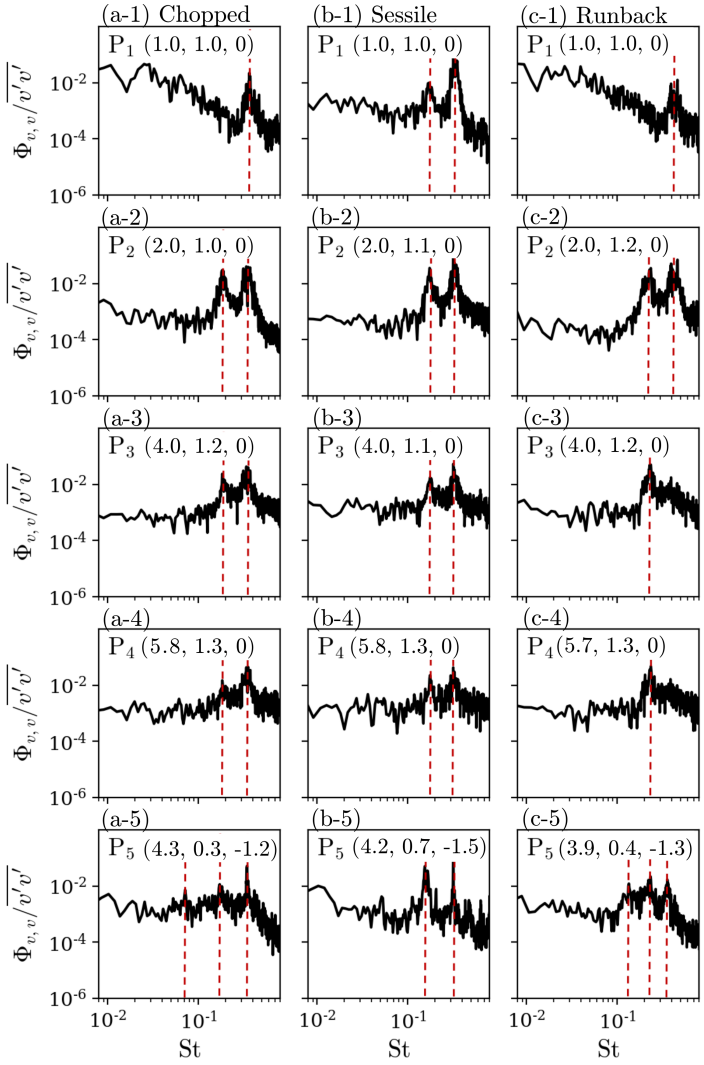

Figure 5.8: Power spectra of wall-normal velocity fluctuations for the chopped (column 1), sessile (column 2), and runback (column 3) models at 5 sampling locations with coordinates (x/h, y/h, z/h), shown schematically as magenta crosses in Fig. 5.2.

Past flow reattachment, the characteristic Strouhal number peaks of the three models evolve differently. Within the model symmetry planes, for the chopped and sessile models, the magnitudes of both peaks diminish at $x/h = 4$ (P_3) and $x/h = 5.8$ (P_4). For the

runback model, however, at P_3 the primary peak no longer appears in the spectrum, and the velocity fluctuations are dominated by the secondary peak. This indicates that the heads of the arch vortices merge more regularly downstream of the runback model than for the other two models. For all three models, the energy contained at higher frequencies increases as the peaks diminish, indicating energy cascading from large vortical structures to smaller eddies.

At P_5, located off the symmetry plane, broad peaks around St_2 and its subharmonics for the chopped and runback models are observed. In contrast, the spectrum of the sessile model is still dominated by the two peaks observed within the model symmetry plane. The origin of the broad low-frequency peaks is considered via proper orthogonal decomposition (POD) analysis [182] of the velocity fields measured on the yz plane located at $x/h \approx 4$. For chopped and runback models, peaks around $St_{1/4}$ are evident in the spectra of temporal coefficients of mode 3 and mode 5, respectively. Contours of wall-normal and spanwise velocity fluctuations of these two modes are localized around the model symmetry planes, corresponding to the passage of arch vortices [72, 210]. This indicates the low-frequency peaks observed in Fig. 5.8 (a-5) and (c-5) are likely caused by the merging events of the arch vortex legs. By contrast, a $St_{1/4}$ peak is not observed in the first twenty modes of the sessile model, which contain over 80% of fluctuating energy. This suggests that, within the captured flow region, merging events of merged arch vortex legs are less common for the sessile model as compared to the other models. To eliminate the possibility that $St_{1/4}$ coincides with the intrinsic oscillations of the horseshoe vortex systems, the power spectra of velocity fluctuations sampled around HSV_1 (see Fig. 5.4 for locations) are considered. The spectra for the chopped and runback models indicate the dominant instabilities peak at $St_{HSV} \approx 0.05$ and 0.07, respectively, which are much lower than their respective $St_{1/4}$. This eliminates the possibility that motion of the horseshoe vortex legs is major contribu-

tor to the peaks near $St_{1/4}$. The slight deviations of the low-frequency peaks from $St_{1/4}$, however, may partially result from the nonlinear interactions between the merged arch vortex legs and the reoriented HSV_1, and partially due to the frequency resolution of the spectra ($\Delta St \approx 0.002$).

The statistical patterns dominating the near wake velocity fluctuations are considered further via snapshot-based proper orthogonal decomposition (POD) analysis [182] of the velocity fields in the symmetry planes of the models. Fig. 5.9 shows the energy distribution over the first twenty POD modes, where the first five modes contain 47%, 43%, and 49% of the energy of the velocity fluctuations in the near wake of the chopped, sessile, and runback models, respectively. The first five spatial POD modes are presented in Fig. 5.10 and Fig. 5.11 for the sessile and runback models, respectively. The chopped model results are similar to those of the sessile model and are thus omitted for brevity. For the sessile model, modes 1 and 2 (Fig. 5.10 rows 1 and 2), and modes 3 and 4 (rows 3 and 4) are two pairs of coupled modes that appear in phase quadrature, representing traveling waves. Mode 5 (row 5) captures the flapping motion of the separated shear layer, which is associated to the temporal expansions and contractions of the recirculating region, referred to herein as the breathing mode [125]. For the runback model, however, modes 1 and 2 (Fig. 5.11 rows 1 and 2), and modes 4 and 5 (rows 4 and 5) are the coupled mode pairs, whereas mode 3 (row 3) is the breathing mode.

The power spectra of modes 1 and 2 for all three models peak around St_2, indicating the modes capture the behavior of merged arch vortices. The power spectra of the other paired modes (3 and 4 for chopped and sessile, and modes 4 and 5 for runback) exhibit a major peak centered around St_1 and a minor peak around St_2, indicating the modes are dominated by initial shedding of the arch vortices. For all three models, the initial wavelength of the vortex shedding events measured from the POD modes is around $1.3h$,

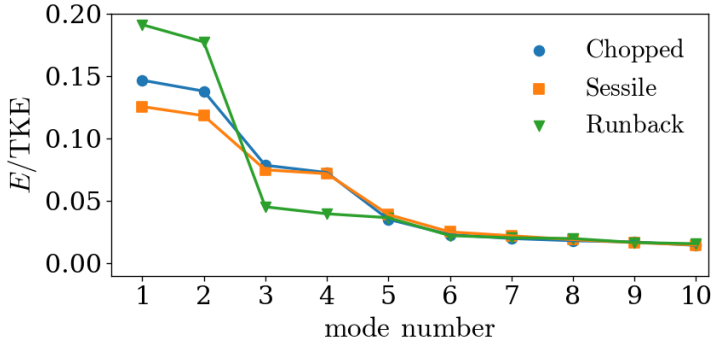

Figure 5.9: Energy distribution over spatial modes in the model symmetry planes.

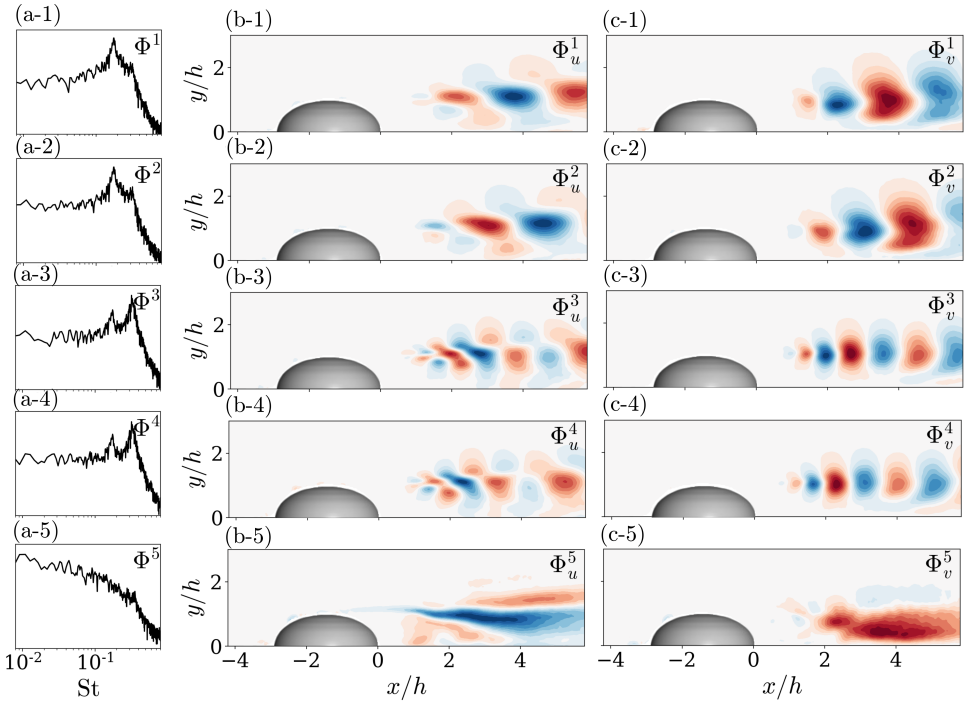

Figure 5.10: Power spectra of temporal coefficients (column 1), and contours of the spatial modes of the streamwise (column 2) and wall-normal (column 3) velocity in the symmetry plane of the sessile model.

which is comparable to that found in the near wake of a surface-mounted micro-ramp [211].

The results presented in Figures 5.9 and 5.10 suggest that the most energetic modes in the

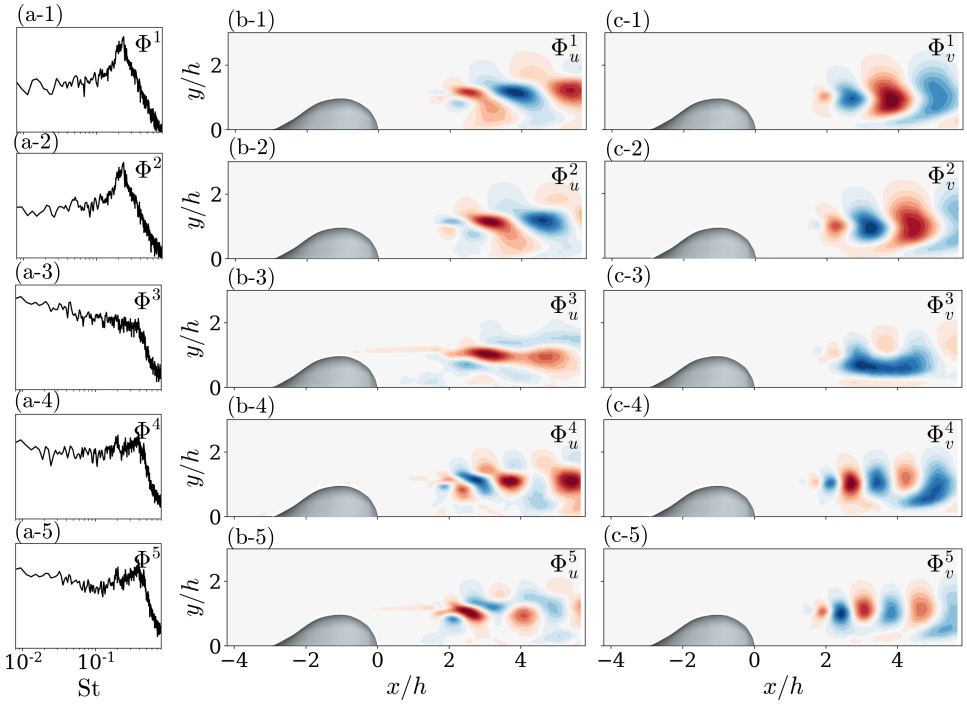

Figure 5.11: Power spectra of temporal coefficients (column 1), and contours of the spatial modes of the streamwise (column 2) and wall-normal (column 3) velocity in the symmetry plane of the runback model.

near wake are associated with the shedding and merging of arch vortices. The aggregate energy in the shedding and merging modes are similar for all three models, though the distribution for the runback model is more heavily weighted by the modes associated with merged arch vortices, consistent with the more regular merging for this model observed in the spectra in Fig. 5.8.

The power spectra of the breathing mode (mode 5 for chopped and sessile, and mode 3 for runback) exhibit a frequency band of St $\sim \mathcal{O}(10^{-2})$. Interestingly, this frequency band resembles the flow behavior downstream of a pressure-induced separation bubble [125], which features similar low frequency activity relative to the higher frequency unsteadiness related to the development of shear layer structures. The cause of this phenomenon is the

subject of active research (e.g., [125, 119]). One possible explanation proposed by [91], as well as [44] and [28], is intermittent shedding of larger vortical structures. Their occurrence may be related to the development of the primary shear layer vortices, either through merging or an increase in their strength, which can be triggered by changes in stability characteristics induced by variations in the incoming flow disturbances [119] or be linked to a global instability mode [189]. However, the relative energy content of the breathing mode observed herein is significantly lower than that associated with the modes associated with shear layer shedding for all three models (see 5.9), and thus the contribution of this mode to the transition process is not considered to be significant.

5.2.2 Transition Mechanisms

Surface-mounted roughness element studies have identified two instability modes associated with turbulent wedge growth, the varicose and sinuous modes [31, 108]. The former is related to Kelvin-Helmholtz instabilities and shedding of arch vortices, and exhibits symmetrical patterns across the model symmetry plane in spatial POD modes; the latter is attributed to the formation of hairpin structures at the periphery of the wake as a result of vortex interactions, and exhibits asymmetry in POD modes [209, 211]. Figures 5.3, 5.4, and 5.7 suggest similar mechanisms for the current droplet-inspired shapes.

To investigate the contributions of the two instability modes in the lateral spreading of velocity perturbations, the velocity fields measured in the yz planes are decomposed into non-harmonic symmetric ($u_{s+\Delta}$, $v_{s+\Delta}$, $w_{s+\Delta}$) and anti-symmetric (u_a, v_a, w_a) fields via Eqs. 5.1, 5.2, and 5.3. The modes that are symmetric in u, v components and anti-symmetric in w components are herein referred to as 'symmetric', while the modes that are anti-symmetric in u, v components and symmetric in w components are referred to

as 'anti-symmetric' [75, 78]. To clearly visualize the contribution of the Kelvin-Helmholtz instability, the non- harmonic symmetric component is further decomposed into slow-drift (Δ) and fast-varying (s) parts. The slow-drift part is calculated by applying a Gaussian moving-average filter [75] on the non-harmonic symmetric component (see Appendix B for filter parameters). For brevity, the fast-varying part will be referred to as 'symmetric' hereafter.

$$u_{s+\Delta}(x,y,z,t) = [u(x,y,z) + u(x,y,-z)]/2, \tag{5.1a}$$

$$u_a(x,y,z,t) = [u(x,y,z) - u(x,y,-z)]/2, \tag{5.1b}$$

$$v_{s+\Delta}(x,y,z,t) = [v(x,y,z) + v(x,y,-z)]/2, \tag{5.2a}$$

$$v_a(x,y,z,t) = [v(x,y,z) - v(x,y,-z)]/2, \tag{5.2b}$$

$$w_{s+\Delta}(x,y,z,t) = [w(x,y,z) - w(x,y,-z)]/2, \tag{5.3a}$$

$$w_a(x,y,z,t) = [w(x,y,z) + w(x,y,-z)]/2. \tag{5.3b}$$

Fig. 5.12 shows the energy distribution normalized by the turbulent kinetic energy (TKE) over the first ten slow-drift, symmetric, and anti-symmetric modes based on POD of the decomposed velocity fields from the stereo-PIV data. At $x/h = 4$, for all three models, the symmetric modes have notably higher contributions to the energy due to the presence of Kelvin-Helmholtz vortices at this location. The runback model exhibits the

highest energy in the lower symmetric modes, while sessile has the least, which was the ordering for the first two POD modes in the symmetry plane as well (see Fig. 5.9). This suggests that the modal energy for the lower symmetric modes is more strongly influenced by merged Kelvin-Helmholtz vortices, since vortex merging is more prevalent in the runback model. The runback model also exhibits the highest energy in the slow-drift mode, indicating this model has the strongest shear layer breathing motion, though the total energy in the slow drift mode is relatively small for all models in comparison with the symmetric and anti-symmetric modes.

Fig. 5.13 shows the first slow-drift mode (row 1), the first two symmetric modes (rows

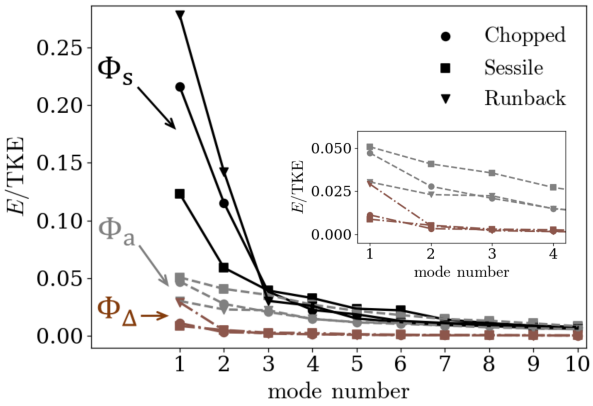

Figure 5.12: Energy distribution over spatial modes of symmetric (s; solid lines), anti-symmetric (a; dashed lines), and slow-drift (Δ; dashed-dotted lines) modes in the yz plane at $x/h = 4.0$. The inset magnifies the region showing the first few anti-symmetric and slow-drift modes.

2 and 3), and the first two anti-symmetric modes (rows 4 and 5) of the sessile model, as an example. While the main energy content of the slow-drift and first symmetric mode is localized around the model symmetry plane, that of the first anti-symmetric modes spreads beyond $|z|/h > 1.5$, ranging into the horseshoe vortex system (see Fig. 5.4). The wider anti-symmetric mode supports the previous speculation that vortex interactions at the

lateral periphery of the wake are the primary mechanism for spanwise spreading of perturbations introduced by droplet shapes. The power spectra of the first two anti-symmetric modes of the sessile model exhibit peaks at the Strouhal number of arch vortex shedding. In contrast, the power spectra of the most energetic anti-symmetric mode of the chopped and runback models (not shown) peak at the Strouhal number corresponding to merged structures. This implies that larger scale lateral structures form in the wake of the chopped and runback models as compared to the sessile model.

The dominance of the lateral structures in advancing the laminar-to-turbulent transition is further confirmed by the streamwise evolution of the so-called streak amplitude, given as

$$Au(x) = \frac{1}{2}[\max_{y,z}(u(x,y,z) - u_{BL}(x,y,z)) - \min_{y,z}(u(x,y,z) - u_{BL}(x,y,z))], \tag{5.4}$$

which is defined as the difference between the maximum and minimum velocity deficits within a given yz plane [4]. As suggested by Andersson *et al.* [4], streak amplitude can be an indicator of the type of instability that dominates the advancement of turbulent kinetic energy to the surrounding flow. For a streak amplitude of $0.26U_\infty < Au < 0.37U_\infty$, the asymmetric sinuous mode associated with spanwise shear becomes unstable. At higher streak amplitude of $Au > 0.37U_\infty$, the symmetric varicose mode originating from the K-H instabilities of the separated shear layer bounding the recirculating region dominates over the sinuous mode. Fig. 5.14 shows the streak amplitude calculated based on the mean streamwise velocity measured at each streamwise location. Prior to flow reattachment ($x/h \leq 3$), the varicose mode dominates the flow as the arch vortices resulting from the K-H instability are formed and amplified in this region. The streak amplitude quickly decays towards $0.37U_\infty$ in the range of $3 \leq x/h \leq 4$ due to the breakdown events of the K-H vortices, indicative of the diminishing importance of the varicose mode. Beyond $x/h \approx 5$,

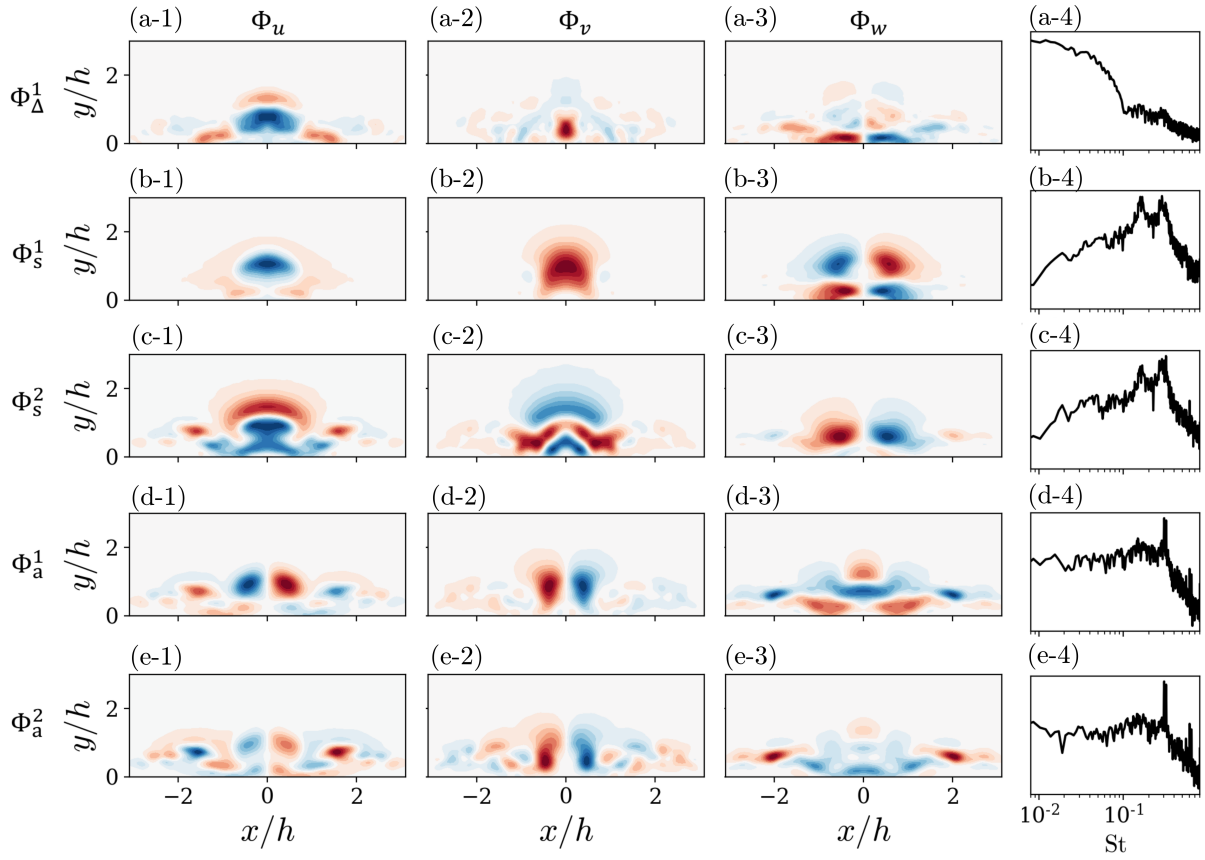

Figure 5.13: Contours of the spatial modes of streamwise (column 1), wall-normal (column 2), and spanwise (column 3) velocities and power spectra of the respective temporal coefficients (column 4) for the first slow-drift mode (row 1) , the first symmetric mode (row 2), the second symmetric mode (row 3), the first anti-symmetric mode (row 4), and the second anti-symmetric mode (row 5) of the sessile model in the yz plane at $x/h = 4.0$. Subscripts Δ, s, and a indicate the slow-drift, symmetric, and anti-symmetric modes, respectively.

notable spanwise spreading is observed for all three models. Streak amplitude in this streamwise range mostly lies within $0.26U_\infty < Au < 0.37U_\infty$, indicating the dominance of the sinuous mode associated with the lateral shear. This confirms the dominant role played by the large-scale coherent structures at the lateral peripheries of the spreading wake.

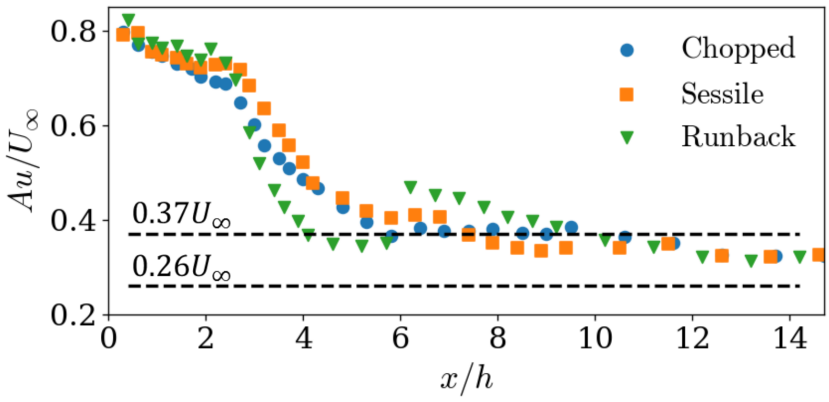

Figure 5.14: Streamwise evolution of streak amplitudes.

5.3 Summary

This chapter discusses flow development around isolated surface-mounted droplet-inspired 3D obstacles (chopped, sessile, and runback) submerged in a laminar boundary layer at flow conditions leading to droplet depinning, with boundary layer thickness to model height ratios around $\delta/h = 1$ and Reynolds number based on model height of approximately $\mathrm{Re}_h = 2070$. The measurement domain captures the roll-up of the boundary layer directly upstream of the obstacles, the shedding of coherent structures in the near wake, and the establishment and spreading of a turbulent wedge downstream.

Similar to the observations for flow around hemispheres and other smooth obstacles, a pronounced horseshoe vortex system is formed at the base of the investigated models. Flow over each obstacle separates from the model surface at approximately the model maximum height and reattaches to the substrate, forming a recirculating region directly downstream of the model. Several important trends between geometric parameters of the obstacles and statistical flow field development are discerned from the results of the three models tested:

(i) An increase in upstream contact angle leads to the increase of vorticity concentration of the horseshoe vortex system;

(ii) For the axisymmetric chopped and sessile models, an increase in downstream contact angle correlates with an increase in recirculating region length.

(iii) The runback model induces base vortices of the highest circulation. The strength of the central upwash is directly proportional to the strength of the base vortices.

(iv) Recovery rate of streamwise velocity deficit is insensitive to the geometric parameters of the models considered in the present study. Comparison with previous studies further indicates similar recovery rate over a range of obstacle geometries under laminar boundary layer incoming flows.

The near wake flow behavior is dominated by arch vortices shed in the separated shear layer and the horseshoe vortex system. For all three models, the shedding frequencies and initial wavelengths of the arch vortices are comparable to those found for hemispheres and micro-ramps. Averaged over time, the arch vortices form a pair of streamwise base vortices in the mean recirculation zone, which are most pronounced for the runback model and may be linked to more regular vortex merging.

Wake growth in both the wall-normal and lateral directions is similar across all models. The mechanisms driving the wall-normal and lateral spreading do, however, appear to differ. POD analysis suggests that shear layer roll-up and shedding is responsible for wall-normal wake growth. Spanwise spreading of the turbulent wedge, however, appears to be mainly the result of interactions of streamwise-oriented horseshoe and legs of the arch vortices at the lateral boundary.

Overall, the relative flow similarity between the chopped and sessile models suggests

that the chopped model is a reasonable proxy for sessile droplets in terms of vortex dynamics. The chopped model, by virtue of its lower contact angle, however, has a somewhat more muted horseshoe vortex system. Similarly, the runback model exhibits a less pronounced horseshoe vortex system, while shed vortices tend to merge more regularly than for the other two models, possibly due to the smaller radius of curvature of the top of the object.

Chapter 6

Aerodynamic loading on droplet-inspired geometries submerged in wall-bounded shear flows

This chapter presents the estimation of aerodynamic drag of droplet-inspired geometries submerged in the boundary layer formed over a flat plate (see Fig. 3.2). The analysis involves the same droplet models considered in Ch. 5, namely, the sessile and runback models. A hemisphere model of similar height as the droplet models is used to evaluate the accuracy of the drag estimation method. This chapter is divided into three sections. Sect. 6.1 presents the analytical considerations involving drag estimation from a control volume analysis, which is used to estimate the drag of droplet models based on the velocity fields measured by PIV. Sect. 6.2 discusses the effect of relative submergence and incoming

flow turbulence intensity on flow development and aerodynamic drag by comparing the velocity fields measured at model symmetry planes and the centreline drag coefficients, providing insights into the link between aerodynamic drag and mean flow characteristics. Sect. 6.3 summarizes the main findings of this chapter. In this chapter, ρ and ν are the density and kinematic viscosity of air, respectively. U_∞ and P_∞ are the freestream velocity and freestream pressure. $\vec{u} = (u, v, w)$ is the instantaneous velocity vector, with u, v, w the instantaneous streamwise (x), wall-normal (y), and spanwise (z) velocity components. p is the instantaneous static pressure in the flow. Bar ($\overline{*}$) and bracket ($< * >$) denote the time-averaged and space-averaged values of a variable ($*$). Prime ($*'$) denotes the fluctuations around the time-averaged value.

6.1 Drag estimation of droplet-inspired geometries submerged in a laminar boundary layer

Based on measured velocity fields, mean aerodynamic drag on the droplet models can be estimated using a wake integral method [115, 69, 70, 3] derived from control volume (C.V.) analysis [202]. The formulation follows that described in [202] and is applied to a control volume which encloses the droplet model (see Fig. 6.1), with surfaces oriented as follows: the upstream surface of the control volume locates sufficiently upstream of the flat plate, such that the freestream velocity U_∞ distributes uniformly over the cross-flow plane; the downstream surface is a cross-flow plane cutting through the wake; the bottom surface is along the substrate surface; and the lateral and top surfaces are bounded by streamlines (indicated by S in Fig. 6.1) connecting the upstream and downstream cross-flow planes. For the incompressible flows in the present study, the total instantaneous drag

on the droplet model $F_D(t)$ and the substrate $F_{D\text{substrate}}(t)$ surface can be determined from conservation of linear momentum applied to the control volume as

$$F_D(t) + F_{D\text{substrate}}(t) = -\rho \iiint_{\mathcal{V}} \frac{\partial u}{\partial t}\,\mathrm{d}\mathcal{V} + \rho \iint_{S_\text{wake}} u(U_\infty - u)\,\mathrm{d}S + \iint_{S_\text{wake}} (P_\infty - p)\,\mathrm{d}S, \tag{6.1}$$

where $\mathcal{V}$ is the fixed control volume, and S_wake is the downstream surface of the control

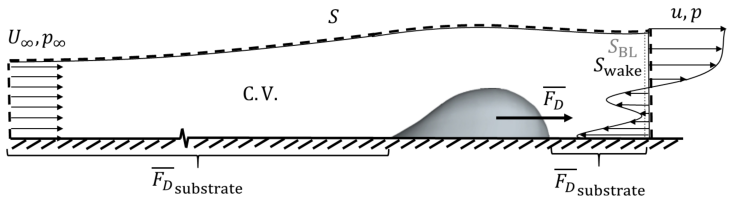

Figure 6.1: Schematic of control volume setup for drag estimation.

volume; u and p are the instantaneous streamwise velocity and static pressure measured on S_wake. Applying Reynolds decomposition to the velocity and pressure and averaging both sides of Eq. 6.1, the time-averaged total drag is formulated as

$$\overline{F_D} + \overline{F_{D\text{substrate}}} = \rho \iint_{S_\text{wake}} \overline{u}(U_\infty - \overline{u})\,\mathrm{d}S - \rho \iint_{S_\text{wake}} \overline{u'u'}\,\mathrm{d}S + \iint_{S_\text{wake}} (P_\infty - \overline{p})\,\mathrm{d}S. \tag{6.2}$$

Velocity fluctuations in the freestream provided by the wind tunnel facility of the present study (see Sect. 3.2.1) are of much smaller amplitude than those in the wake of the droplet models (see Sect. 5.1), and thus their contributions are neglected from Eq. 6.2.

Previous applications of Eq. 6.2 on aircraft [194, 95, 145] or ground vehicles [70, 187] benefit from the absence of significant influence of the substrate. For the present application, however, droplet models are small compared to the length of flat plate over which the laminar boundary layer develops (see Sect. 3.2.2), and thus the substrate drag $\overline{F_{D\text{substrate}}}$ cannot be neglected. Flow development over droplet models (see Sect. 5.1, Fig. 5.3) shows

that the streamwise distance where the baseline boundary layer profile is modified by the presence of the model is much smaller than the distance x_i (see Table 3.4) for boundary layer development. $\overline{F_{D\text{substrate}}}$ can thus be approximated by the momentum deficit computed from the undisturbed boundary layer profile measured directly upstream of the model,

$$\overline{F_{D\text{substrate}}} = \rho \iint_{S_{\text{BL}}} \overline{u_{\text{BL}}}(U_\infty - \overline{u_{\text{BL}}})\,\mathrm{d}S, \tag{6.3}$$

where S_{BL} is the cross-flow plane located at the same distance from the flat plate leading edge as S_{wake}, and $\overline{u_{\text{BL}}}$ is the undisturbed boundary layer velocity measured on S_{BL}. The time-averaged drag on the droplet model can thus be estimated as

$$\begin{aligned}\overline{F_D} = &\overbrace{\underbrace{\rho \iint_{S_{\text{wake}}} \overline{u}(U_\infty - \overline{u})\mathrm{d}y\mathrm{d}z - \rho \iint_{S_{\text{wake}}} \overline{u'u'}\mathrm{d}y\mathrm{d}z}_{\text{①a. Momentum deficit}} + \underbrace{\iint_{S_{\text{wake}}} (P_\infty - \overline{p})\mathrm{d}y\mathrm{d}z}_{\text{①b. Pressure deficit}}}^{\text{① Conventional wake integral (\textit{e.g.} [152, 187]), evaluated on } S_{\text{wake}}} \\ &\underbrace{- \rho \iint_{S_{\text{BL}}} \overline{u_{\text{BL}}}(U_\infty - \overline{u_{\text{BL}}})\mathrm{d}y\mathrm{d}z}_{\text{② } \overline{F_{D\text{substrate}}}\text{, evaluated on } S_{\text{BL}}}.\end{aligned} \tag{6.4}$$

In previous studies (*e.g.*, [186]), the first, second, and third terms on the right-hand-side of Eq. 6.4 are referred to as the momentum term, the Reynolds stress term, and the pressure term, respectively; these three terms form the conventional wake integral (term ① in Eq. 6.4) in applications where the influence of the substrate is negligible [69, 187]. For the remaining discussions of this chapter, the first two terms are grouped into ①a, reflecting the momentum deficit induced by the model. The third term is labeled as ①b, originating from the pressure deficit in the wake downstream of the model. The fourth term is labeled as ②, accounting for the drag contribution from the substrate $\overline{F_{D\text{substrate}}}$.

Terms ①a and ② can be directly computed from the velocity measurements. Figs. 6.2

(a-1), (b-1), and (c-1) show the time-averaged streamwise velocity fields in the wake of sessile, runback, and hemisphere models, respectively. As discussed in Sect. 5.1, flow separates near the model maximum height and a recirculating region forms and extends until mean flow reattachment around $x/h \approx 3$, where h is the droplet height. The lengths of the recirculating regions, when normalized with the model width, are $x_r/c = 1.6$, 1.3, and 1.8, for the sessile, runback, and hemisphere models, respectively. A large deficit in streamwise velocity $\overline{u}$ is observed within the recirculating region, after which it recovers rapidly. Strong wall-normal velocities (see Fig. 5.1, right column; omitted here for brevity) are induced directly downstream of the models and persist up to around $x/h \approx 6$, which enhances the momentum mixing between the wall and the surrounding flow. Turbulence intensities exceed 10% downstream of the recirculating regions for all three models, indicating the wake flows are turbulent (see Fig. 5.7; omitted here for brevity). Within $x/h \lessapprox 6$, velocity fluctuations localized primarily around the model symmetry due to the shedding of arch vortices (see Fig. 5.3). Further downstream, velocity fluctuations around the model symmetry plane decay, while those close to the lateral peripheries of the wake amplify and spread forming a wedge shape.

Unlike terms ①a and ②, estimate of term ①b requires information of static pressure $\overline{p}$ either directly measured or reconstructed based on velocity field measurements. In the present study, the static pressure is obtained from the velocity measurements within each cross-flow plane (see Sect. 3.2.2, Fig. 3.3(b) for experimental setup) by solving the Poisson equation for pressure [68],

$$\frac{\partial^2 p}{\partial y^2} + \frac{\partial^2 p}{\partial z^2} = -\rho f_{yz}, \tag{6.5}$$

which is a direct rearrangement of the Navier-Stokes equations [202], with the source term in a given yz plane, f_{yz}, formulated as

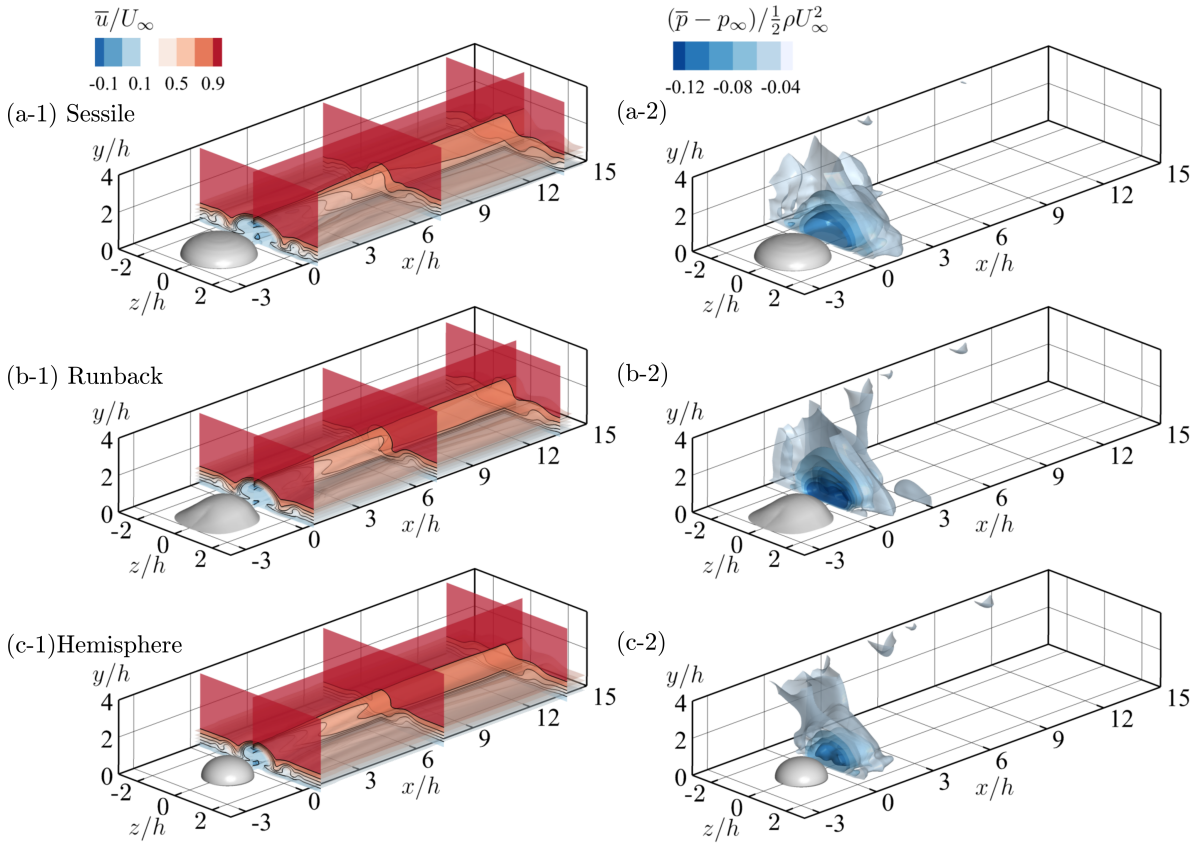

Figure 6.2: Time-averaged streamwise velocity ($\overline{u}$, left column) and reconstructed pressure ($\overline{p}-p_\infty$, right column) in the wake of the sessile (row 1), runback (row 2), and hemisphere (row 3).

$$
\begin{aligned}
f_{yz} = & \left[\left(\frac{\partial v}{\partial y}\right)^2 + 2\frac{\partial v}{\partial z}\frac{\partial w}{\partial y} + \left(\frac{\partial w}{\partial z}\right)^2\right] \\
& + \left[\frac{\partial(\nabla_{yz}\cdot\vec{u})}{\partial t} + (\vec{u}\cdot\nabla)(\nabla_{yz}\cdot\vec{u}) + \frac{\partial u}{\partial y}\frac{\partial v}{\partial x} + \frac{\partial u}{\partial z}\frac{\partial w}{\partial x}\right] \\
& - \nu\nabla_{yz}\cdot(\nabla^2\vec{u}),
\end{aligned}
\tag{6.6}
$$

where $\nabla_{yz} \cdot \vec{u} = \partial v/\partial y + \partial w/\partial z$ is the in-plane divergence of the velocity vector $\vec{u}$. Applying Reynolds decomposition to the velocity and pressure and averaging both sides of Eq. 6.5, the time-averaged static pressure $\overline{p}$ can be computed from

$$\frac{\partial^2 \overline{p}}{\partial y^2} + \frac{\partial^2 \overline{p}}{\partial z^2} = -\rho \overline{f_{yz}}, \tag{6.7}$$

with

$$\begin{aligned} \overline{f_{yz}} = & \left[\left(\frac{\partial \overline{v}}{\partial y} \right)^2 + 2 \frac{\partial \overline{v}}{\partial z} \frac{\partial \overline{w}}{\partial y} + \left(\frac{\partial \overline{w}}{\partial z} \right)^2 \right] \\ & + \left[(\vec{\overline{u}} \cdot \nabla)(\nabla_{yz} \cdot \vec{\overline{u}}) + \frac{\partial \overline{u}}{\partial y} \frac{\partial \overline{v}}{\partial x} + \frac{\partial \overline{u}}{\partial z} \frac{\partial \overline{w}}{\partial x} \right] \\ & + \left[\frac{\partial \overline{v'v'}}{\partial y^2} + \frac{\partial \overline{w'w'}}{\partial z^2} + \frac{\partial \overline{u'v'}}{\partial x \partial y} + 2 \frac{\partial \overline{v'w'}}{\partial y \partial z} + \frac{\partial \overline{u'w'}}{\partial x \partial z} \right] \\ & - \nu \nabla_{yz} \cdot (\nabla^2 \vec{\overline{u}}). \end{aligned} \tag{6.8}$$

The wall-normal and spanwise gradients ($\partial/\partial y$ and $\partial/\partial z$, respectively) of the time-averaged velocity in Eq. 6.8 are computed within each cross-flow plane using a central differencing scheme; the streamwise gradients ($\partial/\partial x$) are estimated by the slope of a linear fit of velocity measurements on three consecutive cross-flow planes (see Sect. 3.2.2, Fig. 3.3(b) for experimental setup). The streamwise gradients cannot be neglected from $\overline{f_{yz}}$ since they are of comparable order to the in-plane ones. Neumann boundary conditions are prescribed for the bottom (Eq. 6.9(a)) and lateral boundaries (Eq. 6.9(b)) of each cross-flow plane (see Fig. 6.2, left column), formulated as

$$\left.\frac{\partial \overline{p}}{\partial y}\right|_{y/h=0} = 0, \tag{6.9a}$$

$$\left.\frac{\partial \overline{p}}{\partial z}\right|_{z/h=\pm 3} = -\rho\left[\vec{\overline{u}}\cdot\nabla\overline{w} + \left(\frac{\partial \overline{u'w'}}{\partial x} + \frac{\partial \overline{v'w'}}{\partial y} + \frac{\partial \overline{w'w'}}{\partial z}\right) - \nu\nabla^2\overline{w}\right]. \tag{6.9b}$$

Dirichlet conditions are assigned for the top boundary (Eq. 6.10), with local static pressure values estimated using the Bernoulli equation [202],

$$\overline{p}\,|_{y/h=4} = P_\infty - \frac{1}{2}(\overline{u}^2 + \overline{v}^2 + \overline{w}^2) - \frac{1}{2}(\overline{u'u'} + \overline{v'v'} + \overline{w'w'}). \tag{6.10}$$

Figs. 6.2 (a-2), (b-2), and (c-2) show the reconstructed pressure fields of the sessile, runback, and hemisphere models, respectively. A strong pressure deficit is confined within the recirculating region of $x/h \lesssim 3$. This is comparable to the observations made by Hooshanginejad and Lee [77] which suggests that the impact of the adverse pressure gradient induced by an upstream hemisphere on droplets downstream diminishes at a spacing of around 2.8 hemisphere height. The pressure deficit of the runback model is notably stronger than that for the other two models, which is likely associated with the stronger base vortex pair within its shorter recirculating region (see Sect. 5.1).

Fig. 6.3(a) shows the terms in Eq. 6.4 computed with S_{wake} located in the range of $0.3 \lessapprox x/h \lessapprox 15$ from the droplet model trailing edge. Blue markers present the momentum integrals defined by the term ①a in Eq. 6.4. Brown markers account for the pressure variation in the wake (term ①). Considering the difference between blue and brown markers, it can be seen that the pressure term contributes significantly to the drag estimate within $x/h \lesssim 3$. This is aligned with the reconstructed pressure fields (Fig. 6.2(a-2), (b-2), (c-2)), where strong pressure deficit is present within the recirculating region. For com-

parison, drag on the plate due to undisturbed laminar and turbulent boundary layers are presented by black dashed and grey dashed-dotted lines, respectively. The drag of the fully-developed turbulent boundary layer is estimated using the correlations proposed by Prandtl [203] (see Eq. 2.5) and assuming a virtual origin of the turbulent boundary layer at the flat plate leading edge. The presence of droplet models increase the total drag on the control volume as compared to the laminar baseline. As the turbulent wake spreads laterally and the near-wall velocity deficit recovers, the total drag exhibits a higher rate of increase (as indicated by red dashed line in Fig. 6.3) with streamwise locations than that of the laminar baseline in the range of $x/h \gtrapprox 8$, and is close to the slope of a turbulent boundary layer.

Fig. 6.3(b) shows the droplet model drag computed using Eq. 6.4 with S_{wake} located in the range of $0.3 \lessapprox x/h \lessapprox 15$ from the droplet model trailing edge. The drag on the plate $\overline{F_{D\text{substrate}}}$ (term ② in Eq. 6.4) is estimated from the undisturbed laminar boundary layer. The steep slope observed in the range of $x/h \lessapprox 4$ results from the underestimation in pressure deficit within the recirculating region. This underestimation is caused by approximating the streamwise gradients of velocities in the Poisson source term by the slope of linear fit over consecutive cross-flow planes. Although the spacing between two cross-flow planes is 2 mm in this region (the smallest effective spacing for stereo-PIV setup, see Sect. 3.2.2), the streamwise spatial resolution is not sufficient for the near wake to yield reliable pressure reconstruction, and thus S_{wake} should be placed downstream of $x/h \approx 4$. For $x/h \gtrapprox 9$, $\overline{F_D}$ values increase notably as S_{wake} moves downstream. This is due to the increasing drag contributions from the turbulent boundary layer as the wake spreads laterally. A similar trend is demonstrated by the coarse estimation of $\overline{F_{D\text{substrate}}}$ based on the wall shear stresses measured directly from the velocity fields in the cross-flow planes. A higher rate of increase in $\overline{F_{D\text{substrate}}}$ with streamwise locations is observed for $x/h \gtrapprox 9$

than that further upstream. However, the limited spatial resolution in the near-wall region (1 velocity vector within the viscous sublayer of a turbulent boundary layer of the same Re_x [202]) prevents the accurate estimation of the wall shear stress. Since it is difficult to segregate the drag contributions from the model and the turbulent boundary layer, S_{wake} should locate upstream of $x/h \approx 9$. In the range of $4 < x/h < 9$, the drag computed for all three models present a plateau, and hence the time-averaged drag $\overline{F_D}$ are evaluated in the range of $5 \lessapprox x/h \lessapprox 8$ for each model. The values of $\overline{F_D}$ on the sessile, runback, and hemisphere models are 0.56 ± 0.036 mN, 0.49 ± 0.036 mN, and 0.44 ± 0.026 mN, respectively, with the uncertainties estimated from the standard deviations of $\overline{F_D}$ within the selected streamwise range. The drag on the runback model is slightly lower compared to that of the sessile model of the similar volume, indicating that droplet deformation under wind-forcing leads to a slight reduction in aerodynamic loading. The reduced drag on the runback model can be expected from its more muted spanwise vortex system as compared to the sessile model (see Ch. 5), which introduces less disturbances to the ambient shear flow.

The drag coefficient, $\overline{C_D} = \overline{F_D}/(\rho U_\infty^2 A/2)$, where A is the frontal area of the models (see Table 3.3), is presented in Fig. 6.4 for S_{wake} in the range of $0.3 \lessapprox x/h \lessapprox 15$ from the model trailing edge. $\overline{C_D}$ varies with the streamwise location of S_{wake} following a similar trend as that of $\overline{F_D}$, and hence the time-averaged drag coefficients $\overline{C_D}$ are also evaluated in the range of $5 \lessapprox x/h \lessapprox 8$ for each model. The drag coefficients of the sessile, runback, and hemisphere models are 0.36 ± 0.023, 0.35 ± 0.025, and 0.41 ± 0.024, respectively, with the uncertainties estimated from the standard deviations of $\overline{C_D}$ within the selected streamwise range. The drag coefficient of the hemisphere found in the present study is close to that reported by [185] and [131], and that of spheres in a freestream in the same Reynolds number range, as summarized in Fig. 2.5. Droplet models have lower $\overline{C_D}$ as

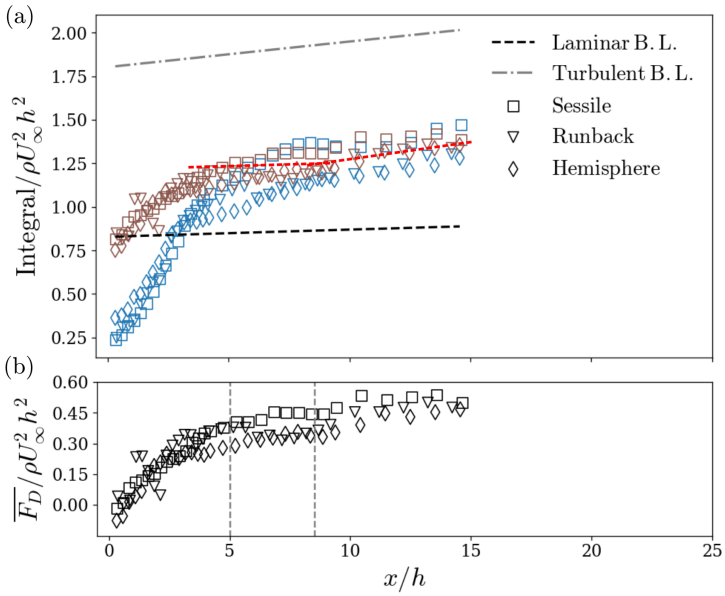

Figure 6.3: (a) Velocity and pressure integrals and (b) droplet model drag $\overline{F_D}$ computed within cross-flow planes placed at multiple locations along the streamwise direction. Blue markers: term ①a in Eq. 6.4; brown markers: terms ①a + ①b in Eq. 6.4. The red dashed lines in (a) demarcated the rate of increase in substrate drag with streamwise locations. The vertical dashed lines in (b) denote the region over which $< \overline{F_D} >$ is measured for comparison.

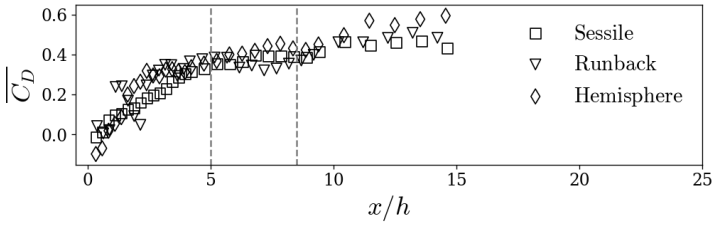

Figure 6.4: Drag coefficients estimated from S_{wake} located at vaired streamwise locations. The vertical dashed lines denote the region over which $< \overline{C_D} >$ is measured for comparison.

compared to hemisphere when submerged in a laminar incoming boundary layer with a relative submergence of $\delta/h = 1.0$. This indicates that estimating aerodynamic loading in

a droplet depinning process with the $\overline{C_D}$ of hemispheres can result in an overestimation of approximately 10%. The sessile and runback models exhibit no discernible difference in drag coefficients. Hence, the lower drag on the runback model is mainly attributed to the smaller frontal area by approximately 9% as compared to that of the sessile model (see Table 3.3).

6.2 Influence of incoming boundary layer regime on drag

In real-world applications, droplets under wind-forcing can experience different near-wall velocity profiles (see Sect. 4.2.3) depending on the locations of droplets relative to the origin of the near-wall shear flows, and the flow regime being either laminar or turbulent. This section discusses the influence of relative submergence and boundary layer regime. The range of boundary layer parameters considered in this section are listed in Table 3.4.

It is first instructive to consider the flow development at the model symmetry planes. Figs. 6.5 and 6.6 show the flow development at the symmetry plane of the sessile and runback models, respectively, under the influence of laminar boundary layers of two relative submergences and turbulent boundary layers of three submergences (see Table 3.4). Column 1 shows the time-averaged steamwise velocity ($\overline{u}$) overlaid with the in-plane streamlines; the white dashed lines represent the zero streamwise velocity contours bounding the recirculating region. Column 2 shows the contours of time-averaged wall-normal velocities ($\overline{v}$). Column 3 shows the normalized relative pressure contours, with the time-averaged static pressure reconstructed based on the velocity fields measured by 2D-2C PIV within the model symmetry plane. The pressure fields are obtained by solving the Poisson equa-

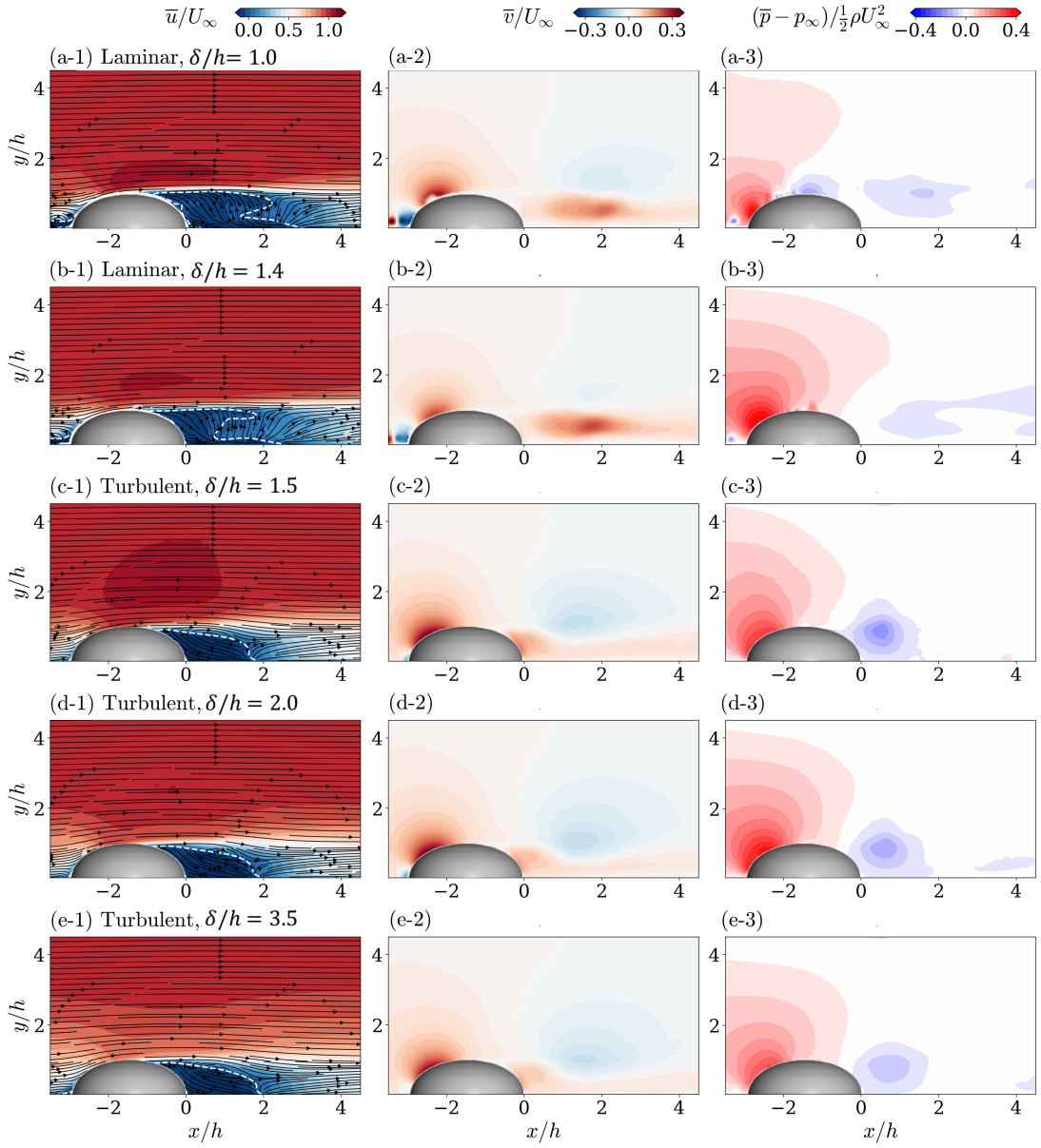

Figure 6.5: Time-averaged streamwise velocity ($\overline{u}$) overlaid with streamlines (column 1), wall-normal velocity ($\overline{v}$, column 2) and relative pressure ($\overline{p}-p_\infty$, column 3) in the symmetry plane of the sessile model. White dashed lines: contours of zero streamwise velocity.

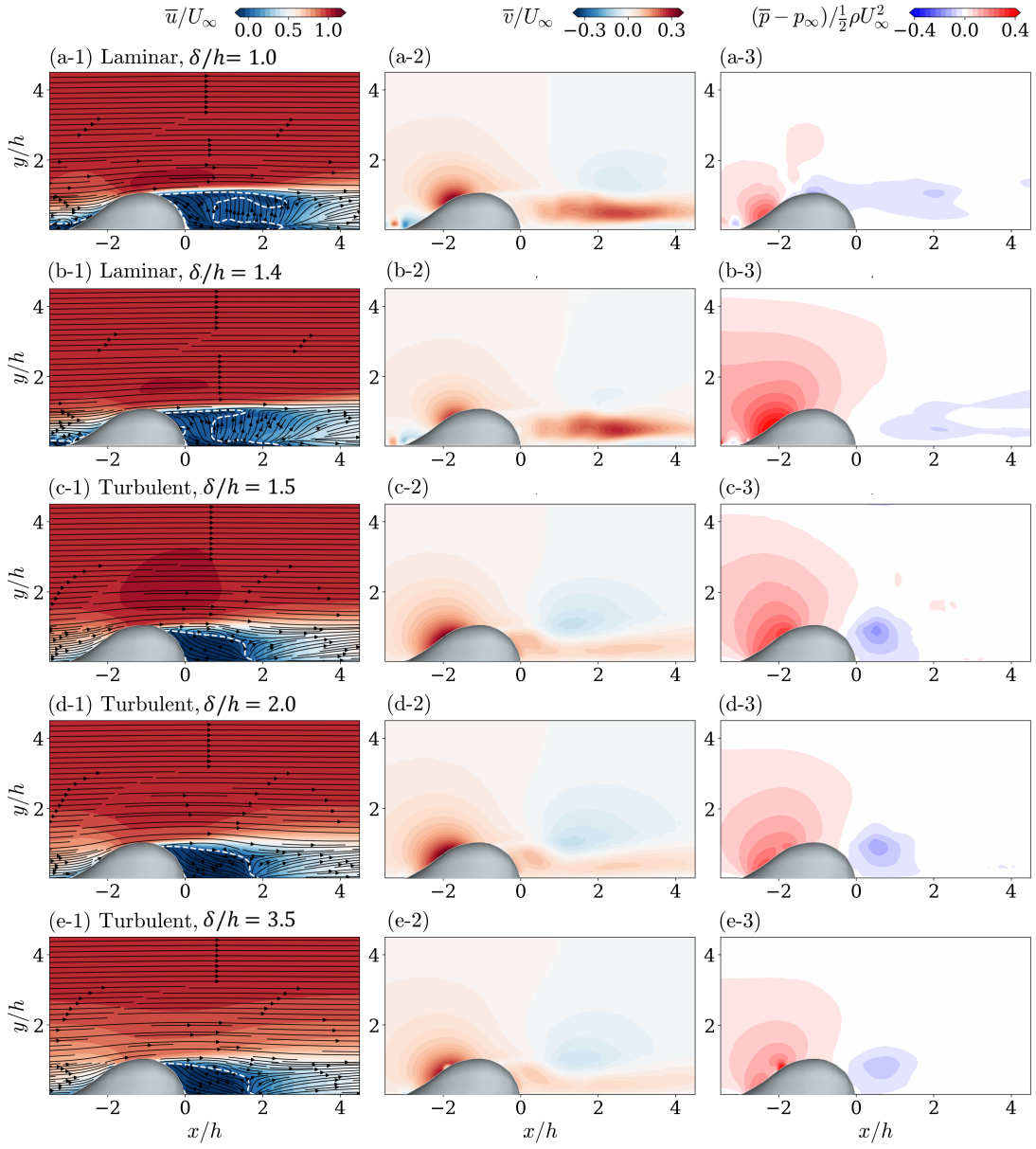

Figure 6.6: Time-averaged streamwise velocity ($\overline{u}$) overlaid with streamlines (column 1), wall-normal velocity ($\overline{v}$, column 2) and relative pressure ($\overline{p}-p_\infty$, column 3) in the symmetry plane of the runback model. White dashed lines: contours of zero streamwise velocity.

tion following the formulation in [195],

$$\frac{\partial^2 \overline{p}}{\partial x^2} + \frac{\partial^2 \overline{p}}{\partial y^2} = -\rho \overline{f_{xy}}, \tag{6.11}$$

with the assumptions that the velocity component and gradients in the spanwise direction are negligible in the source term

$$\begin{aligned} \overline{f_{xy}} = & \left[\left(\frac{\partial \overline{u}}{\partial x} \right)^2 + 2 \frac{\partial \overline{u}}{\partial y} \frac{\partial \overline{v}}{\partial x} + \left(\frac{\partial \overline{v}}{\partial y} \right)^2 \right] \\ & + \left[\frac{\partial \overline{u'u'}}{\partial x^2} + 2 \frac{\partial \overline{u'v'}}{\partial x \partial y} + \frac{\partial \overline{v'v'}}{\partial y^2} \right] \\ & - \nu \nabla_{xy} \cdot (\nabla^2 \vec{\overline{u}}). \end{aligned} \tag{6.12}$$

Neumann boundary conditions are prescribed for the upstream, downstream, and bottom boundaries of the field-of-view (see Fig. 3.3(b)); Dirichlet boundary condition is assigned to the top boundary, with local static values estimated using Bernoulli equation [202]. For all the cases considered (Figs. 6.5 and 6.6, column 3), a high pressure region is formed on the upstream surface of the model where the stagnation streamlines attach to the fore-body. As the flow accelerates over the model surface, pressure decreases. Directly downstream, a low pressure region is formed in the recirculating region, as discussed earlier for the pressure fields reconstructed based on stereo-PIV measurements (see Fig. 6.2, right column). In laminar boundary layers, a small low pressure region is observed at the base upstream of the droplet model, corresponding to the core of the horseshoe vortex.

For droplet models submerged in the laminar boundary layer of $\delta/h = 1.0$, Fig. 6.7 compares the velocity measurements and pressure reconstruction obtained from the 2D-2C (blue lines) and stereo-PIV (red lines) measurements in the model symmetry plane. Streamwise velocity profiles ($\overline{u}$; Fig. 6.7, row 1) measured by the two PIV setups show

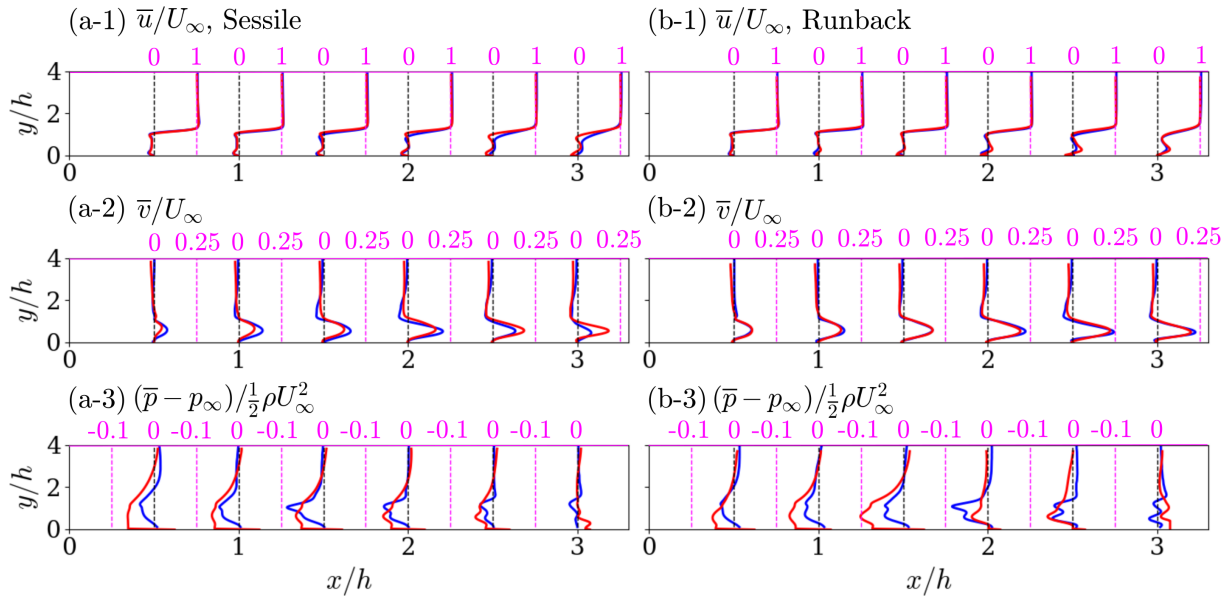

Figure 6.7: Comparison of time-averaged streamwise velocity ($\overline{u}$, row 1), wall-normal velocity ($\overline{v}$, row 2) and relative pressure ($\overline{p}-p_\infty$, row 3) in the symmetry planes of the sessile (column 1) and runback (column 2) models from 2D-2C PIV (blue lines) and stereo-PIV (red lines) measurements.

good agreement in the range of $x/h \lessapprox 1.5$. Further downstream, discrepancies in $\overline{u}$ profiles are observed in the near-wall region ($y/h \lessapprox 0.3$) and around the separated shear layer ($y/h \approx 1$). The difference in streamwise velocity deficit measured by the two PIV setups is up to around 15%, which is likely associated with the amplifying shear layer instabilities and enhanced three-dimensional velocity fluctuations (see Fig. 5.3). Wall-normal velocity profiles ($\overline{v}$; Fig. 6.7, row 2) measured by the two PIV setups agree well in the region away from the wall ($y/h > 2$). In the proximity of the wall, while the $\overline{v}$ profiles of the runback model (Fig. 6.7 (b-2)) show reasonably good agreement between the two PIV setups, larger discrepancies are observed for the sessile model (Fig. 6.7 (b-1)). The discrepancies observed for the sessile model is largely attributed to the misalignment between the spanwise location

of velocity measurements and the model symmetry plane. While $\overline{u}$ is relatively insensitive to the laser sheet position, $\overline{v}$ changes significantly at an offset on the order of the laser sheet thickness from the model symmetry plane (see Fig. 5.1). The discrepancies in $\overline{v}$ profiles increases significantly in the range of $2 \lessapprox x/h \lessapprox 3$ with the amplification of the base vortex pair (see Fig. 5.4, left column). Qualitatively, the relative pressure reconstructed based on both 2D-2C and stereo-PIV measurements shows similar trend in that pressure deficit is the strongest directly downstream of the model and quickly recovers as the flow reattaches to the substrate. Quantitatively, however, the difference in maximum pressure deficit reconstructed from velocity fields measured by 2D-2C and stereo-PIV setups at a given streamwise location is up to around 50%. The large discrepancies in the pressure profiles are mostly attributed to the omission of the spanwise components and gradients of velocities in the source term of the 2D Poisson equation (see Eq. 6.12).

In laminar boundary layers (Figs. 6.5(a-1),(b-1); Figs. 6.6(a-1),(b-1)), the recirculating region downstream of the model exhibits a "C"-shape, with a concavity around the model half-height $y/h = 0.5$; close to the separated shear layer and in the near-wall region, lobes of reversed flow extend further downstream. The formation of this typical shape is attributed to the base vortex pair, which pushes the low momentum fluids away from the wall and brings the high momentum fluids towards the wall (see Sect. 5.1). Increasing the relative submergence from $\delta/h = 1.0$ to 1.4, the upper lobe of reversed flow shortens, indicating a faster recovery of the velocity deficit near the separated shear layer. An increase in relative submergence also reduces the strength of the horseshoe vortices, as indicated by the wall-normal velocity contours upstream of the model, in the region of $x/h < -3$ and $y/h < 0.5$ (Fig. 6.6(a-2), (b-2)).

At comparable relative submergence of around $\delta/h \approx 1.5$, changing the boundary layer regime from laminar (Fig. 6.5 (a-2) and Fig. 6.6 (a-2)) to turbulent (Fig. 6.5 (a-3) and

Fig. 6.6 (a-3)) significantly alters the topology of recirculating region. The separation point on the model surface moves from the maximum height towards the aft-body of the models. The lengths of the recirculating regions decreases from $x_r/c \approx 1.4$ to 1.2, and from $x_r/c \approx 1.3$ to 1.0, for the sessile and runback models, respectively. For the hemisphere model, the recirculating region length decreases from $x_r/c \approx 1.6$ to 1.4 (also reported in Table 6.1). A similar trend has been reported by Savory and Toy [159] for hemispheres, which shows the length of the recirculating region decreases from $x_r/c \approx 1.25$ to 1.1 by increasing the incoming flow turbulence using a vortex generator. The delay in flow separation from the model surface and the advance in reattachment on the substrate were attributed to the scale and intensity of turbulence in the incoming flow rather than the velocity profile by [158], in that the separated shear layer thickens more rapidly with increased boundary layer turbulence and results in larger shear layer curvature. Unlike in laminar boundary layers, recirculating regions formed in turbulent boundary layers (Fig. 6.5(a-3) and Fig. 6.6(a-3)) do not exhibit the concavity around the model half-height. This is likely due to the weakened base vortices, as indicated by the significant reduction in the strength of central upwash (Fig. 6.5(b-3) and Fig. 6.6(b-3)). Although the pressure deficit downstream of the model is higher in the turbulent boundary layer (Fig. 6.5(c-3) and Fig. 6.6(c-3)), pressure recovery is notably faster than in the laminar boundary layer (Fig. 6.5(c-2) and Fig. 6.6(c-2)) merited by the enhanced turbulent mixing. Furthermore, mean flow development over a given model submerged in a turbulent boundary layer is insensitive to the relative submergences in the range of $1.5 \lessapprox \delta/h \lessapprox 3.5$ (Fig. 6.5, row 3 to 5, and Fig. 6.6, row 3 to 5) as compared to the laminar cases.

As previously discussed in Sect. 5.2.1, flow development in the recirculating region is largely influenced by the shedding of vortical structures. Figs 6.8 and 6.9 present the spectral content of the wall-normal velocity fluctuations in terms of Strouhal number St =

Table 6.1: Flow statistics at model symmetry plane.

	Sessile	Runback	Hemisphere
Laminar, $\delta/h = 1.0$			
Recirculating region length, x_r/h	4.7 ± 0.03	3.9 ± 0.03	3.7 ± 0.03
Recirculating region length, x_r/c	1.6 ± 0.01	1.3 ± 0.01	1.8 ± 0.02
Characteristic frequency, St	0.34 ± 0.002	0.42 ± 0.002	0.41 ± 0.002
Centreline drag coeff., $\overline{C_{D_{\mathrm{cl}}}}$	$0.76^{+0.038}_{-0.005}$	$0.81^{+0.041}_{-0.008}$	$0.76^{+0.038}_{-0.021}$
Centreline drag coeff., $\overline{C^*_{D_{\mathrm{cl}}}}$	$2.11^{+0.106}_{-0.015}$	$2.23^{+0.112}_{-0.022}$	$2.09^{+0.105}_{-0.058}$
Laminar, $\delta/h = 1.4$			
Recirculating region length, x_r/h	4.1 ± 0.03	3.8 ± 0.03	3.3 ± 0.03
Recirculating region length, x_r/c	1.4 ± 0.01	1.3 ± 0.01	1.6 ± 0.02
Characteristic frequency, St	0.32 ± 0.002	0.38 ± 0.002	0.39 ± 0.002
Centreline drag coeff., $\overline{C_{D_{\mathrm{cl}}}}$	$0.87^{+0.044}_{-0.033}$	$0.93^{+0.047}_{-0.034}$	$0.75^{+0.038}_{-0.028}$
Centreline drag coeff., $\overline{C^*_{D_{\mathrm{cl}}}}$	$3.52^{+0.176}_{-0.133}$	$3.77^{+0.189}_{-0.138}$	$3.02^{+0.151}_{-0.113}$
Turbulent, $\delta/h = 1.5$			
Recirculating region length, x_r/h	3.5 ± 0.03	3.1 ± 0.03	2.8 ± 0.03
Recirculating region length, x_r/c	1.2 ± 0.01	1.0 ± 0.01	1.4 ± 0.02
Characteristic frequency, St	NA	NA	NA
Centreline drag coeff., $\overline{C_{D_{\mathrm{cl}}}}$	$0.72^{+0.040}_{-0.047}$	$0.76^{+0.046}_{-0.048}$	$0.63^{+0.032}_{-0.025}$
Centreline drag coeff., $\overline{C^*_{D_{\mathrm{cl}}}}$	$1.35^{+0.074}_{-0.088}$	$1.42^{+0.085}_{-0.090}$	$1.17^{+0.059}_{-0.046}$
Turbulent, $\delta/h = 2.0$			
Recirculating region length, x_r/h	3.5 ± 0.03	3.1 ± 0.03	2.8 ± 0.03
Recirculating region length, x_r/c	1.2 ± 0.01	1.0 ± 0.01	1.4 ± 0.02
Characteristic frequency, St	NA	NA	NA
Centreline drag coeff., $\overline{C_{D_{\mathrm{cl}}}}$	$0.79^{+0.040}_{-0.037}$	$0.77^{+0.041}_{-0.040}$	$0.72^{+0.036}_{-0.016}$
Centreline drag coeff., $\overline{C^*_{D_{\mathrm{cl}}}}$	$1.59^{+0.080}_{-0.074}$	$1.55^{+0.082}_{-0.080}$	$1.44^{+0.072}_{-0.032}$
Turbulent, $\delta/h = 3.5$			
Recirculating region length, x_r/h	3.5 ± 0.03	3.1 ± 0.03	2.8 ± 0.03
Recirculating region length, x_r/c	1.2 ± 0.01	1.0 ± 0.01	1.4 ± 0.02
Characteristic frequency, St	NA	NA	NA
Centreline drag coeff., $\overline{C_{D_{\mathrm{cl}}}}$	$0.55^{+0.028}_{-0.011}$	$0.60^{+0.030}_{-0.010}$	$0.54^{+0.027}_{-0.010}$
Centreline drag coeff., $\overline{C^*_{D_{\mathrm{cl}}}}$	$1.28^{+0.064}_{-0.026}$	$1.41^{+0.071}_{-0.023}$	$1.28^{+0.064}_{-0.023}$

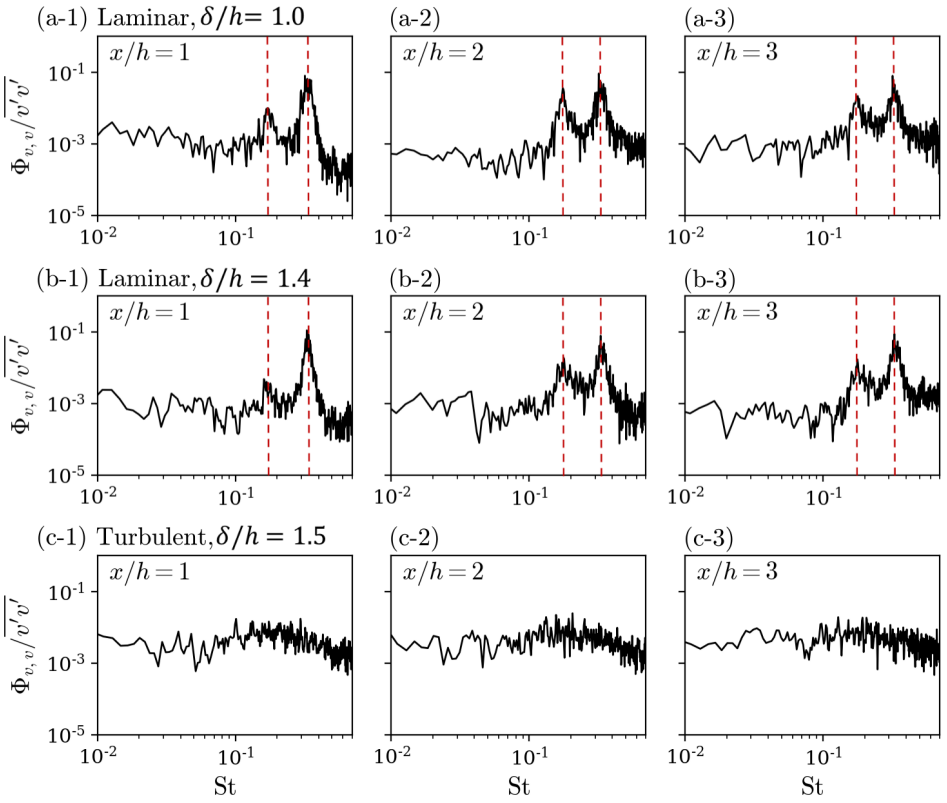

Figure 6.8: Power spectral of wall-normal velocity fluctuations for the sessile model under laminar incoming flow with $\delta/h = 1.0$ (row 1) and 1.4 (row 2), and turbulent incoming flow with $\delta/h = 1.5$ (row 3). The sampling locations are within the free shear layer at $x/h = 1$ (column 1), 2 (column 2), and 3 (column 3).

fh/U_∞ for the sessile and runback models, respectively. The hemisphere model exhibits similar trends in power spectra as the runback model, and thus is omitted here. The spectra are sampled in the separated shear layer at streamwise locations of $x/h \approx 1$, 2, and 3. The power spectra for both submergences $\delta/h = 1.0$ (row 1) and 1.4 (row 2) of laminar boundary layers are presented. The power spectra of all three submergences of turbulent boundary layers are similar, and for brevity, only the results of $\delta/h = 1.5$ (row 3) are presented. In laminar boundary layers, at the submergence of $\delta/h = 1.0$, at $x/h = 1$,

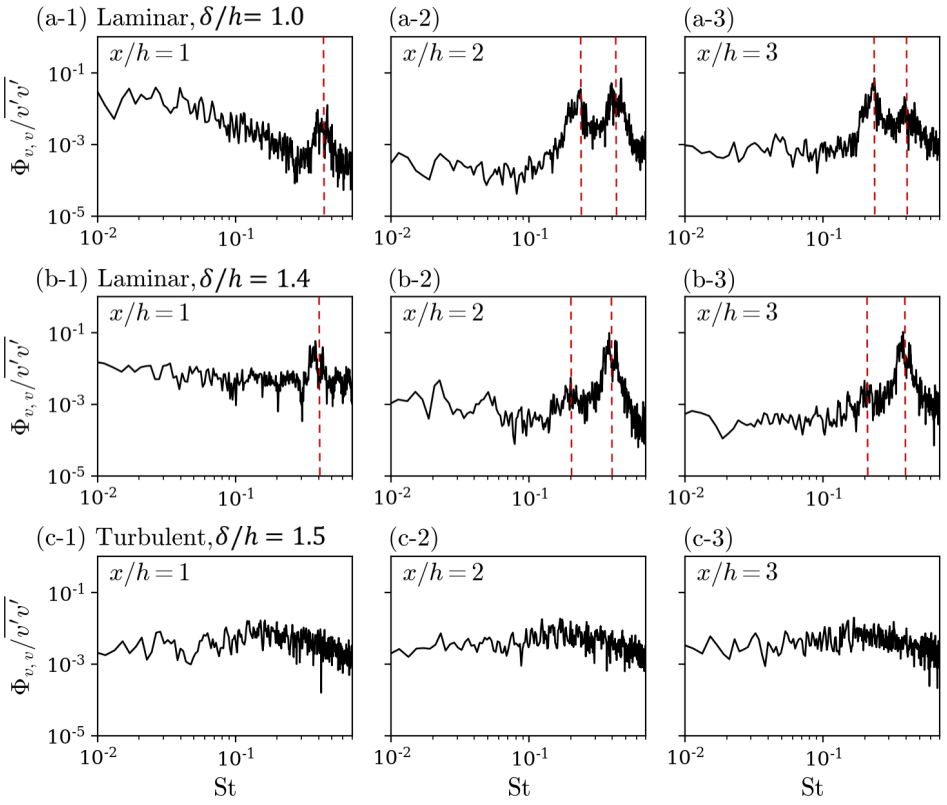

Figure 6.9: Power spectral of wall-normal velocity fluctuations for the runback model under laminar incoming flow with $\delta/h = 1.0$ (row 1) and 1.4 (row 2), and turbulent incoming flow with $\delta/h = 1.5$ (row 3). The sampling locations are within the free shear layer at $x/h = 1$ (column 1), 2 (column 2), and 3 (column 3).

primary peaks centred around $\mathrm{St}_1 = 0.34$ and 0.42 are observed for the sessile and runback models, respectively (Fig. 6.8(a-1) and 6.9(a-1)). As the flow develops downstream, a secondary peak is observed at the subharmonic frequency $\mathrm{St}_{1/2}$ for both models, which is attributed to merging of the arch vortices (Fig. 6.8(a-2) and 6.9(a-2)), as discussed in Sect. 5.2.

Increasing the relative submergence from $\delta/h = 1.0$ to 1.4 leads to a slight decrease in shedding frequency (see Table 6.1). A larger submergence in a laminar boundary layer

significantly suppresses the merging of shear layer vortices. While the sessile model still exhibit a secondary peak with a relatively low energy content (Figs 6.8(b-2)), subharmonic peak is hardly observed for the runback model(Fig. 6.9(b-2)).

In turbulent boundary layers (Figs. 6.8 and 6.9, row 3), the shedding of shear layer vortices is completely suppressed by the incoming flow turbulence. This results in the absence of strong base vortices, and consequently the reduction in central upwash (Figs. 6.5 and 6.6) and change in recirculating region topology (Figs. 6.5 and 6.6).

As discussed in Ch. 5, flow perturbations induced by the presence of droplet models are the strongest around the model symmetry plane directly downstream of the model. Thus, centreline drag coefficient, formulated as $\overline{C_{D_{\mathrm{cl}}}} = \overline{F_{D_{\mathrm{cl}}}}/(\rho U_\infty^2 h/2)$, with $\overline{F_{D_{\mathrm{cl}}}}$ reflecting the portion of drag induced by the thin slice of model around the symmetry plane, can be used as an indicator to evaluate the influence of relative submergence and boundary layer regime on the aerodynamic drag of a specific geometry [185, 159, 27]. Although it is not representative of the overall drag on a 3D model, trends can be estimated for a given model. By invoking the conservation of momentum on a control volume as illustrated in

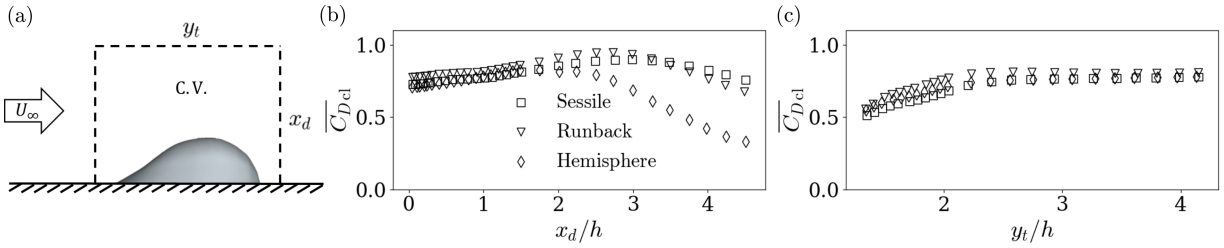

Figure 6.10: (a) Schematic of control volume setup for calculating centreline drag coefficient ($\overline{C_{D_{\mathrm{cl}}}}$). As an example, change in $\overline{C_{D_{\mathrm{cl}}}}$ with control volume (b) downstream and (c) top boundary locations is illustrated for laminar incoming flow with $\delta/h = 1.0$.

Fig. 6.10(a), $\overline{F_{D_{\mathrm{cl}}}}$ can be determined as,

$$\begin{aligned}\overline{F_{D_{\mathrm{cl}}}} = & \underbrace{\rho\left[\int_0^{y_t}(\overline{u}^2\mid_{x=x_u}-\overline{u}^2\mid_{x=x_d})\,\mathrm{d}y-\int_{x_u}^{x_d}\overline{uv}\mid_{y=y_t}\,\mathrm{d}x\right]}_{\text{① Mean momentum flux}} \\ & + \underbrace{\rho\left[\int_0^{y_t}(\overline{u'u'}\mid_{x=x_u}-\overline{u'u'}\mid_{x=x_d})\,\mathrm{d}y-\int_{x_u}^{x_d}\overline{u'v'}\mid_{y=y_t}\,\mathrm{d}x\right]}_{\text{② Contribution of Reynolds stresses}} \\ & + \underbrace{\int_0^{y_t}(\overline{p}\mid_{x=x_u}-\overline{p}\mid_{x=x_d})\,\mathrm{d}y}_{\text{③ Pressure deficit}}.\end{aligned} \tag{6.13}$$

Load estimation based on 2D-2C PIV measurements intrinsically assumes that out-of-plane velocity components and gradients are negligible. To minimize the propagation of bias and random errors originating from velocity measurements and pressure reconstruction into the estimation of $\overline{C_{D_{\mathrm{cl}}}}$, the placement of control volume boundaries is chosen by systematically varying the boundary locations, as devised in [118]. As an exemplar, the effect of control volume boundary locations is illustrated by the flow field over the runback model submerged in the laminar boundary layer of $\delta/h = 1.0$. Fig. 6.10(b) shows the estimated values of $\overline{C_{D_{\mathrm{cl}}}}$ with varying downstream boundary locations x_d, with the upstream boundary fixed at $0.1h$ upstream of the model leading edge, and the top boundary at $3h$ from the substrate. The range of $0.5 < x_d/h < 1$ is used to estimate $< \overline{C_{D_{\mathrm{cl}}}} >$ in laminar boundary layers, where the values are insensitive to the change in x_d. With similar method, $0.5 < x_d/h < 0.8$ is chosen for cases in turbulent boundary layers. Closer to the model surface, drag estimation is susceptible to increased errors in PIV velocity measurements due to model surface reflection and the averaging within the interrogation window. Downstream of $x_d/h \approx 1.5$, the decrease in computed $\overline{C_{D_{\mathrm{cl}}}}$ values is most likely due to the omission of $\overline{u'w'}$ in the formulation of Eq. 6.13 and the underestimation in streamwise

velocity deficit (see Fig. 6.7, row 1), since the out-of-plane motions are no longer negligible with the amplifying shear layer instabilities (see Fig. 5.3). For drag estimations based on stereo-PIV measurements, it is favourable to place the downstream boundary of the control volume in the streamwise range where pressure deficit is relaxed (Sect. 6.1). However, to satisfy the 2D assumption required for drag estimation with 2D-2C PIV measurements, the construction of the control volume should be prioritized to bound minimum regions of 3D flow phenomena [118]. Despite that the pressure reconstruction based on 2D-2C PIV underestimates the pressure deficit up to around 50% in the streamwise range of $x/h \lessapprox 1.5$, the contribution of the pressure deficit to the centreline drag $\overline{F_{D_{\mathrm{cl}}}}$ is one order of magnitude lower than the streamwise velocity deficit in the model symmetry plane (see Fig. 6.7, rows 1 and 3). Thus, for $x_d \lessapprox 1.5$, the underestimation in pressure deficit based on 2D-2C PIV measurements can lead to an underestimation of up to 5% in $\overline{F_{D_{\mathrm{cl}}}}$.

Theoretically, the placement of y_t should not affect the drag estimation significantly. In practice, as discussed earlier, the misalignment between the laser sheet and the model symmetry plane introduces on the order of the laser sheet thickness can lead to a bias error in wall-normal velocity measurements up to around 30% within the streamwise range of $x \lessapprox 2$, while the deviation in streamwise velocity is negligible. Fig. 6.10(c) shows $\overline{C_{D_{\mathrm{cl}}}}$ values with varying top boundary locations y_t, with the upstream boundary fixed at $0.1h$ upstream of the model leading edge, and the downstream boundary fixed at $x_d/h = 0.8$. The influence of laser sheet misalignment diminishes at around $2.5h$ from the wall, and $y_t/h = 3$ is used to estimate $\overline{C_{D_{\mathrm{cl}}}}$.

Fig 6.11(a) shows the influence of relative submergence and boundary layer regime on the estimated $\overline{C_{D_{\mathrm{cl}}}}$ values of models investigated (also reported in Table 6.1). The lower bound of the error bars is estimated by the minimum $\overline{C_{D_{\mathrm{cl}}}}$ value within the selected x_d range. Between the maximum $\overline{C_{D_{\mathrm{cl}}}}$ value within the selected x_d range and the value of

105% $< \overline{C_{D_{\mathrm{cl}}}} >$, the upper bound of the error bars is estimated by the larger of the two. Specifically, for the hemisphere model, $\overline{C_{D_{\mathrm{cl}}}}$ values for both laminar cases are around 0.75. A similar value is found by extrapolating the curve given in [159] (see their Fig. 6) to the Reynolds number under investigation in the present study. For the laminar case of $\delta/h = 1$, the runback model exhibits the highest $\overline{C_{D_{\mathrm{cl}}}}$, seemingly contradicting the drag estimation based on stereo-PIV measurements, which suggests the runback model demonstrate a similar overall drag coefficient $\overline{C_D}$ and a slightly lower drag $\overline{F_D}$ than the sessile model (see Sect. 6.1). However, it should be noted that $\overline{C_{D_{\mathrm{cl}}}}$ only considers the drag induced by the thin slice of model around the model symmetry plane, while $\overline{C_D}$ reflects the averaged drag across the entire model span. As discussed in Ch. 5, the runback model induces stronger central upwash (see Fig. 5.1) and shear layer breathing (see Fig. 5.11) than the sessile model does. The higher $\overline{C_{D_{\mathrm{cl}}}}$ of the runback model is likely attributed to these stronger flow disturbances induced around the model symmetry plane. On the other hand, the sessile model has a larger frontal area and induces velocity deficit in a wider

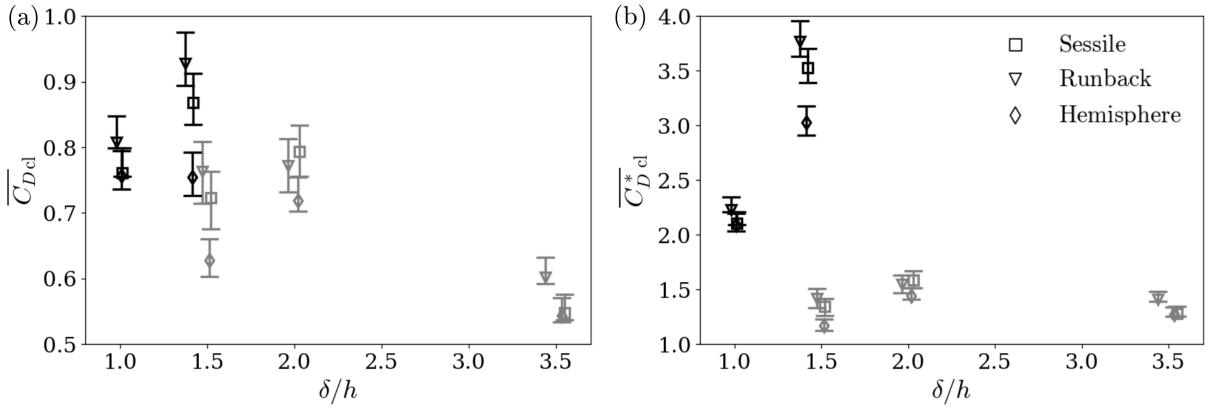

Figure 6.11: Centreline drag coefficients based on (a) freestream velocity ($\overline{C_{D_{\mathrm{cl}}}}$) and (b) bulk velocity $U_b = \int_0^h \overline{u_{BL}}\,\mathrm{d}y/h$ ($\overline{C^*_{D_{\mathrm{cl}}}}$) versus relative submergences δ/h. Black: laminar incoming flows. Grey: turbulent incoming flows.

spanwise range (Fig. 5.5), resulting a higher overall drag than the runback model.

For a given model geometry, $\overline{C_{D_{\mathrm{cl}}}}$ decreases with increasing boundary layer turbulence, which is likely attributed to the delay in flow separation from the model surfaces (see Figs. 6.5 and 6.6, column 1). A similar trend has been reported for spheres submerged in freestreams of varied turbulence intensities [126]. This indicates that laminar flow can be more effective in surface cleaning applications. To account for the effective flow rate averaged over the model height with varied boundary layer velocity profiles, bulk velocity $U_b = \int_0^h \overline{u_{BL}}\,\mathrm{d}y/h$ is used to define a modified centreline drag coefficient, formulated as $\overline{C^*_{D_{\mathrm{cl}}}} = \overline{F_{D_{\mathrm{cl}}}}/(\rho U_b^2 h/2)$. As shown by Fig 6.11(b), for models in turbulent boundary layers of $1.5 \leq \delta/h \leq 3.5$, the influence of relative submergence on $\overline{C^*_{D_{\mathrm{cl}}}}$ is negligible, which is not surprising given the higher near-wall momentum in turbulent boundary layers.

6.3 Summary

This chapter presents the estimation of aerodynamic drag on droplet-inspired obstacles based on flow field measurements using stereo-PIV. The models are submerged in a laminar boundary layer with a relative submergence of $\delta/h = 1$ and Reynolds number of $\mathrm{Re}_h \approx 2070$, simulating the critical droplet depinning conditions. The drag coefficient estimated for the baseline hemisphere model agrees reasonably well with previous studies. The drag coefficients of the two droplet models are approximately 10% lower than the drag coefficient of the hemisphere. While the sessile and runback models exhibit no discernible difference in drag coefficients, the runback model shows a slight drag reduction as compared to the sessile model, which is mainly attributed to its smaller frontal area.

The impacts of relative submergence and boundary layer regime on flow development and drag coefficient are estimated based on flow field measurements at model symmetry

planes. In laminar boundary layers, increase in relative submergence significantly changes the recirculating region topology. In turbulent boundary layer, however, flow development is insensitive to relative submergence within the range of $1.5 \lessapprox \delta/h \lessapprox 3.5$. Increase in incoming flow turbulence intensity shortens the recirculating region and suppresses the shedding of coherent structures. For a given model geometry, centreline drag coefficient is used as an indicator of the change in overall drag. Notable reduction in centreline drag coefficient is observed with increasing turbulence intensity, indicating laminar flows can be more effective for surface cleaning applications.

Chapter 7

Droplet depinning under the impact of wall-bounded shear flows

This chapter discusses droplet response to wall-bounded shear flows. Wall-bounded shear flows formed by a laminar flat plate boundary layer ($\alpha = 0°$) and impinging jet flows of four orientation angles ($\alpha = 30°$, $45°$, $60°$, and $90°$) at eight wall locations are considered (see Table 3.6); the incoming flows ramp up with three accelerations, $\mathrm{d}U/\mathrm{d}t = 1.2$, 2.2, and 4.4 $\mathrm{m/s^2}$, which are measured within the freestream for the flat plate boundary layer case and at the jet exit for the impinging jet cases. Depinning criteria of droplets of volumes $V = 75$, 90, 105, and 120 μL are investigated by side-view imaging, as described in Sect. 3.3.

This chapter is divided into five sections. Sect. 7.1 introduces the post-processing procedures used in quantifying the key geometric parameters from side-view images. Sect. 7.2 presents the typical droplet response under accelerating flow and the critical depinning conditions identified for each droplet volume, acceleration, and flow configuration. Sect. 7.3

performs a dimensional analysis for droplet depinning and identifies relationships between dimensionless groups dominating the process. Sect. 7.4 estimates the typical value of three-dimensional contact angle distribution for wind-forced droplets at depinning based on the side-view images of water droplets and the drag coefficients estimated for droplet-inspired solid models (see Ch. 6). Sect. 7.5 summarizes the main findings of this chapter.

7.1 Droplet image post-processing

Typical images of a droplet acquired in the experiments described in Sect. 3.3 are shown in Fig. 7.1. The origin of the coordinate system is at the upstream edge of the droplet in the sessile configuration, with the x coordinate pointing downstream and y oriented in the wall normal direction. The position of the upstream and downstream extent of the droplet are indicated by x_u and x_d, respectively. Characteristic geometric parameters directly measurable from droplet side-view images are droplet height (h), contact length (L_b), and upstream (receding) and downstream (advancing) contact angles (θ_u and θ_d, respectively). These geometric parameters can be approximately related to the droplet volume (V) and projected frontal area (A) by [176],

$$A = h^2 \frac{\overline{\theta_c} - \sin(\overline{\theta_c})\cos(\overline{\theta_c})}{(1-\cos(\overline{\theta_c}))^2}, \tag{7.1a}$$

$$V = \frac{\pi h^3 (2+\cos\overline{\theta_c})}{6\sin^2(\overline{\theta_c}/2)}, \tag{7.1b}$$

where $\overline{\theta_c} = (\theta_u + \theta_d)/2$. These relations approximate the droplet by a spherical cap with contact angle $\overline{\theta_c}$.

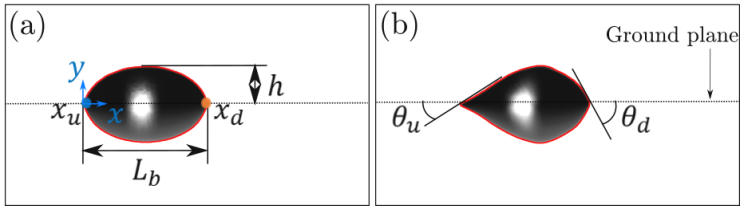

Figure 7.1: Side-view geometry of a 120 μL droplet (a) in the sessile state and (b) prior to depinning, with geometric parameters annotated in the images. Note that the droplet image is reflected by the ground plane.

The quantitative assessment of droplet response to incoming shear flows requires extraction of higher resolution spatial data from the images. To this end, sub-pixel polynomial fitting (SPPF) [30] is used to quantify the geometric parameters from the raw droplet images. The SPPF method first detects the droplet boundary with pixel resolution using Canny edge detection with Otsu's threshold [135]; the droplet boundary is separated from the Canny edge map using a marching squares contour finding algorithm [30]. Then, sigmoid functions [74] are fitted to the pixel intensity around each pixel on the detected boundary, and the locations of the refined droplet edge with sub-pixel resolution are found at the saddle points of the sigmoid. Locations of the contact points are found at the intersections between the droplet edge with its reflection (see Fig. 7.1(a)). Contact angles are calculated from the local slope of a fitted second-order polynomial around the contact points; the optimum number of pixels used in curve fitting is found by systematically increasing the number of pixels until variation in calculated contact angles is less than 0.1°. For contact angles in the range of $10° \leq \theta_c \leq 160°$, as in the present study, the uncertainty associated with contact angle measurement using the SPPF method is within 1° [30]. Table 7.1 summarizes the sessile state statistics of the investigated droplets and suggests good consistency in droplet initial geometries, with variability in sessile contact angle estimates of a given droplet volume confined within 3.5°.

Table 7.1: Initial droplet geometry.

Droplet volume $V[\mu\text{L}]$	Initial contact length L_{b_0} [mm]	Initial height h_0 [mm]	Initial contact angle θ_0 [°]
75	7.7 ± 0.1	2.5 ± 0.1	82.0 ± 2.5
90	8.3 ± 0.2	2.6 ± 0.1	81.2 ± 3.2
105	8.7 ± 0.2	2.7 ± 0.1	83.0 ± 2.9
120	9.1 ± 0.2	2.8 ± 0.1	83.5 ± 3.4

7.2 Critical droplet depinning conditions

Selecting a droplet of $V = 120\,\mu L$ subjected to a wall jet formed at $x^* = 70\,\text{mm}$ downstream of the stagnation point of a 45° impinging jet at the acceleration of $\mathrm{d}U_j/\mathrm{d}t = 4.4\text{m/s}$ as an example, Fig. 7.2 shows the typical response of a droplet (Fig. 7.2 (b-1) to (b-6)) under the influence of an accelerating shear flow (Fig. 7.2 (a)). As the incoming flow speed increases from zero, the droplet deforms due to aerodynamic loading (t_0 to t_2), achieving a new configuration in which the external loading is balanced by the increase in adhesion. When the aerodynamic loading from the shear flow overcomes capillary forces, the droplet depins from the initial location (t_2) and sheds along the surface (t_3 to t_5).

Fig. 7.3 depicts variation of droplet geometry parameters as a function of jet exit speed for the case presented in Fig. 7.2. Fig. 7.3(a) shows the change of droplet contact point locations with increasing jet exit velocity. The velocity of the droplet along the surface, v_{drop}, can be estimated from the average of the time derivatives computed from the raw data of the contact point locations $\mathrm{d}x_u/\mathrm{d}t$ and $\mathrm{d}x_d/\mathrm{d}t$, as shown in Fig. 7.3(b). Droplet height and contact length can also be calculated from the identified droplet edge, see Fig. 7.3(c). Contact angle hysteresis, $\text{CAH} = [\cos(\theta_u) - \cos(\theta_d)]$, computed from the measured contact angles is shown in Fig. 7.3(d). Trend lines of contact point velocities,

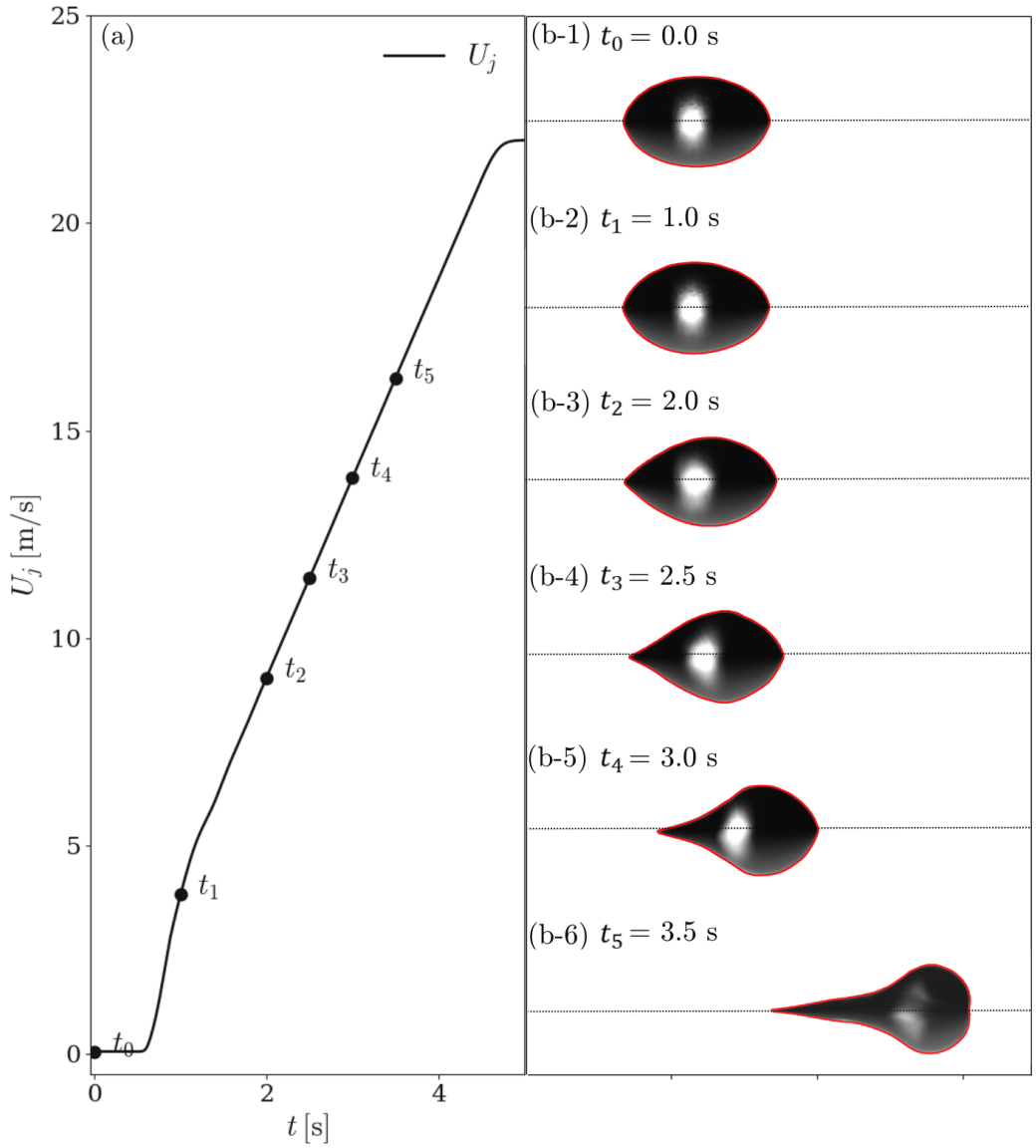

Figure 7.2: (a) Velocity ramp-up profile at jet exit. (b-1) to (b-6) Typical droplet deformation and runback under accelerating shear flows; the motion of a 120 μL droplet under the impact of shear flow formed at $x^* = 70$ mm downstream of the stagnation point of a $\alpha = 45°$ accelerating impinging jet at $\mathrm{d}U_j/\mathrm{d}t = 4.4\,\mathrm{m/s^2}$ is shown as exemplar.

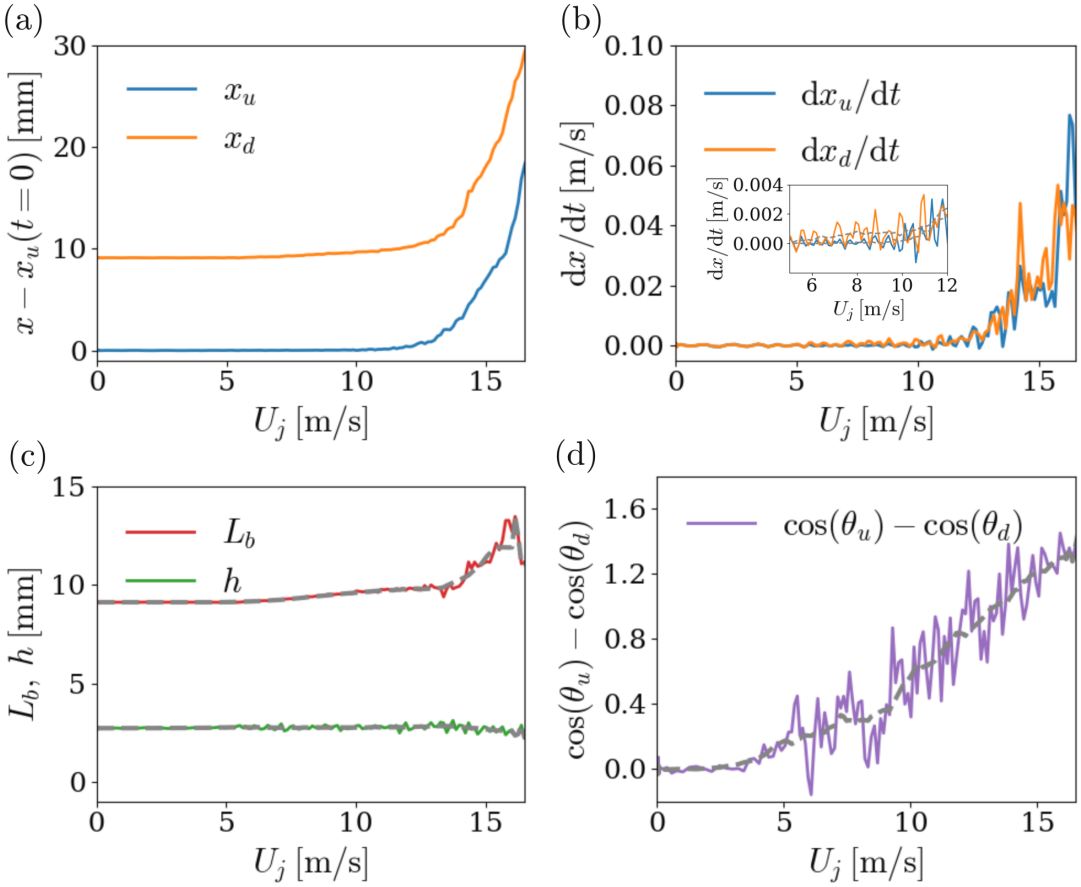

Figure 7.3: Typical (a) displacement and (b) velocity of droplet contact points (blue and orange lines: upstream and downstream contact points, respectively; inset: zoom-in view of contact point velocity in the jet exit velocity range of $U_j \leq 12\,\mathrm{m/s}$), (c) droplet contact length (red line) and height (green line), and (d) contact angle hysteresis (purple line) with increasing jet exit velocity of a 120 μL droplet under the impact of shear flow formed at $x^* = 70\,\mathrm{mm}$ downstream of the stagnation point of a $\alpha = 45°$ accelerating impinging jet at $\mathrm{d}U_j/\mathrm{d}t = 4.4\,\mathrm{m/s^2}$ is shown as exemplar. Trend lines (gray dashed lines) are acquired by computing the moving average with a window size corresponding to $\Delta t = 0.25\,\mathrm{s}$.

droplet height, contact length, and contact angle hysteresis versus the instantaneous jet exit velocity are acquired by computing the moving average with a window size corresponding to $\Delta t = 0.25\,\mathrm{s}$ for statistical analysis.

Berejnov and Thorne [15] identified three transitional events exhibited by a droplet under increasing external forcing: (i) depinning of the downstream portion of the contact line, (ii) depinning of the upstream portion of the contact line, and (iii) depinning of the entire contact line which gives rise to translational motion of the droplet along the surface. At low jet speed of $0 \lessapprox U_j < 5$ m/s, both contact points remain pinned (Fig. 7.3(b)). The slight undulations observed in contact point velocities within this jet speed range are due to uncertainty in the contact point position (Fig. 7.3(a)) which is amplified when the numerical derivative is computed. Increasing the jet speed to the range of $5 \lessapprox U_j < 9$ m/s leads to the onset of the first transitional event, where the downstream contact point first depins while the upstream contact point remains pinned. This leads to the increase in droplet contact length (Fig. 7.3(c)). Fluctuations of contact angle hysteresis around the trend line (Fig. 7.3(d)) reflect the oscillations at the air-water interface as suggested by previous studies [11, 155]. At higher jet speed of $9 \lessapprox U_j \lessapprox 12$m/s, the upstream contact point depins, corresponding to the second transitional event. The alternate non-zero and zero contact point velocity fluctuations of increased amplitude (Fig. 7.3(b) inset) indicate the 'skip' motion of droplets as reported in previous studies [169, 80]. While contact length continues to increase, no discernible change is observed for droplet height (Fig. 7.3(c)). Further increasing the jet speed, both contact points are in continuous motion as the droplet sheds from the surface (Fig. 7.3(b)), corresponding to the third transitional event. Elongation in droplet contact length is more significant than in the first two transitional events, accompanied by a slight decrease in droplet height (Fig. 7.3(c)) and diminished fluctuations of contact angle hysteresis (Fig. 7.3(d)).

The time instant corresponding to droplet depinning is identified from the side-view droplet images when the pixel displacement of the upstream contact point exceeds a set threshold. The selection of the pixel threshold aims at minimizing the overall error in-

troduced by the thresholding procedure and is described in Appendix C. The pixel displacement thresholds used for each case are summarized in Table C.1. Critical velocities measured in the freestream $U_{\infty,\text{crit}}$ or at jet exit velocity $U_{j,\text{crit}}$ and around the droplet height when droplet depinning occurs are presented in Figs. 7.4 (a) and (b), respectively, for the droplet volumes, incoming flow angles, and flow accelerations investigated. The error bars represent the standard deviation over the fourteen trials for each case (see Sect. 3.3

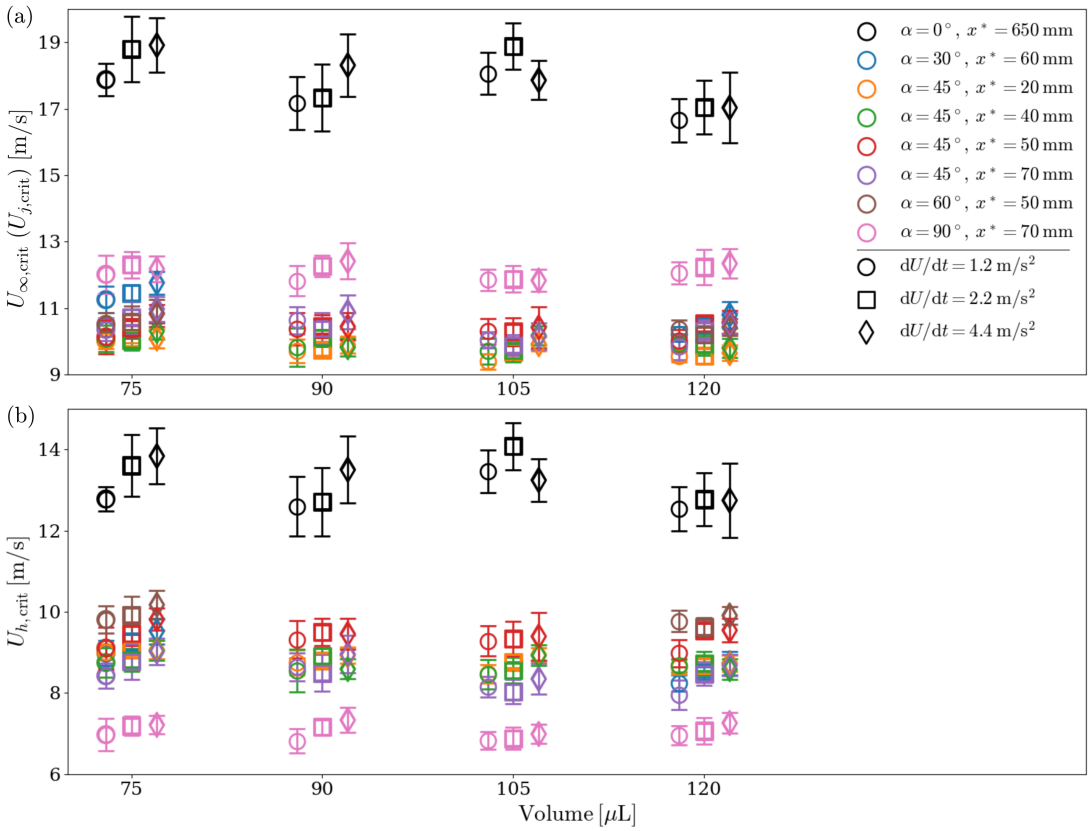

Figure 7.4: Critical droplet depinning velocities (a) measured in the freestream, U_∞, or at the jet exit, U_j, and (b) measured at droplet height, U_h as a function of droplet volume under background flow configurations listed in Table 3.6. Droplet initial locations x^* is the streamwise distance from the flow stagnation point, as characterized in Sects. 4.1.1 and 4.2.2 for flat plat boundary layer and impinging jets, respectively.

for detailed experimental setup). For all definitions of critical velocities, a slight, albeit statistically significant ($p < 0.05$ from paired Student's t-tests [48] between the smallest and largest volumes), decreasing trend with droplet volume is observed, which is aligned with the trend reported in previous studies [121, 153]. Similarly, for all flow configurations, the critical velocity increases slightly ($p < 0.05$ from paired Student's t-tests between the smallest and largest accelerations) with flow acceleration.

In the laminar flat plate boundary layer, the critical velocity measured at the droplet height $U_{h,\mathrm{crit}}$ is much lower than that measured in the freestream $U_{\infty,\mathrm{crit}}$ (Fig. 7.4 black markers). This is due to the high velocity gradient across the droplet height (see Sect. 4.1.2). In impinging jets, since the near-wall velocity profiles are fuller than that of the laminar boundary layer over the flat plate (see Fig. 4.16, column 4), $U_{h,\mathrm{crit}}$ can be approximated by the maximum streamwise velocity $u_{\max}$ of the local wall jet profile (see Fig. 4.3 for schematic). For droplets initially located within five jet slot widths from the impingement point ($x^* \lessapprox 5B$, with $B = 10$ mm for the current jet facility), $U_{h,\mathrm{crit}}$ and $U_{j,\mathrm{crit}}$ exhibit similar values (Figs. 7.4 orange, green, red, and brown markers). This is due to the re-oriented jet potential core within which the jet exit velocity is preserved, and thus the local maximum streamwise velocity $u_{\max}$ is similar to U_j (see Sect. 4.2.2). For droplets initially located beyond five slot widths from the stagnation point ($x^* > 5B$), the increase in difference between $U_{h,\mathrm{crit}}$ and $U_{j,\mathrm{crit}}$ (Figs. 7.4 blue, purple, and magenta markers) results from the faster streamwise decay in $u_{\max}$ observed in this streamwise range (see Fig. 4.6). To facilitate the discussion that follows, the near-wall flow parameters characterized at a steady freestream or jet exit velocity of $U = 10$ m/s at the absence of droplets are summarized in Table 7.2 for reference.

The effects of incoming flow orientation angle α and relative submergence δ^*/h on critical depinning velocity $U_{h,\mathrm{crit}}$ are illustrated by Fig. 7.5(a) and (b), respectively. In the

Table 7.2: Incoming flow conditions and boundary layer parameters characterized at a steady freestream or jet exit velocity of $U = 10$ m/s.

Flow angle α [°]	Initial location x^* [mm]	Boundary layer thickness δ [mm]	Displacement thickness δ^* [mm]	Initial contact angle θ_0 [°]
0	650	4.7	1.6	86.1 ± 2.7
30	60	3.4	0.45	84.4 ± 1.9
45	20	2.6	0.21	81.0 ± 1.5
45	40	2.2	0.34	80.8 ± 2.1
45	50	3.1	0.40	80.5 ± 1.4
45	70	4.2	0.47	85.9 ± 1.3
60	50	3.5	0.42	78.2 ± 2.1
90	70	3.2	0.28	81.8 ± 2.0

flow angle range of $30° \leq \alpha \leq 60°$, the mean depinning velocity is within the range of $8 \lessapprox U_{h,\text{crit}} \lessapprox 10$ m/s. The variation in depinning velocities in these test cases is mainly caused by the heterogeneities of the substrate surface, which leads to the variation in initial contact angles at different initial locations (see Table 7.2). Significantly higher depinning velocities of around $U_{h,\text{crit}} \approx 13$ m/s are found for droplets submerged in the flat plate boundary layer ($\alpha = 0°$), which is mainly due to the higher relative submergence of $\delta^*/h \approx 0.6$ as compared to $0.1 \lessapprox \delta^*/h \lessapprox 0.2$ in the impinging jets (see Fig. 7.5(b)). Lower depinning velocities of around $U_{h,\text{crit}} \approx 7$ m/s are found for droplets under the impact of the normal jet impingement ($\alpha = 90°$), regardless that the relative submergence is similar to those in the oblique jet impingements ($\alpha = 30°$, 45°, and 60°). Similar observations were made by Leung *et al.* [104]. In their experiment, a target plate with scattered millimeter-sized droplets ($h = 1 \sim 3$ mm) was exposed to an accelerating jet and the critical velocity was defined as the velocity when 50% of the droplets were displaced. A smaller critical velocity was found at higher jet orientation angles, upon which the authors presumed that some form of energy other than kinetic energy of the mean flow contributed to droplet

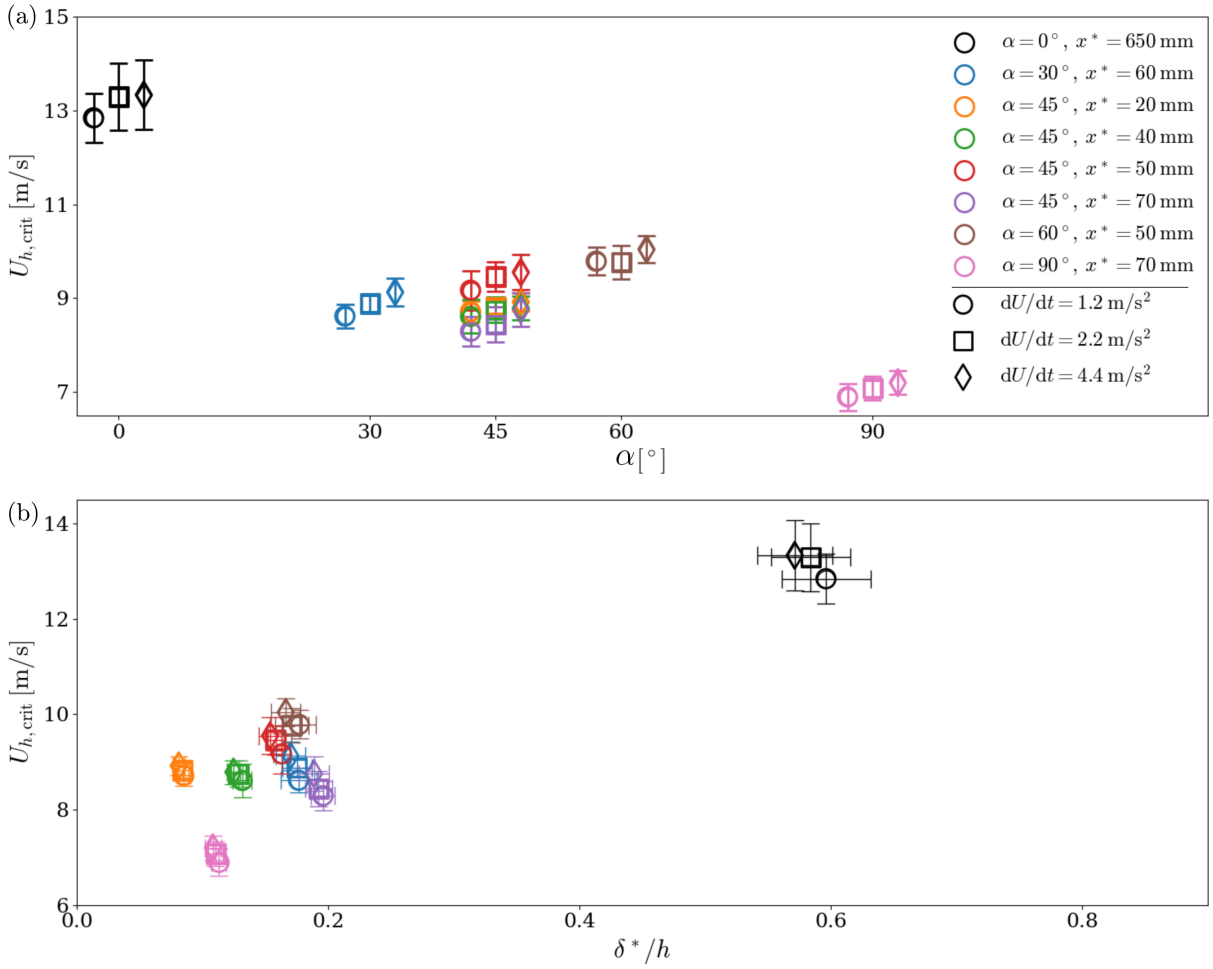

Figure 7.5: Critical droplet depinning velocities, $U_{h,\mathrm{crit}}$, averaged across all droplet volumes tested at each flow configuration and acceleration as a function of (a) background flow orientation angle α, and (b) relative submergence δ^*/h at depinning.

depinning.

Since aerodynamic drag and adhesion play competing roles in droplet depinning process and are both related to droplet geometries (see Eqs. 2.12 and 2.10), droplet deformations in response to the varied incoming flow configurations considered in the present study are investigated. The mean droplet side-view contour prior to depinning of each combina-

tion of droplet volume, initial droplet location, incoming flow angle, and flow acceleration is obtained by averaging over fourteen trials, with the uncertainties in the droplet geometries quantified by the standard deviations. As exemplars, Figs. 7.6(a) and (b) shows mean droplet side-view contours acquired under shear flows formed by the flat plat boundary layer and at $x^* = 70$ mm downstream of the stagnation point of the 45° impinging jet, respectively (see Appendix D for other cases); in each subplot, mean contours of all droplet volumes and flow accelerations tested are overlaid. When normalized with the respective initial height and contact length of each droplet tested, the mean contours at depinning under a given combination of incoming flow angle and initial droplet location show similarity across all droplet volumes. Figs. 7.7 shows the effects of flow acceleration and flow orientation angle α on droplet contact length, height, and contact angle hysteresis at depinning, respectively. At lower flow acceleration, droplets elongates in the streamwise direction and flattens in height. Higher flow acceleration slightly suppresses droplet elongation and preserves droplet height (Figs. 7.7 (a) and (b)). The influence of flow acceleration on con-

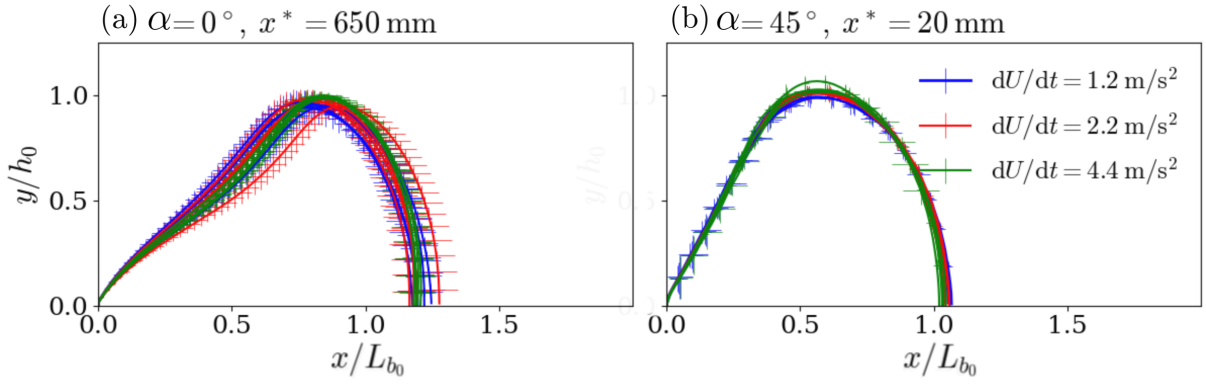

Figure 7.6: Mean side-view geometry of droplets prior to depinning under shear flows formed (a) by a flat plate boundary layer and (b) at $x^* = 20$ mm downstream of the stagnation point of impinging jets oriented at $\alpha = 45°$. Lengths in horizontal and vertical directions are normalized by initial droplet contact length and height, respectively.

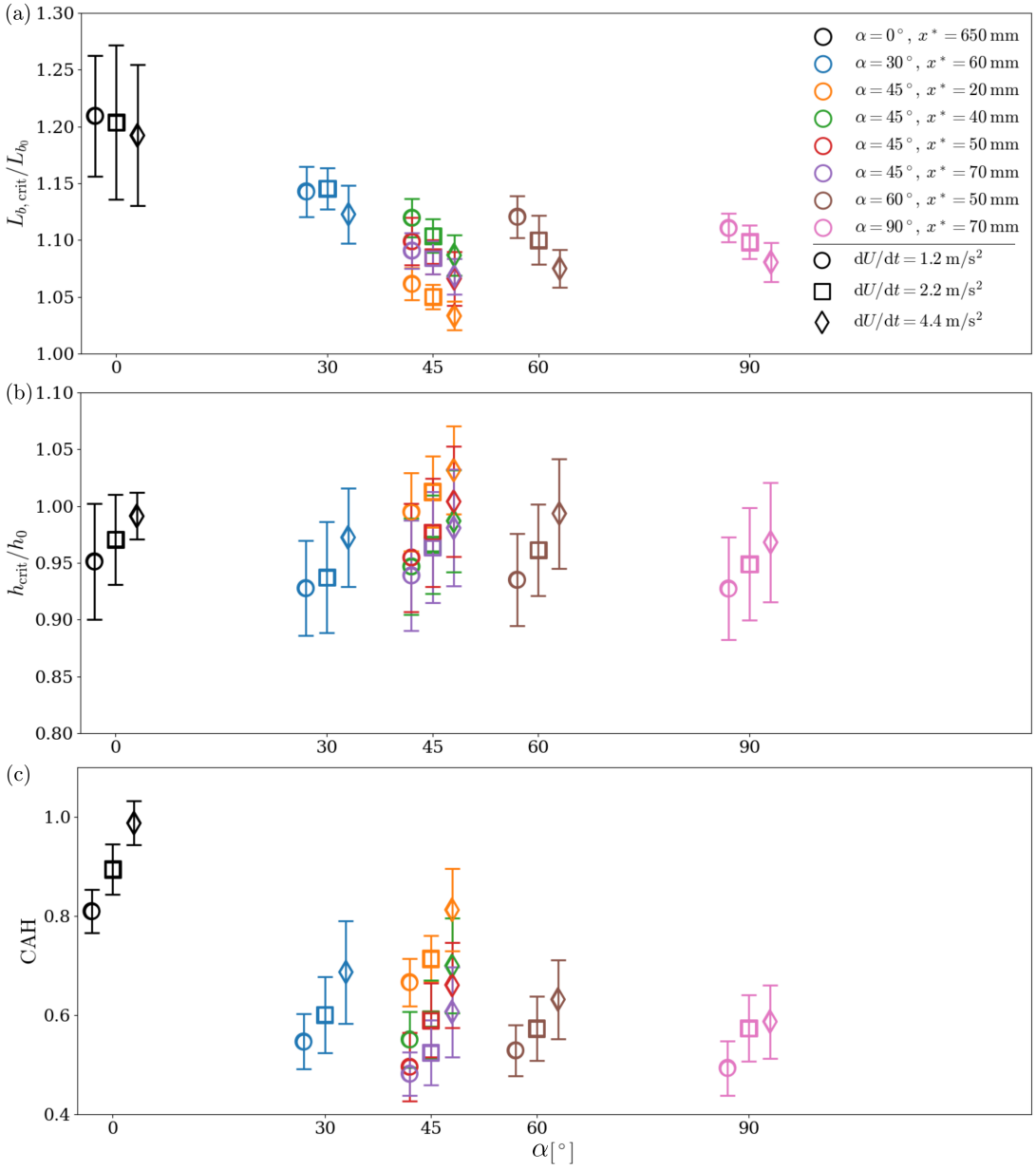

Figure 7.7: Droplet (a) contact length $L_{b,\mathrm{crit}}$, (b) height h, and (c) contact angle hysteresis CAH at depinning, averaged across all droplet volumes tested at each flow configuration and acceleration as a function of background flow orientation angle α.

tact angle hysteresis is more notable than on contact length and droplet height. Increase in flow acceleration significantly increase the contact angle hysteresis prior to depinning (Fig. 7.7 (c)), and thus leads to the increase in critical depinning velocity (Fig. 7.4). The impact of flow orientation angle α is more notable on droplet contact length and contact angle hysteresis than on height prior to depinning. For droplets in impinging jets, droplet contact length and contact angle hysteresis are relatively insensitive to α, confirmed by Student's t-tests [48] ($p > 0.05$ between each combination of jet angles in the range of $30° \leq \alpha \leq 90°$). In contrast, droplets submerged in the flat plate boundary layer elongate more in the streamwise direction and exhibit higher contact angle hysteresis ($p < 0.05$ between $\alpha = 0°$ and $30° \leq \alpha \leq 90°$), which increase adhesion. They also exhibit a more concave windward geometry (Fig. 7.6(a)), which is likely due to the streamwise velocity gradients over the droplet height (see Fig. 4.2(d)) as compared to those formed by impinging jets (see Fig. 4.16(d)); this windward concavity may also lead to a more aerodynamic geometry, as discussed in Ch. 5. Both factors contribute to the higher critical velocities demonstrated by droplets submerged in the laminar flat plate boundary layer.

7.3 Dimensional analysis of critical depinning conditions

As discussed in Sect. 7.2, critical velocity $U_{h,\text{crit}}$ and droplet side-view geometries at depinning, such as droplet height h, contact length L_b, and contact angle hysteresis CAH, are largely influenced by incoming flow orientation angle α and relative submergence δ^*/h (Figs. 7.4 and 7.7). Dimensional analysis of the observed correlations is performed in this section to achieve comparative measures with depinning conditions reported in previous

studies.

The depinning process is governed by the force balance between the driving and the resisting forces. Fig. 7.8 shows the force diagram at the critical depinning condition of a wind-forced droplets. The driving force for droplet depinning is the aerodynamic loading F_D, which consists of the pressure drag and the skin friction at the air-water interface; the two forces resisting the onset of droplet motion are the adhesion F_{adh} due to contact angle hysteresis, and the viscous force F_μ resulting from droplet elongation.

Adhesion is proportional to the contact length L_b and contact angle hysteresis CAH,

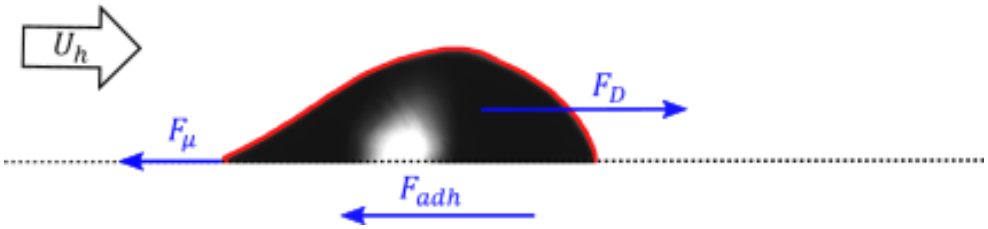

Figure 7.8: Force diagram of a droplet prior to depinning. F_D: aerodynamic loading; F_{adh}: adhesion as a result of contact angle hysteresis; F_μ: viscous force in the propagating water droplet.

and thus the order of magnitude can be estimated by $F_{\text{adh}} \propto \gamma L_b(\cos\theta_u - \cos\theta_d)$, with γ being the surface tension of water [43, 121, 153]. The viscous force F_μ due to moving contact line can be estimated by $F_\mu \approx \mu_L v_{\text{drop}} L_b^2/h$ [176], where μ_L is the dynamic viscosity of water, and v_{drop} is the velocity of the droplet center of mass, which is approximately the speed of the downstream contact point, which is below 10^{-3} m/s, as shown by Fig. 7.3(b). With $h \sim L_b \sim \mathcal{O}(10^{-3})$ [m], $\gamma \sim \mathcal{O}(10^{-1})$ [N/m], $\mu_L \sim \mathcal{O}(10^{-3})$ [Pa $\cdot$ s], CAH $\sim \mathcal{O}(10^{-1})$, and $v_{\text{drop}} \sim \mathcal{O}(10^{-3})$ [m/s], F_μ is four order of magnitudes smaller than F_{adh} and can thus be neglected for the present study. Further, the contribution of droplet center of mass acceleration to the force balance at droplet depinning is also four to five order of magnitudes smaller than F_D. As treated in [121], the force balance at droplet depinning

is simplified to

$$F_D = F_{\text{adh}}. \tag{7.2}$$

The primitive variables in Eq. 7.2 are functions of

$$F_D = f_1(\rho, \mu, U_h, \delta^*, h, \psi(l), \theta(l)), \tag{7.3a}$$

$$F_{\text{adh}} = f_2(\gamma, \psi(l), \theta(l)), \tag{7.3b}$$

where δ^* is the displacement thickness of the near-wall velocity profile, which relates to the velocity distribution over the droplet height; $\psi(l)$ and $\theta(l)$ are 3D contact line shape and contact angle distribution along the contact line, respectively (see Fig. 2.10). With side-view droplet geometries measured using 2D droplet imaging, $\theta(l)$ is crudely approximated by the upstream and downstream contact angles, θ_u and θ_d, respectively, and $\psi(l)$ is reduced to the contact length L_b. It should be noted that θ_u and θ_d are dimensionless parameters which do not contribute to the number of primary dimensions. Combining Eqs. 7.2 and 7.3, it can be shown that the critical depinning velocity is a function of several variables,

$$U_h = f(\rho, \mu, \gamma, \delta^*, h, L_b, \theta_u, \theta_d). \tag{7.4}$$

Using ρ, γ, and h as repeating variables, this dimensional relation can be reduced to the following six dimensionless parameters,

$$\Pi_1 = \frac{\rho U_h^2 h}{\gamma}, \tag{7.5a}$$

$$\Pi_2 = \frac{(\rho h \gamma)^{1/2}}{\mu}, \tag{7.5b}$$

$$\Pi_3 = \frac{h}{L_b}, \tag{7.5c}$$

$$\Pi_4 = \frac{\theta_u + \theta_d}{2}, \tag{7.5d}$$

$$\Pi_5 = \cos(\theta_u) - \cos(\theta_d), \tag{7.5e}$$

$$\Pi_6 = \frac{\delta^*}{h}. \tag{7.5f}$$

Π_1 (Eq. 7.5(a)) is the dimensionless depinning parameter, which corresponds to the Weber number based on droplet height We_h. The group of fluid properties and droplet geometry in Π_2 (Eq. 7.5(b)) is equivalent to $\mathrm{Re}_h/\sqrt{\mathrm{We}_h}$, or the square root of modified Laplace number $\sqrt{\mathrm{La}}$. Π_3 (Eq. 7.5(c)) is the aspect ratio AR of droplet at depinning. Rearranging θ_u and θ_d result in Π_4 (Eq. 7.5(d)) and Π_5 (Eq. 7.5(e)). The former is the mean contact angle $\overline{\theta_c}$ at depinning, which can be used to approximately relate droplet projection geometry to droplet volume and frontal area (Eq. 7.1); the latter is the contact angle hysteresis CAH which directly relates to adhesion, as identified at the beginning of this chapter. Π_6 (Eq. 7.5(f)) corresponds to the relative submergence of droplet height with respect to the displacement thickness of the incoming shear flow. Droplet depinning condition can thus be described by the following dimensionless relation

$$\mathrm{We}_h = \mathcal{F}(\sqrt{\mathrm{La}}, AR, \overline{\theta_c}, \mathrm{CAH}, \delta^*/h). \tag{7.6}$$

Overall, under the influence of the laminar flat plate boundary layer of the present study, droplets depin within a Weber number range of $7 \leq \mathrm{We}_h \leq 8$, which is comparable to 7.9 reported by White and Schmucker [201] for water droplets on aluminium surface submerged in a comparable incoming flow. For droplets in impinging jets, however, notably lower values of $2 \leq \mathrm{We}_h \leq 4$ are observed. To consider a broader range of key dimensionless parameters in Eq. 7.6, values of these parameters reported by previous studies are summarized in Table 7.3. Critical Weber numbers (Π_1) versus dimensionless parameters Π_2 to Π_6 measured at droplet depinning are presented in Figs. 7.9 to 7.13, respectively. The results of the present study are complemented by the data obtained for water droplets on substrates of varied wettabilities reported in literature (see Table 7.3).

Figs. 7.9 and 7.10 show the critical Weber number We_h versus the square-root of

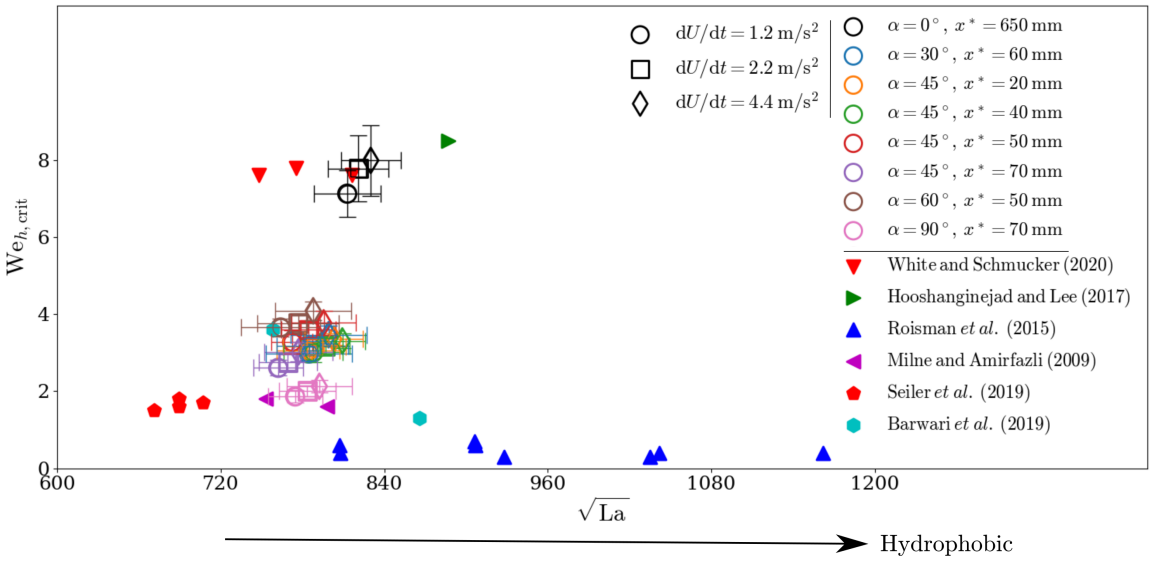

Figure 7.9: Critical Weber number based on droplet height $\mathrm{We}_{h,\mathrm{crit}}$ as a function of $\sqrt{\mathrm{La}}$ at depinning.

Laplace number $\sqrt{\mathrm{La}}$ and aspect ratio AR at droplet depinning, respectively. Despite the notable difference in side-view geometry observed in the flat plate boundary layer and

Table 7.3: Critical depinning conditions for water droplets reported in literature; studies marked with ✠ are experiments conducted in turbulent channel flows, and otherwise in laminar boundary layers formed over flat plates. Droplet geometries reported in the table are partially extracted from digitized plots or estimated based on geometric correlations (Eq. 7.1). Displacement thickness is estimated based on the Blasius solution and Prandtl approximation [202] for laminar boundary layers and turbulent channel flows, respectively.

	Substrate	V [μL]	$\sqrt{\text{La}}$	AR	$\mathcal{K}$	$\overline{\theta}_c$ [°]	CAH	δ^*/h	We_h
Milne and Amirfazli [121]	PMMA	58	753	0.33	1.02	66	0.181	0.131	1.8
		100	798	0.28	0.93	66	0.175	0.117	1.6
Roisman *et al.* [153]	PDMS	50	807	0.41	0.92	79	0.510	0.127	0.6
		100	906	0.41	0.92	79	0.510	0.101	0.7
	PMMA	50	808	0.42	0.92	80	0.310	0.127	0.4
		100	907	0.42	0.92	80	0.310	0.101	0.6
	Teflon	50	928	0.75	1.31	113	0.150	0.096	0.3
		100	1042	0.75	1.31	113	0.150	0.076	0.4
	SHS	50	1035	1.88	4.28	150	0.054	0.077	0.3
		100	1162	1.88	4.28	150	0.054	0.061	0.4
Hooshanginejad and Lee [77]	Aluminium (rough)	130	887	0.28	0.61	49	0.543	0.066	8.5
White and Schmucker [201]	Aluminium (rough)	75	748	0.24	0.76	51	0.543	0.093	7.6
		100	775	0.23	0.75	51	0.543	0.087	7.8
		125	816	0.24	0.76	51	0.543	0.078	7.6
Seiler *et al.* [176]✠	Aluminium	35	707	0.31	0.82	63	0.891	0.469	1.7
	Aluminium (varnished)	35	689	0.29	0.81	60	0.517	0.494	1.6
	PMMA	35	671	0.27	0.85	59	0.369	0.521	1.5
	Steel (varnished)	35	689	0.29	0.83	60	0.866	0.494	1.8
Barwari *et al.* [11]✠	PMMA	39.9	758	0.38	0.92	51	0.632	0.598	3.6
	Silicon (coated)	39.9	866	0.65	1.20	90	0.518	0.459	1.3

impinging jets (see Fig. 7.6), droplets under all the flow configurations considered in the present study exhibit Laplace numbers in the range of $750 \leq \sqrt{\text{La}} \leq 850$ (Fig. 7.9), and aspect ratios of $0.25 \leq AR \leq 0.30$ (Fig. 7.10). Combining with the data reported in lit-

erature, it can be inferred that these two parameters are predominantly influenced by the substrate wettability, *i.e.*, increase in substrate hydrophobicity leads to increase in $\sqrt{\text{La}}$ and AR. We_h exhibits general decreasing trends with $\sqrt{\text{La}}$ and AR. The monotonic relation between We_h and AR, however, is stronger than that between We_h and $\sqrt{\text{La}}$.

Figs. 7.11 and 7.12 show the dependence of We_h on mean contact angle $\overline{\theta_c}$ and contact angle hysteresis CAH, respectively. Droplets submerged in the laminar boundary layer and impinging jets of the present study exhibit similar mean contact angles of around 60°. Contact angle hysteresis of droplets in impinging jets clusters around CAH $\approx$ 0.6, while higher values around CAH $\approx$ 0.9 are exhibited by droplets submerged in the flat plate boundary layer. Combining with the data reported in the literature suggests increasing substrate hydrophobicity leads to increase in $\overline{\theta_c}$ and decrease in CAH. The latter leads to the decrease in adhesion between droplet and substrate, and consequently results in lower $\text{We}_{h,\text{crit}}$.

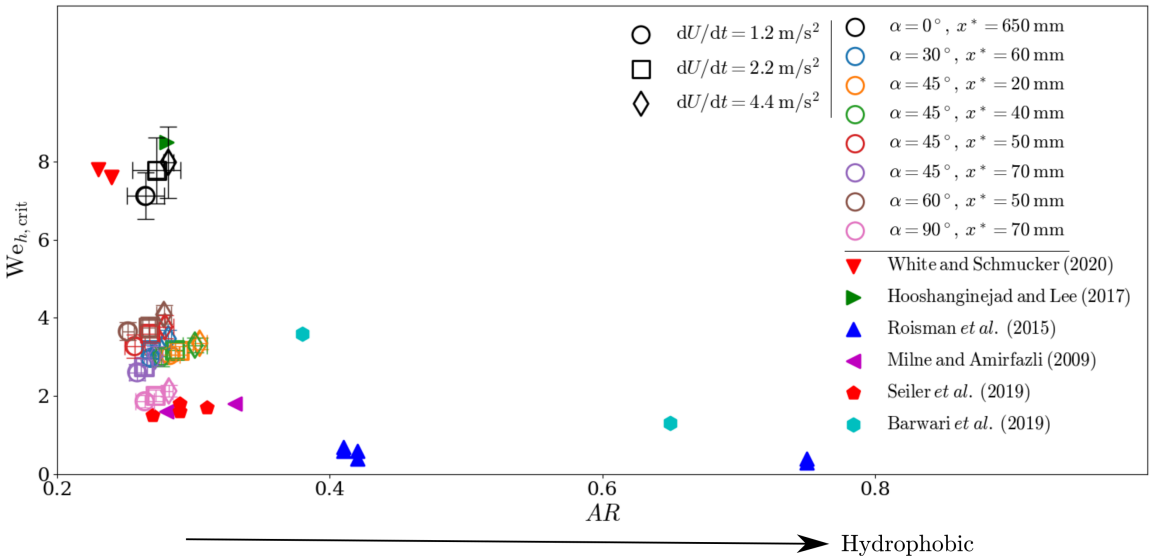

Figure 7.10: Critical Weber number based on droplet height $\text{We}_{h,\text{crit}}$ as a function of aspect ratio AR at depinning.

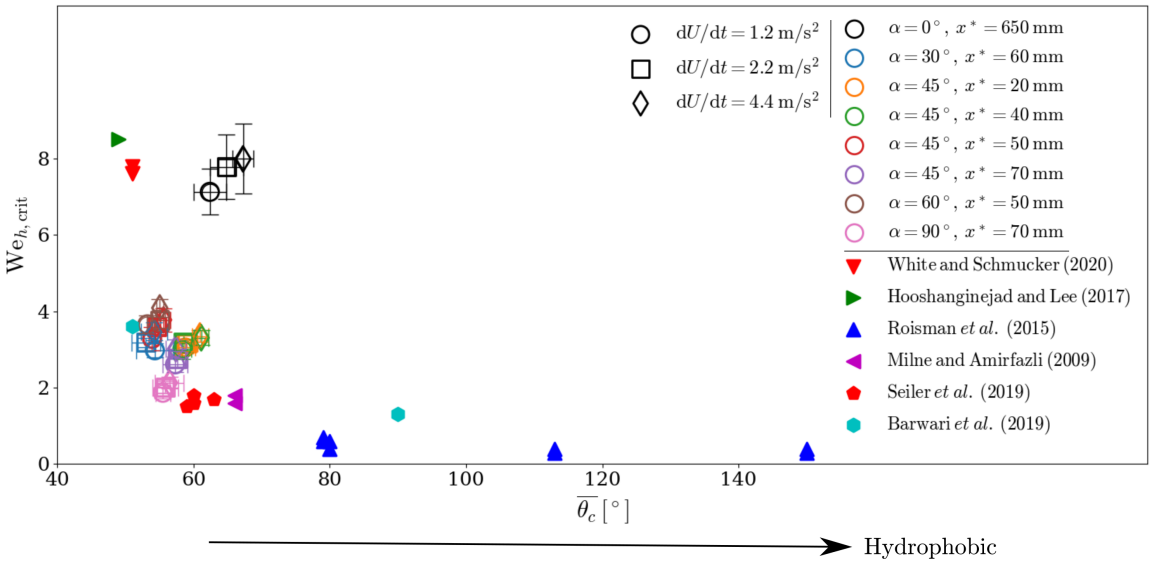

Figure 7.11: Critical Weber number based on droplet height $\mathrm{We}_{h,\mathrm{crit}}$ as a function of mean contact angle $\overline{\theta_c}$ at depinning.

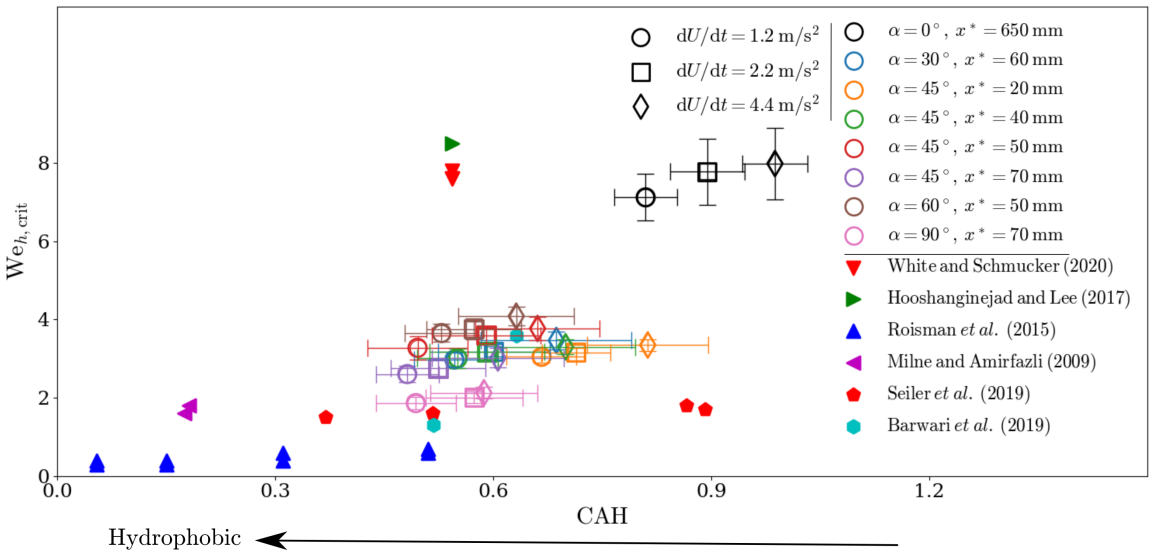

Figure 7.12: Critical Weber number based on droplet height $\mathrm{We}_{h,\mathrm{crit}}$ as a function of contact angle hysteresis CAH at depinning.

Fig. 7.13 shows the dependence of We_h on relative submergence δ^*/h. Droplets in the

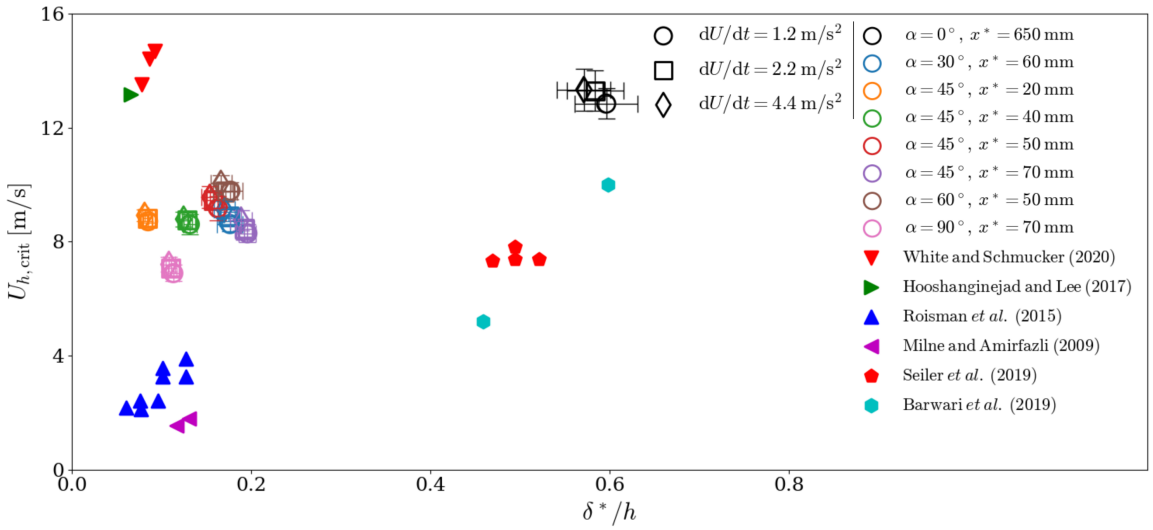

Figure 7.13: Critical Weber number based on droplet height $We_{h,\mathrm{crit}}$ as a function of relative submergence δ^*/h at depinning.

impinging jets of the present study exhibit an increasing trend of We_h with δ^*/h, which is expected since a higher submergence indicates a lower effective velocity averaged over the droplet height as compared to U_h. Similar trends are seen in data from Milne and Amirfazli [121] (purple triangles), Roisman *et al.* [153] (blue triangles), and Barwari *et al.* [11] (cyan hexagons). However, statistics from different studies do not follow the same trend line, which is due to the variation in other parameters. Comparing the critical Weber number in the laminar boundary layer of the present study (black markers) to those in turbulent channel flows reported by Seiler *et al.* [176] (red pentagons) and Barwari *et al.* [11] (cyan hexagons), droplets depin at lower We_h in turbulent channel flows than in laminar boundary layer of similar δ^*/h. The reduced We_h in turbulent channel flows is due to a higher effective velocity averaged over the droplet height, which results from a fuller near-wall velocity profile as compared to that in laminar boundary layers of the same δ^*.

Table 7.4: Monotonic dependence of Π_1 on Π_2 to Π_6 and $\mathcal{K}$ evaluated by Spearman's rank correlation coefficients [48]. Red, orange, blue, and green indicate very strong, strong, moderate, and weak correlations, respectively.

	Π_2	Π_3	Π_4	Π_5	Π_6	$\mathcal{K}$
Π_1	-0.23	-0.62	-0.67	0.69	0.30	-0.88

The monotonic dependence of Π_1 on Π_2 to Π_6 is evaluated using Spearman's rank correlation coefficients (ϱ_S) [48], as summarized in Table 7.4. While Π_1 is strongly monotonically related to Π_3, Π_4, and Π_5, its correlations with Π_2 and Π_6 are much weaker. This indicates for a given combination of working fluids (*i.e.*, air and water in the present study), the critical Weber number at depinning is dominated by the dimensionless groups associated with droplet depinning geometries.

Theoretically, Π_2 to Π_6 should form a linearly independent basis. However, the trends of variation in We_h with respect to $\sqrt{\mathrm{La}}$, AR, and $\overline{\theta_c}$ (see Figs. 7.9, 7.10, and 7.11, respectively) appear to indicate a potential interdependence between these Π groups. The linear correlation among Π_2 to Π_6 is measured statistically using Pearson correlation coefficient (ϱ_P) [48], as summarized in Table 7.5. Very strong ($\varrho_P \geq 0.80$) linear correlations

Table 7.5: Linear correlations between parameters among Π_2 to Π_6 measured by Pearson correlation coefficients [48]. Red, orange, blue, and green indicate very strong, strong, moderate, and weak correlations, respectively.

	Π_2	Π_3	Π_4	Π_5	Π_6
Π_2	1	0.88	0.91	-0.58	-0.18
Π_3		1	0.94	-0.64	-0.22
Π_4			1	-0.69	-0.16
Π_5				1	0.56
Π_6					1

are demonstrated by each combination of two parameters among Π_2, Π_3, and Π_4, which indicates the effect of surface wettability is revealed by droplet geometry at depinning. Π_5 exhibits a moderate ($\varrho_P \geq 0.40$) linear correlation with Π_2, and strong ($\varrho_P \geq 0.60$) correlations with Π_3 and Π_4, which is not surprising given the droplet geometric correlations (see Eq. 7.1). While correlations between Π_6 and Π_2, Π_3, and Π_4 are weak ($\varrho_P \leq 0.39$), a moderate correlation is observed with Π_5. The positive correlation between Π_5 and Π_6 indicates droplets in the laminar flat plate boundary layer of higher submergence exhibit higher contact angle hysteresis than those in the impinging jets of lower submergence.

Given the correlations among Π_2 to Π_6, they may potentially be assimilated into one dimensionless parameter which assimilates their overall influence on We_h. Since Π_3 and Π_4 demonstrate strong monotonic correlation with Π_1 (see Table 7.4), and are strongly interrelated with parameters among Π_2 to Π_6 (see Table 7.5), they are used to construct the new dimensionless parameter. Combining with the droplet geometric correlation equations (Eq. 7.1), a volumetric shape factor $\mathcal{K} = V/(\pi h L_b^2/6)$ is formulated, which quantifies the deformation of droplet at depinning by comparing the droplet volume to that of a semi-ellipsoid with height h and base diameter L_b. It also incorporates the effect of the substrate wettability. For a given droplet volume, droplets on hydrophilic substrates exhibit larger contact length and smaller droplet height, and consequently a smaller $\mathcal{K}$ as compared to those on hydrophobic substrates. Increase in substrate hydrophobicity leads to increase in $\mathcal{K}$. Since Π_1 demonstrates a much stronger correlation with $\mathcal{K}$ than with other Π groups (see Table 7.4), the dimensionless relation of Eq. 7.6 can be approximated by

$$\mathrm{We}_h \approx \mathcal{F}^*(\mathcal{K}). \tag{7.7}$$

Fig. 7.14 shows We_h versus $\mathcal{K}$. Volumetric shape factor of droplets in impinging jets clusters in the range of $0.80 \leq \mathcal{K} \leq 0.90$, while the values of droplets in the laminar bound-

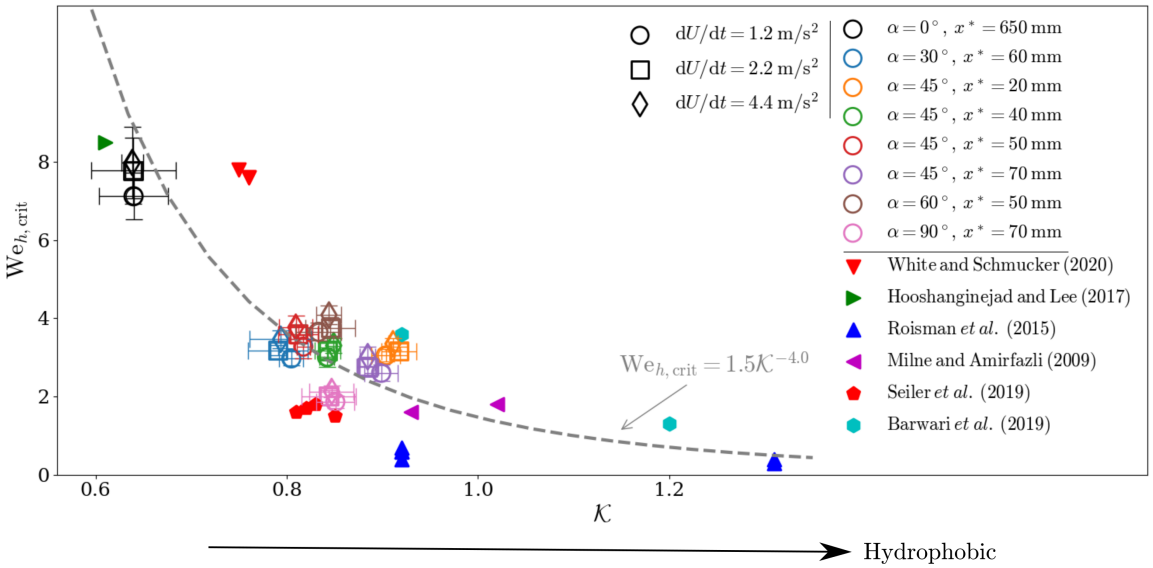

Figure 7.14: Critical Weber number based on droplet height $\mathrm{We}_{h,\mathrm{crit}}$ as a function of volumetric shape factor $\mathcal{K}$ at depinning; the latter compares the droplet volume to that of an ellipsoid with base diameter L_b and height h.

ary layer of the present study is notably lower at around $\mathcal{K} \approx 0.65$. When compared with depinning conditions reported for droplets on substrates of varied wettabilities reported in literature, the depinning geometries of droplets in impinging jets exhibit geometric characteristics of those submerged in boundary layer flows over a more hydrophobic surface. The experimental results of the present study and the data reported by previous studies collapse along a same trend line, which indicates a strong power-law relation between We_h and $\mathcal{K}$. With power-law curve-fitting of

$$\begin{gathered} \mathrm{We}_{h,\mathrm{crit}} \approx a\mathcal{K}^{-\beta}, \\ \text{with } \ a = 1.5 \pm 0.17, \ \ \beta = 4.0 \pm 0.34, \end{gathered} \tag{7.8}$$

the critical depinning velocity can thus be estimated based on droplet volume, contact length and height measured at depinning using the empirical relation

$$U_{h,\text{crit}} \approx \frac{\gamma^{1/2}\pi^2 h^{3/2} L_b^4}{2\rho^{1/2} V^2}. \tag{7.9}$$

Eq. 7.9 provides an easier approach in estimating the critical depinning velocity experimentally, since this correlation only requires contact length L_b and droplet height h as inputs to calculate the critical velocity $U_{h.\text{crit}}$. Unlike the computational-demanding sub-pixel resolution required to measure of contact angles with high accuracy, droplet contour yielded by Canny edge detection is sufficient for droplet height h and contact length L_b measurements. In addition, as can be observed in Figs. 7.2 (b-3) to (b-5), droplet height and contact length do not change significantly around the time instant of depinning; thus, the measurement of h and L_b does not require identifying the exact time instant when droplet depins.

7.4 Drag coefficients and contact angle distribution along three-dimensional contact line

As shown by Eq. 7.2, droplet dynamics at depinning is largely governed by the competing aerodynamic loading F_D and adhesion F_{adh}. Modeling forces in the depinning process using Eqs. 2.12 and 2.11 requires the information of drag coefficient C_D and contact angle distribution k. Drag coefficient C_D can be estimated experimentally (see Ch. 6) or numerically (*e.g.*, [155]) from flow development over solid droplet model. For contact angle distribution k, values measured from gravity-forced droplets are often used for wind-forced droplets. However, several studies (e.g. [121, 169]) have suggested the distinctions

of contact lines exhibited by droplets under the two forcing types and hence the potential difference in k values. Since C_D and k are not directly measurable with droplet side-view imaging, the ratio of C_D/k is considered as a grouped variable, which is suggested and used in previous studies (*e.g.*, [121]). The following discussions in this section aim at (i) characterizing the influence of incoming flow configurations on C_D/k, and (ii) providing a preliminary estimate of k value range for wind-forced droplets under similar wettability condition as in the present study.

To estimate C_D/k from the side-view geometries, Eq. 2.13 is rearranged to form a

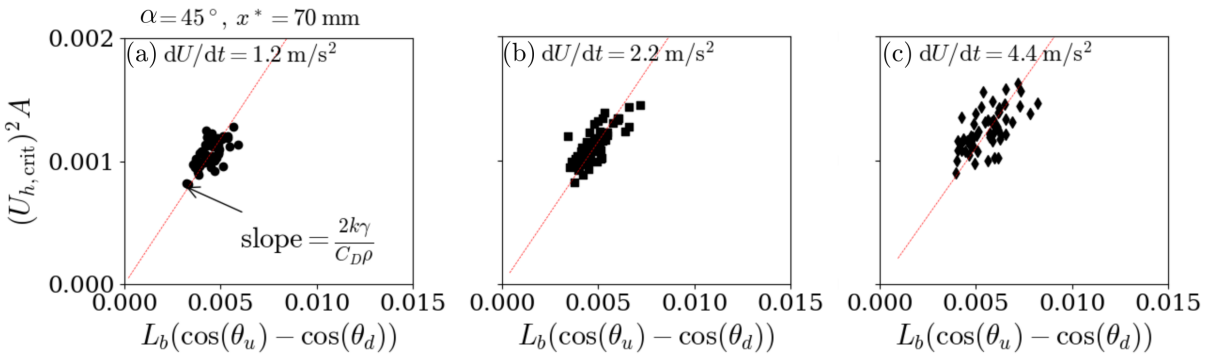

Figure 7.15: Test data from individual runs illustrating the force balance between aerodynamic drag and adhesion under the acceleration of (a) 1.2 m/s^2, (b) 2.2 m/s^2, (c) 4.4 m/s^2; the data acquired for 120 μL droplets under the shear flow formed at $x^* = 70$ mm downstream of the stagnation point of a $\alpha = 45°$ accelerating impinging jet are shown as exemplar. Red dashed lines show the linear regressions of $U_{h,\mathrm{crit}}^2 A$ as a function of $L_b(\cos(\theta_u) - \cos(\theta_d))$; the slopes of the fitted lines are thus $2k\gamma/C_D\rho$.

linear relation

$$(U_{h,\mathrm{crit}})^2 A = \frac{2k\gamma}{\rho C_D} L_b(\cos(\theta_u) - \cos(\theta_d)). \tag{7.10}$$

The value of C_D/k can then be computed from the slope $2k\gamma/\rho C_D$ of the fitted line, as shown in Fig. 7.15. Fig. 7.16 shows the C_D/k computed for each combination of flow orientation angle and acceleration. At jet angles of $30° \leq \alpha \leq 60°$, droplets exhibit

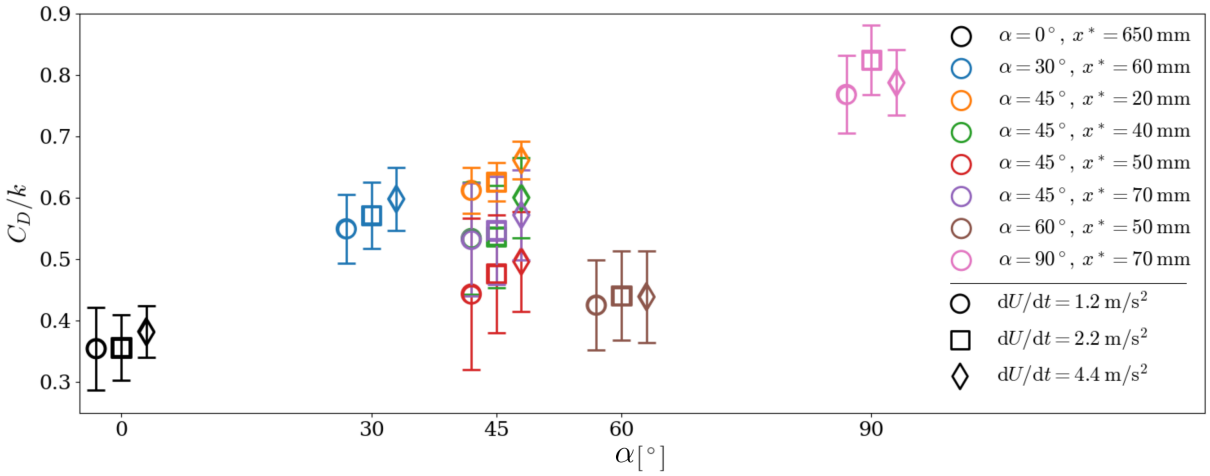

Figure 7.16: Drag coefficients acquired from droplet side-view imaging, C_D/k, averaged across all droplet volumes tested at each flow configuration and acceleration as a function of background flow orientation angle α.

$0.4 \lessapprox C_D/k \lessapprox 0.7$. The slightly low values around $C_D/k \approx 0.35$ shown by droplets submerged in a laminar flat plate boundary layer ($\alpha = 0°$, in Fig. 7.16, black markers) are attributed to the lower effective velocity over the droplet height as compared to U_h, which is expected from the higher relative submergence δ^*/h in the flat plate boundary layer than those in the impinging jets (see Fig. 7.5(b)). Comparing with the drag coefficient $0.35^{+0.03}_{-0.02}$ estimated for the solid runback droplet model in Sect. 6.1, contact angle distribution of $0.8 \lessapprox k \lessapprox 1.2$ is estimated for droplets under wind-forcing. This value range is notably lower than the range of $1.3 \lessapprox k \lessapprox 2$ reported for gravity-forced droplets [19, 41, 50, 51]. The lower k values of wind-forced droplets are likely resulting from the near-parallel lateral contact lines joining the wide upstream and downstream sections of the contact line (see Fig. 1.1), as compared to the more elliptical contact line exhibited by gravity-forced droplets (see Fig. 2 of [50]), meaning that the distribution of contact angles of a wind-forced droplet is well modeled by $k \approx 1$. Numerical simulation by Ding and Spelt [40]

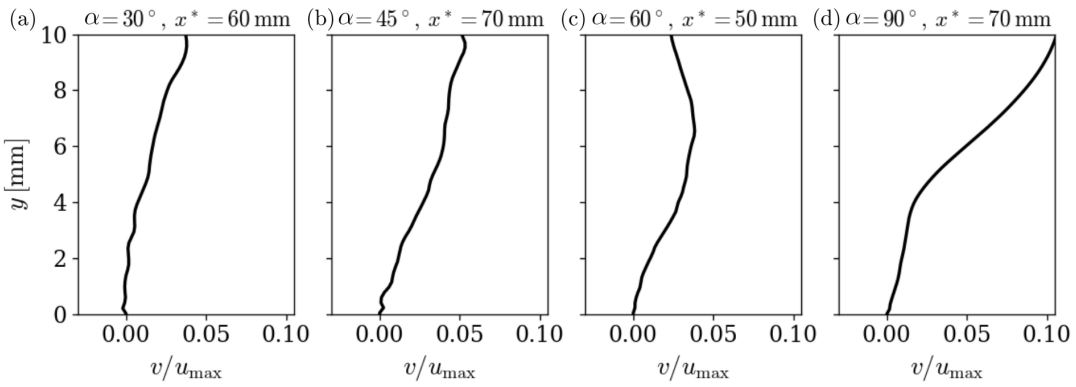

Figure 7.17: Steady near-wall wall-normal velocity profile measured at (a) $\alpha = 30°$, $x^* = 60$ mm, (b) $\alpha = 45°$, $x^* = 70$ mm, (c) $\alpha = 60°$, $x^* = 50$ mm, and (d) $\alpha = 90°$, $x^* = 70$ mm with jet exit velocities $U_j \approx U_{j,\text{crit}}$ of the respective case.

showed an abrupt change from θ_u to θ_d along a contact line with parallel sides, while a elliptical-shaped contact line allows a gradual change in contact angles.

Given the similarity in side-view geometries (see Fig. 7.7) exhibited by the droplets in shear flows formed by impinging jets, the higher values of C_D/k demonstrated by droplets under normal jet impingement ($\alpha = 90°$, in Fig. 7.16, magenta markers) may associate with other near-wall flow events besides the mean streamwise velocity profile which directly dictates the mean aerodynamic drag. A similar presumption was made by Leung *et al.* [104] for the observation of reduced droplet depinning velocity in normally impinging jets. As discussed in Sect. 4.2.3, the wall jet region of jet impingement is dominated by the passage and interactions of large-scale K-H vortices. The time-averaged footprints of these vortical structures are mainly reflected in the deflection of wall jet and induction of wall-normal velocities. Fig. 7.17 shows the wall-normal velocity profiles in the steady jets at varied jet angles with jet exit velocities at around the respective $U_{j,\text{crit}}$ of the given angle. There is a notably higher wall-normal velocity component in the case of $\alpha = 90°$ as compared to other cases, indicating a more salient influence of K-H vortices on the

near-wall flow fields, which potentially gives rise to droplet oscillations of higher magnitudes. Direct measurements of droplet drag by Milne [120] have suggested that droplets experience increase in drag due to droplet oscillations. However, it requires simultaneous measurements of instantaneous near-wall flow field and droplet geometry to validate the presumed vortex-droplet interactions and the discussion is beyond the scope of the present study.

7.5 Summary

This chapter discusses droplet response to wall-bounded shear flows formed by a flat plate boundary layer and impinging jets oriented at angles ranging from 30° to 90°. The critical droplet depinning conditions are investigated at eight wall locations and under three flow accelerations $\mathrm{d}U/\mathrm{d}t$ = 1.2, 2.2, and 4.4 m/s^2. Within the range of parameters investigated, critical velocities demonstrate a slight decrease with increasing droplet volume and decreasing flow acceleration. Notwithstanding the statistical significance, the impacts of droplet volume and flow acceleration are small as compared to the effects of incoming flow orientation angle and relative submergence within the range of parameters considered. By virtue of the smaller relative submergence in the shear flows formed by jet impingements, droplets in obliquely impinging jets ($30° \leq \alpha \leq 60°$) require lower velocities around $U_{h,\mathrm{crit}} \approx 9$ m/s for depinning as compared to $U_{h,\mathrm{crit}} \approx 13$ m/s for those in the laminar flat plate boundary layer. Droplets in the normally impinging jet ($\alpha = 90°$) exhibit a significantly lower critical velocity as compared to those of other jet angles. This may be associated with the stronger droplet oscillations induced by flow events which are distinctive in impinging jets at high jet angles. However, it requires further investigation to fully unveil the potential influence of the transient flow events on droplet depinning.

Combining the droplet depinning conditions presented in this chapter with the flow characterization of impinging jets in Ch. 4, guidelines can be provided for droplet removal operations using impinging jets. The jet nozzle exit should be placed within seven nozzle width from the target surface to provide a near-wall shear flow of high momentum. The optimal jet orientation angle range is $30^\circ \lessapprox \alpha \lessapprox 45^\circ$, within which droplet depinning criteria is insensitive to small changes in jet angle and the near-wall velocity decay rate is minimized. The effect of flow accelerations within $1 \lessapprox \mathrm{d}U/\mathrm{d}t \lessapprox 4\ \mathrm{m/s^2}$ is negligible in engineering applications, and thus blower starting curve should be optimized based on the mechanical design of the blower. It should be noted that these guidelines are based on the depinning criteria of an isolated droplet, and are applicable for removing sparsely spaced droplets. In situations where the target surface is densely populated with droplets, the suggested parameters may require further adjustment.

Dimensional analysis is performed to compare the depinning conditions obtained in the present study to those reported in previous studies for varied substrate wettabilities. A critical Weber number range of $7 \leq \mathrm{We}_{h,\mathrm{crit}} \leq 8$ is observed for droplets in the laminar boundary layer of the present study, comparable to that reported by White and Schmucker [201]. Droplets in impinging jets depin at a lower Weber number range of $2 \leq \mathrm{We}_{h,\mathrm{crit}} \leq 4$. Given the combination of air flow and water droplet, the critical Weber number is dominated by the dimensionless parameters associated with droplet geometries at depinning, *i.e.*, aspect ratio, mean contact angle, and contact angle hysteresis. The effects of these dimensionless parameters can be further assimilated into a volumetric shape factor $\mathcal{K}$, which demonstrates a strong power-law relation with the critical Weber number $\mathrm{We}_{h,\mathrm{crit}}$. An empirical equation is proposed for the determination of droplet depinning velocities based on the fitted power-law equation, which only requires information of droplet volume, contact length, and height around the time instant of droplet depinning. This

empirical equation simplifies droplet image postprocessing by circumventing contact angle measurements.

Values of C_D/k are estimated from droplet side-view geometries and critical depinning velocity measured in the present study. Combining with the drag coefficient C_D acquired from solid runback model in Ch. 6, the contact angle distribution of wind-forced droplets is estimated as $0.8 \lessapprox k \lessapprox 1.2$, which is much lower than the values reported for gravity-forced droplets.

Chapter 8

Conclusions and Future Work

This thesis has studied the interactions between an isolated droplet residing on a solid surface and wall-bounded shear flows, which was inspired by the wide-ranging occurrence of this phenomenon in daily life and engineering applications. The investigations mainly focused on physical phenomena associated with the onset of droplet motion, specifically, (i) the critical flow conditions for droplet depinning, and (ii) the influence of droplets on the development of the surrounding flow.

Droplet volumes of 75, 90, 105, and 120 μL were tested in the shear flows formed by a laminar flat plate boundary layer and impinging jets at orientation angles of 30°, 45°, 60°, and 90° with respect to the target surface. The combination of water droplets, anodized aluminium surface, and air flow was considered. The effect of flow acceleration on droplet depinning was investigated at freestream or jet centreline accelerations of $\mathrm{d}U/\mathrm{d}t = 1.2$, 2.2, and 4.4 m/s^2. The background flow fields were characterized using hot-wire and PIV (Ch. 4). Aerodynamic assessment of droplet conformations under wind-forcing was performed on scaled-up solid models, which represent the morphological shapes of a sessile

droplet and a deformed droplet under wind-forcing immediately prior to depinning (Chs. 5 and 6). A predictive model for droplet depinning criteria was proposed based on the range of droplet volume, background flow configuration and acceleration, and substrate wettability investigated in the present study and reported in previous studies (Ch. 7). Key performance parameters associated with droplet depinning, such as drag coefficient and contact angle distribution, were evaluated (Chs. 6 and 7). The main findings of this study are summarized in Sect. 8.1, and the suggestions for future research are given in Sect. 8.2.

8.1 Conclusions

Droplets in the laminar flat plate boundary layer ($\alpha = 0°$) investigated in the present study were found to depin at a critical velocity around $U_{h,\text{crit}} \approx 13$ m/s, while those in impinging jets depin at lower velocities of $U_{h,\text{crit}} \lessapprox 9$ m/s. The higher depinning velocity required in the laminar boundary layer is directly attributed to the lower near-wall momentum compared to that of the impinging jets. Droplets in the laminar boundary layer exhibit longer contact length and higher contact angle hysteresis demonstrated at depinning compared to those in the impinging jets, which contribute to the increase in adhesion. A more concaved windward geometry was also observed for droplets in the laminar boundary layer, which likely reduces the aerodynamic drag. For droplets in impinging jets, the critical side-view geometries at depinning were found to be insensitive to jet orientation angles.

Within the range of parameters investigated, critical velocities demonstrate a slight increase with decreasing droplet volume and increasing flow acceleration. A smaller droplet volume corresponds to a higher shear flow submergence, which leads to lower effective velocity across the droplet height. Under higher flow accelerations, droplets were found

to exhibit notably higher contact angle hysteresis. Although statistically significant, the impacts of droplet volume and flow acceleration are small as compared to flow orientation angles.

With dimensional analysis, droplets in flat plate boundary layer were found to have a constant depinning threshold of $\mathrm{We}_{h,\mathrm{crit}} = 7.5 \pm 0.5$, comparable to that reported in [201]. By contrast, droplets in impinging jets exhibit much lower thresholds in the range $2 \leq \mathrm{We}_{h,\mathrm{crit}} \leq 4$. Complemented by the data reported in literature, it has been found that with increasing substrate wettability, critical Weber number, Laplace number, aspect ratio, and mean contact angle at droplet depinning increase, while contact angle hysteresis decreases. Critical Weber number was found to be strongly correlated with dimensionless groups associated with critical droplet geometric parameters, *i.e.*, aspect ratio, mean contact angle, and contact angle hysteresis, and weakly correlated with Laplace number and relative boundary layer submergence. Strong interdependencies were also found amongst the critical aspect ratio, mean contact angle, and contact angle hysteresis. A volumetric shape factor $\mathcal{K}$ was formulated based on these three parameters to quantify the overall deformation of the depinning droplet from the sessile state. A strong power-law relation was found between $\mathrm{We}_{h,\mathrm{crit}}$ and $\mathcal{K}$, based upon which an empirical relation was established to predict the critical depinning velocity based on droplet volume, length, and height.

Flow development over solid models of scaled-up droplet geometries was found to be similar to those of hemispheres and other smooth obstacles. In laminar boundary layers, a horseshoe vortex system forms at the base upstream of the droplet model. Flow separates at the maximum height of the droplet model and reattaches back to the substrate, forming a typical "C"-shaped recirculating region. At a Reynolds number representative of critical depinning conditions ($\mathrm{Re}_h = 2070$), the near wake flow behavior is dominated by arch

vortices shedding in the separated shear layer and the reoriented horseshoe vortex system. The sessile model induces a more pronounced horseshoe vortex system which influences a wider spanwise range downstream. Wake growth rates in both wall-normal and lateral directions were found to be similar for the sessile and runback models. Wall-normal and lateral spreadings were found to be associated with different mechanisms. While shear layer vortex shedding is responsible for wall-normal wake growth, lateral spreading of the turbulent wedge is mainly associated with the interactions of streamwise-oriented vortices. The spreading of the turbulent wedge was shown to promote laminar-to-turbulent transition. Flow fields over the sessile model and a truncated spherical cap showed high similarities, indicating that for droplets with contact angles below 90°, a spherical cap with the same base length and height is a reasonable proxy of the sessile droplet with regard to aerodynamics. With elevated turbulence intensity in the incoming flow, the horseshoe vortex system diminishes, the recirculating region shortens, and arch vortex shedding is suppressed.

Aerodynamic drag on solid models of scaled-up droplet geometries submerged in a laminar boundary layer of $\delta/h = 1$ was estimated based on flow field measurements using stereo-PIV. The drag coefficient of the baseline hemisphere model was found to be 0.41, which agreed reasonably well with previous studies. The drag coefficients found for the sessile and runback models are $C_D \approx 0.36$ and 0.35, respectively, approximately 10% lower than the drag coefficient of the hemisphere. Although the difference in drag coefficients are not discernibly different, the runback model demonstrated a reduction in drag force as compared to the sessile model, which results from a proportional reduction in the frontal area. For a given droplet model, a centreline drag coefficient was used as an indicator of the overall drag. The centreline drag coefficient was observed to decrease significantly with increasing turbulence intensity in the incoming flow, indicating laminar flows can be more

effective for surface cleaning applications.

For real water droplets, values of C_D/k were estimated from the velocity and side-view geometries measured at droplet depinning. Comparing C_D/k of water droplets in laminar boundary layers with the C_D obtained for the runback model submerged in laminar boundary layer of the same relative submergence, a contact angle distribution range of $0.8 \lessapprox k \lessapprox 1.2$ was found for droplets under wind-forcing, which is notably lower than the range of gravity-forced droplets reported in previous studies.

A direct engineering relevance of the present study lies in offering guidelines for the design and optimzation of impinging jet configuration in cleaning/drying systems. The nozzle-to-plate spacing should be within seven nozzle widths to effectively make use of the high momentum in jet potential core. The optimal jet orientation angle range is $30^\circ \lessapprox \alpha \lessapprox 45^\circ$, within which the near-wall velocity decay rate is minimized and droplet depinning criteria are relatively insensitive to the small change in jet angle. Flow acceleration within $1 \lessapprox \mathrm{d}U/\mathrm{d}t \lessapprox 4\ \mathrm{m/s^2}$ does not affect droplet depinning significantly, and can be selected based on the performance of the blower used to generate the flow. It should be noted that the aforementioned guidelines are based on droplet depinning tests of an isolated droplet, and are applicable for removing sparsely spaced droplets. For surfaces that are densely populated with droplets, the suggested parameters may require further adjustment.

8.2 Future work

Based on the outcome of the present study, there are several recommendations for the future research, generally divided into i) droplet oscillations, ii) impact of substrate wettability, and iii) droplet dynamics and aerodynamics of droplet array and consecutive

agglomerates. Specific future research directions in the context of the present study are as follows.

As discussed in Ch. 7, droplets subjected to a normally impinging jet ($\alpha = 90°$) depin at a notably lower critical velocity. Videos capturing these test runs showed strong bulk oscillations prior to depinning. Flow measurements of normal jet impingement with $U_j \approx U_{j,\text{crit}}$ in Ch. 4 indicate the passage of large-scale coherent structures in the wall jet region, which induce significant wall-normal velocity component and instantaneous flow separations. These point to potential vortex-droplet interactions which may alter the path to droplet depinning. To elucidate the influence of the instantaneous flow events on droplet depinning, simultaneous measurements of instantaneous flow field and droplet geometry is required.

In addition, this study focused on one specific combination of liquid (water), solid (anodized aluminium) and gas (air), which results in spherical cap-shaped sessile droplets with initial contact angle around 80°. The influence of substrate wettability was only inferred by comparing the experimental measurements of the present study against the depinning criteria reported in previous studies for droplets submerged in flat plate boundary layer on varied substrate wettabilities. Whether droplets in impinging jets on substrates of varied wettabilities will follow the same predictive trend proposed in Ch. 7 should be further validated by future experiments.

Furthermore, this study exclusively considered the behaviour of an isolated droplet in wall-bounded shear flows. However, in real-world applications, such as cleaning, drying, and anti-icing, it is common for more than one droplet to be exposed to the flow. Ch. 5 has shown that a droplet-shaped obstacle submerged in a laminar boundary layer serves as a roughness element, which introduces flow perturbations that significantly alter the near-wall velocity profile and may subsequently change the depinning criteria for

droplets downstream. The behaviours of multiple droplets in close proximity submerged in wall-bounded shear flows have been the subject of a limited number of studies, such as [124, 77, 149, 148]. While these studies revealed the influence of array configurations on the depinning condition of each individual droplet within the array, they opened up more questions regarding the surrounding flow fields and the consecutive droplet agglomeration. Building on the mean flow field and vortex dynamics of an isolated droplet presented in Ch. 5 and the mean velocity fields characterized by [149] for solid sessile droplet arrays, future studies should shed light on the interactions between the vortices shed by the upstream droplet and the downstream droplet. The instantaneous loading on the downstream droplet associated with impinging vortical structures may also offer insight into oscillations and 'skip' motions of the downstream droplet. Analogous to the approaches taken in Ch. 5 and Ch. 6, flow development over solid models representative of depinning droplet geometries in arrays and intermediate droplet agglomerates can be used as lower order approximations of liquid droplets. Evolutions of the velocity field, vortex topology, and aerodynamic loading at different stages of droplet depinning and agglomeration processes assessed from the solid model tests may provide insights into the driving force behind droplet motions within an array.

References

[1] MS Acarlar and CR Smith. A study of hairpin vortices in a laminar boundary layer. part 1. hairpin vortices generated by a hemisphere protuberance. *Journal of Fluid Mechanics*, 175:1–41, 1987.

[2] ZU Ahmed, YM Al-Abdeli, and MT Matthews. The effect of inflow conditions on the development of non-swirling versus swirling impinging turbulent jets. *Computers & Fluids*, 118:255–273, 2015.

[3] S Amant. Drag prediction and decomposition, from wake surveys and calculations, in subsonic flows. In *19th AIAA Applied Aerodynamics Conference*, page 2446, 2001.

[4] P Andersson, L Brandt, A Bottaro, and DS Henningson. On the breakdown of boundary layer streaks. *Journal of Fluid Mechanics*, 428:29–60, 2001.

[5] M Angioletti, RM Di Tommaso, E Nino, and G Ruocco. Simultaneous visualization of flow field and evaluation of local heat transfer by transitional impinging jets. *International Journal of Heat and Mass Transfer*, 46:1703–1713, 2003.

[6] C Antonini, M Innocenti, T Horn, M Marengo, and A Amirfazli. Understanding the effect of superhydrophobic coatings on energy reduction in anti-icing systems. *Cold Regions Science and Technology*, 67(1-2):58–67, 2011.

[7] T Astarita and G Cardone. Convective heat transfer on a rotating disk with a centred impinging round jet. *International Journal of Heat and Mass Transfer*, 51(7-8):1562–1572, 2008.

[8] CJ Baker. The laminar horseshoe vortex. *Journal of Fluid Mechanics*, 95(2):347–367, 1979.

[9] P Bakke. An experimental investigation of a wall jet. *Journal of Fluid Mechanics*, 2:467–472, 1957.

[10] GI Barenblatt, AJ Chorin, and VM Prostokishin. The turbulent wall jet: A triple-layered structure and incomplete similarity. *Proceedings of the National Academy of Sciences of the United States of America*, 102:8850–8853, 2005.

[11] B Barwari, S Burgmann, A Bechtold, M Rohde, and U Janoske. Experimental study of the onset of downstream motion of adhering droplets in turbulent shear flows. *Experimental Thermal and Fluid Science*, 109:109843, 2019.

[12] S Beltaos. Oblique impingement of plane turbulent jets. *Journal of the Hydraulics Division*, 102:1177–1192, 1976.

[13] LH Benedict and RD Gould. Towards better uncertainty estimates for turbulence statistics. *Experiments in Fluids*, 22(2):129–136, 1996.

[14] JL Bennington. *Effects of various shaped roughness elements in two-dimensional high Reynolds number turbulent boundary layers.* PhD thesis, Virginia Tech, 2004.

[15] V Berejnov and RE Thorne. Effect of transient pinning on stability of drops sitting on an inclined plane. *Physical Review E*, 75(6):066308, 2007.

[16] A Betz. A method for the direct determination of profile drag. *Z. Flugtechn. Motorluftschiffahrt*, 16:42, 1925.

[17] H Blasius. Grenzschichten in flüssigkeiten mit kleiner reibung. *Zeitschrift fixr Mathematik und Physik*, 56(1), 1908.

[18] BA Bradshaw and MT Gee. *Turbulent wall jets with and without an external stream*. HM Stationery Office, 1962.

[19] RA Brown, FM Orr Jr, and LE Scriven. Static drop on an inclined plate: analysis by the finite element method. *Journal of Colloid and Interface Science*, 73(1):76–87, 1980.

[20] S Burgmann, B Barwari, and U Janoske. Oscillation of adhering droplets in shear flow. In *Proc. 5th Intl. Conf. on Experimental Fluid Mechanics*, page 500, 2018.

[21] G Byun and RL Simpson. Structure of three-dimensional separated flow on an axisymmetric bump. *AIAA Journal*, 44(5):999–1008, 2006.

[22] GM Carlomagno and A Ianiro. Thermo-fluid-dynamics of submerged jets impinging at short nozzle-to-plate distance: a review. *Experimental Thermal and Fluid Science*, 58:15–35, 2014.

[23] IA Carr and MW Plesniak. Three-dimensional flow separation over a surface-mounted hemisphere in pulsatile flow. *Experiments in Fluids*, 57(1):9, 2016.

[24] WG Cartwright and PJ Russell. Paper 32: Characteristics of a turbulent slot jet impinging on a plane surface. In *Proceedings of the Institution of Mechanical Engineers, Conference Proceedings*, volume 182, pages 309–319. SAGE Publications Sage UK: London, England, 1967.

[25] ABD Cassie and S Baxter. Wettability of porous surfaces. *Transactions of the Faraday society*, 40:546–551, 1944.

[26] Z Chen and RJ Martinuzzi. Shedding of dual structures in the wake of a surface-mounted low aspect ratio cone. *Physics of Fluids*, 30(4):045107, 2018.

[27] CM Cheng and CL Fu. Characteristic of wind loads on a hemispherical dome in smooth flow and turbulent boundary layer flow. *Journal of Wind Engineering and Industrial Aerodynamics*, 98(6-7):328–344, 2010.

[28] NJ Cherry, R Hillier, and MEMP Latour. Unsteady measurements in a separated and reattaching flow. *Journal of Fluid Mechanics*, 144:13–46, 1984.

[29] D-T Chin and M Agarwal. Mass transfer from an oblique impinging slot jet. *Journal of The Electrochemical Society*, 138:2643–2650, 1991.

[30] SF Chini and A Amirfazli. A method for measuring contact angle of asymmetric and symmetric drops. *Colloids and Surfaces A: Physicochemical and Engineering Aspects*, 388(1-3):29–37, 2011.

[31] M Choudhari, F Li, and J Edwards. Stability analysis of roughness array wake in a high-speed boundary layer. In *47th AIAA Aerospace Sciences Meeting including The New Horizons Forum and Aerospace Exposition*, page 170, 2009.

[32] TS Chow. Wetting of rough surfaces. *Journal of Physics: Condensed Matter*, 10(27):L445, 1998.

[33] MK Chyu and V Natarajan. Heat transfer on the base surface of threedimensional protruding elements. *International Journal of Heat and Mass Transfer*, 39(14):2925–2935, 1996.

[34] FH Clauser. The turbulent boundary layer. In *Advances in applied mechanics*, volume 4, pages 1–51. Elsevier, 1956.

[35] NL Coleman. Bed particle reynolds modelling for fluid drag. *Journal of Hydraulic Research*, 17(2):91–105, 1979.

[36] C Cornaro, AS Fleischer, and RJ Goldstein. Flow visualization of a round jet impinging on cylindrical surfaces. *Experimental Thermal and Fluid Science*, 20:66–78, 1999.

[37] N Dalili, A Edrisy, and R Carriveau. A review of surface engineering issues critical to wind turbine performance. *Renewable and Sustainable Energy Reviews*, 13(2):428–438, 2009.

[38] N De Tullio, P Paredes, ND Sandham, and V Theofilis. Laminar–turbulent transition induced by a discrete roughness element in a supersonic boundary layer. *Journal of Fluid Mechanics*, 735:613–646, 2013.

[39] N Didden and C-M Ho. Unsteady separation in a boundary layer produced by an impinging jet. *Journal of Fluid Mechanics*, 160:235–256, 1985.

[40] H Ding and PDM Spelt. Onset of motion of a three-dimensional droplet on a wall in shear flow at moderate reynolds numbers. *Journal of Fluid Mechanics*, 599:341–362, 2008.

[41] EB Dussan. The moving contact line. waves on fluid interfaces. In *Proceedings of a Symposium, Academic Press, New York*, pages 303–324, 1983.

[42] EB Dussan. On the ability of drops to stick to surfaces of solids. 3. the influences of the motion of the surrounding fluid on dislodging drops. *J. Fluid Mech.*, 174:381–397, 1987.

[43] EB Dussan and RT-P Chow. On the ability of drops or bubbles to stick to non-horizontal surfaces of solids. *Journal of Fluid Mechanics*, 137:1–29, 1983.

[44] JK Eaton and JP Johnston. Low frequency unsteadyness of a reattaching turbulent shear layer. In *Turbulent Shear Flows 3*, pages 162–170. Springer, 1982.

[45] RY Emami. Characteristics of air flow over a sessile droplet at the verge of shedding. 2020.

[46] HW Emmons. The laminar-turbulent transition in a boundary layer-part i. *Journal of the Aeronautical Sciences*, 18(7):490–498, 1951.

[47] A Esposito, AD Montello, YG Guezennec, and C Pianese. Experimental investigation of water droplet–air flow interaction in a non-reacting pem fuel cell channel. *Journal of Power Sources*, 195(9):2691–2699, 2010.

[48] B Everitt and A Skrondal. *The Cambridge dictionary of statistics*, volume 106. Cambridge University Press Cambridge, 2002.

[49] CW Extrand. Criteria for ultralyophobic surfaces. *Langmuir*, 20(12):5013–5018, 2004.

[50] CW Extrand and AN Gent. Retention of liquid drops by solid surfaces. *Journal of Colloid and Interface Science*, 138(2):431–442, 1990.

[51] CW Extrand and Y Kumagai. Liquid drops on an inclined plane: the relation between contact angles, drop shape, and retentive force. *Journal of Colloid and Interface Science*, 170(2):515–521, 1995.

[52] S Farhadi, M Farzaneh, and SA Kulinich. Anti-icing performance of superhydrophobic surfaces. *Applied Surface Science*, 257(14):6264–6269, 2011.

[53] M Fedrizzi, M Giacobello, J Soria, C Atkinson, and M Jones. Experimental investigation of a hemisphere in a thin flat plate boundary layer. *No. December*, pages 18–21, 2012.

[54] H Fernholz. Zur umlenkung von freistrahlen an gekrummten wanden. *Übersicht Uber den Stand der Technik, Jahrbuch*, page 149, 1964.

[55] R Finn. Capillary surface interfaces. *Notices of the AMS*, 46(7):770–781, 1999.

[56] MD Fox, M Kurosaka, L Hedges, and K Hirano. The influence of vortical structures on the thermal fields of jets. *Journal of Fluid Mechanics*, 255:447–472, 1993.

[57] SC Fu, WT Leung, and CYH Chao. Detachment of droplets in a fully developed turbulent channel flow. *Aerosol Science and Technology*, 48(9):916–923, 2014.

[58] L Gao and TJ McCarthy. Contact angle hysteresis explained. *Langmuir*, 22(14):6234–6237, 2006.

[59] N Gao, H Sun, and D Ewing. Heat transfer to impinging round jets with triangular tabs. *International Journal of Heat and Mass Transfer*, 46:2557–2569, 2003.

[60] R Gardon and JC Akfirat. The role of turbulence in determining the heat-transfer characteristics of impinging jets. *International Journal of Heat and Mass Transfer*, 8(10):1261–1272, 1965.

[61] RW Gent, NP Dart, and JT Cansdale. Aircraft icing. *Philosophical Transactions of the Royal Society of London A: Mathematical, Physical and Engineering Sciences*, 358(1776):2873–2911, 2000.

[62] SA Glantz and BK Slinker. *Primer of applied regression and analysis of variance*. Number Sirsi) i9780070234079. 1990.

[63] MB Glauert. The wall jet. *Journal of Fluid Mechanics*, 1:625–643, 1956.

[64] HJ Goett. Experimental investigation of the momentum method for determining profile drag. 1939.

[65] RJ Goldstein, AI Behbahani, and KK Heppelmann. Streamwise distribution of the recovery factor and the local heat transfer coefficient to an impinging circular air jet. *International Journal of Heat and Mass Transfer*, 29(8):1227–1235, 1986.

[66] A Golpaygan and N Ashgriz. Multiphase flow model to study channel flow dynamics of pem fuel cells: deformation and detachment of water droplets. *International Journal of Computational Fluid Dynamics*, 22(1-2):85–95, 2008.

[67] T Guo, MJ Rau, PP Vlachos, and SV Garimella. Axisymmetric wall jet development in confined jet impingement. *Physics of Fluids*, 29:025102, 2017.

[68] R Gurka, A Liberzon, D Hefetz, D Rubinstein, and U Shavit. Computation of pressure distribution using piv velocity data. In *Workshop on Particle Image Velocimetry*, volume 2, 1999.

[69] JE Hackett and A Sugavanam. Evaluation of a complete wake integral for the drag of a car-like shape. Technical report, SAE Technical Paper, 1984.

[70] JE Hackett, JE Williams, and J Patrick. Wake traverses behind production cars and their interpretation. Technical report, SAE Technical Paper, 1985.

[71] M Hadžiabdić and K Hanjalić. Vortical structures and heat transfer in a round impinging jet. *Journal of Fluid Mechanics*, 596:221–260, 2008.

[72] SM Hajimirzaie, CJ Wojcik, and JHJ Buchholz. The role of shape and relative submergence on the structure of wakes of low-aspect-ratio wall-mounted bodies. *Experiments in Fluids*, 53(6):1943–1962, 2012.

[73] B Han and RJ Goldstein. Jet-impingement heat transfer in gas turbine systems. *Annals of the New York Academy of Sciences*, 934:147–161, 2001.

[74] J Han and C Moraga. The influence of the sigmoid function parameters on the speed of backpropagation learning. In *International Workshop on Artificial Neural Networks*, pages 195–201. Springer, 1995.

[75] P Holmes, JL Lumley, G Berkooz, and CW Rowley. *Turbulence, coherent structures, dynamical systems and symmetry*. Cambridge University Press, 2012.

[76] CJ Hoogendoorn. The effect of turbulence on heat transfer at a stagnation point. *International Journal of Heat and Mass Transfer*, 20(12):1333–1338, 1977.

[77] A Hooshanginejad and S Lee. Droplet depinning in a wake. *Physical Review Fluids*, 2(3):031601, 2017.

[78] Z Hosseini, RJ Martinuzzi, and BR Noack. Sensor-based estimation of the velocity in the wake of a low-aspect-ratio pyramid. *Experiments in Fluids*, 56(1):13, 2015.

[79] H Hu, S Huang, and L Chen. Displacement of liquid droplets on micro-grooved surfaces with air flow. *Experimental Thermal and Fluid Science*, 49:86–93, 2013.

[80] H Hu, B Wang, K Zhang, W Lohry, and S Zhang. Quantification of transient behavior of wind-driven surface droplet/rivulet flows using a digital fringe projection technique. *Journal of Visualization*, 18(4):705–718, 2015.

[81] A Ianiro, D Violato, F Scarano, and G Cardone. Three dimensional features in swirling impinging jets. In *15th Int. Symposium on Flow Visualization, Minsk*, 2012.

[82] RG Jacobs and PA Durbin. Simulations of bypass transition. *Journal of Fluid Mechanics*, 428:185, 2001.

[83] CS James. Prediction of entrainment conditions for nonuniform, noncohesive sediments. *Journal of Hydraulic Research*, 28(1):25–41, 1990.

[84] J Jeong and F Hussain. On the identification of a vortex. *Journal of Fluid Mechanics*, 285:69–94, 1995.

[85] BM Jones. *The measurement of profile drag by the pitot-traverse method*. HM Stationery Office, 1936.

[86] RB Kalifa, S Habli, NM Saïd, H Bournot, and G Le Palec. Parametric analysis of a round jet impingement on a heated plate. *International Journal of Heat and Fluid Flow*, 57:11–23, 2016.

[87] SG Kandlikar and ME Steinke. Contact angles and interface behavior during rapid evaporation of liquid on a heated surface. *International Journal of Heat and Mass Transfer*, 45(18):3771–3780, 2002.

[88] J Kaplan. Heated windshield wiper system employing pulsed high speed fluid impingement jets for cleaning and ice/snow removal, May 12 2003. US Patent App. 10/435,305.

[89] K Kataoka, M Suguro, H Degawa, K Maruo, and I Mihata. The effect of surface renewal due to largescale eddies on jet impingement heat transfer. *International Journal of Heat and Mass Transfer*, 30:559–567, 1987.

[90] RJ Kind, MG Potapczuk, A Feo, C Golia, and AD Shah. Experimental and computational simulation of in-flight icing phenomena. *Progress in Aerospace Sciences*, 34:257–345, 1998.

[91] M Kiya and K Sasaki. Structure of a turbulent separation bubble. *Journal of Fluid Mechanics*, 137:83–113, 1983.

[92] K Knowles and M Myszko. Turbulence measurements in radial wall-jets. *Experimental Thermal and Fluid Science*, 17:71–78, 1998.

[93] M Kristiawan, A Meslem, I Nastase, and V Sobolik. Wall shear rates and mass transfer in impinging jets: Comparison of circular convergent and cross-shaped orifice nozzles. *International Journal of Heat and Mass Transfer*, 55:282–293, 2012.

[94] SA Kulinich and M Farzaneh. How wetting hysteresis influences ice adhesion strength on superhydrophobic surfaces. *Langmuir*, 25(16):8854–8856, 2009.

[95] DF Kurtulus, F Scarano, and L David. Unsteady aerodynamic forces estimation on a square cylinder by tr-piv. *Experiments in Fluids*, 42(2):185–196, 2007.

[96] MP Lamb, F Brun, and BM Fuller. Direct measurements of lift and drag on shallowly submerged cobbles in steep streams: Implications for flow resistance and sediment transport. *Water Resources Research*, 53(9):7607–7629, 2017.

[97] CJM Lasance and RE Simons. Advances in high-performance cooling for electronics. *Electronics Cooling*, 11:22–39, 2005.

[98] BE Launder and W Rodi. The turbulent wall jet. *Progress in Aerospace Sciences*, 19:81–128, 1981.

[99] H Lee and S Balachandar. Drag and lift forces on a spherical particle moving on a wall in a shear flow at finite re. *Journal of Fluid Mechanics*, 657:89–125, 2010.

[100] J Lee and S-J Lee. The effect of nozzle aspect ratio on stagnation region heat transfer characteristics of elliptic impinging jet. *International Journal of Heat and Mass Transfer*, 43:555–575, 2000.

[101] S Lei and S Zhang. Flexible 3-d shape measurement using projector defocusing. *Optics Letters*, 34(20):3080–3082, 2009.

[102] S Lei and S Zhang. Digital sinusoidal fringe pattern generation: Defocusing binary patterns vs focusing sinusoidal patterns. *Optics and Lasers in Engineering*, 48(5):561–569, 2010.

[103] D Lentink. Accurate fluid force measurement based on control surface integration. *Experiments in Fluids*, 59(1):22, 2018.

[104] WT Leung, SC Fu, and CYH Chao. Detachment of droplets by air jet impingement. *Aerosol Science and Technology*, 51(4):467–476, 2017.

[105] N Lin, HL Reed, and WS Saric. Effect of leading-edge geometry on boundary-layer receptivity to freestream sound. In *Instability, Transition, and Turbulence*, pages 421–440. Springer, 1992.

[106] ER Lindgren. Experimental study on turbulent pipe flows of distilled water. Technical report, Oklahoma State Univ. Stillwater School of Civil Engineering, 1965.

[107] JNB Livingood and P Hrycak. Impingement heat transfer from turbulent air jets to flat plates: a literature survey. *NASA Technical Memorandum*, 1973.

[108] J-C Loiseau, J-C Robinet, S Cherubini, and E Leriche. Investigation of the roughness-induced transition: global stability analyses and direct numerical simulations. *Journal of Fluid Mechanics*, 760:175–211, 2014.

[109] D Lytle and BW Webb. Air jet impingement heat transfer at low nozzle-plate spacings. *International Journal of Heat and Mass Transfer*, 37(12):1687–1697, 1994.

[110] L Ma, Z Zhang, Y Liu, and H Hu. An experimental investigation on the transient runback process of wind-driven water droplets over surfaces with different wettabilities. In *AIAA Scitech 2019 Forum*, page 0632, 2019.

[111] S Madani and A Amirfazli. Oil drop shedding from solid substrates by a shearing liquid. *Colloids and Surfaces A: Physicochemical and Engineering Aspects*, 441:796–806, 2014.

[112] FJ Maher. Wind loads on basic dome shapes. *Journal of the Structural Division*, 91(3):219–228, 1965.

[113] A Marmur. Wetting on hydrophobic rough surfaces: to be heterogeneous or not to be? *Langmuir*, 19(20):8343–8348, 2003.

[114] RH Martin and JM Buchlin. Jet impingement heat transfer from lobed nozzles. *International Journal of Thermal Sciences*, 50:1199–1206, 2011.

[115] EC Maskell. Progress towards a method for the measurement of the components of the drag of a wing of finite span. Technical report, Procurement Executive, Ministry of Defence, Royal Aircraft Establishment, 1972.

[116] PJ Mason and BR Morton. Trailing vortices in the wakes of surface-mounted obstacles. *Journal of Fluid Mechanics*, 175:247–293, 1987.

[117] J McClure and S Yarusevych. Instantaneous piv/ptv-based pressure gradient estimation: a framework for error analysis and correction. *Experiments in Fluids*, 58(8):92, 2017.

[118] J McClure and S Yarusevych. Planar momentum balance in three-dimensional flows: applications to load estimation. *Experiments in Fluids*, 60(3):41, 2019.

[119] T Michelis, S Yarusevych, and M Kotsonis. Response of a laminar separation bubble to impulsive forcing. *Journal of Fluid Mechanics*, 820:633–666, 2017.

[120] AJB Milne. Blown away: The shedding and oscillation of sessile drops by cross flowing air. 2013.

[121] AJB Milne and A Amirfazli. Drop shedding by shear flow for hydrophilic to superhydrophobic surfaces. *Langmuir*, 25(24):14155–14164, 2009.

[122] AJB Milne, B Defez, M Cabrerizo-Vílchez, and A Amirfazli. Understanding (sessile/constrained) bubble and drop oscillations. *Advances in Colloid and Interface Science*, 203:22–36, 2014.

[123] M Mitchell. *Gone with the Wind*. Random House, 2020.

[124] S Moghtadernejad, M Tembely, M Jadidi, N Esmail, and A Dolatabadi. Shear driven droplet shedding and coalescence on a superhydrophobic surface. *Physics of Fluids*, 27(3):032106, 2015.

[125] A Mohammed-Taifour and J Weiss. Unsteadiness in a large turbulent separation bubble. *Journal of Fluid Mechanics*, 799:383–412, 2016.

[126] N Moradian, DS-K Ting, and S Cheng. The effects of freestream turbulence on the drag coefficient of a sphere. *Experimental Thermal and Fluid Science*, 33(3):460–471, 2009.

[127] MV Morkovin. Bypass-transition research: issues and philosophy. In *Instabilities and Turbulence in Engineering Flows*, pages 3–30. Springer, 1993.

[128] D Murakami, H Jinnai, and A Takahara. Wetting transition from the cassie-baxter state to the wenzel state on textured polymer surfaces. *Langmuir*, 30(8):2061–2067, 2014.

[129] GE Myers, JJ Schauer, and RH Eustis. Plane turbulent wall jet flow development and friction factor. *Journal of Basic Engineering*, 85:47–53, 1963.

[130] V Narayanan, J Seyed-Yagoobi, and RH Page. An experimental study of fluid mechanics and heat transfer in an impinging slot jet flow. *International Journal of Heat and Mass Transfer*, 47:1827–1845, 2004.

[131] P Nardone and K Koll. Velocity field and drag force measurements of a cube and a hemisphere mounted on an artificial bed surface roughness. In *E3S Web of Conferences*, volume 40, page 05022. EDP Sciences, 2018.

[132] TS O'Donovan. Fluid flow and heat transfer of an impinging air jet. *Department of Mechanical and Manufacturing Engineering, University of Dublin*, page 145, 2005.

[133] S Okamoto. Turbulent shear flow behind a sphere placed on a plane boundary. *Turbulent Shear Flows*, 2:246–256, 1980.

[134] S Okamoto. Turbulent shear flow behind hemisphere-cylinder placed on ground plane. In *Turbulent Shear Flows 3*, pages 171–185. Springer, 1982.

[135] N Otsu. A threshold selection method from gray-level histograms. *IEEE Transactions on Systems, Man, and Cybernetics*, 9(1):62–66, 1979.

[136] Z Pan, J Whitehead, S Thomson, and T Truscott. Error propagation dynamics of piv-based pressure field calculations: How well does the pressure poisson solver perform inherently? *Measurement Science and Technology*, 27(8):084012, 2016.

[137] P Papadopoulos, L Mammen, X Deng, D Vollmer, and H-J Butt. How superhydrophobicity breaks down. *Proceedings of the National Academy of Sciences*, 110(9):3254–3258, 2013.

[138] CW Park and SJ Lee. Effects of free-end corner shape on flow structure around a finite cylinder. *Journal of Fluids and Structures*, 19(2):141–158, 2004.

[139] S Pieris, X Zhang, S Yarusevych, and S. D. Peterson. Evolution of coherent structures in a two-dimensional impinging jet. In *10th International Symposium on Turbulence and Shear Flow Phenomena , Chicago, IL, July 6-9*, 2017.

[140] Supun Pieris, Xueqing Zhang, Serhiy Yarusevych, and Sean D Peterson. Vortex dynamics in a normally impinging planar jet. *Experiments in Fluids*, 60(5):1–18, 2019.

[141] CO Popiel and O Trass. Visualization of a free and impinging round jet. *Experimental Thermal and Fluid Science*, 4:253–264, 1991.

[142] L Prandtl. Über flüssigkeitsbewegung bei sehr kleiner reibung. In *Verhandlungen des 3 Internationalen Mathematiker-Kongresses Heidelberg*, 1904.

[143] L Prandtl. Bemerkungen über die entstehung der turbulenz. *ZAMM-Journal of Applied Mathematics and Mechanics/Zeitschrift für Angewandte Mathematik und Mechanik*, 1(6):431–436, 1921.

[144] Y Qu. *The Songs of Chu: An Anthology of Ancient Chinese Poetry by Qu Yuan and Others*. Columbia University Press, 2017.

[145] D Ragni, BW Van Oudheusden, and F Scarano. Non-intrusive aerodynamic loads analysis of an aircraft propeller blade. *Experiments in Fluids*, 51(2):361–371, 2011.

[146] N Rajaratnam and KA Mazurek. Impingement of circular turbulent jets on rough boundaries. *Journal of Hydraulic Research*, 43:689–695, 2005.

[147] A Ramekar. Drag coefficient study of two wall-mounted obstacles. *Aerospace Department, University of Maryland*, page 95, 2018.

[148] A Razzaghi and A Amirfazli. Shedding of a pair of sessile droplets. *International Journal of Multiphase Flow*, 110:59–68, 2019.

[149] A Razzaghi, SA Banitabaei, and A Amirfazli. Shedding of multiple sessile droplets by an airflow. *Physics of Fluids*, 30(8):087104, 2018.

[150] I Reba. Applications of the coanda effect. *Scientific American*, 214:84–93, 1966.

[151] E Reshotko. Boundary-layer stability and transition. *Annual review of fluid mechanics*, 8(1):311–349, 1976.

[152] DE Rival and BW Van Oudheusden. Load-estimation techniques for unsteady incompressible flows. *Experiments in Fluids*, 58(3):20, 2017.

[153] IV Roisman, A Criscione, C Tropea, DK Mandal, and A Amirfazli. Dislodging a sessile drop by a high-reynolds-number shear flow at subfreezing temperatures. *Physical Review E*, 92(2):023007, 2015.

[154] S Roux, M Fénot, G Lalizel, L-E Brizzi, and E Dorignac. Experimental investigation of the flow and heat transfer of an impinging jet under acoustic excitation. *International Journal of Heat and Mass Transfer*, 54:3277–3290, 2011.

[155] A Saal, PM Seiler, D Rettenmaier, M Ade, IV Roisman, R Berger, H-J Butt, and C Tropea. Shuffling gait motion of an aerodynamically driven wall-bound drop. *Physical Review Fluids*, 5(9):094006, 2020.

[156] JB Sakipov. Experimental study of semibounded jets. *collection: Problems of Thermoenergetics and Applied Thermophysics [in Russian], no.1, Applied Thermophysics*, 1964.

[157] A Sarkar, N Nitin, MV Karwe, and RP Singh. Fluid flow and heat transfer in air jet impingement in food processing. *Journal of Food Science*, 69, 2004.

[158] E Savory and N Toy. The flow regime in the turbulent near wake of a hemisphere. *Experiments in Fluids*, 4(4):181–188, 1986.

[159] E Savory and N Toy. Hemisphere and hemisphere-cylinders in turbulent boundary layers. *Journal of Wind Engineering and Industrial Aerodynamics*, 23:345–364, 1986.

[160] E Savory and N Toy. The separated shear layers associated with hemispherical bodies in turbulent boundary layers. *Journal of Wind Engineering and Industrial Aerodynamics*, 28(1):291–300, 1988.

[161] M Sbragaglia, AM Peters, C Pirat, BM Borkent, RGH Lammertink, M Wessling, and D Lohse. Spontaneous breakdown of superhydrophobicity. *Physical Review Letters*, 99(15):156001, 2007.

[162] Ronald W Schafer. What is a savitzky-golay filter?[lecture notes]. *IEEE Signal Processing Magazine*, 28(4):111–117, 2011.

[163] JJ Schauer. The flow development and heat transfer characteristics of plane, turbulent, impinging jets. *Mechanical Engineering, Stanford University*, page 84, 1964.

[164] JJ Schauer and RH Eustis. *The flow development and heat transfer characteristics of plane turbulent impinging jets*. Dept. of Mechanical Engineering, 1963.

[165] AD Schleizer and RT Bonnecaze. Displacement of a two-dimensional immiscible droplet adhering to a wall in shear and pressure-driven flows. *Journal of Fluid Mechanics*, 383:29–54, 1999.

[166] H Schlichting and K Gersten. *Boundary-layer theory*. Springer, 2016.

[167] MW Schmeeckle and JM Nelson. Direct numerical simulation of bedload transport using a local, dynamic boundary condition. *Sedimentology*, 50(2):279–301, 2003.

[168] MW Schmeeckle, JM Nelson, and RL Shreve. Forces on stationary particles in near-bed turbulent flows. *Journal of Geophysical Research: Earth Surface*, 112(F2), 2007.

[169] JA Schmucker. *Experimental investigation of wind-forced drop stability*. Texas A&M University, 2012.

[170] JA Schmucker, JC Osterhout, and EB White. Speckle technique for dynamic drop profile measurement on rough surfaces. *Experiments in Fluids*, 52(1):123–136, 2012.

[171] H Schrader. *Trocknung feuchter Oberflächen mittels Warmluftstrahlen: Strömungsvorgänge und Stoffübertragung*. VDI-Verlag, 1961.

[172] GB Schubauer and PS Klebanoff. Contributions on the mechanics of boundary-layer transition. *NACA-TR-1289*, 1955.

[173] WH Schwarz and WP Cosart. The two-dimensional turbulent wall-jet. *Journal of Fluid Mechanics*, 10:481–495, 1961.

[174] A Sciacchitano and B Wieneke. Piv uncertainty propagation. *Measurement Science and Technology*, 27(8):084006, 2016.

[175] RA Seban and LH Back. Velocity and temperature profiles in a wall jet. *International Journal of Heat and Mass Transfer*, 3:255–265, 1961.

[176] PM Seiler, M Gloerfeld, IV Roisman, and C Tropea. Aerodynamically driven motion of a wall-bounded drop on a smooth solid substrate. *Physical Review Fluids*, 4(2):024001, 2019.

[177] A Sigalla. Measurements of skin friction in a plane turbulent wall jet. *The Aeronautical Journal*, 62:873–877, 1958.

[178] R Simon and E White. Vortex shedding and depinning of wind-forced liquid drops. In *APS Meeting Abstracts*, page G11.004, November 2018.

[179] RL Simpson, CH Long, and G Byun. Study of vortical separation from an axisymmetric hill. *International Journal of Heat and Fluid Flow*, 23(5):582–591, 2002.

[180] K Sodjavi, B Montagné, P Bragança, A Meslem, P Byrne, C Degouet, and V Sobolik. Piv and electrodiffusion diagnostics of flow field, wall shear stress and mass transfer

beneath three round submerged impinging jets. *Experimental Thermal and Fluid Science*, 70:417–436, 2016.

[181] R Tagore. *The gardener*. Macmillan, 1916.

[182] K Taira, SL Brunton, STM Dawson, CW Rowley, T Colonius, BJ McKeon, OT Schmidt, S Gordeyev, V Theofilis, and LS Ukeiley. Modal analysis of fluid flows: An overview. *AIAA Journal*, pages 4013–4041, 2017.

[183] T Tanaka and E Tanaka. Experimental studies of a radial turbulent jet: 2nd report, wall jet on a flat smooth plate. *Bulletin of JSME*, 20:209–215, 1977.

[184] Z Tang, N Rostamy, DJ Bergstrom, JD Bugg, and D Sumner. Incomplete similarity of a plane turbulent wall jet on smooth and transitionally rough surfaces. *Journal of Turbulence*, 16:1076–1090, 2015.

[185] S Taniguchi, H Sakamoto, M Kiya, and M Arie. Time-averaged aerodynamic forces acting on a hemisphere immersed in a turbulent boundary. *Journal of Wind Engineering and Industrial Aerodynamics*, 9(3):257–273, 1982.

[186] W Terra, A Sciacchitano, and F Scarano. Aerodynamic drag of a transiting sphere by large-scale tomographic-piv. *Experiments in Fluids*, 58(7):83, 2017.

[187] W Terra, A Sciacchitano, and YH Shah. Aerodynamic drag determination of a full-scale cyclist mannequin from large-scale ptv measurements. *Experiments in Fluids*, 60(2):29, 2019.

[188] A Theodorakakos, T Ous, M Gavaises, JM Nouri, N Nikolopoulos, and H Yanagihara. Dynamics of water droplets detached from porous surfaces of relevance to pem fuel cells. *Journal of Colloid and Interface Science*, 300(2):673–687, 2006.

[189] V Theofilis. Global linear instability. *Annual Review of Fluid Mechanics*, 43:319–352, 2011.

[190] V Thoreau, B Malki, G Berthome, L Boulange-Petermann, and JC Joud. Physico-chemical and dynamic study of oil-drop removal from bare and coated stainless-steel surfaces. *Journal of Adhesion Science and Technology*, 20(16):1819–1831, 2006.

[191] MJ Tummers, J Jacobse, and SGJ Voorbrood. Turbulent flow in the near field of a round impinging jet. *International Journal of Heat and Mass Transfer*, 54:4939–4948, 2011.

[192] BG van der Hegge Zijnen. Measurements of the velocity distribution in the boundary layer along a plane surface. *Electrical Engineering, Mathematics and Computer Science, Delft University of Technology*, page 48, 1924.

[193] BW Van Oudheusden. Piv-based pressure measurement. *Measurement Science and Technology*, 24(3):032001, 2013.

[194] BW Van Oudheusden, F Scarano, and EWF Casimiri. Non-intrusive load characterization of an airfoil using piv. *Experiments in Fluids*, 40(6):988–992, 2006.

[195] BW Van Oudheusden, F Scarano, EWM Roosenboom, EWF Casimiri, and LJ Souverein. Evaluation of integral forces and pressure fields from planar velocimetry data for incompressible and compressible flows. *Experiments in Fluids*, 43(2-3):153–162, 2007.

[196] D Violato, A Ianiro, G Cardone, and F Scarano. Three-dimensional vortex dynamics and convective heat transfer in circular and chevron impinging jets. *International Journal of Heat and Fluid Flow*, 37:22–36, 2012.

[197] M Visbal, D Rizzetta, and J Mathew. Large eddy simulation of flow past a 3-d bump. In *45th AIAA Aerospace Sciences Meeting and Exhibit*, page 917, 2007.

[198] AE Von Doenhoff and AL Braslow. The effect of distributed surface roughness on laminar flow. In *Boundary layer and flow control*, pages 657–681. Elsevier, 1961.

[199] RN Wenzel. Resistance of solid surfaces to wetting by water. *Industrial & Engineering Chemistry*, 28(8):988–994, 1936.

[200] EB White and JA Schmucker. A runback criterion for water drops in a turbulent accelerated boundary layer. *Journal of Fluids Engineering*, 130(6), 2008.

[201] EB White and JA Schmucker. Wind- and gravity- forced drop depinning. *arXiv preprint arXiv:2009.04059*, 2020.

[202] FM White. *Fluid mechanics*. Tata McGraw-Hill Education, 1979.

[203] FM White and I Corfield. *Viscous fluid flow*, volume 3. McGraw-Hill New York, 2006.

[204] PL Wiberg and JD Smith. Calculations of the critical shear stress for motion of uniform and heterogeneous sediments. *Water resources research*, 23(8):1471–1480, 1987.

[205] B Wieneke. Stereo-piv using self-calibration on particle images. *Experiments in Fluids*, 39(2):267–280, 2005.

[206] G Wolansky and A Marmur. Apparent contact angles on rough surfaces: the wenzel equation revisited. *Colloids and Surfaces A: Physicochemical and Engineering Aspects*, 156(1):381–388, 1999.

[207] JN Wood, G de Nayer, S Schmidt, and M Breuer. Experimental investigation and large-eddy simulation of the turbulent flow past a smooth and rigid hemisphere. *Flow, Turbulence and Combustion*, 97:79–119, 2016.

[208] OV Yakovlevskii and SY Krasheninnikov. Spreading of a turbulent jet impinging on a flat surface. *Fluid Dynamics*, 1:136–139, 1966.

[209] Q Ye, FFJ Schrijer, and F Scarano. Boundary layer transition mechanisms behind a micro-ramp. *Journal of Fluid Mechanics*, 793:132–161, 2016.

[210] Q Ye, FFJ Schrijer, and F Scarano. Geometry effect of isolated roughness on boundary layer transition investigated by tomographic PIV. *International Journal of Heat and Fluid Flow*, 61:31–44, 2016.

[211] Q Ye, FJ Schrijer, and F Scarano. On reynolds number dependence of micro-ramp-induced transition. *Journal of Fluid Mechanics*, 837:597–626, 2018.

[212] S Yokobori, N Kasagi, M Hirata, M Nakamaru, and Y Haramura. Characteristic behaviour of turbulence and transport phenomena at the stagnation region of an axi-symmetrical impinging jet. In *2nd Symposium on Turbulent Shear Flows*, pages 4–12, 1979.

[213] S Yokobori, N Kasagi, M Hirata, and N Nishiwaki. Role of large-scale eddy structure on enhancement of heat transfer in stagnation region of two-dimensional, submerged, impinging jet. In *Sixth International Heat Transfer Conference*, volume 5, pages 305–310, 1978.

[214] T Young. Iii. an essay on the cohesion of fluids. *Philosophical Transactions of the Royal Society of London*, (95):65–87, 1805.

[215] FY Zhang, XG Yang, and CY Wang. Liquid water removal from a polymer electrolyte fuel cell. *Journal of the Electrochemical Society*, 153(2):A225, 2005.

[216] X Zhang, BA Tuna, S Yarusevych, and SD Peterson. Flow development over isolated droplet-inspired shapes. *International Journal of Heat and Fluid Flow*, 88, 2021.

[217] X Zhang, S Yarusevych, and SD Peterson. Experimental investigation of flow development and coherent structures in normal and oblique impinging slot jets. *Experiments in Fluids*, 60(1):11, 2019.

Appendix A

Uncertainty Quantification of PIV-Based Flow Measurements

A.1 Uncertainties in mean flow statistics

Under the assumption of N independent samples and a normal distribution of experimental error, the uncertainty of mean velocity (taking streamwise velocity $\overline{u}$ as an exemplar) is [13]

$$\varepsilon_{\overline{u}} = \frac{\sigma_u}{\sqrt{N}}, \tag{A.1}$$

where σ_u is the standard deviations of velocity fluctuations. With $N \sim \mathcal{O}(10^3)$ temporally uncorrelated velocity samples, the uncertainty of mean velocity is minuscule.

A.2 Uncertainties in turbulent statistics

The uncertainty quantification of turbulent statistics is based on Sciacchitano and Wieneke [174]. The uncertainty of Reynolds normal stress (taking $\overline{u'u'}$ as an exemplar) and shear stress (taking $\overline{u'v'}$ as an exemplar) are given in Eq. A.2 and A.3, respectively, as

$$\varepsilon_{\overline{u'u'}} = \frac{1}{N-1}\sqrt{\frac{2}{N}}\sum_{p=1}^{N}(u_p - \overline{u})^2, \tag{A.2}$$

$$\varepsilon_{\overline{u'v'}} = \frac{1}{N-1}\sqrt{\frac{1+\rho_{uv}^2}{N}}\sqrt{\sum_{p=1}^{N}(u_p - \overline{u})^2}\sqrt{\sum_{p=1}^{N}(v_p - \overline{v})^2}, \tag{A.3}$$

where ρ_{uv} is the cross-correlation coefficient between velocity component u and v. For impinging jet flows, the non-time-resolved measurements (see Ch. 4) span over a duration of around 4×10^4 and 8×10^4 shedding cycles for Re = 3000 and Re = 6000, respectively. The time interval between two samples taken for mean flow field characteristics is at least 30 times the characteristic time scale of the flow [140]. For flow development over droplet models (see Ch. 5), the non-time-resolved stereo PIV measurements span over a duration of around 1.7×10^4 shedding cycles. The time interval between two samples taken for mean flow field characteristics is approximately 12 times the characteristic time scale of arch vortex shedding. It can thus be assumed for both flow configurations that $\rho_{uv} = 0$.

Spatial derivatives of velocity components are computed using central differencing scheme

$$\frac{\partial \overline{u_i}}{\partial x_j} = \frac{1}{2\Delta x_j}[u_i(x_i, x_j + \Delta x_j) - u_i(x_i, x_j - \Delta x_j)], \tag{A.4}$$

and the uncertainty of spatial derivatives is formulated as

$$\varepsilon_{\partial \overline{u_i}/\partial x_j} = \frac{\sqrt{2}\varepsilon_{\overline{u_i}}}{2\Delta x_j}. \tag{A.5}$$

Propagating uncertainties in Eqs. A.2, A.3, and A.5 into TKE (defined in Eq. 4.6) and $\mathcal{P}$ (defined in Eq. 4.7) leads to

$$\varepsilon_{TKE} = \sqrt{\varepsilon_{\overline{u'u'}} + \varepsilon_{\overline{v'v'}} + \varepsilon_{\overline{w'w'}}}, \tag{A.6}$$

$$\varepsilon_{\mathcal{P}} = \sqrt{[(\overline{u'u'})^2 + 2(\overline{u'v'})^2 + (\overline{v'v'})^2]\varepsilon^2_{\partial\overline{u}/\partial y} + (\frac{\partial \overline{u}}{\partial x})^2\varepsilon^2_{\overline{u'u'}} + (\frac{\partial \overline{u}}{\partial y} + \frac{\partial \overline{v}}{\partial x})^2\varepsilon^2_{\overline{u'v'}} + (\frac{\partial \overline{v}}{\partial y})^2\varepsilon^2_{\overline{v'v'}}}. \tag{A.7}$$

For flow development over droplet models (see Ch. 5), all three velocity components are directly measured using stereo PIV. For impinging jets, the spanwise velocity fluctuations $\varepsilon_{\overline{w'w'}}$ can be estimated from the 2D-2C PIV measurements within the xy plane under the assumption of isotropic turbulence, formulated as

$$\varepsilon_{\overline{w'w'}} = \frac{\varepsilon_{\overline{u'u'}} + \varepsilon_{\overline{v'v'}}}{2}. \tag{A.8}$$

A.3 Uncertainties of curve-fitting

Growth rate γ_i and decay rate ζ discussed in Ch. 4 are acquired from fitting power-law equations to the experimental data. Taking X as the argument, Y as the dependent variable, and α as the power-law coefficient, Eq. 4.4 and 4.3 can be generalized as

$$Y = X^{\alpha}. \tag{A.9}$$

Taking logarithms of both sides of Eq. A.9, α can be calculated by finding a linear regression function of data $1/\ln(X)$ and $\ln(Y)$ which satisfies

$$\alpha = \frac{\ln(Y)}{\ln(X)}. \tag{A.10}$$

Two types of errors contribute to the uncertainty of α: (i) errors from PIV measurements $\varepsilon_{\alpha 1}$, and (ii) errors from linear regression $\varepsilon_{\alpha 2}$.

$$\varepsilon_\alpha = \sqrt{\varepsilon_{\alpha 1}^2 + \varepsilon_{\alpha 2}^2} \tag{A.11}$$

Error from PIV measurements

The error from the measurements of X and Y propagates into α by adding in quadrature,

$$\varepsilon_{\alpha 1} = \sqrt{\left(\left.\frac{\partial \alpha}{\partial X}\right|_{X=\overline{X}}\right)^2 (\varepsilon_X)^2 + \left(\left.\frac{\partial \gamma}{\partial Y}\right|_{Y=\overline{Y}}\right)^2 (\varepsilon_Y)^2}. \tag{A.12}$$

Specifically, the equation is written as

$$\varepsilon_{\alpha 1} = \sqrt{\left[\frac{1/\overline{Y}}{\ln(\overline{X})}\right]^2 (\varepsilon_Y)^2 + \left[-\frac{\ln(\overline{Y})}{[\ln(\overline{X})]^2}\frac{1}{\overline{X}}\right]^2 (\varepsilon_X)^2} \tag{A.13}$$

In both Eq. 4.4 and 4.3, X takes the value of wall location x. The error of x-coordinates comes from PIV calibration, which can be estimated as half of the pixel size. With a pixel size of 7.4μm and a magnification factor of $M = 0.148$,

$$\varepsilon_x = \frac{1/2 \text{ px}}{M} \approx 0.025\text{mm}. \tag{A.14}$$

In Eq. 4.4, Y takes the value of wall-normal location $y_{1/2,i}$. $y_{1/2,i}$ is calculated by linear interpolation between two vector locations, and thus the uncertainty can be estimated as half of the vector pitch,

$$\varepsilon_Y = \frac{1/2 \text{ vector pitch}}{M} \approx 0.3\text{mm}. \tag{A.15}$$

In Eq. 4.3, Y takes the value of the local maximum streamwise velocity $u_{\max}$, the uncertainty of which is quantified following the formulation in Sect. A.1.

Error from curve fitting

The error from curve fitting is evaluated from the coefficient of determination R^2 [62],

$$\frac{\varepsilon_{\alpha 2}}{\alpha} = \sqrt{\frac{\frac{1}{R^2} - 1}{N - 2}}. \tag{A.16}$$

Appendix B

Gaussian Filter Parameters for Decomposition of Velocity Fluctuations

Gaussian moving-average filter is defined following [75] and is given by

$$g(t) = \frac{1}{\sqrt{2\pi}\sigma} e^{-\frac{t^2}{2\sigma^2}}, \tag{B.1a}$$

$$< u >_G (t) = \int_{-\infty}^{\infty} u(\tau) g(t-\tau) \mathrm{d}\tau. \tag{B.1b}$$

The bandwidth of the Gaussian filter is defined based on the integral timescale of the velocity fluctuations, which is obtained from the auto-correlation coefficients of the temporal coefficients of the first symmetric POD mode ($\Phi^1_{s+\Delta}$, see Sect. 5.2.2 for definition). As shown in Fig. B.1, a Gaussian function is fitted to the correlation coefficients and the integral timescale $1/f_\tau$ is calculated as two standard deviations of the fitted Gaussian

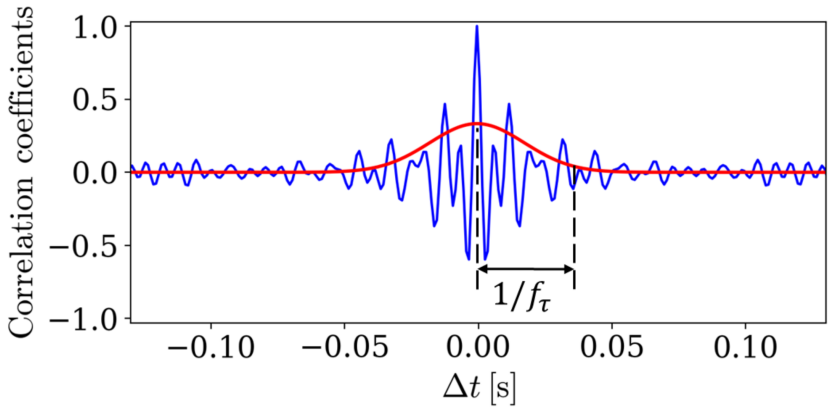

Figure B.1: Integral timescale of the first symmetric POD mode ($\Phi^1_{s+\Delta}$) of the unfiltered velocity field.

distribution. The frequencies corresponding to the integral timescales for the chopped, sessile, and the runback models are $f_\tau = 1/6 f_c$, $f_\tau = 1/8 f_c$, and $f_\tau = 1/5 f_c$, respectively, with f_c representing their respective shedding frequencies of K-H vortices. To satisfy the Nyquist criterion, the cut-off frequency is set at $2f_\tau$, and thus bandwidths of $\sigma = \sqrt{1/6}/f_c$, $\sqrt{1/8}/f_c$, $\sqrt{1/5}/f_c$ is obtained for the Gaussian filter applied on the chopped, sessile, and runback models.

Appendix C

Selection of Droplet Depinning Criteria

Droplet depinning is identified from the side-view droplet images when the pixel displacement of the upstream contact point exceeds the pixel threshold. Using large pixel displacement threshold for droplet depinning identification increases the bias error, since it requires the droplets to displace a longer distance after depinning; small pixel displacement threshold reduces the bias error, but on the other hand, increases the random error due to optical aberrations. To minimize the overall error of the procedure, pixel displacement threshold is systematically increased from 1 px to 100 px to find the depinning velocity of each test run of a given droplet volume, flow acceleration, and flow configuration. Mean and standard deviation in depinning velocities over the fourteen test runs are calculated for each pixel displacement threshold. Difference in mean depinning velocity between two consecutive thresholds ('mean differential') is then calculated to reflect the 'bias' in depinning velocity due to the increment of one pixel.

Fig. C.1 shows the typical results of 'mean differential' (blue markers) and 'standard

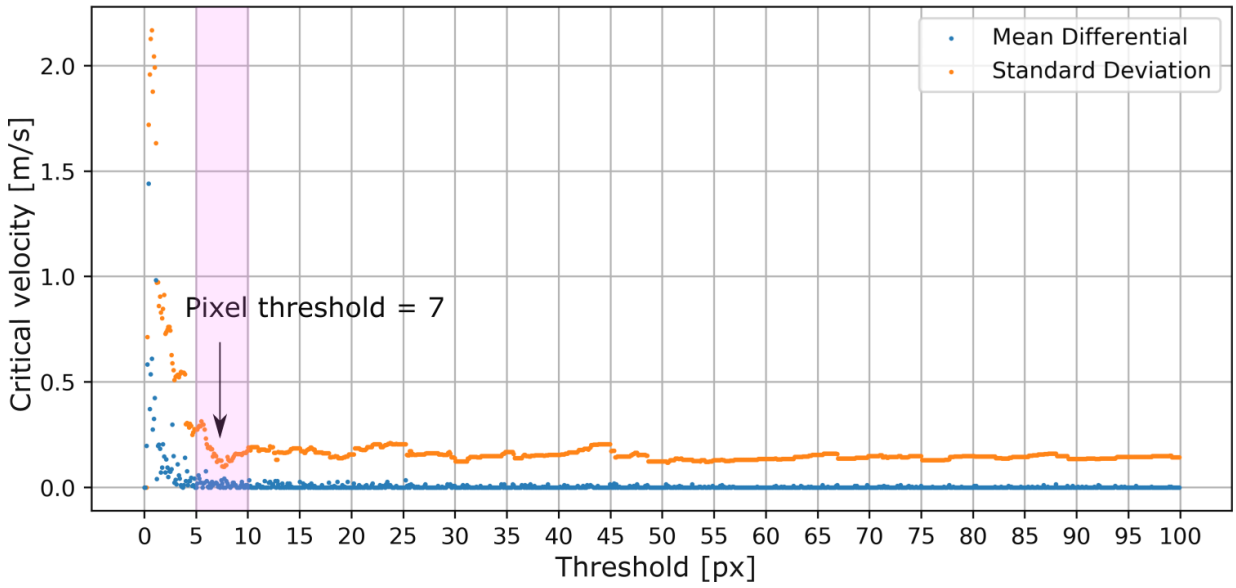

Figure C.1: Typical procedure of pixel threshold selection. The result of 75 μL droplets under the impact of shear flow formed at $x^* = 20$ mm downstream of the stagnation point of an $\alpha = 45°$ accelerating impinging jet at $\mathrm{d}U_j/\mathrm{d}t = 2.2$ m/s is shown as exemplar. Blue markers: difference in mean critical depinning velocity determined by two consecutive pixel thresholds; Orange markers: standard deviation in critical depinning velocities identified by a given pixel threshold over fourteen droplet samples.

deviation' (amber markers) over the threshold range tested. The optimum threshold is chosen where both 'mean differential' and 'standard deviation' depinning velocity are small and their changes with pixel increment level off. For the example given in Fig. C.1, these are observed in the range of 5 to 10 px; the threshold of 7 px is chosen manually from this range.

The threshold eventually used for a given flow configuration is the mean of the thresholds identified for all the droplet volumes and flow accelerations tested for this configuration (see Table C.1).

Table C.1: Pixel threshold for droplet depinning.

Incoming flow angle α [°]	Droplet initial location x^* [mm]	Depinning threshold [px]
0	650	8
45	20	7
45	40	6
45	50	6
45	70	7
90	70	6
30	60	6
60	50	6

Appendix D

Mean Droplet Side-View Geometry at Depinning

Figs. D.1 shows mean droplet side-view contours acquired under shear flows formed by flow configurations as summarized in Table 3.6. In each subplot, mean contours of all droplet volumes and flow accelerations tested are overlaid. When normalized with the respective initial height and length of each droplet tested, the mean contours at depinning under a given combination of incoming flow angle and initial droplet location show similarity across all droplet volumes.

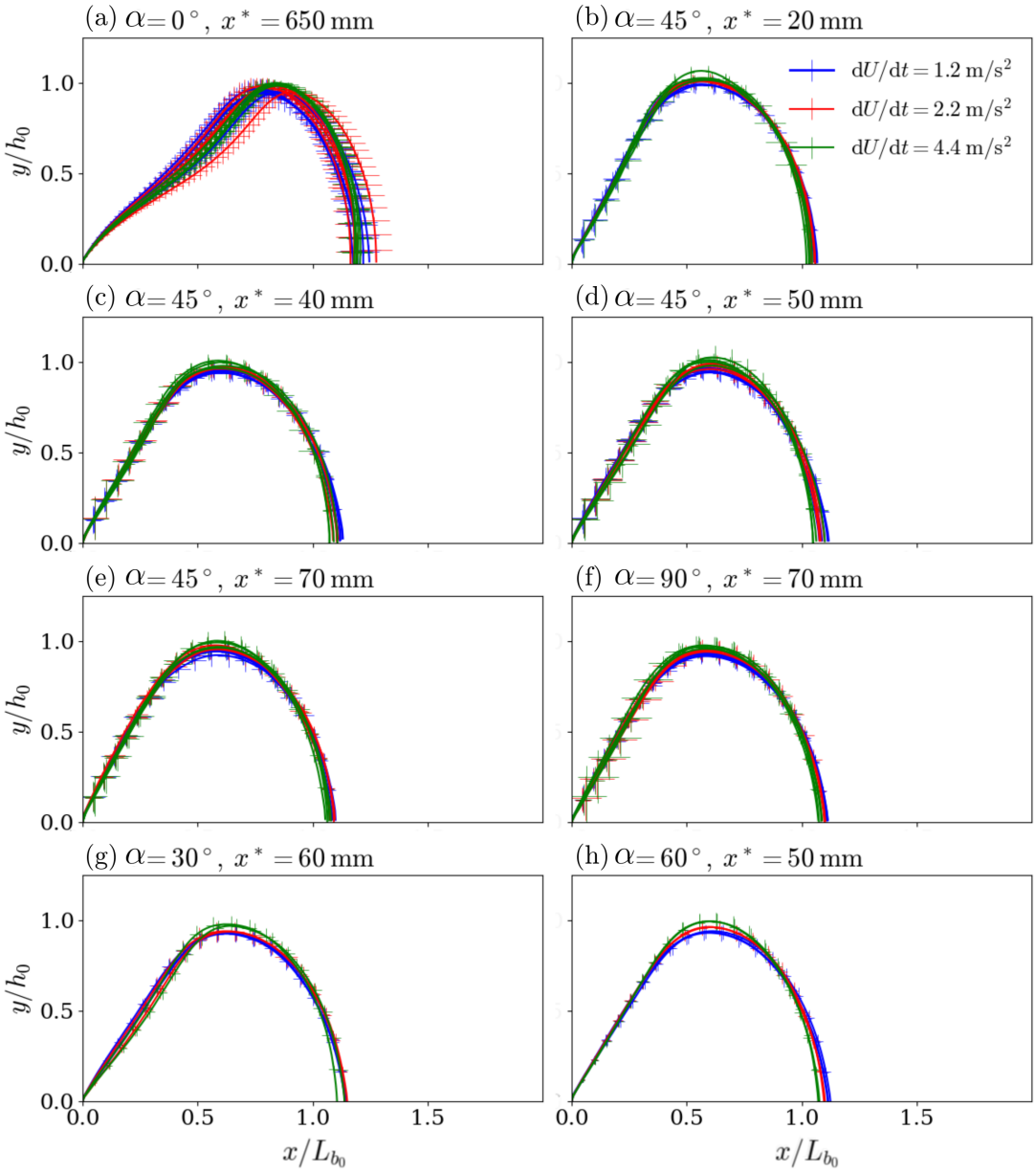

Figure D.1: Mean side-view geometry of droplets prior to depinning under shear flows formed by flow configurations as summarized in Table 3.6. Lengths in horizontal and vertical directions are normalized by initial droplet contact length and height, respectively.